ITTC2024

30TH INTERNATIONAL TOWING TANK CONFERENCE
22–27 SEPTEMBER 2024 | HOBART TASMANIA AUSTRALIA

Report of the Ocean Engineering Committee

OCEAN ENGINEERING COMMITTEE

1. INTRODUCTION

1.1 Membership and Meetings

The members of the Ocean Engineering Committee of the 30th ITTC are:

- Prof. Longfei Xiao (Chair), Shanghai Jiao Tong University, China;
- Prof. Yasunori Nihei, Osaka Prefecture University, Japan;
- Dr. Nuno Fonseca, SINTEF Ocean, Norway;
- Prof. Narakorn Srinil, Newcastle University, United Kingdom;
- Dr. Nick Markov, Bulgarian Ship Hydrodynamics Centre, Bulgaria;
- Dr. Guillaume Ducrozet, École Centrale de Nantes, France;
- Dr. Hasanat Zaman, National Research Council of Canada, Canada;
- Prof. Kwang-Hyo Jung, Pusan National University, Korea;
- Dr. Pedro Mello, University of São Paulo, Brazil.

Two virtual committee meetings have been held during the work period:

- Virtual meeting, December 19th, 2022;
- Virtual meeting, January 16th, 2023.

1.2 Tasks based on the Recommendations of the 29th ITTC

The Ocean Engineering Committee covers moored and dynamically positioned ships and floating structures. For the 30th ITTC, the modelling and simulation of waves, wind and current is the primary responsibility of the Ocean Engineering Committee with the cooperation of the Seakeeping and the Stability in Waves Committees.

The recommendations for the work of the Ocean Engineering Committee as given by the 29th ITTC were as follows:

(1) Update the state-of-the-art for predicting the behaviour of bottom founded or stationary floating structures, including moored and dynamically positioned ships, emphasizing developments since the 2021 ITTC Conference. The committee report should include sections on:

   a. the potential impact of new technological developments on the ITTC;

   b. new experimental techniques and extrapolation methods;

c. new benchmark data;

d. the practical applications of computational methods for prediction and scaling;

e. the need for R&D for improving methods of model experiments, numerical modelling and full-scale measurements.

(2) Review ITTC Recommended Procedures relevant to ocean engineering, including CFD procedures, and

a. identify any requirements for changes in the light of current practice, and, if approved by the Advisory Council, update them;

b. identify the need for new procedures and outline the purpose and contents of these.

(3) Review and identify areas of concern in modelling and simulation of waves, wind and currents. In particular:

a. report on methods to generate extreme wave packets for studying responses to extreme waves in a towing tank. Examine the effects of wave breaking and statistics of occurrence on the wave spectrum, its spectral shape, extreme wave generation, and the role of wind-wave interaction on wave breaking occurrence;

b. investigate the influence of the vertical wind profile on the aerodynamic loads experienced by platforms and other offshore objects. Develop a standard vertical wind profile for model testing purposes and methods for modeling it both numerically and experimentally.

c. Continue work on using a small controllable fan to mimic forces developed during a floating offshore wind turbine test due to the turbine itself. Expand the work on Software-in-the-Loop (SiL) systems for modeling wind turbine loads to be used as a general tool to model many types of wind loads. For example, wind loads on a ship during a maneuvering in waves test. Liaise with the SC on Ocean Renewable Energy and the Seakeeping Committee.

d. Develop specifications for a benchmark test program for wind loads and their influence on the motions of floating structures. Compare wind loads developed using SiL to model the wind loads versus using fans to produce an actual model scale wind. Among other data, repeatability, and consistency between the methods and between different facilities should be reported. The benchmark study may also include CFD comparisons.

e. Report on state-of-the-art for wave-current interactions. In particular, the role played in terms of the generation of extreme waves.

(4) Review the state-of-the-art in offshore aquaculture systems since the 2021 report of the Ocean Engineering committee including large volume closed containment systems, extreme wave environments, and modelling of entire systems.

(5) The benchmark tests with the square cylinders are complete. However, it is recommended that, owing to the complicated wave-column interactions, more experimental and CFD studies should be considered for four-column cases with different configurations and more extreme waves such as focused waves. In addition, local wave impact loads on the columns are also critical and deserve further in-depth studies.

(6) The work on the CFD benchmark study of two-bodies in close proximity shall be continued. Smaller gaps need to be studied

and the procedure for 2-body model tests shall be updated based on the CFD benchmark study.

(7) Investigate extraction methods of nodules from the seabed. Develop a guideline for testing Nodule Mining Machines in a towing tank including their riser systems.

(8) Investigate testing methods to characterise the influence of changing bottom bathymetry and coastline for tankers at offloading terminals.

2. REVIEW OF STATE-OF-THE-ART

2.1 Bottom Founded Structures

Bottom founded structures are widely used as production or oil recovering platforms in shallow or moderate waters but have been also applied as offshore wind turbine supporting structures in recent years.

Zhang & Teng (2021) present the development of a time-domain nonlinear potential flow model based on the weak scatterer approximation using High-Order BEM to deal with the interaction of surface-piercing bodies and moderately steep waves. The main objective of their work is to provide an improved numerical model for computing higher-harmonic wave loads and ringing response of offshore wind turbine foundations. The numerical model is validated on the classical configuration of a vertical cylinder subjected to regular waves of different steepnesses. The wave runup profile around the cylinder as well as the higher-harmonic wave forces are studied and compared to different nonlinear wave models and experiments. Finally, the ringing response of a monopile in moderately steep focused waves is investigated for several wave conditions. The effects of peak frequency, input wave amplitude and damping ratio on the ringing response are discussed. The importance of including higher-harmonic components for an accurate estimate of the response, especially for large wave steepness and small damping ratio is demonstrated.

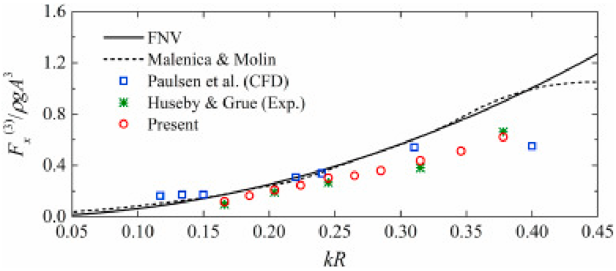

Figure 1: Amplitudes of the third-harmonic horizontal force on the vertical cylinder (Zhang & Teng, 2021)

Kim et al (2021) evaluates higher-order diffraction forces on vertical cylinders using a 3D fully nonlinear numerical wave tank (NWT). The NWT accurately determines hydrodynamic pressure using potential theory, the boundary element method, and a mixed Eulerian-Lagrangian (MEL) approach. In the fully nonlinear NWT simulation, all higher-order terms are produced simultaneously using a fast Fourier transformation (FFT). The results demonstrate an increased third-order sum-frequency force in shallow water long waves when compared to experiments and perturbation-based data. The incident waves are linear, Stokes 2nd and 3rd order waves. Results are compared for hydrodynamic pressure, and forces for different mono- and bichromatic waves on the cylinder surface for first-order, second-order mean-double, and third-order triple frequency waves altogether.

Suja-Thauvin et al. (2020) conducted model experiments of a monopile structure subjected to different severe irregular sea states, see Figure 2. The experimental model was designed to reproduce the first and second natural frequencies of the NREL 5MW reference wind turbine monopile. The paper compares the experimental results to four different hydrodynamical models of increasing complexity: i) Morison equation with second-order wave kinematics, ii) Morison equation with fully-nonlinear wave (FNL) kinematics, iii) model proposed by Kristiansen and Faltinsen, with FNL kinematics and iv) the model proposed by Rainey, with FNL kinematics. Those hydrodynamical loads are then used as input in a finite element solver. The Morison equation with second-order kinematics matched the main population of events well but underestimated the largest measured shear forces. The models using fully non-linear kinematics predicted the most extreme shear forces reasonably well, but they were not in general conservative. These three force models generally matched the main population of measured acceleration reasonably well, with underprediction, however, of the extreme accelerations. It was found that the models generally overpredicted the first mode acceleration but underpredicted the second mode acceleration for large response events. This was expected since no slamming load model is implemented in the current analysis.

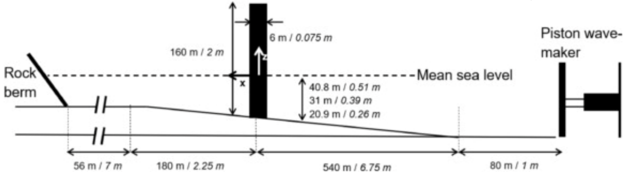

Figure 2: Experimental set-up (Suja-Thauvin et al., 2020)

Moghtadaei et al. (2022) utilized a RANS (Reynolds Average Navier-Stokes) model employing the volume of fluid (VOF) method to assess wave kinematics, shear forces, and moments arising from the interaction of near-breaking to weakly nonlinear waves with a bottom-seated cylindrical pile, representing a 5MW wind turbine. This comprehensive study incorporates both regular and irregular waves, with the latter adopting JONSWAP wave spectra. To address turbulence effects, a k-w model is employed. To validate the numerical model, relevant experiments are conducted. In these experiments, a load cell is integrated at the point where the cylinder meets the bottom of the wave basin, enabling the recording of time series data for shear force and bending moment resulting from wave loads induced by the incoming wave field. The findings reveal that inertia force dominates the shear force in all regular waves. For irregular waves, a larger KC number leads to the amplification of higher-order wave loads. The paper highlights that the nonlinearity of wave forces is a consequence of the interplay between inertia forces from nonlinear waves, diffraction, and associated turbulence.

The analysis of Vijoy et al. (2020) involves utilization of the two-dimensional small-amplitude water wave theory to study the interaction of gravity waves with a normally incident monochromatic wave when Bragg breakwaters are present. In this study, they investigated wave scattering caused by multiple submerged structures of various shapes, including rectangular, trapezoidal, semi-trapezoidal, triangular, semicircular, and quarter-circular configurations. The research returns reflection, transmission and energy loss coefficients. Additionally, the study examines the effects of structural width, thickness, barrier spacing, number of structures, and their specific shapes in the interaction processes.

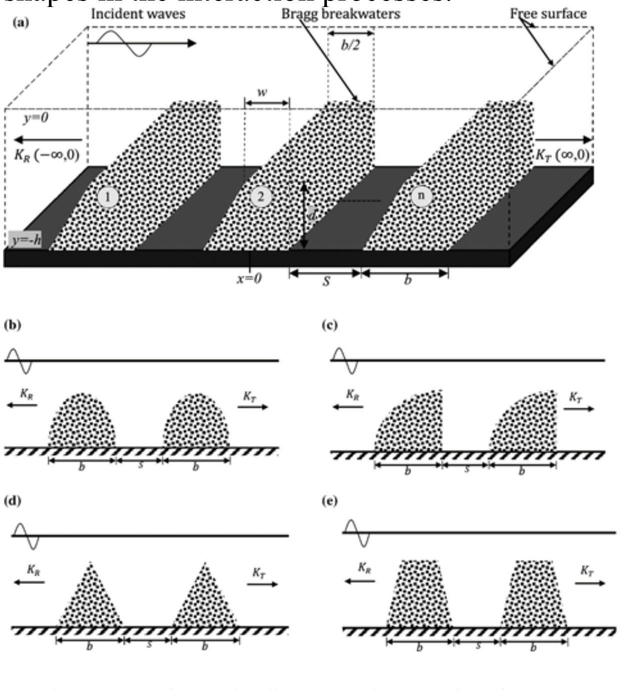

Figure 3: Schematic diagram of Bragg breakwaters having a) semi-trapezoidal, b) semicircular, c) quarter-circular, d) triangular, and e) trapezoidal configurations (Vijoy et al., 2020)

The comparison between impermeable and porous breakwaters clearly shows that the impermeable ones exhibit higher transmission coefficients. Due to the increased reflections, the trapezoidal and semi-trapezoidal shapes demonstrate lower transmission capabilities.

Multiple triangular structures damp waves minimally. As the breakwater number increases, Bragg's reflection sharpens and bandwidth decreases; quarter-circular shapes minimize this effect compared to others.

In their work, Mackay et al. (2021) introduce a boundary element method (BEM) model for analyzing wave forces on structures featuring both porous and solid surfaces. This model accommodates porous surfaces with linear or quadratic pressure-velocity relations. Notably, for quadratic pressure-velocity relationships, the model concurrently addresses the structure's combined motion response and wave forces. Moreover, the model encompasses solutions for diffraction and radiation scenarios as specific cases.

The credibility of their approach is evidenced by an analytical solution applied to a submerged vertical cylinder featuring a porous outer boundary. This arrangement operates under a linear pressure-velocity relation for excitation forces and the far-field drift force. Their technique effectively mitigates the impact of irregular frequencies on different forces. They investigated wave forces on a porous-solid truncated cylinder with a quadratic pressure system. The outer cylinder generally amplifies excitation force and added mass compared to no outer cylinder. Notably at low and high frequencies, where radiation damping is weak, porous surface dissipation notably boosts damping. This combined increase in added mass and damping reduces the resonant frequency and motion response amplitude.

Stansberg (2020) studies the impact loads on horizontal decks with a particular application to Gravity-Based Structures (GBS). To address this problem from the practical point of view, he proposes a simple a simple 2D analytical slamming model, based on the rise velocity from the incoming wave elevation. Based on previous GBS wave-in-deck experiments and despite a significant random scatter in the results (that increases with increasing velocities), reasonable correlation between measured deck impact loads (see Figure 4) and the underlying wave rise velocity is demonstrated, corroborating the idea underlying the simple model development. This is confirmed with the overall good comparison between the simple model and the experiments, especially regarding the fact that the model provides an approximate upper limit for the measured impact loads.

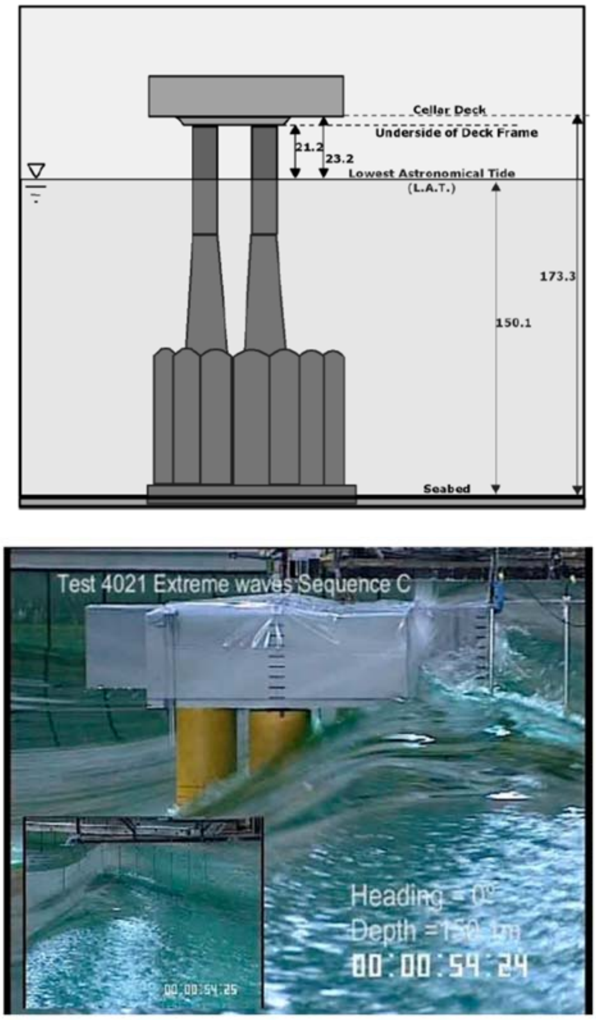

Figure 4: Experimental arrangement of the GBS (top) and picture of the wave impact on the GBS (bottom) (Stansberg, 2020)

Mackay et al. (2021) present a numerical and experimental study dealing with the interaction of waves with fixed and floating porous cylinders, see Figure 5. The paper focuses on wave forces on fixed porous cylinders with and without a solid inner cylinder and wave-induced motions of floating cylinder with and without a porous outer cylinder. The numerical model is based on Boundary Element Method (BEM) with a pressure drop proportional to the square of the velocity across porous surface. Its ability to accurately predict the nonlinear variation of the forces with wave amplitude or motion amplitude is demonstrated. The addition of a porous outer cylinder to a solid vertical cylinder increases the excitation force on the combined structure. However, it is shown that for low Keulegan Carpenter numbers, the damping coefficient for a porous cylinder is significantly higher than the viscous damping on a solid cylinder, which could be interesting for the damping of floating structures.

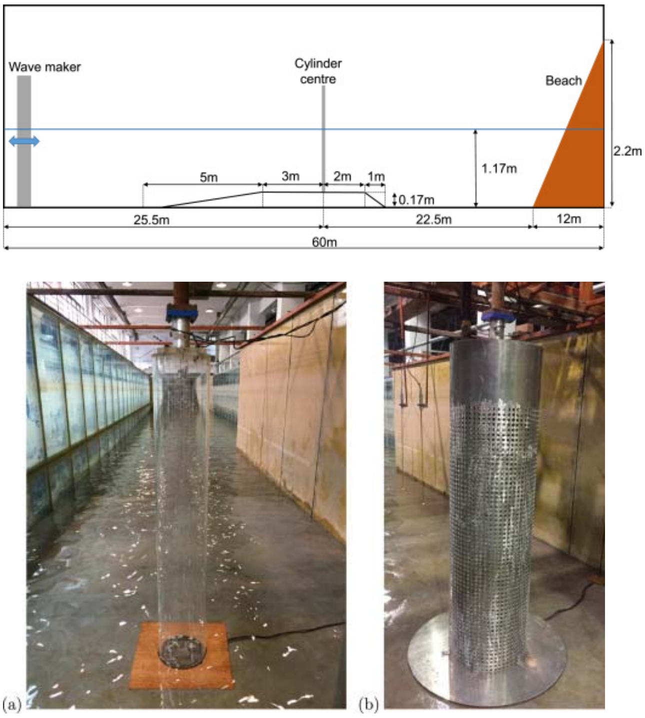

Figure 5: General experimental set-up (top) and picture of the solid cylinder (bottom left) and porous cylinder (bottom right) (Mackay et al., 2021)

Shi et al (2023) studied how the ice-breaking cones affect the nonlinear force and runup on the monopile in a focused wave group by a three-dimensional numerical. They used the commercial Star-CCM+ tool to integrate the VOF technique with the incompressible Navier-Stokes equations. A phase decomposition method through a ‘Stokes-like’ formulation was adopted to extract and investigate higher harmonics. In a viscous numerical wave tank, numerical simulations are run. They reported that comparing the installed ice-breaking cone to the uninstalled cone, the second harmonic coefficient typically rises by about 40%. They stated that an upward-downward-type ice-breaking cone increases the third harmonics, whereas an inverted-type ice-breaking cone exhibits the opposite behavior when compared with the uninstalled cone.They showed that the presence of two ice-breaking cone types raises wave loads. Contrary to monopiles, upward-downward cones boost wave load by about 6%, while inverted cones boost it by 1.5 to 3 times, depending on the wave's steepness and the amount of cone edge-induced breaking. They also compared the locations of the highest and lowest runup in the presence and absence of ice-breaking cones.

Li and Fuhrman (2022) used a coupled higher-order boundary element method (HOBEM) with FEM. A weak-scattering approach determined higher harmonic loads, while the linear Euler-Bernoulli beam model assessed structural ringing response. They reported that the peak force resulting from initial wave breaking can be accurately predicted without any turbulence model but for the prediction of the secondary force, a turbulence model is necessary as the process involves both turbulence production and flow separation behind the vertical pile. They observed that the Reynold stress–ω model is more accurate than a two-equation k–ω turbulence model for the prediction of the secondary load due to better prediction of flow separation points and vorticity.

In Zeng et al. (2021), the effects of breaking wave impact on a monopile-type offshore wind turbine installed at different locations at the edge of a 1:25 slope are investigated. The paper covers a numerical study that makes use of StarCCM+, a commercial CFD model using VoF method and solving Unsteady RANS equations. Dedicated experiments are also included, with the aim of validating the numerical results, see Figure 6. This is achieved through comparisons of the wave run-up around the monopile and of the forces induced by the waves. Accurate comparisons between experiments and simulations are reported, validating the CFM model that is used afterwards to investigate the wave breaking evolution and impact kinematics for different monopile locations.

Bachynski et al. (2020) report an experimental study dealing with flexible monopile subjected to a set of regular and irregular waves with different seeds, see Figure 7. Compared to the previous campaigns, the larger diameter, inclusion of several damping levels, and increased number of realizations and repetitions allow for drawing new conclusions. The importance of the steepness of the sea state is pointed out: the extreme accelerations, shear forces, and base bending moment tend to be larger for the highest steepness rather than the largest Hs. Furthermore, increasing the damping ratio tends to decrease the accelerations and bending moment for the main body of responses (Pexc > 0:01), but does not have a significant effect on the largest events. In addition, qualitative differences in the exceedance probability distribution of the nacelle acceleration and base shear were noted. Modal contributions to bending moment, shear force, and acceleration near first and second natural frequency are studied. It is found that the importance of the quasi-static response decreases for the largest events, while the importance of the responses at the second mode natural frequency tends to increase. Finally, the correlation between large nacelle accelerations and the wave breaking limits was not as clear as in previous tests

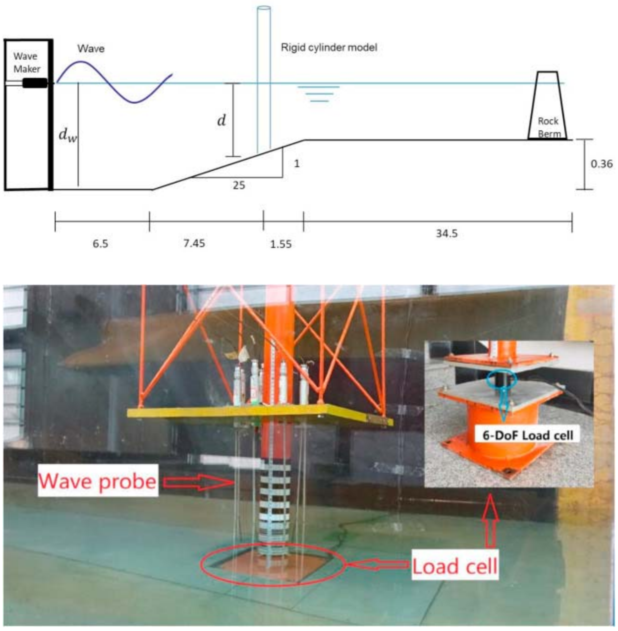

Figure 6: Sketch of the experimental set-up (top) and picture of the arrangement (bottom) (Zeng et al., 2021)

Leroy et al. (2021) present a hydro-elastic model that includes a non-linear hydrodynamic solver based on weak-scatterer approach, coupled to a structural solver based on flexible modes pre-computed from a FEM model. This new model is compared to a more conventional approach based on Morison solver for the hydrodynamic part. The application case studied in the paper is an offshore wind turbine on a monopile foundation. The numerical results are compared to experimental measurements made on a flexible 1/50 Froude-scaled model, which includes the wind turbine tower and an RNA mass and damper and which respects Froude-scaled modal frequencies, see Figure 7 and Bachynski et al. (2020). The load cases include a series of regular waves, with various steepnesses and periods that allowed to characterize the capabilities of the new model.

Teng and Liu (2023) describe an approach in which the incident and scattered wave components of the problem are isolated during computation. They proposed to evaluate the incident wave component using a spectral model. They utilized a coupled higher-order boundary element method (HOBEM) and finite element method (FEM) model based on a weak-scattering approximation for the solution of the scattered wave, where the fluid field would be predicted using HOBEM, and the resulted response would then be addressed using the FEM. To determine the structural ringing response for the monopile foundations of an offshore wind turbine, the linear Euler-Bernoulli beam model was used in their work. When compared to the pertinent published data, they found good agreement for wave elevations and loads. They claimed that the third-harmonic motion or ringing was most intense when the focal position was set at the center of the monopile and that the maximum positive and negative moments appeared when the focused position was on the downstream and upstream sides. The computational domain is shown in Figure 8.

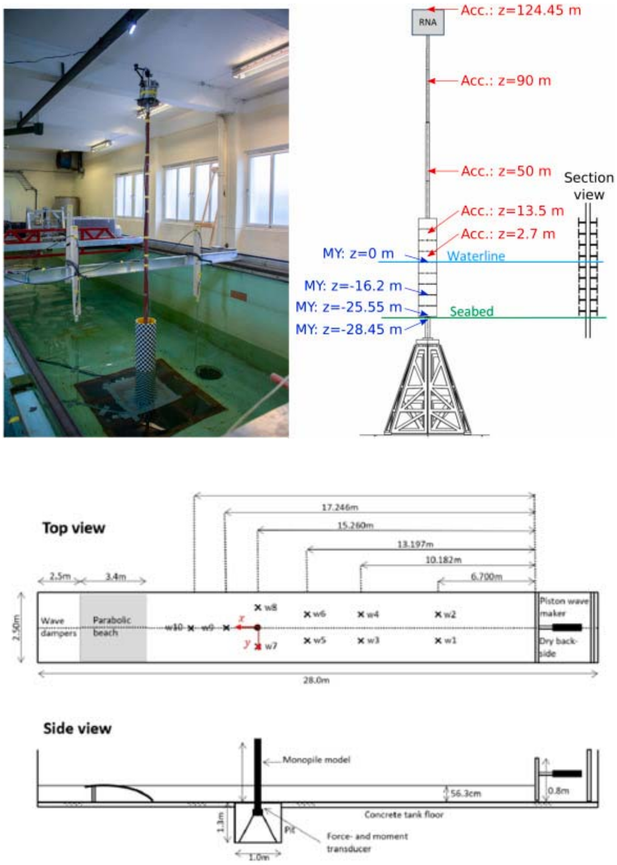

Figure 7: Picture and details of the experimental set-up (Bachynski et al., 2020))

In Jahani et al. (2022), a review of the most important concerns related to the structural dynamics of offshore wind turbines (OWTs) is presented. This details the importance of modal alignment in OWTs. Then, recent articles on aeroelasticity, hydroelasticity and vibrations of OWTs are reviewed. This is followed by a study on the interactions between OWTs and their support structures. Up to date in situ and lab-based experiments on structural dynamics of OWTs are reviewed. Finally, major topics that require further investigation on the structural dynamics of OWTs are outlined.

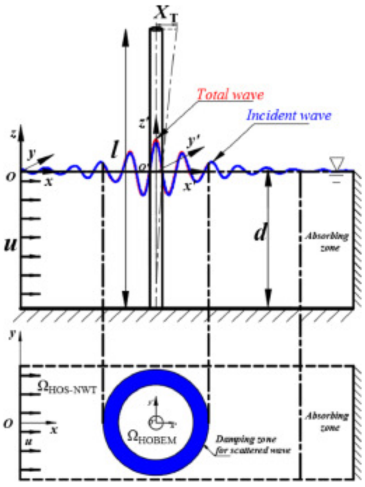

Figure 8: The computational domain (Teng and Liu, 2023)

2.2 Stationary Floating Moored Structures

Stationary floating structures addressed in this section include FPSOs, semisubmersibles, TLPs, spars, VLFS, FLNG, and their riser/mooring and dynamic positioning systems. Unless specified, this section is focused on platforms for oil and gas industry.

2.2.1 FPSOs

Park et al (2022) describe an experimental study about slamming at the FPSO bow. A set of pressure sensors installed in different heights and aside the center line map the pressure distribution of impact by different irregular waves response periods (10yr, 50yr, 100yr and 1000yr) and current. A treatment of pressure data was defined to discard wrong pressure peaks for rise time and decay time calculation. Pressure distribution was analyzed concluding that the location of maximum pressure changes to up with a tendency to wave crests increases. However, the maximum impact point was not occurred exact in each sensor's discrete location. The maximum and average pressure peak values were a tendency to move to up with wave heights, but the sensor needs to be allocated in the exact point to record it. For higher wave steepness the same behavior was observed when impact pressure increases. The tendency of higher-pressure peaks was associated with short pressure rise time. The current direction propagation associated with the wave at the same direction shift the wave steepness to lower values and reduce the severity of the impact peaks at the FPSO bow.

Chen et al (2021), presents a study based in OpenFOAM CFD to evaluate the runup around a FPSO shape vessel. In order to verify the CFD modelling, experimental tests in wave flume and wave diffraction analysis were carried out. A group of waves was executed in four phase shifts in frequency domain, focus on to generate a runup in the bow of the FPSO. The vessel was free to move by a soft mooring anchor at the flume sides. Wave probes attached to the model monitoring the runup of waves. It was used a separation method to extract the harmonics of the wave group of non-linear waves decomposition associated of Stokes perturbation expansion method. In the experimental and numerical data, the scattered waves from the bow of the vessel shows harmonics associated with the runup elevation. The vessel movement in wave presents predominantly linear behavior and the runups are mostly decomposed by low-harmonics and high-harmonics of the second harmonic of waves. The separation method described could be useful to predict the runups for others type of vessels and shapes in numerical and experimental tests with better results than linear theory models to predict runup and green water.

Zhang et al (2022), studied the green water in OpenFOAM simulating the events of impact in a bow of a hull. The hull presents a deck and a superstructure assembled over then. A Peregrine Breather solution of nonlinear Schrödinger equation (NLS) was used to generate a freak wave at the inlet boundary of numerical model. The freak wave was focus on the region of the bow of the hull. The wave created reach the bow generating a green water event of the type plugging dam break (PDB). A virtual mesh of virtual pressure probes mapping the pressure distribution on deck and a superstructure over the deck. The maximum pressure occurs close to the joint of the deck to the superstructure in the midship. Close to the superstructure the pressure presents two or three peaks due water drops in contact with the superstructure. The simulation in 2D and 3D were evaluated, and the second type is adequate for freak wave green water events simulation. The relationship between wave heights and periods of the freak waves was verified in the pressure impacts on the deck and superstructure during the green water occurrences. The parameter combination changes the characteristics of green water events and the pressure distribution.

The article of Fontes et al (2021), shows qualitative aspects of green water classification in relation of format of the events over the deck of a generic structure. An image-based technique analysis was applied to measure different aspects of the events occurrences during several regular waves realized in a wave flume experiment. The work classified the green water events in three types: dam break (DB), plugging dam break (PDB) and hammer fist (HF). The authors explore the characteristics of each type of green water such as: free board elevation, volume of water over deck, wave characteristic highlighting the steepness and in time event evolution. In the sequence article Fontes et al (2022), the applicability to modelling green water over de deck with analytical model considering terms of advection-diffusion equations solution of Navier-Stokes model, was investigated. The premise is to develop an analytical tool for estimating green water for project phase of vessels and offshore structures. An analytical convolution approach was investigated to describe in time evolution of single-valued water elevations of different types of green water events generated by incident wave trains impact to the bow of structure, particularly dam break, plunging dam break and hammer first described early. The convolution analytical model was compared to the experimental data captured by image-based technique for a single event and a sequence of events of green water propagating from the edge of the bow and so on over the deck in time domain. The results show an improvement due the traditional dam break theory. The decay tendency of water peak evolution in time were acceptable representation. However, the peaks of water propagation over the deck are over predicted in comparison of experimental data. The coefficients value needs to be investigated in future works to obtain better approximation related the deck characteristics in special the rugosity. Nonetheless the analytical model is useful to simulate the green water events in simplified way.

Lee et al (2022) perform an experiment to study the green water behaviour in wave flume in a captive FPSO bow simplified structure varying the flare angles of 45°, 60°, 75° and 90° (vertical bow). Regular waves hit the bow of the FPSO, and a camera record the water elevation and air bubbles trapped in the interface. The BIV (bubble image velocimeter) technique serve as to quantify the liquid velocity. The dam breaks phenomenon occurs over the deck structure and a set of five pressure gages record the pressure distribution at the surface during the events of green water. A comprehensive methodology analysis of pressure and BIV measurement was presented to modelling the dam break events and predict the pressure distribution and green water wave elevation.

Kwon et al (2023) realized an experimental and numerical study regarding the riser hand-over operation between an installation vessel and a FPSO. The study was realized with two model in the test in regular waves. Due to the depth of the basin, the riser truncation was applied to modelling the similarity in the hand-over operation. The vessels hydrodynamic interaction observed was confirmed in the numerical simulation, highlighted in the heave and pitch motions affected in two wave headings. The numerical model with hydrodynamic interaction of vessels confirmed the transfer functions of the load behaviour in the riser, observed in the wave basin tests. Under lower load transfer percentage between 0 and 5%, cables snapping phenomenon occurs and increasing the load transfer up to 50%, vessels interactions increase and tension transfer function increase to 80-90% above initial values.

Ha et al (2024) use a FPSO model in experiments with irregular waves to study green water at the side walls and at the bow in oblique waves incidences. A set of 12 wave probes attached to the model measures de relative waves elevation over the deck. Cylindrical pillars over the deck were used to measure forces due green water events. Video cameras record the events of green water waves occurrences in a qualitative way. The results treated using correlation between motion and relative wave elevations shows some aspects important to explain the phenomenon. In highlight, there is a close correlation between heave motions and side walls green water. At the same way, pitch and roll motion are important to explain the bow green water.

2.2.2 Semi-submersibles

Semi-submersibles have attracted much more attention in the recent years due to their suitability in reducing wave-induced motions of the floating system. However, there are still various challenges related to damage mooring conditions. Size of mooring, columns, pontoon shape and airgap help in the mitigation of dynamic responses in waves and wind, but their effects need to be further investigated during damage occurrence. Artificial intelligence methods are being introduced in the global performance evaluation.

Yu et al. (2021) investigated parametric resonance of the deep draft semi-submersible under regular waves experimentally and numerically. The focus was on the occurrence of parametric resonance in damage mooring condition. Model tests with and without mooring chains were conducted in a wave flume. For a model with 12 mooring lines representing intact mooring, parametric resonance did not occur. Whereas for the model with four mooring chains, representing the damage mooring condition, parametric resonance occurred. It was observed that parametric resonance occurred when wave period is about the natural period of heave and half of the natural period of Pitch or Roll. Numerical simulations of the test conditions were conducted using a potential-theory based weakly nonlinear model. Parametric resonance was successfully reproduced numerically. It was found that the numerical model accurately predicted the parametric resonance amplitudes and periods except for the damage mooring cases.

These findings should be verified in a larger wave basin to evaluate potential distortions due to blockage effects caused by the nearby basin walls (Figure 9).

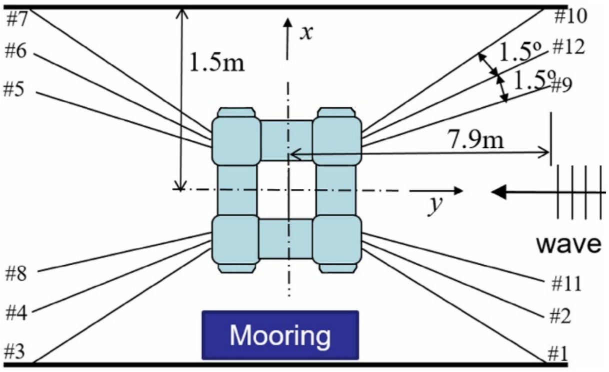

Figure 9: Model test setup with 12 mooring lines

The station-keeping system of offshore platforms is susceptible to complex metocean conditions. The failure of the mooring line is of concern due to uncertainty in the mooring lines behaviour and the potentially severe aftermath of an incident. Once the mooring line breakage occurs, the remaining mooring lines should provide sufficient tension to warrant the safety of the personnel and protection of the environment. Mao et al. (2022) proposed a deep neural networks (DNN) approach to predict the dynamic mooring line tension under one mooring line failure condition. First, the tension change of mooring lines induced by a mooring failure was investigated in two hydrodynamic models. The tensions of the mooring line with maximum sensitivity to failure was selected as the output objective. Second, two datasets of different hydrodynamic models were generated using the global response of the floating structures and their mooring tensions (Figure 10). Two DNN models were trained utilizing grid search to determine the optimal network structure. Finally, some case studies with different mooring arrangements and sea state conditions were employed to verify the feasibility and adaptability of two established DNN models and compare their accuracy.

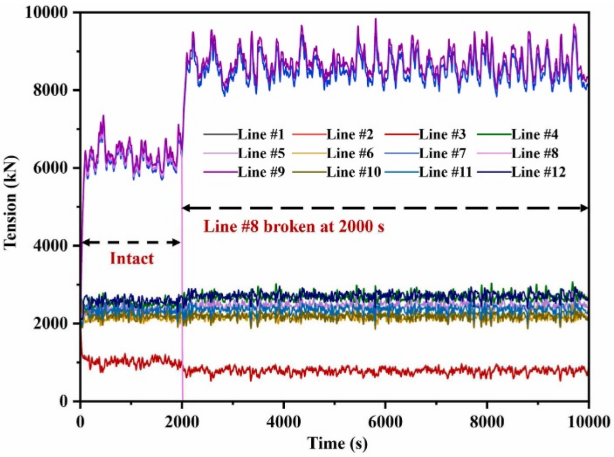

Figure 10: Time-domain analysis results

The results imply significantly increased sway and surge motions due to the mooring damage. Based on the study, it may be possible to combine in a practical way the input from GPS and the remaining intact mooring line tensions to monitor and control the mooring damage condition in real time.

Semi-submersible platforms can suffer slamming damage from extreme waves, making it crucial to improve their airgap performance. To address this issue, Liu et al. (2023) propose an innovative flare barrier that can be attached to the surface of a column at a certain height above the waterline, drawing on bow flares used in ship design. This study conducts a series of experiments to investigate the effectiveness of the flare barrier in mitigating wave run-up and motion response of a semi-submersible platform. The experiment simulates the wave field in 100-year irregular waves in headings 180° and 135°. Two different wave seeds are considered for each wave heading to reduce the transient effect. The results show that the flare barrier significantly mitigates wave run-up, especially at the height of the lowest edge of the barrier. Adding a flare barrier has no adverse effect on the surge, heave and pitch response. In heading 180°, it even has a slight mitigation effect on heave and pitch. The mitigation effect is also demonstrated in the power spectral analysis. Considering the wave run-up and motion response, a flare barrier is recommended to mitigate wave run-up on the column and improve the airgap performance under extreme waves.

(a) Front (b) Side

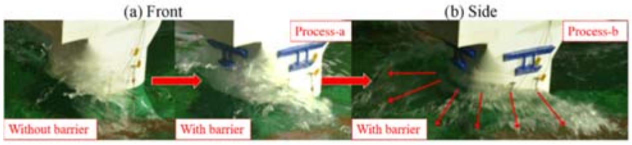

(c) Mitigation process

Figure 11: Flare barrier performance in 100-yr waves (Liu et al., 2023)

Additional model tests are recommended to validate the flare barrier design because two wave seeds may be insufficient to generate reliable wave run-up statistics.

Zhao et al. (2023) investigate the influence of mooring line disconnections on the response of a semi-submersible system (Figure 12) under regular waves and irregular waves. Two failure modes were performed and compared according to the disconnected positions of mooring lines: the top breakage and bottom unlatch. A numerical model of a fully coupled hull/mooring/riser system was created using in-house software to obtain the detailed behaviour of each component. The results indicated that the platform motion became a 4-period nonlinear response containing a super-harmonic motion when three moorings were unlatched. The disconnected moorings produced a large deformation due to the sliding of their anchor points. The riser tension exhibited robustness under mooring failure because of its low tension level and the robustness of the platform heave. Compared with bottom unlatch conditions, the platform under top breakage conditions showed larger-amplitude fluctuations and a slightly greater offset particularly when three moorings disconnected. The total mooring force during top breakage conditions would lose more fairlead tension at the failure time, thus inducing a lower mooring force to the platform.

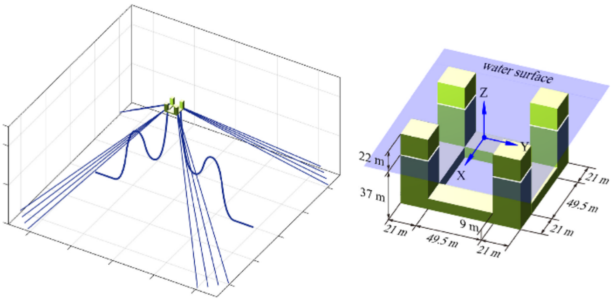

Figure 12: General view

Yeon et al (2022) investigated the wind loads on a semi-submersible rig using computational fluid dynamics. A maritime atmospheric boundary layer model for wind profile was implemented such that the wind profile shapes were retained throughout the computational domain.

Wind loads on the semi-submersible rig were calculated under the maritime atmospheric boundary layer and matched well with the results from the wind tunnel within a ±20% error. Among the topside structures, five structures, including the deck box (Figure 13), were selected and analyzed on the contribution to the wind load, particularly overturning moments, by decomposing the moments into drag and lift components. Overall, moments ignoring lift components tended to overestimate overturning moments by approximately 20% at maximum. The majority of the lift components originated from the deck box, which served as a lifting body owing to the accelerated streamlines between the waterline and the bottom of the deck box.

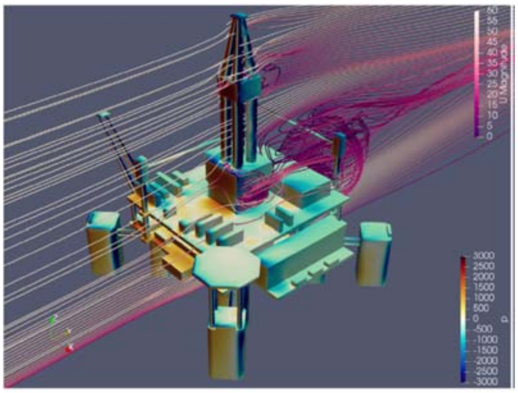
(a) top view

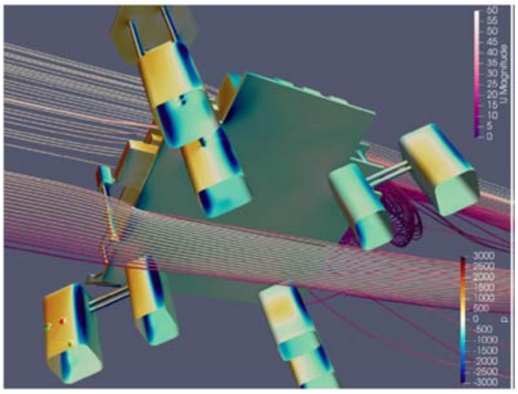
(b) bottom view

Figure 13: Streamlines around semi-submersible

The uncertainty level should be reduced to validate better the conclusions related to the lift effect on the overturning moment.

Jeon et al. (2023) analyzed a moored buoy's motions using a solver developed by coupling a computational fluid dynamics platform (OpenFOAM) with a lumped mass mooring line model (MoorDyn). The time-marching interface transferring the shared variables was developed to maximize the robustness and accuracy of the solver. The developed coupled solver was validated in waves using a moored cubic-shaped box model. Different mesh configurations, mesh generation techniques and mooring line discretization were considered in the numerical study. The cubic-shaped box moored with tensioned lines was simulated, and the results were compared with experimental results. The motion responses of a moored semi-submersible platform designed by the Korean Research Institute of Ship and Ocean Engineering (KRISO) were predicted numerically. The mooring line forces acting on the platform, the anchor, and the platform's motion performance were analyzed. Comparisons between the numerical results and experimental data were presented.

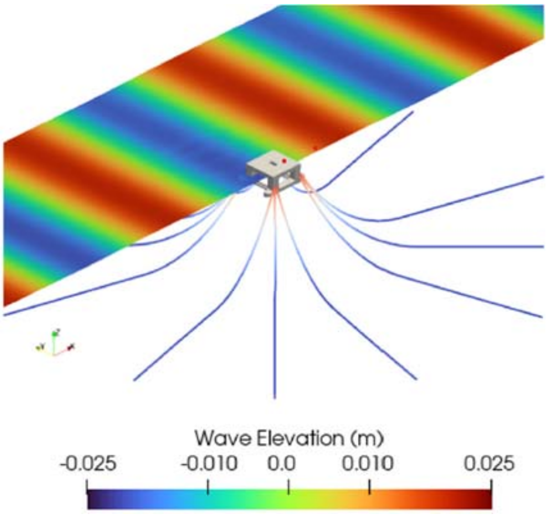

Figure 14: A snapshot of wave elevation around K-SEMI

Carmo et al. (2023) developed a slender-body approximation to evaluate the first- and second-order wave loads acting on a floating structure comprised of slender cylinders. It combines Rainey’s equation, which can be seen as an extension of the inertial part of Morison’s equation to include nonlinear terms, with

Pinkster’s formulation for the low-frequency second-order loads on floating bodies. The objective is to obtain expressions that allow the evaluation of second-order wave loads considering the mean body position so that an Inverse Fast Fourier Transform algorithm can efficiently compute the second-order wave loads in realistic sea conditions directly in the time domain. Similarly to Morison’s equation, this approach cannot model wave scattering and radiation effects, but this is acceptable if the diameters of the cylinders that compose the structure are small in the face of the length of the incoming waves. To verify the method, it was applied to the computation of the slow motions of a simplified semi-submersible FOWT model, first under the action of bichromatic waves and then in an irregular sea state. The results were compared with results from WAMIT, OpenFAST and experiments (Figure 15).

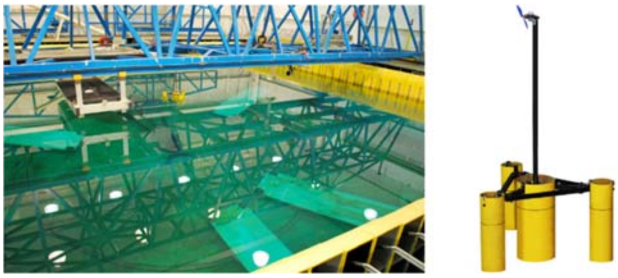

Figure 15: São Paulo wave basin (left) and the semi model

Under complex operating conditions of a semi-submersible platform, significant differences exist between the measured data in full-scale and the numerically simulated or experimental model-scale data. Yuan et al.'s (2023) study uses the measurement data collected during the operation of the semi-submersible ocean platform "Deepsea One" to train, validate, and test an artificial intelligence model, compensating for the lack of actual measurement data samples in previous studies. Their work provides a hybrid method for predicting mooring tension on semi-submersible maritime platforms based on VMD, error correction, and the convolutional neural network–long short-term memory (CNN-LSTM, Figure 16) and convolutional neural network–bidirectional long short-term memory (CNN-BiLSTM) models. The proposed hybrid prediction model was trained, validated, and tested using monitored mooring tension data acquired from the "Deepsea One" semi-submersible ocean platform in the South China Sea under different orientations and sea conditions.

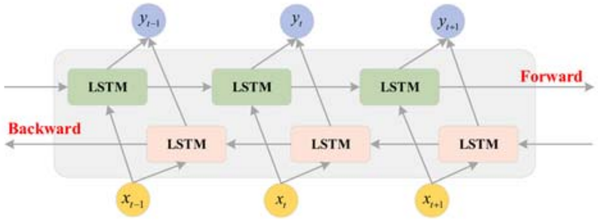

Figure 16: Structure of bidirectional long short-term memory neural network.

The results showed that the proposed hybrid prediction model for mooring tension on semi-submersible offshore platforms had lower values of the root mean square error, mean absolute error, and mean absolute percentage error and higher values of the coefficient of determination (R^2) than almost all of the other comparison models when predicting complex time series data of the actual monitored mooring tension. This indicated that the proposed hybrid prediction model had better precision and stability than other models. Furthermore, this method can be used to anticipate nonlinear, nonstationary time series data in different fields of maritime engineering.

2.2.3 TLPs

During the review period, TLPs behaviour has been investigated numerical and experimentally with special focus on responses under extreme and damage conditions. The experimental work related to vortex-induced motions also continues. An experimental investigation of the global performance responses of a TLP under different environmental conditions is presented by Jin et al. (2021). The TLP model included platform, tendons and risers (Figure 17). Regular and irregular waves, current, and a combination of irregular waves and current were generated during the tests. The influence of different headings on the motion responses in the in-line (IL) and cross-flow (CF) directions are presented. The motion spectra, wavelet transform, and motion trajectories were used to analyse the time histories. Statistical analysis of motion characteristics of TLP under different environmental conditions was presented and the governing for design heading pinpointed. With an increase of reduced velocity, the vortex-induced motion (VIM) of the platform first increased and then decreased, and multi-frequency time-varying coupling characteristics were presented in the cases of large reduced velocity. The VIM in this experiment were compared with towing tank were compared. In addition, the influence of free surface waves on the VIM has been illustrated through qualitative and quantitative analysis.

Figure 17: TLP tendons model

Cheng et al (2021) studied failure of tendons that might induce continuous failure and lead to the platform capping (Figure 18). The study modelled a typical TLP under tendon breakage. Time-domain analysis for a floating hull coupled with mooring lines was used to analyse the equilibrium position and amplitude of the steady-state response. The change laws of the balance positions of the motions and the reasons for the changes in the movement amplitudes were explored. By changing the wave parameters, the change rules of nonlinear motions and the damage caused by the change in the natural period were investigated.

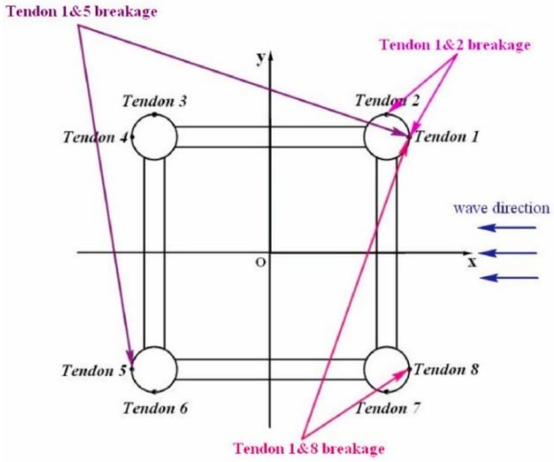

Figure 18: Schematic diagram of tendon failure modes

Zhi et al (2022) present an experimental study investigating the effect of draft, current heading and mooring stiffness on the Vortex-Induced Motion (VIM) responses of a Tension-Leg Platform (TLP) with four circular columns (Figure 19). The nominal transverse and yaw amplitudes and the corresponding spectra obtained by fast Fourier Transform (FFT) and continuous wavelet transform (CWT) are analysed to examine the characteristics of the motion responses. Four headings from 0° to 45° are adopted in the model test. The results show that the maximum response amplitude in both transverse and yaw directions is achieved at 0° current incidence. The maximum nominal amplitude decreases for the transverse response, and the lock-in range narrows as the current heading increases. The spectral analyses for the transverse and yaw motions at 0° current heading show that the dominant peak frequencies increase as the reduced velocity increases. It is observed that the low-frequency spectral peak of the in-line motion amplitude spectra increases as reduced velocity increases. A colour band or a ribbon concentrates stably around the frequency of $f<0.05$ in the wavelet analysis. It is primarily caused by the initial acceleration of the model in the towing tank. The absolute values of correlations between the spring tensions and the transverse motion of the platform are much larger than those between the spring tensions and the in-line or yaw motions. Moreover, it is found that the VIM trajectories of the TLP are primarily always along the direction perpendicular to the current heading.

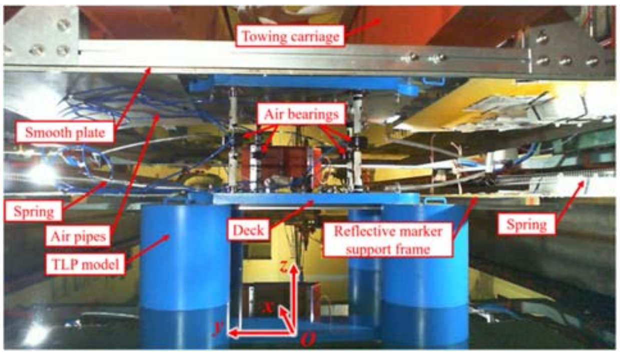

Figure 19: Experimental set-up in the towing tank

The experimental study conducted by Du et al (2023) investigated the dynamic response of a tension-leg platform (TLP) in complex flows, with the objective to improve the fatigue life of the mooring and riser systems. In this study, full-water-depth tendons and top-tension risers (TTRs) were modelled. Linear horizontal springs were installed instead of a mooring system used in other traditional models. Different types of shear flow with non-uniform distribution along the water depth were set to study the TLP response in heading 45° (Figure 20). Significant VIM and lock-in phenomena were observed, with the maximum amplitude occurring at *Vr = 7*. The response of the TLP when local flow accelerates around the columns and pontoons was discussed.

The reasons for the motion amplitude increase outside the lock-in region were clarified, and the mooring system's non-linear effect was demonstrated experimentally. To better understand the forces during the motion of TLP, the authors propose a method to reconstruct the fluid force, dividing it into two parts: the disturbing force and the radiation force.

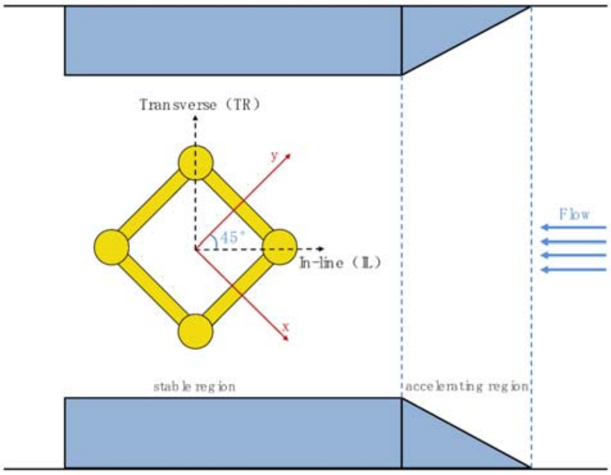

Figure 20: Arrangement of the model and the local flow velocity enhancement device

Kang et al. (2023) studied the nonlinear motion characteristics in the coupled behaviour of a Tension Leg Platform (TLP) combined with a Tender-assisted Drilling Unit. A time-domain numerical model was developed accounting for the nonlinear behaviour of mooring systems and the hydrodynamic interferences. Experiments were performed to validate the numerical model (Figure 21). Nonlinear motion characteristics of the steady-state response of the time-domain results were analysed using Poincaré mapping and fast Fourier transform.

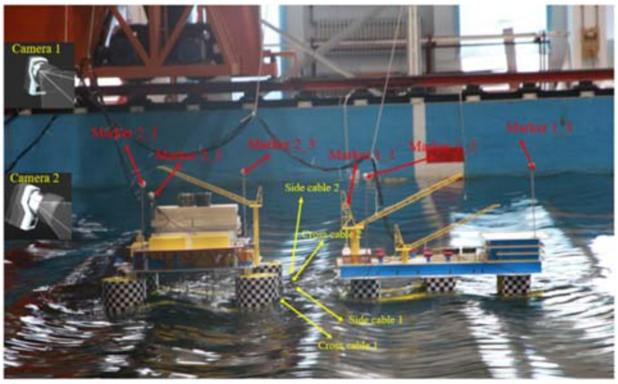

Figure 21: The experimental model of the coupled system

The study focused on investigating the motion response of the TLP in three degrees of freedom under coupled states. The surge motion consisted mainly of the wave frequency and half-wave frequency subharmonic components.

Meanwhile, the wave-frequency, subharmonic, and super-harmonic vibration components were observed in both heave and pitch motions. Three types of nonlinear regimes, namely chaos, transition, and multiple periodic, were identified in the heave and pitch motions under different wave conditions.

Investigating further how the vortex-induced motion would contribute to the coupled motion responses may be necessary. Also, would the designed hawser length be sufficient to keep their maximum tensions within practical limits?

During service life, a TLP is under potential damage caused by attendant vessel collisions. The influence of local dents on the maximum strength of TLP is a challenge in ocean engineering structures. Proper regulations outside the industrial practices are required to identify and rehabilitate the strength of these structures subjected to collision. Existing design methods require improvement to accurately predict the ultimate strength of TLPs subjected to accidental collision. Thus, it is imperative to develop viable approaches for predicting the residual ultimate strength of such structures.

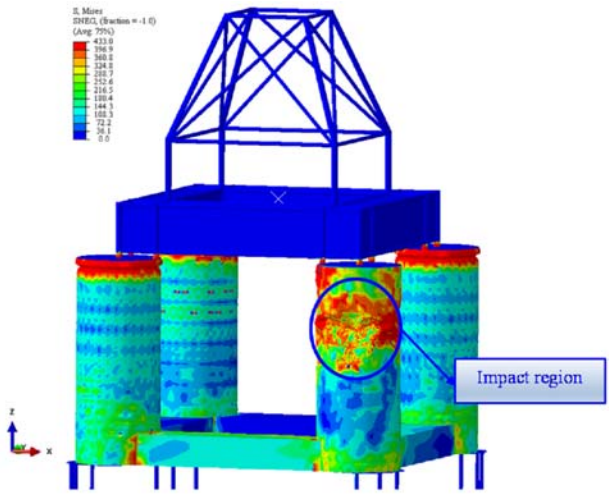

Figure 22: Deformed shape of a dented TLP column

This paper aims to establish practical modelling techniques and equations to predict the residual strength of dented TLPs subjected to combined axial compression and hydrostatic pressure.

The computational models proposed by Do et al. (2023) employ nonlinear finite element analyses (NFEA) considering the dynamic effects of materials properties such as strain rate and dynamic fracture strain. A series of NFEA of actual TLP with different collision scenarios and parameters were carried out using ABAQUS software (Figure 22). The empirical equations were provided through the database out of the NFEA results. The reliability of derived empirical formulations was compared with NFEA results, existing formulations, and test data.

2.2.4 Spars

Spar platform has become one of the most attractive floating platforms allowing top-tensioned riser operations thanks to its superior stability and low Heave motions in deep-water offshore sites. The focus of the listed below studies is on heave plate, strake performance, viscous drag and parametric resonance in relation to the spar motions.

Rao et al (2021) predict the hydrodynamic parameters of heave plates, namely, damping and added mass of the floater not only at its natural frequency, which can be obtained from free decay tests but also at other frequencies because the floater response is of interest over a wide range of amplitudes and frequencies. Forced oscillation tests in calm water can aid the investigation of these parameters at various motion frequencies and amplitudes. Heave damping and added mass of classic spar with heave plate were investigated in this study using experiments and numerical simulations of forced heave oscillation of a 1:100 scale model in calm water for various frequency-amplitude combinations. The least square method was used to determine the added mass and damping using three damping models, namely, linear, quadratic, and linear-plus-quadratic, and their applicability assessed. The effect of amplitude and frequency of oscillation on the parameters are discussed for various heave plate configurations with the aid of flow visualization from numerical simulations Figure 23. Added mass effect was examined using flow visualization of the fluid acceleration field. The scale effect on the parameters was also addressed.

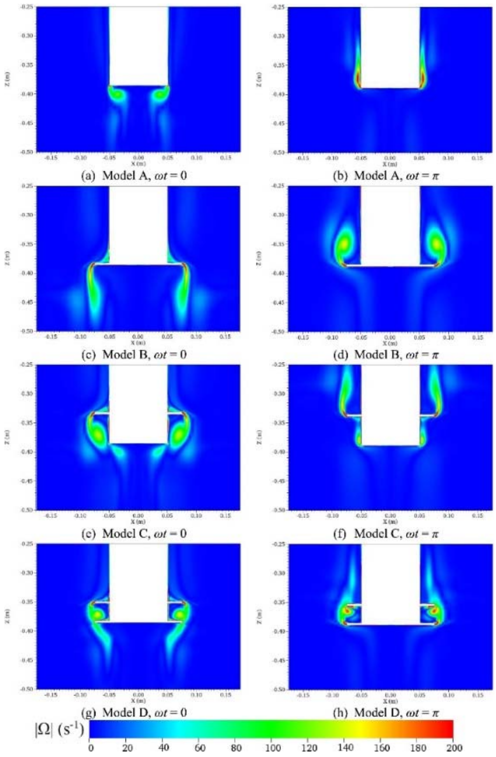

Figure 23: Vorticity magnitude contours around spar models

Kharazmi et al (2022) performed a numerical study aiming to reduce the Spar hull surge and sway response due to marine currents for various arrangements of strakes. The interaction of the marine current with a Spar model was numerically simulated. The results were compared with the VIM response of existing Spars with conventional strake design to validate the model. Different strake patterns and a conventional bare hull Spar equipped with strakes (base model, Figure 24) were used to model the VIM response of the platform. The results demonstrated the possibility of the Spar VIM response reduction due to improved design of the strakes. The best proposed configuration showed 58% suppression in sway motion and 9% in surge VIM response.

Figure 24: Bare model with strakes

Rao et al (2021) carried out experimental and numerical investigation on heave damping and added mass of a scaled model of spar with a variety of heave plate configurations (Figure 25) using free heave decay for a range of initial heave displacements. Applicability of the linear and quadratic damping models were assessed for all configurations. The effects of parameters such as heave plate diameter, location of heave plate above the keel, and spacing between two plates on damping and added were also studied. Flow fields obtained from numerical simulations were presented, and their implication on damping discussed.

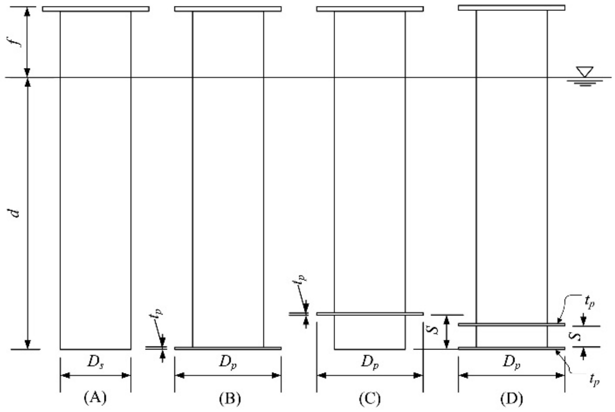

Figure 25: Experimental setup

Hegde and Nallayarasu (2023) investigated a classic spar and buoy form spar with a heave plate attached at the keel and near the free surface (Figure 26) for its effectiveness in reducing the overall response by conducting experimental studies in the wave basin and parametric studies using numerical simulations. The experimental investigations have been carried out using 1:100 scale models in the laboratory wave basin and compared with numerical simulations. It is observed that the buoy form spar with a heave plate attached near the free surface reduces peak heave motion response by about 75% and peak pitch response reduction by about 30% compared to classic spar without a heave plate. The motion response of the buoy form spar with different heave plate positions and diameters are compared, and the buoy form with heave plate near the free surface has been found to be effective in reducing the motion response considerably and hence recommended for use in practical design.

The findings should be confirmed in a lower than 1:100 model scale to reduce potential scaling distortions.

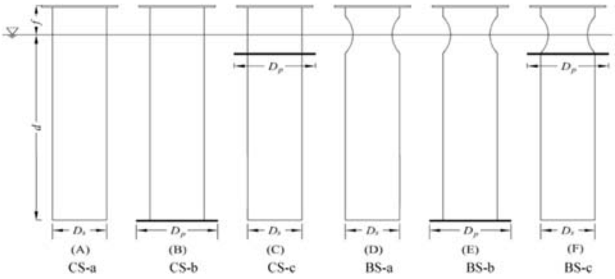

Figure 26: Experimental Setup

Wright et al (2022) proposed a novel method for the numerical–experimental fitting of non-constant drag damping to decay curves in still water, current and sinusoidal waves. The authors applied it to a moored advanced spar platform (Figure 27). The method involving a combined potential flow and Morison's equation model is used to calculate the drag coefficients and added mass from decay tests in still water, monochromatic sinusoidal waves and current flows. An inverse KC number drag coefficient relationship was observed for still water and wave cases. With increasing current flow velocity, the KC number drag coefficient tendency decays to a constant value equal to the steady state drag coefficient. A similar inverse KC number drag coefficient relationship is shown from the full-scale Fukushima FORWARD's floating substation. Discussions on the flow behaviour and recommendations on simulation techniques are given.

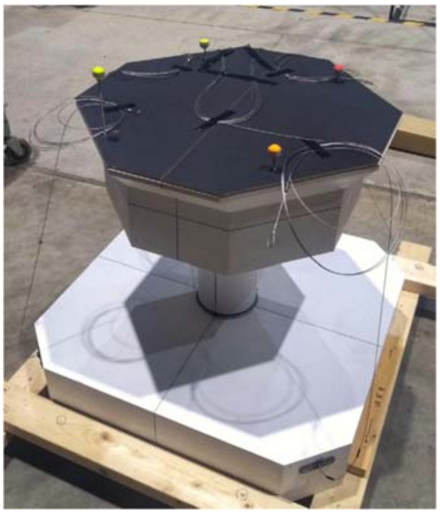

Figure 27: Advanced spar model

Parametric resonance is a phenomenon caused by time-varying changes in the parameters of a system which may result in undesirable motion responses and instability. Floating bodies like ships and spar buoys are prone to Mathieu instability mainly due to the instantaneous change of the metacentric height. With the fast-growing developments in Ocean Renewable Energy systems, spar buoys are commonly used for wave energy converters and floating wind turbines.

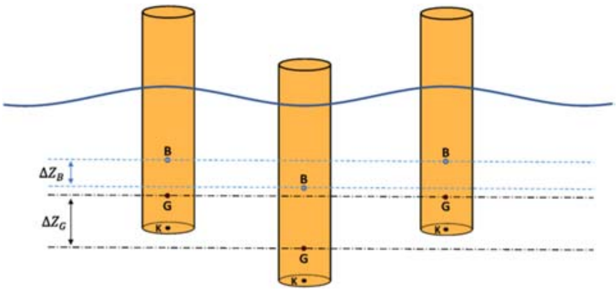

Figure 28: Vertical oscillations of center of buoyancy and center of gravity in heave motion

Undesirable, unstable motions resulting from the parametric resonance can be problematic as it may cause inefficiency in operations and structural risk integrity. Aziminia et al (2022) developed a new approach to investigate these nonlinear oscillations and analyse the conditions when parametric resonance occurs. The hydrodynamic loads are calculated using the linear approach, and the motion responses of the floating body coupled in heave, pitch and surge are determined (Figure 28). It is shown that the eigenvalues obtained from Floquet Theory can be used as indicators of stability under different wave conditions. This procedure can be practically used with little computational cost to determine factors affecting the equilibrium status of a system in regular waves.

Multi-body systems are becoming common in engineering practice, such as the catamaran float-over installation for a Spar platform, one of the most complex marine system designs (Figure 29). The gap resonance phenomenon occurs in the catamaran float-over system due to strong hydrodynamic interactions, inducing inaccuracy in evaluations of the hydrodynamic coefficients. To obtain reasonable hydrodynamic coefficients, Chen et al. (2023) first validated the damping lid method in AQWA, which provides viscous correction for the potential flow theory. Then, they applied it to the model in this study. It is found that the damping lid can deal with the gap resonance phenomenon. With the introduction of the damp lid method in the catamaran float-over system with α = 0.20, the relative error between the frequency-domain and time-domain declined from 690% to 1.7%.

Based on the corrected frequency-domain results a time-domain model, considering various types of mechanical coupling components in the float-over system, including leg mating units (LMUs), deck support units (DSUs), steel-to-steel impacts on LMUs, lateral constrains of LMUs and DSUs, sway fenders, hawsers, and the mooring system. The first and last contact stages were simulated under different incident wave angles. It was observed that the relative motions in the quartering sea during the first contact stage are the largest. Furthermore, to reveal the coupling mechanism, different configurations of the barges and Spar are investigated for the first contact stage under irregular waves. It is found that the relative heave motions on the LMUs are larger when the deck and barges are rigidly connected to form a catamaran-barge.

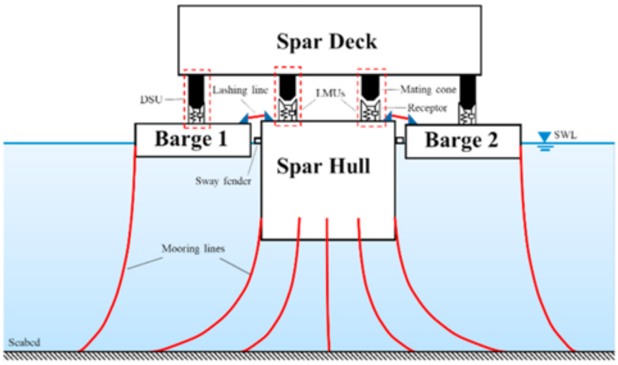

Figure 29: Front view of the catamaran float-over system

2.2.5 VLFS

Huang et al. (2023) predicted hydroelastic responses of a single module VLFS in extreme wave conditions using CFD-FEA coupling method. Freak waves, as a kind of strong nonlinear waves, have a great threat to the safety of Very Large Floating Structures (VLFS). Freak wave produces enormous wave height, which caused the hydroelastic responses on the VLFS to increase significantly. Nevertheless, due to the complexity of the highly nonlinear interactions between waves and VLFS, studies of wave-induced loads and the hydroelastic responses of VFLS in freak waves are rare. In this paper, a fluid-structure interaction technique that strongly connects the CFD and FEA solvers is proposed to evaluate the wave-induced loads and hydroelastic responses of a single module VLFS under freak wave circumstances. The result shows that the freak wave will lead to the global motion of VLFS being multiplied several times and largely increasing the instantaneous maximum vertical bending moment.

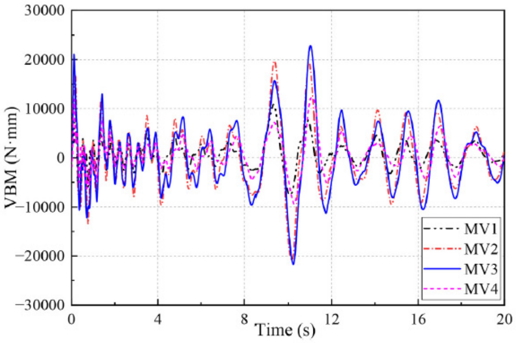

Figure 30: Time histories of VBM at different sections in freak waves

Yang et al. (2023) proposed boundary controller for floating beam system in irregular waves under one end pinned to reduce hydroelastic response. The structural stability is of great importance in research and development of VLFS. The structural stability is of great importance in research and development of VLFS. The vibration reduction on VLFS would not only prevent the structural fatigue but also improve the platform serviceability. Yang et al. investigate a boundary control method for a floating beam system with irregular waves in this paper. Through utilizing Lyapunov direct method, a boundary controller is proposed to reduce the hydroelastic response of the floating beam system restrained at its downstream end. The numerical simulation with experimental calibration is given to verify the effectiveness of the suggested control strategies on the floating beam system.

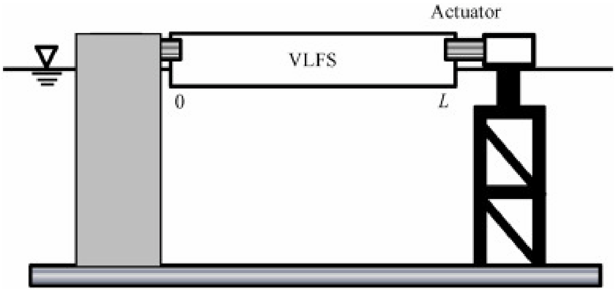

Figure 31: Very large-scale floating structure with one end pinned with mooring system

Jiang et al. (2023) reviewed advances in modeling hydrodynamics and hydroelasticity for very large floating structures. VLFSs have the potential to serve various functions such as maritime airports, logistic hubs, and even floating cities, thereby enhancing ocean utilization and management. This paper aims at providing a state-of-the-art review of the recent advancements and developments in the key technologies required for VLFSs, including a clear classification of their shapes, applications, connection systems, and mooring systems.

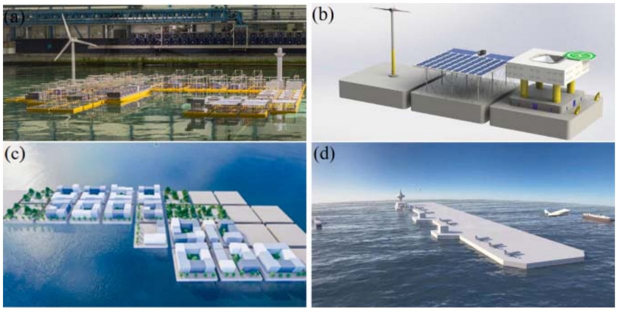

Figure 32: Examples of VLFSs for various applications: (a) logistics, (b) energy, (c) living, (d) others designed for specific tasks (the first three figures are from the Space@Sea project, and the fourth is adapted from the Mega-float) (Jiang et al., 2023)

Chen et. al. (2023) extended the discrete-module-finite-element (DMFE) method into the interconnected large floating flexible structures. DMFE method has been proposed and well-developed to analyze the hydroelasticity of floating flexible structures, in which the structure is discretized into several macro-submodules (for hydrodynamic analysis) and each of them is further discretized with finite element (for consideration of deformation). The DMFE method omits the determination of optimal modal combination, which is sometimes difficult for the mode superposition method in analyzing floating structures with complex geometric features and maintains greater computational efficiency over the direct method in analyzing floating structures with huge size. In this present paper, it is investigated in the framework of the DMFE method the hydroelasticity of interconnected floating structures.

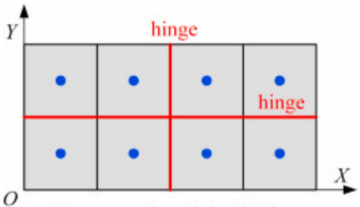

(a) macro-submodule division

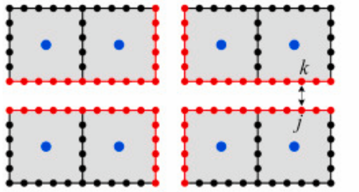

(b) node numbering

Figure 33: A schematic of a VLFS with two hinge connections. (a) Macrosubmodule division, a Y-axis-parallel hinge and a X-axis-parallel hinge; (b)reserved boundary nodes and lumped masses after elimination of inner nodes (Chen et. al., 2023)

Sakthivel et. Al. (2023) numerically investigated dynamic responses of serially connected truss pontoon-MOB. Very large floating structures (VLFS) are typically made up of several modules of offshore platforms, such as semi-submersibles, connected by mechanical connectors. The Truss Pontoon Mobile Offshore Base (TPMOB) is a new type of offshore platform based on the truss pontoon semi-submersible design. The design of the connectors is crucial for the functionality of the structure. The flexible connectors are modeled witha 3D source distribution method and the wave forces are estimated with 3D linear potential theory in this paper. The opensource finite element-based numerical model, HYDRAN-XR, is used to analyze the structural responses and connector forces in both regular and irregular wave conditions. The results indicate significant differences in responses between single and multi-module cases, especially in extreme waves. Loads on the connector change greatly for three- and five-module cases, with maximum values at specific wave angles.

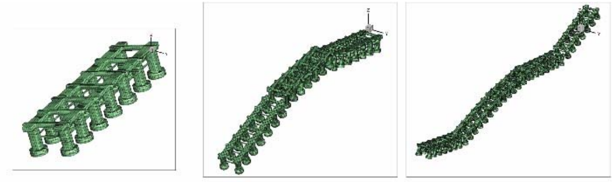

(a) Mode 1; single module (b) Mode 1; unconnected three-module (c) Mode 1; unconnected five-module

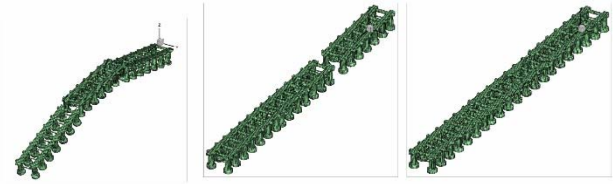

(d) Mode 1; connected three-module (e) Mode 2; connected three-module (f) Mode 3; connected three-module

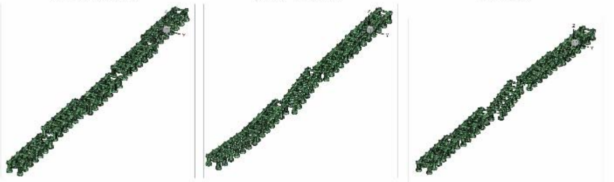

(g) Mode 1; connected five-module (h) Mode 2; connected five-module (i) Mode 3; connected five-module

Figure 34: The dry mode shapes of a single module, multi-module are both unconnected and connected cases

Tay (2023) used Artificial neural network framework for prediction of hydroelastic response of very large floating structure. The response of a VLFS must take into consideration the elastic deformation of the structure (commonly termed hydroelastic response) under wave action. Conventionally, the hydroelastic response could be computed by using the coupled finite element-boundary element (FE-BE) method, where the mat-like structure is modelled using plate theory and the water modelled using the potential theory. To accelerate the computational time in predicting the hydroelastic response of the VLFS, a surrogate model trained using the feed-forward neural network is proposed in this paper. The hydroelastic responses under different wavelengths, structural stiffnesses and wave directions are first generated where these data are split into three groups for training, validation, and testing (prediction) purposes.

Huang et al. (2023) established a method to predict hydroelastic responses of a VLFS under waves and moving loads. A VLFS can be simplified as a multi-floating-body model connected by universal joints, and its elastic deformation can be reflected by the rotation of the joints. According to displacement and torsional angle equivalent of the elastic beam model and multi-floating-body model in static analysis, the equivalent rotation stiffness of universal joints can be determined. The proposed method is verified against the results obtained from relative references and 3D-hydroelasticity theory. Then, a VLFS under oblique regular waves and moving loads are further investigated.

Gusev et al. (2023) developed the numerical algorithms for shallow water models. The results are validated using potential flow model. A cutout in the body bottom increases the transmitted wave amplitude. The basin bottom irregularity has the most effect on the interaction when located directly under the body. The bottom protrusion located behind the structure may slightly decrease the wave force.

Liu et al. (2022) reports a novel hybrid modular floating structure (HMFS) system consisting of a certain number of outermost box-type modules and inner semi-sub modules. Semi-sub modules are connected with ball joints in both longitudinal and transverse directions. Box-type modules are connected with adjacent semi-sub modules with pitch hinges. Outermost box-type modules mainly function as wave energy converters (WECs) and breakwaters. Based on the rigid module and flexible connector (RMFC) method, the effects of different wave directions, longitudinal expansion, positions of modules and connectors on hydrodynamic responses of the HMFS system are emphatically investigated under typical sea conditions.

Rodrigues et al. (2022) presented an experience in designing and carrying out a model test campaign of a generic floating bridge. The tested model represents a truncated segment of a generic full straight bridge at a fjord crossing in Norway. Environmental conditions comprise combinations of regular and irregular waves, current and wind, including a spectral amplitude inhomogeneous condition realization. A novel approach for carrying out static pull-outs, decays, and inducing inhomogeneous wind conditions, is applied using winch actuators. A dataset of time series and selected video recordings is publicly shared for selected measurements and test runs. Recommendations for testing of floating bridges in a basin are given.

Figure 35 Hydroelastic bridge model and instrumentation (Rodrigues et al., 2022)

Zhang et al. (2022) proposed a cut-off scheme to model large arrays of modularized floating structures. The radiation interaction effects among multiple rectangular boxes are quantified. Some critical curves showing the optimal cut-off radius are depicted. Two cases are designed to examine the accuracy and efficiency of the proposed scheme.

Li et al. (2022) clarified hydrodynamic response of VLFS under typhoon-driven waves is clarified by numerical tank test. Jonswap spectral characteristic parameters could effectively simulate Typhoon Megi. An FMRC modeling method for VLFS satisfying longitudinal slope of airport runways is proposed. Mechanisms of energy conversion between Marine airport and environmental loads are revealed.

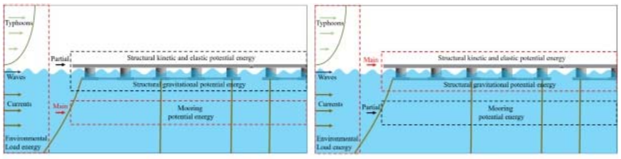

(a) Initial stage of under typhoon-driven waves (b) Stable stage of marine airport

Figure 36 Energy transfer mechanisms of the marine airport under typhoon-driven waves (Li et al., 2022)

Zhang et al. (2022) reviewed an experimental and numerical investigations on continuous floating elastic structures with focus on models and methods. A new category of Very Flexible Floating Structures (VFFS) is introduced based on motion response characteristics. The applicability of hydroelastic theory to the newly envisaged VFFS is assessed.

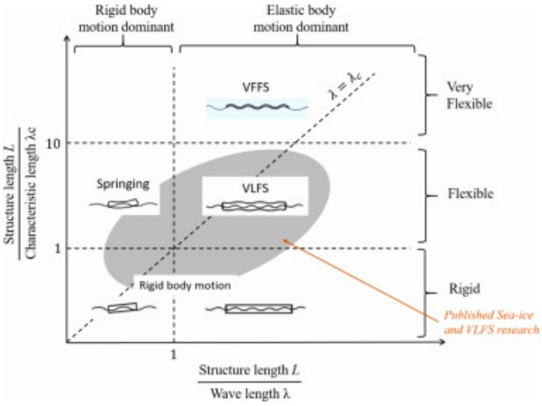

Figure 37 Mapping of global response of floating structures (Zhang et al., 2022)

Chen et al. (2022) constructed a numerical framework of one dimensional discrete-module-beam hydroelasticity method. Unsteady external excitations are categorized and corresponding dealing procedures are regulated. A hybrid integration-interpolation method is developed to calculate structural force response of a VLFS in time domain. Motion and internal force/moment responses of a VLFS in four engineering scenarios are given.

Sakthivel et al. (2022) investigated A novel-Truss Pontoon Mobile Offshore Base (TP-MOB) VLFS experimentally under regular wave conditions for different heading angles. Details of the fabrication of the 1:150 scaled model are presented. Responses of the model, namely vertical displacement besides roll and pitch motion are measured by sensors at three locations. Response Amplitude Operators (RAOs) are obtained, and these plots show the characteristic diminishing peaks of the elastic body responses within the wave excitation range, unlike the case of a barge. Results ascertained that the frequency response curve obtained is consistent with existing literature.

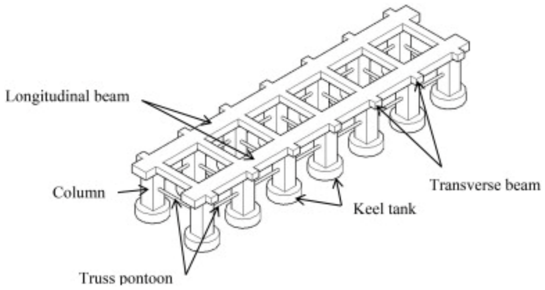

Figure 38 A schematic representation of TP-MOB in isometric view (Sakthivel et al., 2022)

Xu et al. (2022) analyzes nonlinear model for strong hydro-elastics of very large floating structures. The floating structure is modeled as a nonlinear Euler Bernoulli–von Kármán (EBVK) beam coupling with water beneath. A multi-time-scale perturbation method leads to hierarchic partial differential equations by introducing the wave steepness squared as the perturbation. Pontoon structures and LPOFPV are studied and compared.

Figure 39 Large-scale polymer offshore floating structure for photovoltaics (Xu et al., 2022)

Iijima et al. (2022) measured the waves propagating along a long thin plate floating at the water surface using digital image correlation (DIC) method. The effectiveness of the measurement by the DIC is shown. The tank test model is made of closed cell rubber foam. The material properties are measured by a static four-point-bending test and vibration test. The uncertainty with respect to the material properties is discussed. The measured results are compared with numerical simulation results based on linear potential theory. The overall agreement is found good in terms of wave length, response amplitude, and distribution. Nonlinearity of deflection waves on the floating plate, which is similar in some point to Stokes wave is identified for the first time by measurement.

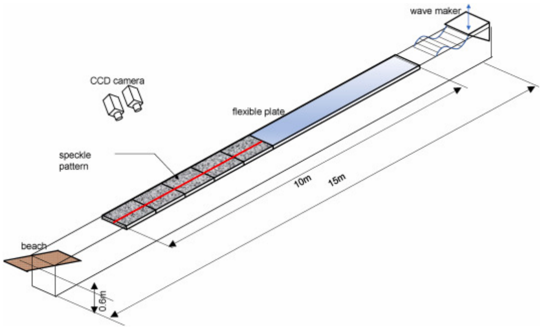

Figure 40 Schematic of a long thin plate model (Iijima et al., 2022)

Wang (2022) Performance of closed-form RAO solutions for Modular floating structures (MFS) benchmarked against smoothed particle hydrodynamics. Heave and roll damping ratio of 0.1 recommended for conservative assessment of MFS. Building slenderness and building/pontoon mass ratio on human comfort explored. Analytical procedure enables the preliminary design of MFS prior to CFD modeling.

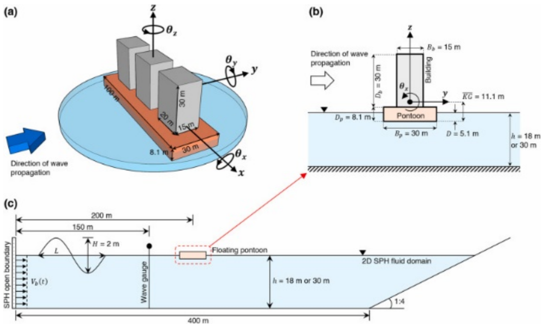

Figure 41 Module9000 MFS model for dynamic analysis (Wang, 2022)

Jiang et al. (2021) evaluated various structural systems for concrete floating modules and developed optimal structural solutions of modular units for engineering practice. Hydroelastic responses of VLFS with the hybrid BEM – FEM code are investigated. Preferable geometrical shapes and connection properties for VLFS are explored.

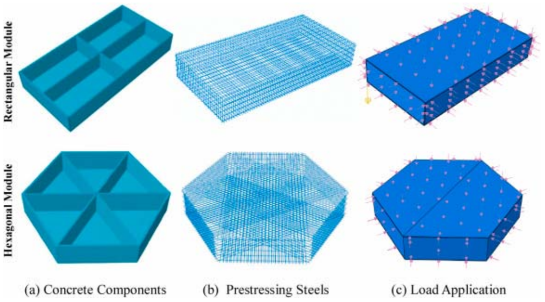

(a) Concrete Components (b) Prestressing Steels (c) Load Application

Figure 42 Finite element models of different floating modules (Jiang et al., 2021)

2.2.6 Other stationary floating structures

According to the IGU World LNG report (2022 edition), the global LNG fleet is relatively young due to the rapid increase in LNG trade over the past two decades. In other words, vessels under 20 years of age make up 90% of the active fleet with newer vessels. And in 2022, a total of 45 FSRUs make up 7% of the active global LNG fleet. It is necessary to study the hydrodynamic characteristics of the floating structure such as FLNG and FSRU for LNG utilization is continuously needed.

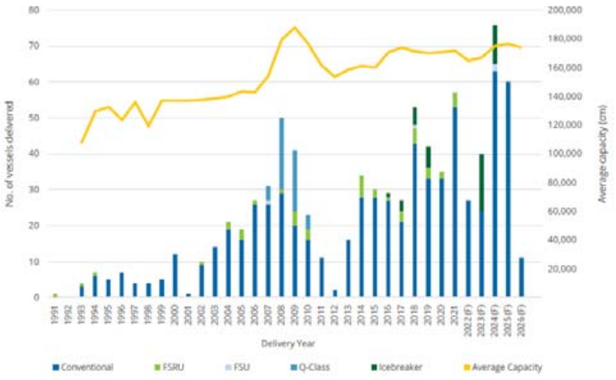

Figure 43: Global active LNG fleet and orderbook by delivery year and average capacity, 1991-2026

Kang et al. (2022) carried out a study focusing to develop and verify a one-side spread mooring system, an alternative spread mooring system to be applied to FLNG operated in West Africa. The mooring line analysis utilized various numerical analyses (Ariane8, OrcaFlex, WADAM, SIMA) in accordance with the ABS position mooring rules. The one-side mooring system was satisfied with ULS(Ultimate Limit State) and ALS (Accidental Limit State) requirements of ABS design criteria. Also, design offsets for both intact and damaged mooring condition were within the offset limit. The operability of side-by-side offloading was more than 99%, and thus safe offloading was expected during almost life time.

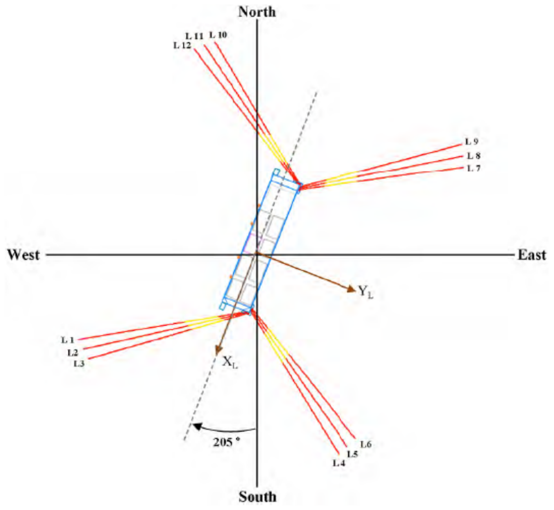

Figure 44: One-side mooring arrangement

Jung et al. (2022) presented the hydrodynamic characteristics of a rectangular structure that wave excitation force, damping coefficients, and 3-DOF motion response were experimentally studied in various wave and water depth conditions in a 2-D wave tank. The rectangular structure was installed in fixed and soft spring moored conditions in beam sea condition, and the experiment was performed in regular wave conditions of the range of wave period with varying the ratio of the water depths and draft. And the results were validated and compared to the simulations (HydroStar) based on potential theory. The results showed trends of added mass and damping coefficients getting larger at shallower water depth and emphasized that the water depth to draft ratio was less than 2.0. And, they suggested that viscous damping effect should be considered to find RAOs of roll and heave motions at less than 2.0 of the water depth to draft ratio.

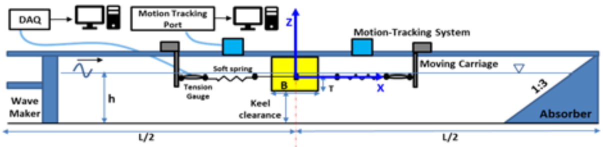

Figure 45: Experimental schematics of fixed structure in 2D wave tank

Nwafor J.C. (2022) carried out the nonlinear coupling of the gap resonance and the hydrodynamics of FLNG and LNG carrier in proximity for the offloading operation in side-by-side configuration was investigated numerically. The numerical analysis was conducted to understand how the variation in loading conditions and environmental factors affect the side-by-side offloading operation. The numerical results demonstrated that the LNG carrier had a larger vessel motion compared to the FLNG and the bow and aft lines were affected by relative sway while the spring lines were affected by surge, hence further improvements on the optimal hawser line arrangement needed to be further investigated for different loading conditions.

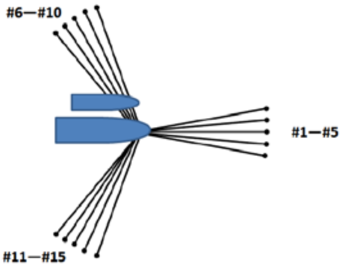

Figure 46: General arrangement of mooring system

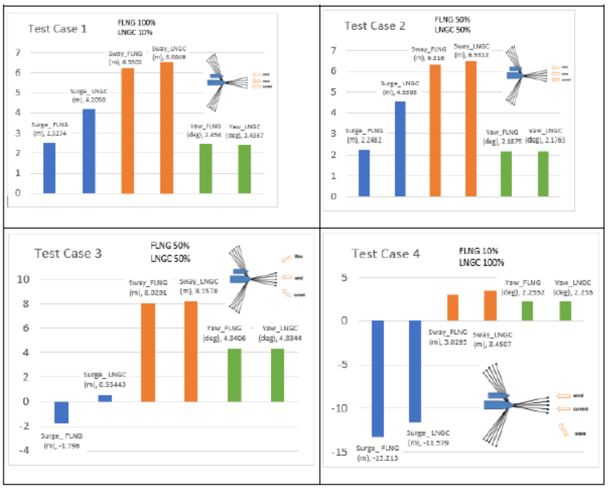

Figure 47: Comparison of Low frequency motion for FLNG and LNGC

Qi et al. (2021) conducted experiments to investigate the hydrodynamic performance of singly-moored FSRU and side-by-side moored FSRU-LNGC and assess the security of the quay-mooring system. The model tests were mainly divided into two parts including a quay-moored test of a single FSRU and a test of FSRU and LNG carrier moored side by side to the quay.

Figure 48: Model-set up for the quay mooring system (Whole system)

In singly-moored FSRU case, the loads of mooring lines and fenders (mooring system) were sensitvie to the wave direction and all the maximum loads on the mooring system was less than the break strength. However, during the test of FSRU and LNGC moored side by side condition, under all the beam sea condition, motions of the LNG carrier was larger than FSRU and the largest tension acting on the mooring line was larger than its break strength. Therefore, it was necessary to improve performance of the mooring system or to stop the operation work under worse sea conditions.

Rudan et al. (2021) presented the methodology for direct analysis of the mooring system of LNG carrier using finite element method. First, rule-based calculations were made first to obtain the properties of the mooring lines and fenders. Numerical analysis based on potential theory was conducted to solve the hydrodynamic coefficients such as added mass, damping, etc. Based on those results, commercial software (LS-Dyna) and numerical code (MCOL) used to perform the analysis of non-linear problem with the suggestion of a spring fender to simulate a rubber fender effect. The spring fender model could reduce the computing time, but its results differed from the analysis of rubber fender model. Forces along the ropes of the spring fender model were resulted into somewhat higher values than those of the rubber fender model. It showed that 'MCOL' could be useful tool for assessing ship hydrodynamic response in real time, within the highly non-linear explicit dynamics analysis. However, it was unstable in long-term simulations due to underlying theory was not coded correctly.

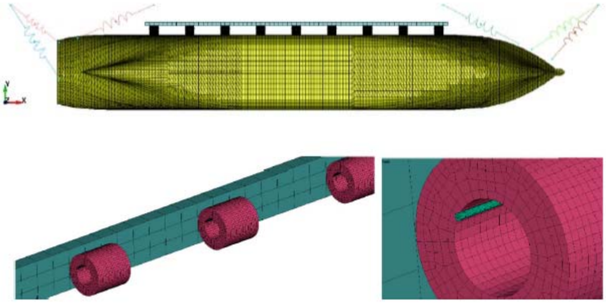

Figure 49: Moored ship and fenders FEM models

Shen et al. (2020) gave the results of a numerical study based on three-dimensional frequency domain potential flow theory of the effects of different spacings and different draft (different loading) on the resonance of the intermediate water body. During the ship to ship operation system of FSRU and LNG under the head sea condition, the value of the maximum resonance wave elevation, significantly, decreased with the increasing of the distance between the two ships, and the wave period corresponding to the maximum resonance wave elevation increased. In beam sea consition, the maximum resonance wave elevation increased with the increasing of the distance between the two ships, and the wave period corresponding to the maximum resonance wave elevation increased with the increasing of the distance between ships.

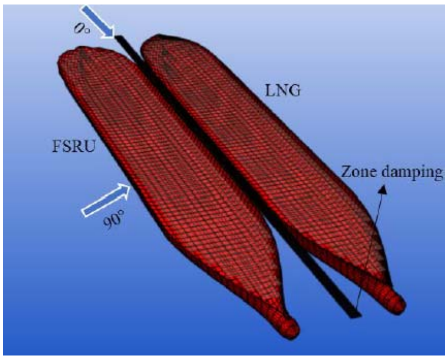

Figure 50: Ship to ship operation

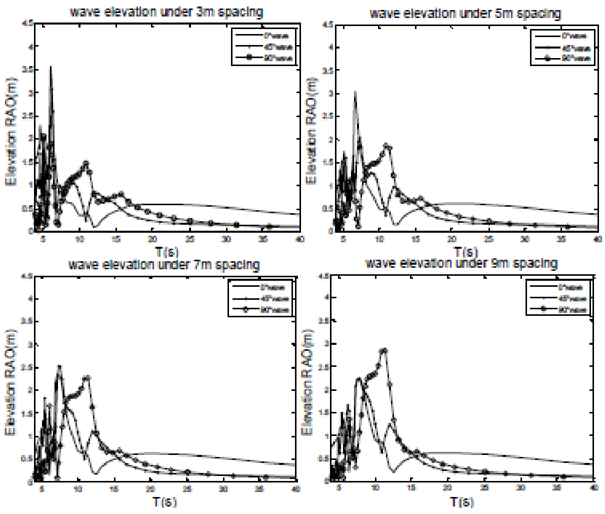

Figure 51: Wave surface elevation at different intervals

Teng et al. (2022) presented the hydrodynamic characteristics of floating structures using rectangular floating barge by numerical methods. Numerical analysis of the hydrodynamic coefficient and motion response of the barge were carried out using commercial software (WAMIT and STAR-CCM+). The six-water depth and three-bathymetry conditions were used in numerical analysis. From this study, the hydrodynamic coefficients such as the added mass, viscous damping, and current drag coefficients were found to be significantly affected by changes in shallower water depth. In addition, it was confirmed that both added mass and viscous drag coefficients were further increased at the steeper bottom slope when the water depth reduced.

2.3 Dynamically Positioned Floating Structures

Dynamic positioning (DP) is a computer-controlled system to automatically maintain the position of floating structures and heading by using its own propellers and thrusters. Position reference sensors, combined with wind sensors, motion sensors and gyrocompasses, provide information to the computer pertaining to the position of floating structure and the magnitude and direction of environmental forces affecting its position.

The computer program contains a mathematical model of the floating structure that includes information pertaining to the wind and current drag of the floating structure and the location of the thrusters. This knowledge, combined with the sensor information, allows the computer to calculate the required steering angle and thruster output for each thruster. This allows operations at sea where mooring or anchoring is not feasible due to deep water, congestion on the sea bottom (pipelines, templates) or other problems. Some of the most relevant recent works are described as follows:

Zhang et al. (2020) presented a novel robust neural event-triggered control algorithm to achieve the dynamic positioning operation of marine surface ships in the presence of actuator faults. In the algorithm, the model uncertainty and the “explosion of complexity” were addressed by fusion of the robust neural damping and dynamic surface control techniques. The gain related adaptive law was constructed to compensate the gain uncertainties and the unknown actuator faults, which improved the stability of the ship dynamic loop system. Furthermore, the event-triggered mechanism was introduced to reduce the communication load between the controller and actuator. For merits of the aforementioned design, the proposed algorithm was with the advantages of concise form and easy to be implemented in practical ocean engineering. Based on the Lyapunov theory, rigorous analysis was proved to guarantee the semi-global uniform ultimate boundedness (SGUUB) of the closed-loop system.

Conventional dynamic positioning (DP) systems on larger ships compensate primarily for slowly time-varying environmental forces. In doing so, Halvorsen et al. (2020) used wave filtering to prevent the DP from compensating for the first-order wave motions. This reduced wear and tear of the thruster and machinery systems. The overall control system architecture can be seen in Figure 52. In the case of smaller autonomous vessels, the oscillatory motion of the vessel in waves may be more significant, and the thrusters can be more dynamic. This motivated the use of DP to compensate for horizontal wave motions in certain operations. They studied the design of DP control and filtering algorithms that employ acceleration feedback, roll damping, wave motion prediction, and optimal tuning. Six control strategies were compared in the case study, which was a small autonomous surface vessel where the critical mode of operation was launch and recovery of an ROV through the wave zone.

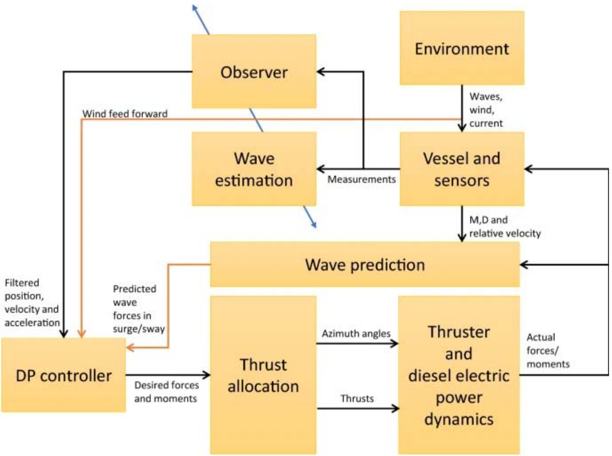

Figure 52: Block diagram of the control architecture. (Orange arrows are feed-forward terms and blue arrow indicates adapting gains.)

In Hosseinnajad et al. (2020), a new control system was proposed for dynamic positioning (DP) of marine vessels with unknown dynamics and subjected to external disturbances. The control system was composed of a substructure for wave filtering and state estimation together with a nonlinear PD-type controller. For wave filtering and state estimation, a cascade combination of a modified notch filter and an estimation stage was considered. In estimation stage, a modified extended-state observer (ESO) was proposed to estimate vessel velocities and unknown dynamics. The main advantage of the proposed method is its robustness to model uncertainties and external disturbances and it does not require prior knowledge of vessel model parameters. Besides, the stability of the cascade structure was analyzed and input to state stability (ISS) was guaranteed. Later on, a nonlinear PD-type controller with feedforward of filtered estimated dynamics was utilized. Detailed stability analyses were presented for the closed-loop DP control system and global uniform ultimate boundedness was proved using large scale systems method.

Martelli et al. (2020) aimed to present a novel approach to design a dynamic positioning system by using a dynamic model based-design approach. The proposed study has been performed to both develop and preliminarily test the control logic that should be implemented on a model scale vessel. Indeed, the proposed tool has been designed for a fully actuated tug vessel equipped with two azimuthal thrusters and one bow-thruster, emulated in behaviour with a dynamic simulator. Thanks to the model actuation, it was possible to design a unique, optimised allocation logic able to fulfil both open-loop and closed-loop commands, sufficiently proved and tuned before the installation onboard. Moreover, a thorough comparison between different design methods, static and dynamic performance evaluation has been carried out. Figure 53 shows the difference between a standard DP capability polar plot and the one obtained with the dynamic analysis. Two different operational modes were tested, and the results were presented: joystick and station keeping.

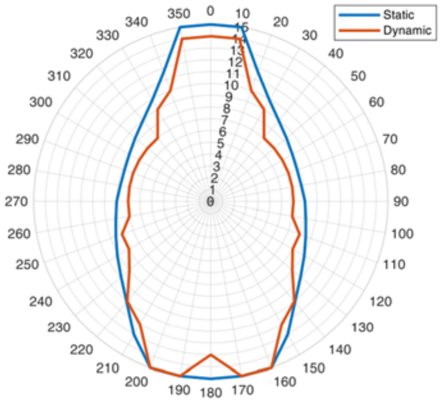

Figure 53: Comparison between static and "dynamic" DP capability plot.

It is possible to perform combined analysis of station keeping and seakeeping problems, determining seakeeping criteria for dynamic positioning (DP) due to ship motions, and use it as effective limiting environmental criteria for capability plots. In any case, even though seakeeping operational criteria are probably more restrictive than DP ones, it can be useful to investigate the effective operability of the DP system. For this purpose, Mauro et al. (2020) developed an enhanced and innovative procedure to establish the effective DP operability of an offshore vessel, by explicitly considering the vessel geographic operational area. The procedure has been tested on a pipe-lay vessel (PLV), as shown in Figure 54, and compared with the standard DP calculations, considering all the possible failures requested by regulations. Differences obtained from the comparison are significant and constitute a matter for further discussions.

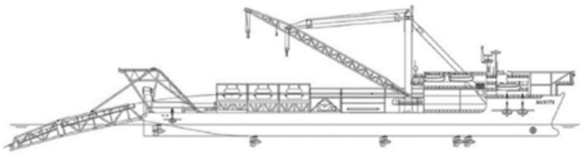

Figure 54: Generic PLV used as reference ship for the study.

It is nontrivial to tune the control parameters, and the station-keeping performance varies with environmental or loading conditions since the dynamics of the vessel were essentially nonlinear. In Xu et al. (2020), a fuzzy rule-based PID controller was evaluated, which took the estimated positioning error and low-frequency velocity as inputs, and outputs the time-varying PD control coefficients through fuzzy inference, while the integral control parameters were kept constant. The performance of the proposed controller was evaluated numerically through a time domain simulation of a dynamically positioned semi-submersible platform operating in variable environmental disturbances. Simulation results were compared with the conventional fixed gain PID controller, and the comparison results show that the proposed fuzzy PID controller can automatically tune the PD control coefficients according to the positioning accuracy and significantly improve the performance of the dynamic positioning system.

When considering the characteristics of a dynamic positioning (DP) vessel involving uncertain modelling and unknown disturbances, the vessel control problem becomes a mismatched nonlinear control issue. To resolve this issue, Hu et al. (2021)proposed a control method based on the sliding mode control (SMC) and the uncertainty and disturbance estimator (UDE). The total disturbance in the DP vessel was determined using the UDE, whereas the trajectory tracking function of the vessel was achieved via SMC. The effectiveness of the proposed control strategy was verified via simulations. The control system for the DP vessel is presented in Figure 55.

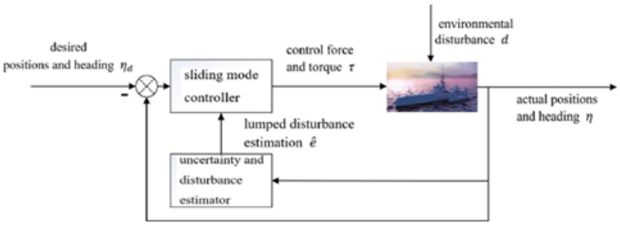

Figure 55: Schematic of the vessel tracking control system

In Liang et al. (2021), a robust adaptive neural networks control based on minimal–parameter-learning (MLP) was proposed for dynamic positioning (DP) of ships with unknown saturation, time delay, external disturbance and dynamic uncertainties. Through the velocities backstepping method, radial basis function (RBF) neural networks and robust adaptive control were incorporated to design a novel controller of which an appropriate Lyapunov-Krasovskii Function (LKF) was constructed to overcome the effect caused by time-delay. In additional, a robust adaptive compensate term was introduced to estimate the bound of the lumped disturbance including the unknown saturation, unknown external disturbance and the approximate error of neural networks control while the robustness of MLP was improved and the unknown saturation was compensated. The developed control law made the DP closed-loop system be uniformly ultimately stable which can be proved strictly through Lyapunov theory.

Zhang et al. (2021) presented a novel event-triggered cooperative dynamic positioning control algorithm for multiple marine surface ships in the presence of actuator faults. In this algorithm, the undirected interaction topology was employed to construct the communication networks among marine surface ships, and the assumption that the information of leader can be available to all followers was relaxed successfully. To avoid the unnecessary information transmission among ships, the event-triggered mechanism was incorporated in control design. And the strict positive lower bound on interevent interval was proved, which indicated no accumulation of triggering instants. Only two adaptive parameters were designed to estimate the actuator fault parameters online, they were updated when the event-triggered condition was violated and held otherwise. Considerable effort was made to guarantee the semi-global uniform ultimate bounded (SGUUB) stability by the extension of Lyapunov approach. Finally, numerical simulations were provided to verify the effectiveness and feasibility of the proposed algorithm. Under the interaction topology in Figure 56, the formation trajectories are shown in Figure 57 for three DP ships.

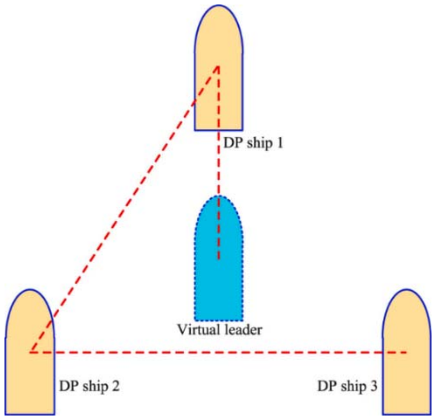

Figure 56: Interaction topology diagram among ships

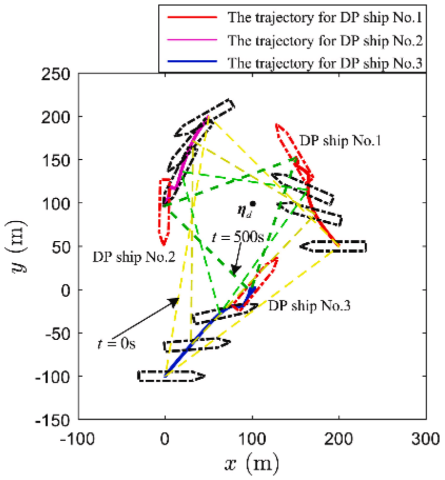

Figure 57: The formation trajectories for DP ships

Wang et al. (2021) investigated the trajectory tracking control problem of dynamic positioning ship subject to modeling uncertainties, environment disturbances, and unmeasurable velocity. A high-gain observer was constructed to estimate the unmeasurable velocity vector. Then, a special finite-time performance function was introduced to impose performance specifications in advance on the output tracking errors according to the mission requirements. Subsequently, through introducing error transformation functions, the tracking control problem with guaranteed transient performance was transformed to the output constrained control problem. In view of this, an asymmetric barrier Lyapunov function was designed to ensure that the transformed errors remain within specified ranges. By virtue of Lyapunov theory, it was shown that all the closed-loop signals were uniformly ultimately bounded and the tracking errors strictly comply with the prescribed performance envelops, despite the presence of modeling uncertainties, environmental disturbances and unmeasurable velocity. The simulation results of proposed controller are provided in Figure 58.

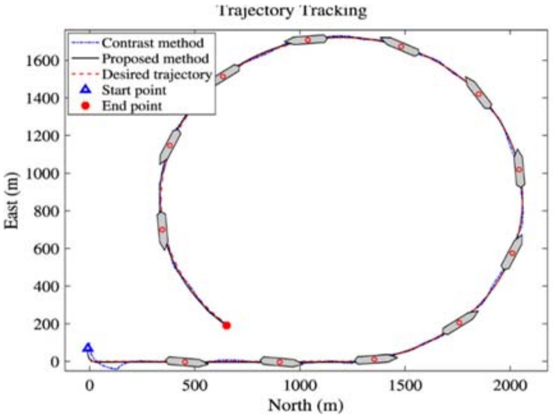

Figure 58: Time response of the trajectory tracking with proposed method and contrast method

A Dynamic Positioning (DP) system enables vessels and rigs to accurately maintain a predetermined position and heading or track, the role of the DP operator (DPO) was considered to monitor and keep the vessel in position. In Hogenboom et al. (2021), Applied cognitive task analysis (ACTA) was performed to analyze how the different operational settings influence the role and decision-making of the DPO. Recommendations for the improvement of safety, the design of the DP system, training and set-up of DP operations were formulated in this research.

In the “DP in Ice” Project, the authors conducted two extensive physical model test programs to generate a dataset on the managed ice- DP vessel interactions. One of the ice basin testing objectives was to generate a comprehensive dataset on the effects of managed ice-field characteristics on the thruster forces and moment encountered by DP-controlled vessels. The test case consisted of a vessel moving through a field of ice floes and brash ice, as shown in Figure 59. The test programs were executed at the ice basin of the NRC-OCRE using a non-proprietary DP system installed on two model vessels and a suite of sensors to acquire a dataset of ice-field and DP vessel interactions in various managed ice conditions. A series of physical modelling programs formed the basis of the empirical and numerical models developed in the “DP in Ice” program. Further details of the two test programs can be found in Islam et al. (2016), Wang et al. (2016), Islam et al. (2018), Islam et al. (2021), Islam et al. (2021a), Islam et al. (2022) and Islam et al. (2022a).

Figure 59: View of the ice basin and the model DP vessel

Islam et al. (2022) presented the methodologies and validations of a novel numerical model based on empirical-statistical techniques for predicting dynamically positioned (DP) vessels and ice-field interactions. The workflow for the development of the model is outlined in Figure 60. The authors developed multiple regression models for predicting the time-averaged and average peaks of thruster forces and yawing moment of the DP vessel due to managed ice actions. The model showed reasonable accuracy in predicting the effects of several ice-field parameters on the forces and moments of two DP-controlled vessels. Subsequently, integration of the model into a DP-in-ice validation platform was offered, which can simulate and optimize the performance of a DP-controlled vessel in ice-infested water.

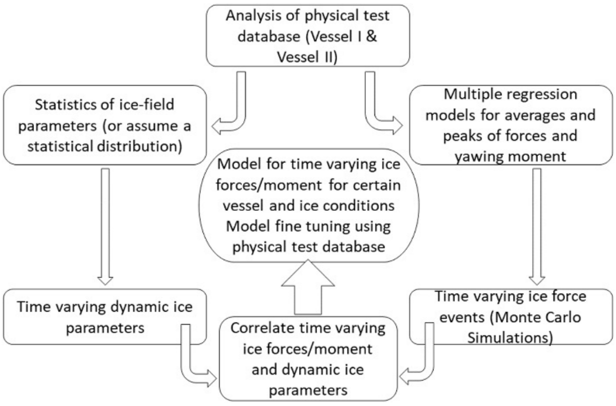

Figure 60: Flow chart of empirical-statistical modelling technique

Islam et al. (2022a) presented the tools, techniques and outcomes of a model testing program of a dynamically positioned (DP) Ice-1A classed Anchor Handling Tug Supply (AHTS) vessel called the "Magne Viking" in different managed ice environments. A total of 168 test runs were carried out in 7 ice sheets to evaluate the vessel's thruster forces and moment on the horizontal plane and the vessel's 6-DOF motions and accelerations. The time series and probability of exceedance plots of thruster forces and yawing moments were presented, along with the vessel's positioning relative to a set-point in various managed ice conditions. Overall, the study demonstrated the capability of the DP-controlled ship to maintain the station for most head-on tests and the oblique ice tests not exceeding 15°.

Li et al. (2022) presented a dedicated robust adaptive neural network control (RANNC) scheme for dynamic positioning (DP) of marine vessels with a prescribed performance under model uncertainties, external disturbances and input saturation. The command filter, RBFNN, auxiliary dynamic system (ADS), adaptive control and minimal learning parameter technique were adopted to design the RANNC scheme and guarantee the transient performance of DP vessel, as shown in Figure 61. The RANNC scheme was developed with the backstepping technique, and the method of command filter was introduced to avoid the "dimension disaster" problem. Moreover, minimal learning parameter technique was introduced to minimize the computational burden triggered by weight update of neural networks. Finally, comparison simulation results were provided to illustrate the performance of the proposed RANNC scheme.

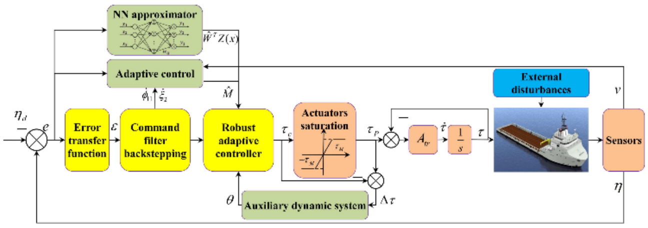

Figure 61: Control scheme of RANNC

Gustavo et al. (2022) discussed the application of the motions of a dynamically positioned platform supply vessel to perform inferences by means of a Bayesian method. The method was formulated considering a methodology for hyperparameter calibration based on an optimization process, and the definition of an iterative estimation scheme. Small-scale seakeeping tests in irregular waves were carried out with the model of a platform supply vessel (PSV) equipped with a dynamic positioning (DP) system, which was calibrated to be consistent with a typical real system. For evaluating any possible influence the DP responses might have had on the motion-based wave estimations, the same test conditions were also performed with the model moored by means of an equivalent soft-mooring configuration. Estimation results were obtained from the motions measured in the experiments, showing that wave parameters could be computed with good precision in both arrangements.

(Li 2022a) investigated the prescribed performance trajectory tracking control problem for dynamic positioning vessels in the presence of velocity constraints and thruster faults. By using a structurally simple error transformation, the issue of guaranteeing prescribed transient and steady state tracking performance was converted to a general state-constraint problem, which together with the velocity constraints form a trajectory tracking control problem with full-state constraint. Neural network and adaptive techniques were incorporated to construct a fault-tolerant trajectory tracking controller, which can not only estimate thruster faults, but also provide better robustness against model uncertainties and external disturbance. Finally, tracking control task for dynamic positioning systems was carried out to illustrate the merits of the proposed method. The simulation results are presented in Figure 62.

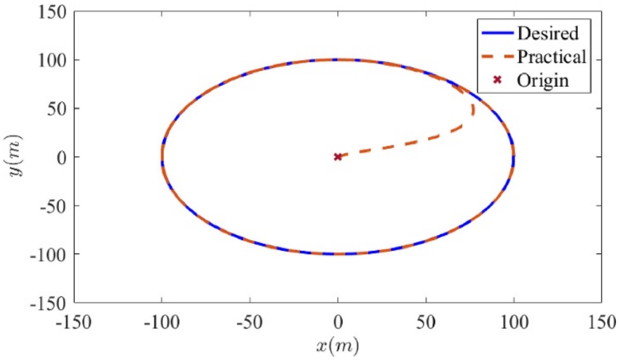

Figure 62: Simulation results of tracking the desired trajectory

Li et al. (2022b) studied the trajectory tracking control method for dynamic positioning vessels with state constraints and parameter uncertainties. A composite learning method was introduced to identify unknown parameters online. The structure of the control system was depicted in Figure 63. Regressor filtering together with dynamic regressor extension and mixing procedure were combined not only to relax the dependence of parameter estimation convergence process on the persistent excitation condition, but also to ensure the independence and flexibility of each parameter. Subsequently, a finite-time composite learning controller was designed based on asymmetric integral barrier Lyapunov functions, which guaranteed the asymmetric constraints on vessel states.

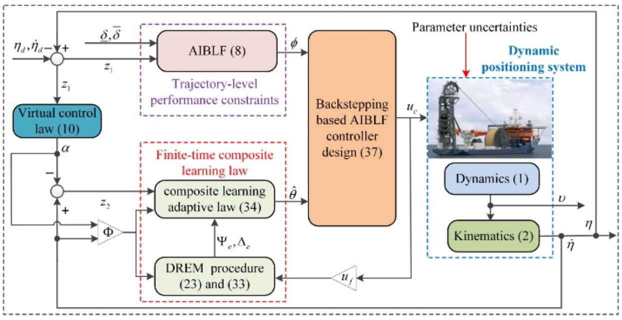

Figure 63: Block diagram of the control system

Martelli et al. (2022) presented the procedure for designing a Dynamic Positioning system and evaluating its performance using a dynamic approach. The proposed Time-domain Dynamic Positioning Capability Plots were obtained by a model-based design approach using a ship's dynamic simulator. The dynamic simulator was based on a fully actuated testing model. Indeed, the proposed tool has been designed on a tug vessel equipped with two azimuth thrusters and one bow-thruster. In particular, two force allocation logics for the station keeping manoeuvres have been developed; one is an optimised thrust allocation logic, the other is obtained with the primary goal to reduce as much as possible azimuth thrusters rotation. In Figure 64, the schematic system's view was reported. Eventually, the comparison between static capability plots and the capability plots obtained by several dynamic simulations has been provided, presented, and discussed.

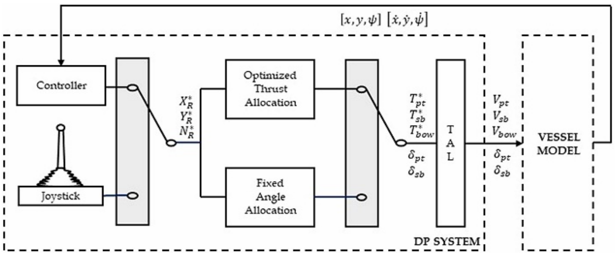

Figure 64: Dynamic positioning system structure

In Mauro et al. (2022), using known wind–waves joint distributions for the long-term environmental conditions further improved the scatter diagram approach, assessing the operability of a Dynamic Positioning system through a Quasi-Monte Carlo sampling of the joint distribution. Analysing the results of the Quasi-Monte Carlo process, it was possible to obtain a site-specific capability plot. The application of this novel method in the case of quasi-static calculations both to a reference supply vessel and a pipe-lay vessel showed the flexibility of the proposed approach for site-specific Dynamic Positioning capability predictions.

In Gopmandal et al. (2022), the ship dynamics with hydrodynamic parameter uncertainties was represented in an uncertain state-space descriptor form. Then, the design of feedback gains of 2-DOF PID controller for the uncertain descriptor plant was converted into a state feedback design for an augmented uncertain descriptor plant. the 2-DOF MIMO PID controller to be used was shown in Figure 65. Next, a linear matrix inequality-based condition was obtained to solve this state feedback problem in order to ensure a desired linear quadratic (LQ) performance, even in presence of uncertainties. Finally, to further improve the tracking performance, the feedforward gain of the 2-DOF PID controller was designed using H∞ approach. The DP performance of the proposed controller was tested for the considered ship model along with uncertainties, actuator constraints, and environmental disturbances. A comparison with the existing PID controllers was also carried out to show superiority of the proposed controller.

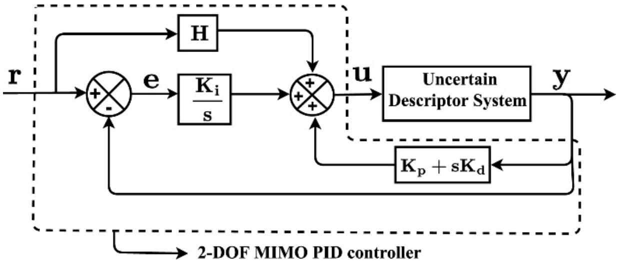

Figure 65: Feedback interconnection of the proposed controller and uncertain plant

Tang et al. (2022) proposed a robust control approach based on nonlinear model predictive control (NMPC) for dynamic positioning (DP) ships. An improved nonlinear disturbance observer (INDO) based on super-twisting control was constructed for disturbances estimation and attenuation. Furthermore, the NMPC optimization problem was formulated to reject the disturbances by combining the disturbance estimates into the prediction model. In light of this, a detailed time-iteration NMPC algorithm for DP ships was presented. Numerical simulations based on the INDO-based NMPC (INDO-NMPC) strategy under the scenario of trajectory tracking were performed to explore the robustness of DP system. Control architecture of DP system was given in Figure 66. Theoretical analysis and simulation results well proved the effectiveness and superiority of the proposed control law.

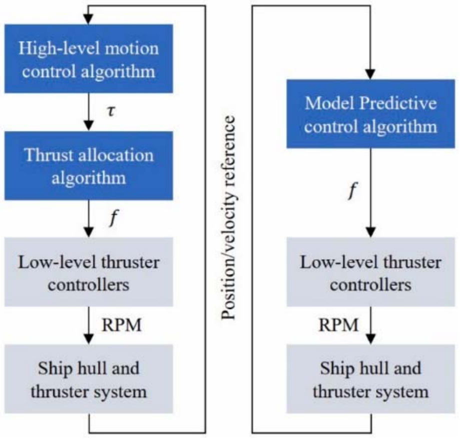

Figure 66: Control architecture of DP system (Left: INDO-NMPC-TA, Right: INDO-NMPC)

In order to establish the maximum environmental conditions in which a DP vessel can maintain its position and heading for a proposed thruster configuration, a DP capability analysis (DPCAP) must be carried out. The most crucial step in a DPCAP was to estimate the environmental loads due to the wind, current and waves in an accurate, consistent and efficient manner. In Aydin et al. (2022), semi-empirical methods and a RANS based analysis tool were compared in order to determine the reliability of such approaches for the purpose of early assessment of wind, wave and current loads. The main focus of this approach was to cross validate the semi-empirical and CFD based procedures so that the initial rough estimates on the loads could be refined accurately as well as to provide a comprehensive example of a reference work for the literature. Typical DP capability polar plots for an offshore supply vessel were presented to illustrate the application of the computational analysis procedure.

DNVGL-ST-111(DNVGL2021) Assessment of Station Keeping Capability of Dynamic Positioning Vessels, defines clear and consistent methodical requirements for DP station-keeping capability assessments. The standard also set requirements for the documentation of the calculations and for the presentation and verifiability of the results. It defined three different DP capability levels based on the Beaufort environmental scale, each requiring a specific assessment method. DP capability plots shall be generated for each level, and the result of the assessment was expressed as a DP capability number. In addition, the standard defined two DP capability assessment levels that allowed the inclusion of site-specific environmental data and external forces: Level 2-Site and Level 3-Site. The results of the site-specific analyses were presented by plots indicating the relevant wind speed limits for the given conditions.

3. REVIEW OF THE EXISTING PROCEDURES

The Committee reviewed and updated the following procedures and guidelines:

- 7.5-02-07-01.1 Laboratory Modelling of Multidirectional Irregular Wave Spectra;
- 7.5-02-07-01.2 Laboratory Modelling of Waves;
- 7.5-02-07-01.4 Confidence Intervals for Significant Wave;
- 7.5-02-07-01.5 Laboratory Modelling of Wind;
- 7.5-02-07-01.6 Laboratory Modelling of Currents;
- 7.5-02-07-03.1 Floating Offshore Platform Experiments;
- 7.5-02-07-03.2 Analysis Procedure for Model Tests in Regular Waves;
- 7.5-02-07-03.5 Passive Hybrid Model Tests of Floating Offshore Structures with Mooring Lines;
- 7.5-02-07-03.6 Dynamic Positioning System Model Test Experiments;
- 7.5-02-07-03.10 Guideline for VIV Testing;
- 7.5-02-07-03.11 Guideline for model tests of stationary multi-bodies operating in close proximity;
- 7.5-02-07-03.13 Guideline for VIM Testing;
- 7.5-02-07-03.14 Analysis Procedure of Model Tests in Irregular Waves.

- 7.5-02-07-03.16 Model Construction of Offshore Systems.

The objective of the review was to update the procedures/guidelines according to the current practices, and to provide references to understand and implement the techniques.

4. REVIEW AND IDENTIFY AREAS OF CONCERN IN MODELLING AND SIMULATION OF WAVES, WIND AND CURRENTS

4.1 Extreme Waves

The main objectives are: 1) to report the main recent literature findings regarding the methods to generate extreme wave packets for studying responses to extreme waves in a towing tank; 2) to examine the effects of wave breaking and statistics of occurrence on the wave spectrum, its spectral shape, extreme wave generation, and the role of wind-wave interaction on wave breaking occurrence. It takes as basis the previous work of Specialists Committee on Modelling Environmental Conditions (28th and 29th ITTC) and describe the new methodologies or questions that raised in this context.

4.1.1 Methods to generate extreme wave packets

SC on Modelling Environmental Conditions of the 28th ITTC listed the main methodologies for the deterministic generation of extreme waves. Different wave sequences may be used as extreme waves during experiments: i) Focusing waves, ii) Deterministic wave sequences embedded in an irregular sea state, iii) Wave tank realization of observed wave record or iv) Analytical extreme wave sequence such as breather-type solution (*e.g.* Peregrine breather). Specific method need to be set-up for the accurate generation of such deterministic wave sequences in a wave tank. This mostly rely on iterative correction of the phases (as well as amplitudes if necessary) to advocate the nonlinear effects.

For the 29th ITTC, this SC complement the methodologies, including improved phase-correction methods (Niu et al. (2020)), combined numerical and experimental procedures using non-linear wave models and Time-Reversal methodology (Ducrozet et al. (2020)).

Most of the recent works involving the generation of extreme wave events are based on the approaches described previously. The focus hereafter is on new methodologies.

Klein et al. (2023) study the effect of extreme waves on a LNG Carrier. In the context of extreme responses, they compare reference long-term irregular wave tests with different extreme wave sequences. This includes different analytical breather type solutions as well as the recreation of the measured at sea Draupner wave. By comparing the motions, vertical wave bending moment, green water column and slamming pressures it is concluded that the breather solutions are a powerful and efficient tool for the generation of design extreme waves of certain critical wave lengths for wave/structure investigations on different subjects.

Esandi et al. (2020) propose an experimental study on wave forces on a vertical cylinder due to spilling breaking and near-breaking wave groups. The extreme waves are generated as focused waves, which are corrected iteratively in amplitude and phase. One specificity of the method, that ensures a faster convergence is that the amplitude spectrum is measured near the wave generator and the phase spectrum is measured at the focus position.

Klein et al. (2021) introduce the use of envelope solitons as design waves for wave-structure interactions. They show that envelope soliton solutions can be used for generating tailored extreme design waves that causes extreme ship response. Then, they compare the impact of steep envelope solitons with results obtained in extreme waves such as Peregrine breather solution and the Draupner wave. The Peregrine breather is seen as more appropriate for design questions associated with the highest possible waves and wave breaking (e.g. green water on deck, local loads at the bow or other structures as well as air-gap investigations). Other design questions, where steep wave events are relevant but wave breaking not, may be better investigated by the envelope soliton due to the very short duration of such steep wave group.

Houtani et al. (2022) present a numerical and experimental study of modulated wave trains. It is found that the phases of all the spectral wave components of the nonlinearly evolving modulated wave trains coincided at the peak of the modulation. This phase convergence process contributes to the crest enhancement of modulated wave trains beyond the solution of the cubic Non-Linear Schrödinger Equation. In addition, it is demonstrated that the free-wave spectral broadening energizes the bound-wave production at high wavenumbers. The bound wave components can contribute more than a quarter of the maximum crest height at an initial wave steepness of 0.115.

Ma et al. (2022) introduce an additional correction step to the Time-Reversal methodology in order to account for possible inaccuracies associated to wave generation or to non-conservative phenomena during wave propagation. This step consists in a classical correction of amplitude and phase between measured and target elevation. The proposed methodology is successfully validated on the experimental reproduction of four different wave profiles extracted from measurements at sea. The authors then analyze the physics of the formation of those extreme waves with wavelet-based bicoherence.

Wang et al. (2020) investigate the generation of extreme waves as a result of the focusing of two wave groups with different peak frequencies. This particular mechanism has been observed during the formation of rogue waves and may be a candidate to generate representative extreme wave profiles. Phase shifts and amplitude changes are observed during the propagation as a result of third-order non-linearity.

Kim et al. (2022) present a novel methodology for the generation of the so-called Equivalent Design Wave (EDW). This paper focus on wave-only problem, the EDW being defined as the most probable wave with a crest amplitude corresponding to a given probability of occurrence. The novelty in the construction of the EDW comes from the use of a High-Order Spectral Numerical Wave Tank (HOS-NWT) together with an optimization algorithm based on First-Order Reliability Method (FORM). As a result, the methodology provide a wavemaker motion able to generate this extreme wave. The approach has been validated with dedicated experiments that compared the Monte-Carlo irregular time series and the EDW results. The geometrical similarity between the measured EDW wave signal and the corresponding irregular wave signals measured in a given sea state was reviewed. It confirmed that the FORM-based EDW generates a comparable wave profile.

Xu et al. (2021) numerically investigate the effects of amplitude distribution of wave components on focusing wave generation, including the focusing wave crest elevation and the focusing position. Wave amplitude spectra with three types of variation across the frequency range are constructed. It is expected that the findings will help for amplitude spectra type selection or construction for efficiently generating tailored focusing waves (or extreme waves) in physical or numerical wave tank.

4.1.2 Effects of wave breaking and wind-wave interaction

SC on Modelling Environmental Conditions of the 28th ITTC provides a brief overview of the effect of wave breaking on statistics. It covers some numerical high-fidelity CFD as well as some experimental works. Effect of wind on wave breaking is not addressed. A more detailed review on the effect of breaking on spectral content is provided in the work of the SC for the 29th ITTC. The referenced works cover different type of wave conditions:

- Irregular sea states in experiments and high-fidelity CFD: reduction of energy in the high-frequency range
- Modulational instability: experimental and numerical simulations indicating the down shifting consecutive to the breaking
- Two uni-directional wave field interacting locally with an angle (X-arrangement): severity of breaking increase with the angle between the two components

Up to the 29th ITTC, research on the effect of wind-wave interaction on wave breaking occurrence was mostly limited to the study of localized events (focusing wave, modulational instability) with and without wind to identify the effect on the breaking occurrence. Numerical and experimental works have been reported on this topic.

In Craciunescu and Christou (2020) an experimental study on wave breaking energy dissipation in focused waves is presented. An accurate two-camera set-up is used to evaluate the local wave geometry during breaking process and define breaking characteristics. Those measurements are used to propose a new parametrization of an existing wave breaking model that is used in nonlinear wave models.

Eeltink et al. (2022) present a blended machine learning framework in which a physics-based nonlinear evolution model for deep-water, non-breaking waves and a recurrent neural network are combined to predict the evolution of breaking waves. Wave tank measurements are used for training data and as reference data for comparisons. The proposed framework gives accurate predictions of breaking events and their effects on wave propagation. This might be a first step toward the use of such procedure to characterize the effect of breaking on wave field characteristics.

As part of the JIP ‘Reproducible CFD Modeling Practices for Offshore Applications’, experiments on unidirectional breaking sea conditions have been conducted and serves as basis to the benchmark of potential-based numerical wave tanks (Fouques et al. (2021)) as well as CFD based NWT (Bouscasse et al. (2021)). The probability of exceedance of wave crests as well as elevation rise velocity are reported for qualified wave spectrum (i.e. following accurately the target wave spectrum despite the wave breaking). Same wave spectrum is generated in two different experimental facilities and at different scales in Canard et al. (2022).

In Khait et al. (2022), the energy dissipation associated to wave breaking is simulated with a coupled potential and high-fidelity CFD solver. Main purpose of the study is to decompose the energy dissipation into a potential part and a non-potential part, representing the effect of vertical structures. For breaking waves, there is a strong non-potential motion triggered by breaking wave and that persists in the flow for dozens of wave periods.

Lee and Monty (2020) studied the statistical properties and development of wave fields with different wind forcings in a unidirectional configuration. If breaking waves are not studied specifically, it is observed that when waves develop under the competing effects of wind forcing and nonlinear wave interaction, wind–wave interaction due to wind forcing dominates the growth mechanism over the wave–wave interaction. The exceedance probability of wave crests is found to depend on wind speed most obviously for the lowest probability (largest) waves, where a deviation from empirical second-order models is clearly evident. At lower wind speed, the Forristall distribution underestimates the probability of occurrence of the high amplitude waves, yet overpredicts at high wind speeds. This overprediction is mainly because, at the high wind speeds, the growth of extreme waves is limited by the wave breaking mechanism as the local wave steepness increases with wind speed.

4.2 Vertical Wind Profiles

Vertical profile of horizontal wind (shortened to wind profile) refers to the horizontal wind vector as a function of height. Due to the surface influence wind speed in boundary layer can change significantly from the surface values. The exact shape of the wind profile depends on surface roughness and atmospheric stability. Wind direction is approximately constant near the surface and begins to change only in the Ekman layer above. For this reason, wind profile near the surface usually refers to simply wind speed as a function of height.

The standard vertical wind profile offers a choice of mean wind velocity profiles. The velocity profiles determine the mean velocity at each height for the length of the numerical and experimental simulation. For velocity profiles that use a reference height and wind speed, the standard uses the inputs z_r and u_r as the reference point and velocity to calculate the mean velocity at other vertical heights.

(1) Power-Law Wind Profile

The power-law mean velocity profile uses the input parameter α to calculate the average wind speed at height z using the equation:

$$u_z = u_r \left(\frac{z}{z_r}\right)^{\alpha}$$

where u_z is the wind speed (in metres per second) at height z (in metres), and u_r is the known wind speed at a reference height z_r. The exponent (α) is an empirically derived coefficient that varies dependent upon the stability of the atmosphere. For neutral stability conditions, α is approximately 1/7, or 0.143. The value of 1/7 for α is commonly assumed to be constant in wind resource assessments, because the differences between the two levels are not usually so great as to introduce substantial errors into the estimates (usually < 50 m). However, when a constant exponent is used, it does not account for the roughness of the surface, the displacement of calm winds from the surface due to the presence of obstacles (i.e., zero-plane displacement), or the stability of the atmosphere. In places where trees or structures impede the near-surface wind, the use of a constant 1/7 exponent may yield quite erroneous estimates, and the log wind profile is preferred. Even under neutral stability conditions, an exponent of 0.11 is more appropriate over open water (e.g., for offshore wind farms), than 0.143, which is more applicable over open land surfaces.

When the wind speed is strong enough, the relationship between the roughness length z_0 and power law exponent α can be given as follows (Nakajima et al, 2020):

$$\alpha = 0.24 + 0.096(\log z_0) + 0.016(\log z_0)^2$$

The power law is often used in wind power assessments where wind speeds at the height of a turbine (>50 m) must be estimated from near surface wind observations (~10 m), or where wind speed data at various heights must be adjusted to a standard height prior to use. Wind profiles are generated and used in a number of atmospheric pollution dispersion models.

The wind profile of the atmospheric boundary layer (surface to around 2000 meters) is generally logarithmic in nature and is best approximated using the log wind profile equation that accounts for surface roughness and atmospheric stability. The relationships between surface power and wind are often used as an alternative to logarithmic wind features when surface roughness or stability information is not available.

Estimates of wind power density are presented as wind class, ranging from 1 to 7. The speeds are average wind speeds over the course of a year, although the frequency distribution of wind speed can provide different power densities for the same average wind speed.

Table 1 Wind power density presented as wind class

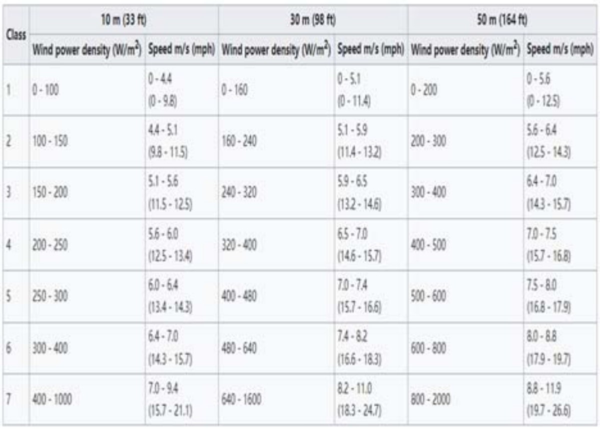

Class	10 m (33 ft)		30 m (98 ft)		50 m (164 ft)	
	Wind power density (W/m²)	Speed m/s (mph)	Wind power density (W/m²)	Speed m/s (mph)	Wind power density (W/m²)	Speed m/s (mph)
1	0 - 100	0 - 4.4 (0 - 9.8)	0 - 160	0 - 5.1 (0 - 11.4)	0 - 200	0 - 5.6 (0 - 12.5)
2	100 - 150	4.4 - 5.1 (9.8 - 11.5)	160 - 240	5.1 - 5.9 (11.4 - 13.2)	200 - 300	5.6 - 6.4 (12.5 - 14.3)
3	150 - 200	5.1 - 5.6 (11.5 - 12.5)	240 - 320	5.9 - 6.5 (13.2 - 14.6)	300 - 400	6.4 - 7.0 (14.3 - 15.7)
4	200 - 250	5.6 - 6.0 (12.5 - 13.4)	320 - 400	6.5 - 7.0 (14.6 - 15.7)	400 - 500	7.0 - 7.5 (15.7 - 16.8)
5	250 - 300	6.0 - 6.4 (13.4 - 14.3)	400 - 480	7.0 - 7.4 (15.7 - 16.6)	500 - 600	7.5 - 8.0 (16.8 - 17.9)
6	300 - 400	6.4 - 7.0 (14.3 - 15.7)	480 - 640	7.4 - 8.2 (16.6 - 18.3)	600 - 800	8.0 - 8.8 (17.9 - 19.7)
7	400 - 1000	7.0 - 9.4 (15.7 - 21.1)	640 - 1600	8.2 - 11.0 (18.3 - 24.7)	800 - 2000	8.8 - 11.9 (19.7 - 26.6)

(2) Logarithmic Wind Profile

The logarithmic profile of wind speeds is generally limited to the lowest 100 m of the atmosphere (i.e., the surface layer of the atmospheric boundary layer). The rest of the atmosphere is composed of the remaining part of the planetary boundary layer (up to around 1000 m) and the troposphere or free atmosphere. In the free atmosphere, geostrophic wind relationships should be used. The equation to estimate the mean wind speed (u_z) at height (z) above the ground is:

$$u_z = \frac{u_*}{\kappa}\left[\ln\left(\frac{z-d}{z_0}\right) + \psi(z, z_0, L)\right] (+Coriolis\ force\ term)$$

where u_* is the friction velocity, κ is the Von Kármán constant (~0.41), d is the zero plane displacement, z_0 is the surface roughness, and ψ is a stability term where L is the Obukhov length from Monin-Obukhov similarity theory. The equation above can be modified to include the Coriolis force-related parameter, 34.5 fz/u_* for a somewhat improved wind profile. Here $f = 2\omega \sin\phi$; where ω is the angular velocity of the earth in rad/s and ϕ is the latitude.

As per DNV(2010), the stability function ψ is zero under neutral atmospheric condition, positive under unstable condition, and negative under stable atmospheric conditions. Ref: DNV(2010): [DNV-RP-C205: Environmental Conditions and Environmental Loads -(October 2010- Recommended Practice]

The general form of the stability function for an unstable atmospheric condition is as follows according to DNV (2010):

$$\begin{aligned}\psi = 2\ln[1 + (1 - 19.3\, z/L)^{0.25}] \\ + \ln[1 + (1 - 19.3\, z/L)^{0.5}] \\ - 2\tan^{-1}[(1 - 19.3\, z/L)^{0.25}]\end{aligned}$$

Under neutral stability conditions, $z/L = 0$ and ψ drops out and the equation is simplified to,

$$u_z = \frac{u_*}{\kappa}\left[\ln\left(\frac{z-d}{z_0}\right)\right]$$

Zero-plane displacement d is the height in meters above the ground at which zero wind speed is achieved as a result of flow obstacles such as trees or buildings. It clarification needed can be approximated as 2/3 to 3/4 of the average height of the obstacles. For example, if estimating winds over a forest canopy of height 30 m, the zero-plane displacement could be estimated as d = 20 m.

Roughness length z_0 is a corrective measure to account for the effect of the roughness of a surface on wind flow. That is, the value of the roughness length depends on the terrain. The exact value is subjective and references indicate a range of values, making it difficult to give definitive values. In most cases, references present a tabular format with the value of z_0 given for certain terrain descriptions. For example, for very flat terrain (snow, desert) the roughness length may be in the range 0.001 to 0.005 m. Similarly, for open terrain (grassland) the typical range is 0.01-0.05 m. For cropland,

and brush/forest the ranges are 0.1-0.25 m and 0.5-1.0 m respectively. When estimating wind loads on structures the terrains may be described as suburban or dense urban, for which the ranges are typically 0.1-0.5 m and 1-5 m respectively.

In order to estimate the mean wind speed at one height (z_2) based on that at another (z_1), the formula would be rearranged,

$$u(z_2) = u(z_1)\frac{\ln((z_2 - d)/z_0)}{\ln((z_1 - d)/z_0)}$$

where $u(z_1)$ is the mean wind speed at height z_1.

Log wind profiles are generated and used in many atmospheric pollution dispersion models. The log wind profile is generally considered to be a more reliable estimator of mean wind speed than the wind profile power law in the lowest 10–20 m of the planetary boundary layer. Between 20 m and 100 m both methods can produce reasonable predictions of mean wind speed in neutral atmospheric conditions. From 100 m to near the top of the atmospheric boundary layer the power law produces more accurate predictions of mean wind speed (assuming neutral atmospheric conditions). The neutral atmospheric stability assumption discussed above is reasonable when the hourly mean wind speed at a height of 10 m exceeds 10 m/s where turbulent mixing overpowers atmospheric instability.

(3) IEC Wind Profile

The IEC wind profile was the wind-speed profile available for wind turbine. This profile uses the power-law wind profile for the wind speeds at heights on the rotor disk and the logarithmic profile for heights not on the rotor disk. For example, if u_r is specified at a z_r below the rotor disk, the logarithmic profile is used to calculate the mean wind speed at hub height. Then the power-law profile would be used with the hub height wind speed to calculate winds across the rotor disk. This profile could cause a discontinuity in the wind profile at the bottom of the rotor disk.

(4) Low-Level Jet Wind Profile

The low-level jet wind profile is derived from Lamar Low-Level Jet Project (LLLJP) 10-minute SODAR measurements and is available with only the Great Plains Low-Level Jet Model spectral model. The Great Plains model is based on measurements from a 120-m tower and from an acoustic wind profiler (SODAR [sonic detection and ranging]) obtained during the Lamar Low Level Jet Project in southeastern Colorado. The tower included three-axis sonic anemometers at 54 m, 67 m, 85 m, and 116 m above the ground; cup anemometers and direction vanes located at 3, 52, and 113 m; and temperature measurements obtained at 3 m, 52 m, 83 m, and 113 m. The SODAR provided measurements of wind speed and direction at 10-m vertical increments from 20 m to 500 m. The spectra and spatial coherence parameters defined in this model are based on 20-Hz time-series data collected at the sonic anemometers.

The Great Plains Low-Level Jet Model defines vertical profiles of shear velocity. This profile type is unique because it generates both wind-speed and wind-direction profiles. The low-level jet wind-speed profile is defined using Chebyshev polynomials,

$$u_z = \sum_{n=0}^{10} c_n \cdot T_n(z)$$

where z is the height above ground, u_z is the mean wind speed at height z, $T_n(z)$ is the n^{th} order Chebyshev polynomial, and c_n is a Chebyshev coefficient. The Chebyshev coefficients are derived from LLLJP data and are a linear combination of the jet wind speed (u_{ZJetMax}), gradient Richardson number (RICH) and u_*

$$c_n = C_{1,n}u_{\mathrm{ZJetMax}} + C_{2,n}\mathrm{RICH} + C_{3,n}u_* + C_{4,n}$$

The coefficients, $C_{i,n}$ =1, 2, 3, 4, are determined by the input parameter *ZJetMax*. The low-level jet wind-direction profile, like the wind-speed profile, is a Chebyshev polynomial with coefficients derived from the same parameters in the LLLJP data.

(5) API Wind Profile

The API wind profile is based on 1-hr mean wind speed at 10 m above sea level, it is defined by the equation

$$u_z = u_r(1 + 0.0573\sqrt{1 + 0.15u_r})\ln z/z_r$$

Where z is the height, u_z is the mean wind speed at height z, u_r is the one-hour mean wind speed, and z_r is 10 meters.

(6) Gust wind profile

Gust wind is a sudden, brief increase in speed of the wind. In contrast with the boundary layer winds, the gust winds are nonstationary due to their transient characteristics. Therefore, the stationary wind model typically used in boundary layer winds may not be valid for gust winds which may be described in terms of time-varying parameters.

The vertical profile of gust winds is critical in evaluating the wind effects on structures, however, very limited full-scale data along the height is available to identify and reliably establish a description of the vertical profile. From a practical viewpoint, the worst scenario for wind loads on structures may be the highest wind speed which occurs at about one downdraft jet diameter from its point of impact. Note that several analytical models have been proposed for vertical profile of gust winds. Although there are some discrepancies among models, especially a profile over z_{max}, all models moderately fit well with a limited full-scale data. Thus, without loss of generality, the following model is utilized due to its simplicity:

$$u_z = 1.354 \cdot V_{max}\left[e^{-0.22(z/z_{max})} - e^{-2.75(z/z_{max})}\right]$$

where V_{max} is maximum horizontal wind speed, z_{max} is the height where V_{max} occurs.

The vertical profile model of a downburst describes a short time averaged maximum mean wind speed at a height, which may be treated as a gust profile as used in the boundary layer wind case. Since z_{max} and V_{max} in the model are unknown, it is necessary to establish a criterion to relate the velocity profile in a gust wind and a boundary layer for design considerations. Two criteria are considered: (i) gust wind speed at 10 m height, is set equal to the boundary layer gust speed at 10 m; (ii) the maximum gust wind speed (V_{max}) is equal to gust speed at the gradient height in boundary layer winds. One may conveniently introduce additional criterion that may better reflect the data or may meet other site-specific requirements when it becomes available in the future.

(7) User-Defined Velocity Profiles

For user-defined velocity profiles, the standard linearly interpolates the input velocity profiles. The profiles are calculated from the mean values of the input time series. The profiles are extrapolated by using a nearest-neighbor approach: the profiles are constant at heights above or below the heights where the input profiles are defined.

4.3 STATE-OF-THE-ART IN HYBRID TESTING – SOFTWARE-IN-THE-LOOP TESTS FOR MODELLING WIND FORCES

The state-of-the-art in hybrid testing of offshore wind turbines are reviewed, to continue work on using a small controllable fan to mimic forces developed during a floating offshore wind turbine test due to the turbine itself, and to expand the work on Software-in-the-Loop (SiL) systems for modeling wind turbine loads to be used as a general tool to model many types of wind loads.

4.3.1 Development of hybrid testing methods for floating wind turbines

Conventional full physical model tests of floating wind turbines (FWTs) typically utilize Froude scaling to preserve gravitational wave loads. However, this approach results in a lower Reynolds number, causing the aerodynamic loads to be out of scale. Additionally, model tests of FWTs require adjusting the blade pitch angle and generator torque to accurately simulate the coupling effects. Nevertheless, designing a specialized apparatus to effectively mimic the control system's performance in the prototype poses a significant challenge (Yu et al., 2017).

To overcome these challenges, particularly the scaling conflict, researchers have employed various methodologies for testing FWTs. One approach is the use of static cables to replicate steady wind forces. Another method involves the utilization of a drag disk at the top of the tower to approximate the thrust force. In Robertson's research, Froude-scaled rotors with increased wind speed were employed to match the correct thrust force. Redesigned rotors, which perform identically to the full-scale rotor at a lower Reynolds number, were also utilized to accurately generate the rotor's aerodynamic loads. Hybrid testing is another technique that combines physical testing and real-time numerical simulation. An actuation system enables the coupling between the simulated wind turbine and the physical floater, either in a wave basin or, conversely, in a wind tunnel.

The concept of real-time hybrid model experiments was initially introduced in civil engineering. Originally, this method was used to study the dynamic responses of large buildings subjected to seismic forces. In 1992, Nakashima et al. (1992) proposed a real-time hybrid model experimental method that utilized the same loading rate as a real earthquake to obtain the actual response of the test components. Over time, this idea expanded and found application in offshore engineering experiments. In hybrid tests, a physical part of the model is replaced by an actuator connected to a numerical tool. This approach can be implemented in wind tunnels or wave basins. By using the hybrid approach, FWTs can be tested under combined wind and wave conditions without the need for a wind generation system. The actuators take the place of the rotors and generate the required aerodynamic loads.

Compared to the conventional full physical testing method, the hybrid model testing approach offers several advantages, which can be summarized as follows (Otter et al., 2022):

- ***Cost-effectiveness***: Hybrid testing can be more cost-effective since it replaces certain physical components with actuators and numerical tools, reducing the need for expensive full-scale physical models.

- ***Flexibility***: The hybrid approach allows for greater flexibility in testing various scenarios and conditions. It can simulate different wind and wave conditions, providing a more comprehensive understanding of the system's behavior.

- ***Time efficiency***: Hybrid testing can significantly reduce the testing time compared to full physical testing. The use of numerical tools enables faster simulations and real-time responses, allowing for quicker data analysis and decision-making.

- ***Scalability***: Hybrid models can be easily scaled up or down, making it possible to test different sizes of FWTs without the need for separate physical models for each size.

- ***Control system emulation***: The hybrid approach enables more accurate emulation of the control system's performance in the prototype. This is achieved by integrating the physical floater with the simulated wind turbine using actuators, resulting in more realistic and reliable results.

However, the hybrid model testing approach also presents certain challenges, which can be summarized as follows (Otter et al., 2022):

- ***Complexity***: Hybrid testing involves the integration of physical and numerical components, which can be technically complex and require advanced expertise in both areas. Designing and implementing the actuation system and ensuring its synchronization with the numerical simulation can be challenging.

- ***Validation***: Validating the accuracy and reliability of the numerical tools used in the hybrid model can be difficult. Ensuring that the numerical simulations accurately represent the behavior of the physical system requires thorough validation and calibration.

- ***Uncertainty***: There may be uncertainties associated with the numerical models used in the hybrid approach, such as the accuracy of the numerical algorithms or the assumptions made in the simulations. These uncertainties can affect the reliability of the test results.

- ***Hardware constraints***: The physical components used in the hybrid model, such as actuators, may have limitations in terms of their load capacity, response time, or other hardware constraints. These limitations can impact the fidelity and realism of hybrid testing.

The advantages and disadvantages of full physical testing and hybrid testing are further summarized in Table 2:

Table 2: The comparison of pros and cons of the full physical method and hybrid method (Otter et al. 2022)

Full physical modeling	
Advantage	• Models aerodynamic thrust, torque, and gyroscopic moment • Captures aerodynamic damping • Turbine control can be applied
Disadvantage	• Requires expensive and bulky wind generation equipment • Difficult to generate high-quality laminar steady wind • Difficult to generate stochastic wind with good repeatability • Requires a unique turbine model for each turbine design and scale • Rotor often requires the aid of an electric motor to reach the correct TSR
Hybrid modeling	
Advantage	• Depending on the number of actuators it is possible to emulate thrust, torque, and gyroscopic moment with good repeatability • Capture aerodynamic damping • Turbine control can be applied • Stochastic wind loads can be implemented without great difficulty • Versatile, can be used for any type of turbine or scale • Requires less space and is considerably cheaper than a wind generation system
Disadvantage	• System latency • Multiple actuators required to emulate all aerodynamic loads add complexity and uncertainty • Phenomena not simulated with the numerical model will not be captured during testing

4.3.2 Types of actuators used in the hybrid testing method

The following recaps the hybrid testing campaigns of FWTs and highlights the advantages of each actuation system employed in these tests.

（1）Propeller actuators

In terms of actuators, researchers commonly use propellers and ducted fans in hybrid testing. One widely applied actuator is the single propeller actuator with SIL, which has been used in various campaigns. For example, at the Kelvin Hydrodynamics Laboratory (KHL) at the University of Strathclyde, a 1:36.67 scale model of the Iberdrola TLP was tested using this actuator (Oguz et al., 2020). However, it should be noted that the single fan actuator is designed to replicate the thrust force only, and does not emulate other aerodynamic loads and gyroscopic moments. Therefore, efforts have been made to develop multi-actuator systems that are capable of reproducing the full aerodynamic tensor.

At the Instituto Hidraulica Cantabria (IHC), an actuator consisting of six drone propellers was developed and utilized in the testing of the TELWIND FWT (Urbán et al., 2020). The propellers were carefully calibrated and tuned to account for the aerodynamic effects resulting from their proximity. The results of these tests were promising, showing only minor deviations compared to the expected load values. Another actuator, developed and calibrated by Hmedi et al. (2022), utilized three propellers to replicate both thrust and aerodynamic moments. While this system performed well overall, it struggled to accurately emulate the high-frequency components of the loads. Additionally, a multi-propeller system was also employed to test a vertical-axis wind turbine (Kanner et al., 2016).

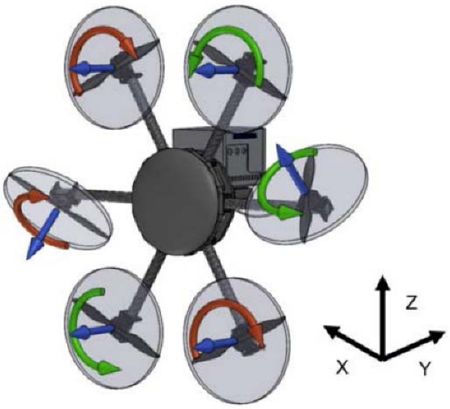

(a) CAD View

(b) Model tests view

Figure 67: The (a) CAD view and (b) Model tests view of multi-fan employed in the hybrid testing of TELWIND FWT (Urbán et al., 2020)

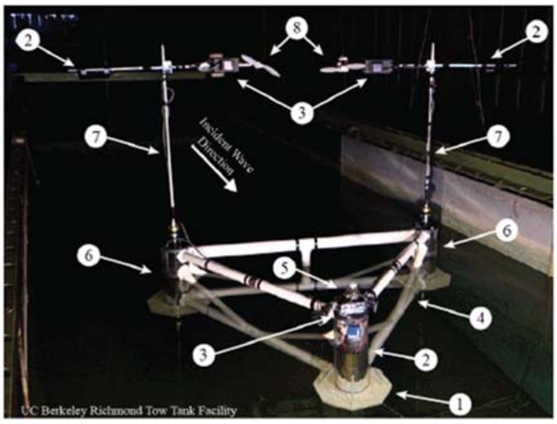

(a) Main components of hybrid testing MIST platform

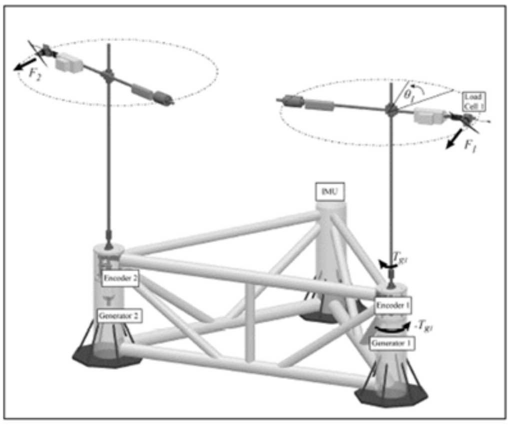

(b) Schematic of sensors and actuators on the MIST platform

Figure 68: The presence of the details of the hybrid testing of a vertical axis floating wind turbine in the UC Berkeley physical-model testing facility (Kanner et al., 2016)

（2）Cable winch actuators

Cable winches have also been employed as actuators in hybrid testing. In the early testing campaigns, static lines or cables were utilized to replicate the static thrust obtained from the thrust curve of the specific turbine being tested. These campaigns encompassed various types of tests, such as decay, regular, and irregular wave tests. Additionally, regular wave tests were conducted with a constant thrust force applied at the top of the tower through the use of cables. However, it is important to note that these cable winches solely focused on reproducing the thrust force and did not take into consideration other aerodynamic loads and interactions, such as turbulent wind, aerodynamic damping, controller effects, and gyroscopic moments.

Indeed, using cable winches as actuators in hybrid testing offers simplicity and efficiency, as it involves a straightforward mechanical system with cables applying static tensions at the top of the tower. However, this method has limitations in terms of control and variability, as it can only replicate static loads. Furthermore, relying solely on the wind turbine's thrust curve does not account for the platform's response when calculating aerodynamic loads. Additionally, gyroscopic effects cannot be emulated using this technique. Moreover, it is important to note that this method only emulates the thrust force and neglects other components of aerodynamic loads.

To overcome the limitations of the static cable method, a significant improvement involves applying tensions instantaneously to the model in real-time, based on the load simulation. This approach is similar to the Software-In-the-Loop (SIL) system with propeller actuators, but instead of using propellers, cable winches are utilized to apply the loads calculated by the numerical tool. By implementing this method, the limitations of static loads and neglecting other aerodynamic load components can be addressed, allowing for a more dynamic and accurate representation of the wind turbine's behavior during testing.

The first real-time hybrid system utilizing cable winches was developed at SINTEF in Norway. This system involves six cables that are connected to a square frame at the hub height of the wind turbine. Researchers at SINTEF (Bachynski et al., 2016) referred to this approach as ReaTHM testing and employed it to test the NOWITECH model, which incorporates the NREL 5 MW wind turbine. This innovative system allows for dynamic and real-time load application, enabling more accurate and comprehensive testing of wind turbine models.

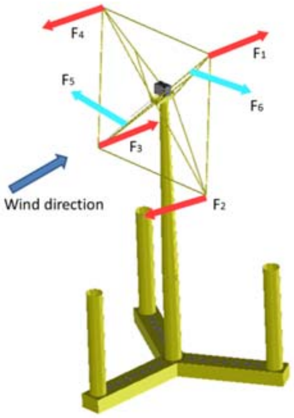

(a) The physical substructure

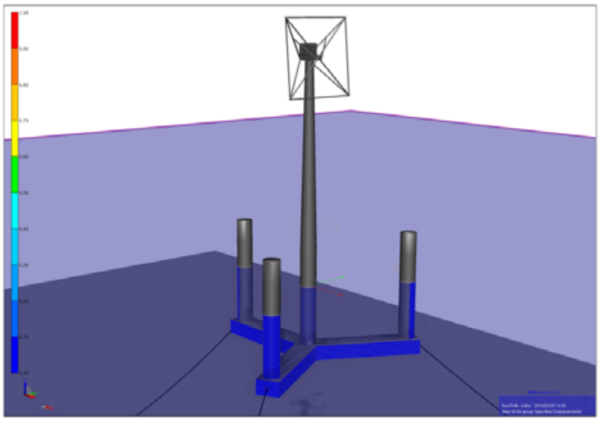

(b) The FWT modeled in SIMA with a frame for the hybrid testing method

Figure 69: The presence of the details of the hybrid testing in the SINTEF in Norway (Bachynski et al., 2016)

Antonutti's research work also utilized a hybrid system with cables similar to the one used at SINTEF (Antonutti et al., 2020). The model tested in Antonutti's research was a semi-submersible platform with the Haliade 6 MW wind turbine. The system consisted of five cables that allowed for the actuation of the surge, pitch, and yaw degrees of freedom (DOFs). The results of the study demonstrated a successful correlation between the experimental and numerical models, indicating the effectiveness of this hybrid testing approach in accurately capturing the behavior of the wind turbine system.

(a) Floating wind turbine model tested at MARIN

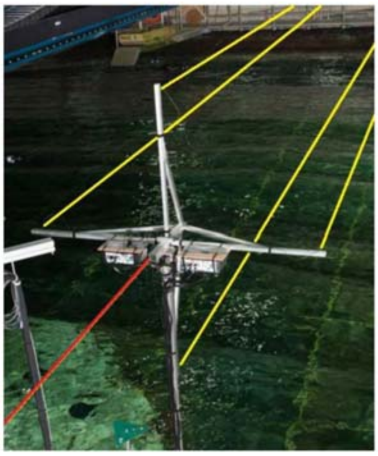

(b) Turbine superstructure with winch lines highlighted

Figure 70: The presence of the details of the hybrid testing of a 6 MW semi-submersible FWT in the MARIN (Antonutti et al., 2020).

（3）Wind tunnel tests

Indeed, hybrid tests with cables and propellers are often conducted in wave basins to study the hydrodynamics of the tested platform. In these tests, the actuators emulate the aerodynamic loads instead of subjecting a scaled rotor to a wind flow. This approach allows for a comprehensive analysis of the platform's behavior in a controlled environment. Another type of hybrid testing takes place in wind tunnels and focuses on studying aerodynamic loads, wakes, and interactions of the wind turbine. In this case, instead of calculating the aerodynamic loads, the motions of the FWT model are simulated using a numerical tool. The physical model, including a physical rotor, is placed in the wind tunnel, and the motions of the FWT are replicated using actuators. This method enables researchers to study the dynamic response of the wind turbine and its interactions with the surrounding flow, providing valuable insights into its aerodynamic performance.

In the study conducted by Schliffke et al. (2020), wind tunnel tests were performed to investigate the influence of surge motion on wake characteristics. The tested model used in this study was the FLOATGEN barge, which supported a 2 MW wind turbine. Instead of using a scaled rotor, a porous disc concept was adopted. The surge displacement of the model was controlled by a linear motor, which was operated using the manufacturer's software. During the tests, a nearly constant delay was observed between the assigned and emulated motion. However, since the focus of the study was on investigating the influence of surge motion on wakes and not on motion dynamics, this delay was considered insignificant. Importantly, the delay remained consistent regardless of the imposed frequency and amplitude of the motion. Furthermore, hybrid tests in wind tunnels were also conducted to examine the impact of pitch motion on the wakes of the FWT. Additionally, the effect of wake interactions on the FWT was investigated in these tests. These studies were carried out by Rockel et al. (2020, 2021), providing valuable insights into the complex dynamics of wakes and their interactions with the FWT.

(a) Photography of experimental facility and scaled wind turbines

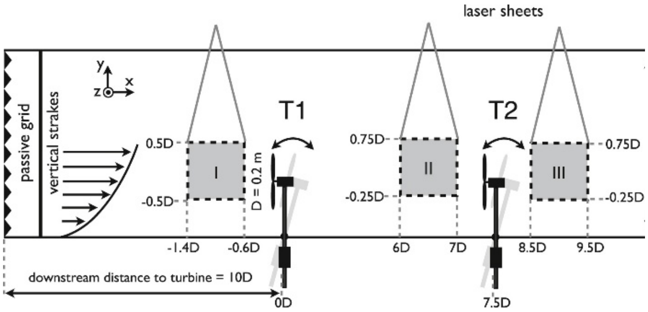

(b) Wind tunnel setup with two model turbines

Figure 71: Details of hybrid wind tunnel testing of two scaled wind turbines (Rockel et al., 2021).

4.3.3 Recent advances and applications of hybrid model tests

Wen et al. (2022) have developed a Multi-drive Aerodynamic Loading Simulator (MALS) that utilizes individually-controlled UAV propellers as actuators. The MALS was designed to generate desired aerodynamic thrust accurately for both steady and unsteady cases. Extensive performance evaluation tests were conducted to assess the capabilities of the MALS. Figure 72 illustrates the procedures used to calculate the target rotor thrust and generate the control command for the MALS. These procedures ensure that the desired aerodynamic thrust is achieved with satisfactory accuracy. To investigate the coupling dynamics of a FWT system, a hybrid model test system was constructed using the proposed MALS. This system allows for the examination of the interactions and dynamics of the FWT system. For comparison and validation purposes, a typical FWT model test system with a physical wind turbine was also constructed. This system serves as a benchmark to assess the performance of the MALS in integrated FWT model tests, as shown in Figure 73.

Overall, the work by Wen et al. (2022) highlights the development and evaluation of the MALS as a versatile tool for studying the aerodynamic characteristics and coupling dynamics of FWT systems.

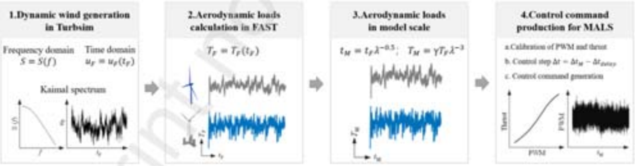

Figure 72: Procedure to produce the control command of MALS for complex aerodynamic loads (Wen et al., 2022).

Figure 73: The presence of a full physical model and hybrid model in the experiment (Wen et al., 2022)

Sun et al. (2022) have proposed a real-time hybrid simulation (RTHS) framework for studying the structural performance of floating offshore wind turbines (FOWTs) under wind-wave loading. The framework, as shown in Figure 74 and Figure 75, combines numerical modeling and physical testing. In the RTHS framework, the blades, nacelle, and tower of the FOWT are numerically modeled, while the floating platform is physically tested in real-time using an actuation system in a laboratory setting. The numerical and physical substructures communicate at the tower-floater interface, enabling the simulation of the FOWT's behavior under wind-wave loading conditions. To evaluate the feasibility of the proposed framework, a 5 MW spar-type FOWT at a scale of 1:50 was simulated. A sensitivity analysis was conducted to quantify the errors caused by delays and noises in the system. The results indicated that the delays in the sensors and actuators had a more significant influence on the performance of the RTHS framework compared to the noises.

Overall, the work by Sun et al. (2022) demonstrates the potential of the RTHS framework for studying the structural performance of FOWTs under wind-wave loading conditions. The findings highlight the importance of minimizing delays in sensors and actuators to improve the accuracy and reliability of the simulation results.

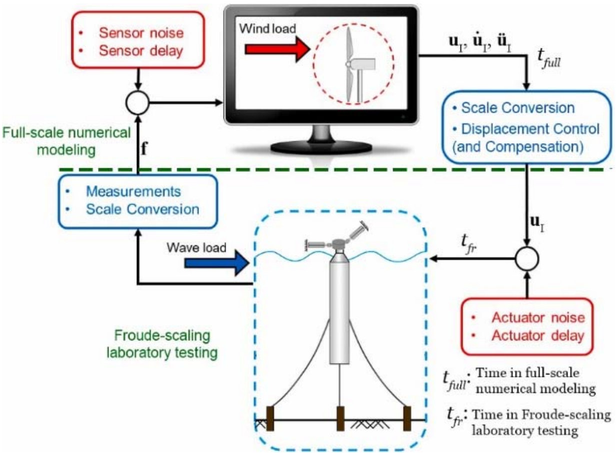

Figure 74: Block diagram of the proposed RTHS framework (Sun et al., 2022)

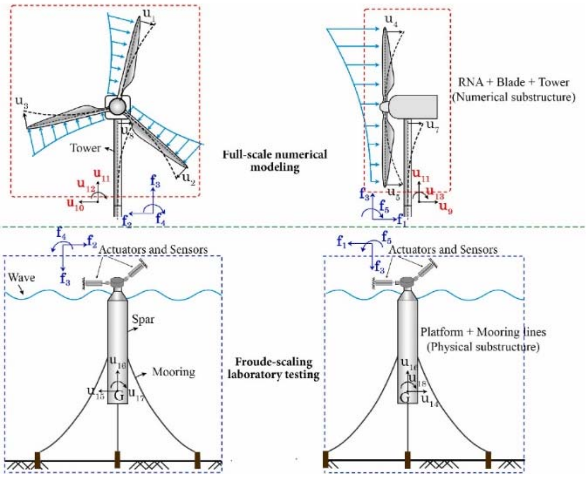

Figure 75: Schematic model for RTHS of spar-type FOWTs (Sun et al., 2022)

To further enhance the capabilities of the real-time hybrid simulation (RTHS) method, a distributed RTHS (dRTHS) approach was proposed, developed, and validated in Sadraddin's doctoral research (2022). This approach (see Figure 76) utilizes geographically distributed wind tunnels and wave tanks that are interconnected through network communications to conduct large-to-full-scale FWT experiments. The dRTHS method takes advantage of the availability of multiple testing facilities located in different geographical locations. By leveraging network communications, these facilities can be connected to create a distributed testing environment. This allows for the simulation of FWT experiments at larger scales, up to full-scale, by combining the capabilities and resources of multiple wind tunnels and wave tanks.

Sadraddin's research focused on the development and validation of the dRTHS approach. The findings demonstrated the feasibility and effectiveness of using distributed testing facilities for conducting FWT experiments. This approach opens up new possibilities for studying the behavior and performance of FWT systems at larger scales, which can provide valuable insights for the design and optimization of offshore wind energy systems.

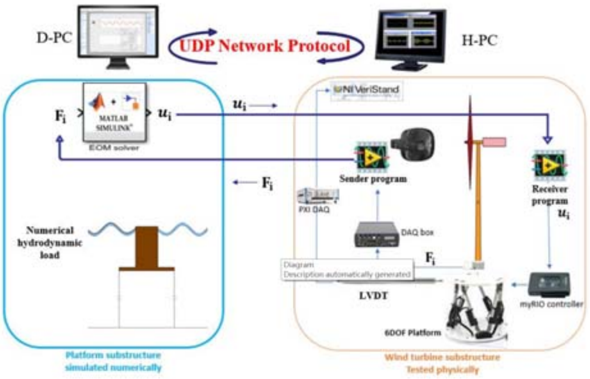

Figure 76: Experimental setup with software (Sadraddin, 2022)

Ha et al. (2023) have proposed a real-time hybrid method for the performance evaluation of a 10 MW class floating offshore wind turbine. In this experimental technique, six duct fans, as shown in Figure 77, were attached at the tower top of the wind turbine to actuate the real-time hybrid method. Figure 78 illustrates the loop of the real-time hybrid method for the 10 MW floating wind turbine. In the model test, the platform motions were measured using Qualisys, and the converted nacelle velocities were used as the relative wind velocities in each direction. Numerical simulations were conducted based on the calculated relative wind velocities and input wind velocity. The duct fans in the model test were operated based on the thrust and yaw moment of the nacelle obtained from the numerical simulation. To validate the model test technique, the experimental results were directly compared with the fully coupled analysis results. Additionally, repetitive tests were performed to investigate the repeatability of the model test technique. From the experimental results, it was observed that the model test technique performed well and exhibited good repeatability. The comparison with the fully coupled analysis results demonstrated the effectiveness and accuracy of the proposed real-time hybrid method for evaluating the performance of the 10 MW floating wind turbine.

Overall, the work by Ha et al. (2023) achieves the successful implementation of the real-time hybrid method using duct fans for performance evaluation of a 10 MW class floating offshore wind turbine. The experimental results validate the model test technique and highlight its repeatability, providing valuable insights for the design and assessment of large-scale wind energy systems.

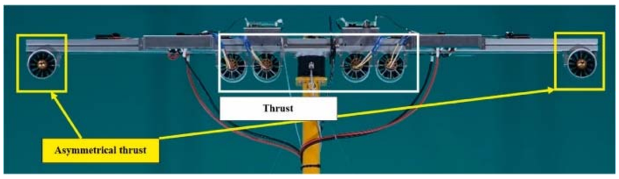

Figure 77: Configuration of the duct fans (Ha et al., 2023)

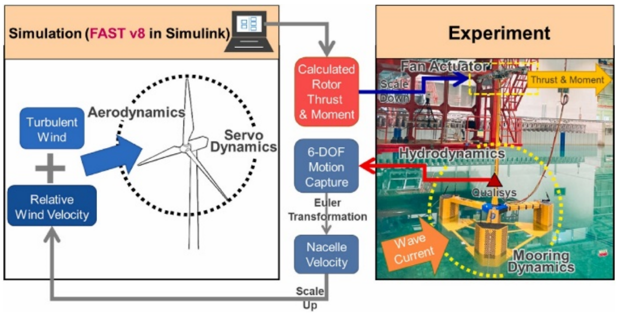

Figure 78: Loop of real-time hybrid method for 10 MW FOWT (Ha et al., 2023)

Wang et al. (2022) conducted a series of tank tests using a scaled spar-type floating offshore wind turbine and employed an AI-based software-in-the-loop hybrid testing method. The tests were carried out in different scenarios, including wave-only cases, wind-only cases, and combined wind-wave cases, to investigate the influence of wave frequency and wind speed on the platform motions. In addition to the tank tests, numerical simulations were also performed to compare the results with the experimental data. It was observed that the numerical calculations generally aligned with the testing results, indicating the accuracy and reliability of the numerical models. Figure 79 illustrates the AI-based real-time hybrid model testing rig developed by Jiang (2020). The tower of the wind turbine is equipped with a fan that generates a real-time thrust force based on Froude's law of similarity. This fan is driven and controlled by a prediction algorithm, which considers the real-time platform motions (such as surge, surge velocity, pitch, pitch velocity, and wind speed) measured by an optical capture system. Thus, the entire experimental procedure of this rig can be viewed as a loop, where the prediction algorithm and real-time measurements drive the fan to provide an equivalent real-time thrust force.

The research allows for the integration of numerical simulations and physical testing, providing a comprehensive and accurate evaluation of the platform motions of floating offshore wind turbines. This approach contributes to the understanding of the effects of wave frequency and wind speed on the performance of such wind turbines.

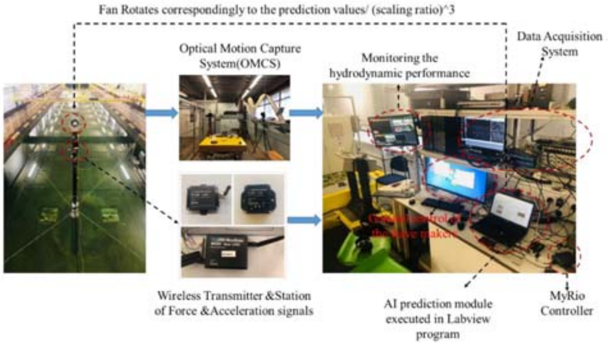

Figure 79: AI-based real-time hybrid model testing rig (Wang et al., 2022)

Yu et al. (2022) conducted a hybrid test campaign for a floating offshore wind turbine (FOWT) at a scale of 1:36. Figure 80 illustrates the setup used in the campaign. Instead of using a scaled physical turbine model, a multi-fan system was employed to create equivalent aerodynamic thrust forces. The aerodynamic loads of the turbine were defined and generated using a hardware-in-the-loop (HIL) system developed at IH Cantabria. The HIL system involved the multi-fan system, which accurately replicated the rotor aerodynamics. Figure 81 shows a block diagram of the HIL system and the integration of the state observer. This allowed for precise control and simulation of the aerodynamic forces acting on the FOWT. Various tests were conducted as part of the campaign to identify and calibrate the FOWT system. These tests included regular waves, irregular waves, and turbulent winds. The dynamic responses of the FOWT system were measured and compared with numerically reproduced results. The comparison showed a good agreement between the experimental and numerical data.

The hybrid test campaign carried out by Yu et al. (2022) demonstrates the effectiveness of using a multi-fan system and HIL technology to simulate the aerodynamic forces on a floating offshore wind turbine. The tests conducted in different wave and wind conditions provide valuable insights into the performance and behavior of FOWTs. The agreement between the experimental and numerical results further validates the accuracy and reliability of the hybrid testing approach.

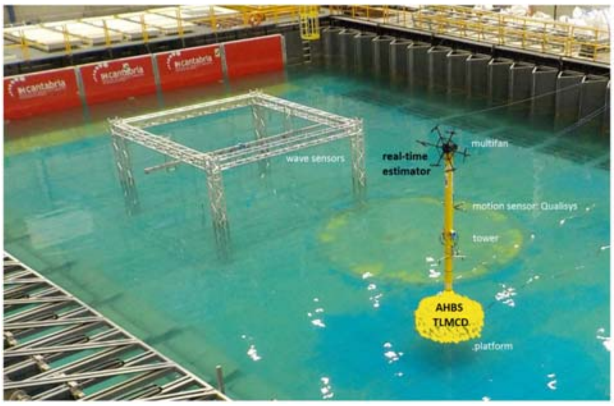

Figure 80: Setup of the wave tank hybrid tests (Yu et al., 2022)

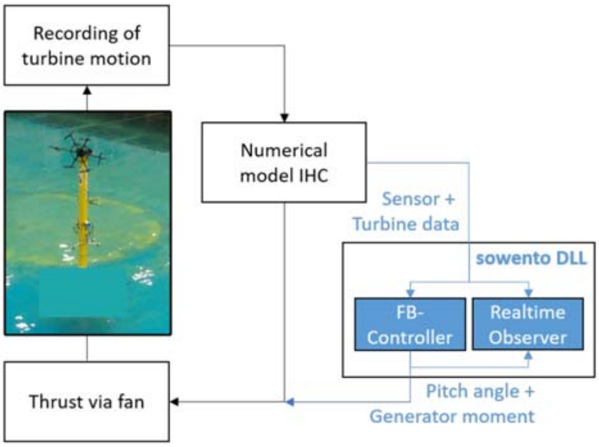

Figure 81: HIL system and the integration of the state observer (Yu et al., 2022)

Vittori et al. (2022) conducted a wave tank test campaign to evaluate a 1/49 scaled SATH 10 MW floating platform. Figure 82 illustrates the setup used in the campaign. To incorporate the wind turbine thrust and in-plane rotor moments, a software-in-the-loop (SIL) hybrid method was employed, as depicted in Figure 83. The experimental results obtained from the wave tank tests were compared with a numerical model developed in OpenFAST for the floating wind turbine. The aim was to validate the numerical model against the physical testing data. In this test campaign, an actuator with four propellers was utilized to introduce rotor loading. Each propeller was powered by a commercial brushless motor typically used in drones. An electronic speed controller (ESC) controlled the motor, which was supplied with power from an industrial AC-DC power supply. The rotational speed of each motor, and consequently the force generated by the propeller, was controlled using a pulse width modulation (PWM) signal. This signal was generated with the LabVIEW control software, utilizing servo libraries for Arduino.

The use of the SIL hybrid method in combination with the wave tank tests allowed for the inclusion of the wind turbine thrust and in-plane rotor moments in the experimental setup. By comparing the experimental results with the numerical model, the study aimed to assess the accuracy and reliability of the numerical modeling approach. The actuator system with propellers provided a means to replicate the rotor loading in the wave tank tests.

The work conducted by Vittori et al. (2022) demonstrates the successful implementation of the SiL hybrid method and the utilization of an actuator system with propellers for wave tank testing of a floating wind turbine. The comparison between the experimental and numerical results contributes to the validation and improvement of numerical models for floating wind turbines.

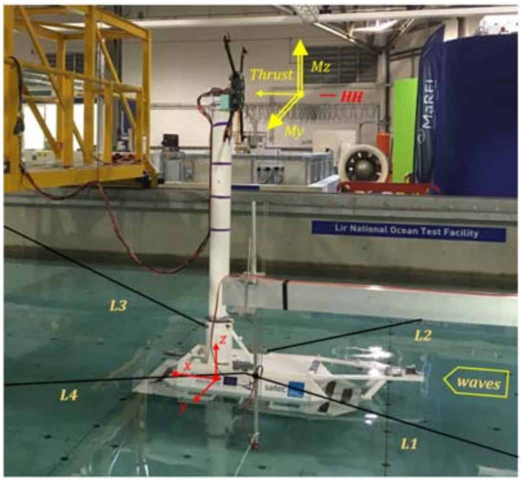

Figure 82: Setup of the wave tank hybrid test (Vittori et al., 2022)

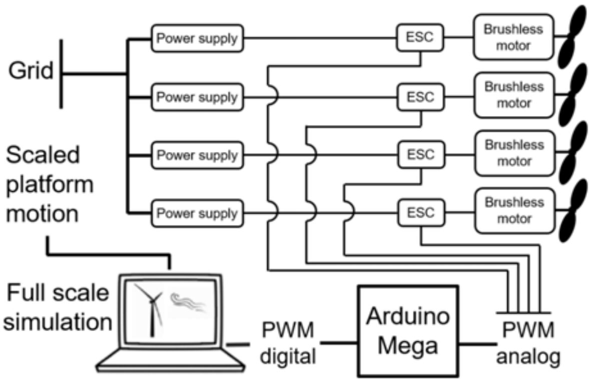

Figure 83: SIL control diagram (Vittori et al., 2020)

Thys et al. (2021) conducted model tests using a scaled model of the INO WINDMOOR 12 MW floating wind turbine in the Ocean Basin at SINTEF Ocean. Real-time hybrid model testing was employed, as depicted in Figure 84, to model the wind turbine rotor and aerodynamic loads. In this study, the physical subsystem consisted of a Froude-scaled floating substructure, tower, and mooring lines. The numerical subsystem utilized a modified version of FAST, a widely-used software for wind turbine simulation, which ran in real-time. The numerical model incorporated measured positions, velocities, and accelerations of the RNA (Rotor-Nacelle Assembly) from the model tests. The simulations provided outputs such as the aerodynamic loads on the tower, the aerodynamic loads on the rotor, and the mass-related rotor loads, including gyroscopic effects. These simulated loads were applied at the top of the tower on the model using a cable-driven parallel robot (CDPR). The real-time hybrid model testing approach employed by Thys et al. allowed for the integration of physical and numerical subsystems to accurately replicate the behavior and loads of the floating wind turbine. The use of the CDPR facilitated the application of the simulated loads on the model.

The model tests conducted in this study provide valuable insights into the performance and behavior of the INO WINDMOOR 12 MW floating wind turbine. The combination of real-time simulation and physical testing enables a comprehensive understanding of the aerodynamic loads and response of the turbine system.

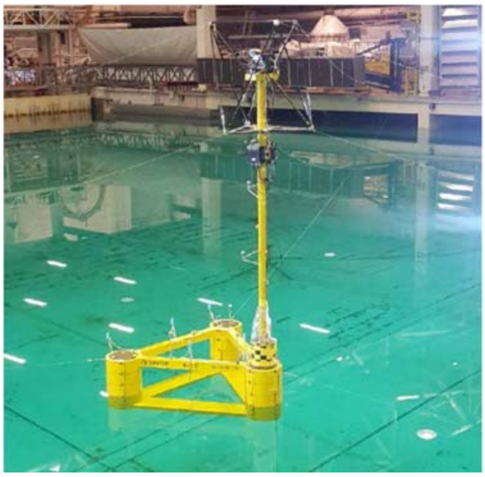

Figure 84: The layout of the hybrid model tests at a scale of 1:40 (Thys et al., 2021)

Cinello et al. (2022) introduced a real-time hybrid modeling technique that combined real-time numerical simulations with basin model tests. The technique was applied to a floating offshore wind turbine, and the study aimed to compare different modeling assumptions and experimental setups. Figure 85 depicts the basin model test setup used in the study. To emulate the thrust load in real-time, the real-time hybrid modeling technique was employed, as illustrated in Figure 86. Initially, basin tests were conducted using a single fan and a numerical model of the turbine with rigid blades. These tests served as a baseline. In the second set of tests, improvements were made. On the experimental side, a dual-rotating fans system was implemented. On the software side, the influence of blade flexibility was incorporated into the numerical model. By incorporating these enhancements, the study aimed to investigate the impact of blade flexibility on the performance of the floating offshore wind turbine. This allowed for a more accurate representation of the turbine behavior in the real-time hybrid modeling approach.

Figure 85: Model in the BGO FIRST basin (Cinello et al., 2022)

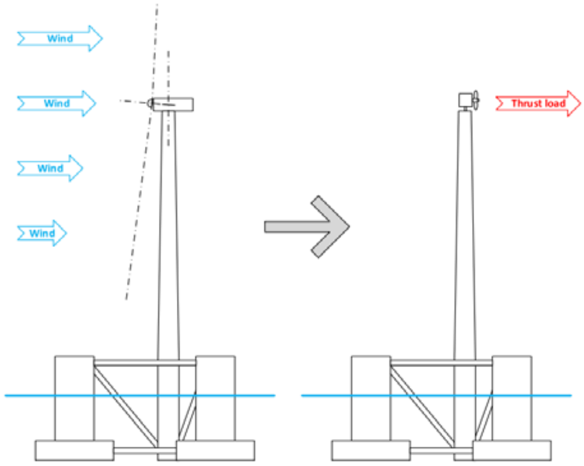

Figure 86: Thrust load emulation (Cinello et al., 2022)

Somoano et al. (2021) analyzed the accuracy of a large-scale experimental testing procedure in an ocean basin facility using real-time hybrid model testing (ReaTHM) techniques. Figure 87 illustrates the ReaTHM setup employed in the study. The analysis was based on a scaled concept for a 15 MW floating offshore wind turbine (FOWT) supported by a concrete semi-submersible platform known as ActiveFloat. This concept was developed within the framework of the COREWIND project. The real-time hybrid model used in the study included a multi-fan system located at the aero-rotor interface. This system allowed for the generation of aerodynamic loads, helping to mitigate the limitations typically associated with scaled models. By utilizing the ReaTHM techniques, Somoano et al. aimed to assess the accuracy of the experimental testing procedure for large-scale floating offshore wind turbines. The analysis focused on the performance and behavior of the scaled concept, specifically the interaction between the FOWT and the concrete semi-submersible platform.

The study by Somoano et al. (2021) provides valuable insights into the accuracy and limitations of large-scale experimental testing procedures for floating offshore wind turbines. The use of real-time hybrid model testing techniques, combined with the multi-fan system, enhances the understanding of the performance and behavior of these systems, ultimately supporting the development and optimization of floating offshore wind turbine technologies.

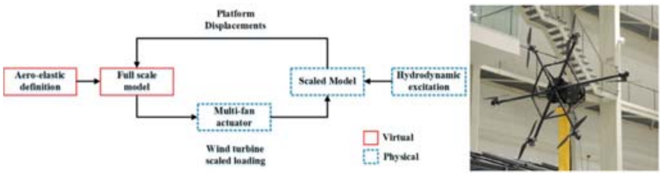

Figure 87: HIL scheme implementation and an overview of the multi-fan actuator system (Somoano et al., 2021)

Ransley et al. (2022) presented a real-time hybrid testing strategy that employed a feedback loop to emulate the aerodynamic forces acting on a floating offshore wind turbine (FOWT) system. The strategy was applied to a 70th-scale IEA Wind 15 MW reference wind turbine mounted on a version of the VolturnUS-S platform, as depicted in Figure 88. Unlike other similar methods, which directly simulate the aerodynamic loads using an aerodynamic code running in parallel with the experiment, this strategy utilized a surrogate model trained on numerical model data calculated in advance. This approach allowed for the inclusion of high-fidelity numerical model data or even physical data in the aerodynamic emulation, without the need for real-time simulation. By employing the feedback loop, which consisted of an onboard fan and a control algorithm, the strategy enabled the emulation of accurate aerodynamic forces on the FOWT system. The surrogate model, trained on pre-calculated numerical model data, facilitated improved loading predictions in the experiments.

This real-time hybrid testing strategy presented by Ransley et al. (2022) offers a novel approach to emulating aerodynamic forces in FOWT systems. By incorporating a surrogate model trained on numerical model data, the strategy allows for more accurate loading predictions without the need for real-time simulation. This approach has the potential to enhance the accuracy and reliability of experimental testing for FOWT systems and support the development and optimization of these technologies.

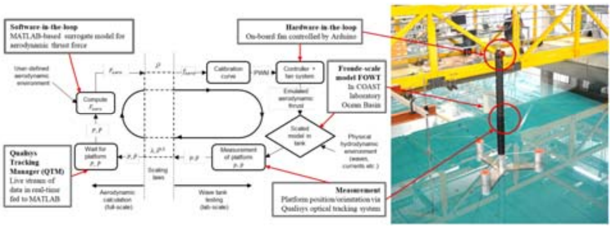

Figure 88: Real-time hybrid testing workflow and layout of hybrid model tests (Ransley et al., 2022)

4.3.4 Comments and recommendations

Indeed, both propeller systems and cable actuators have been used successfully to replicate the thrust force in hybrid testing. However, there are some challenges associated with using propellers to reproduce the aerodynamic moment, as highlighted by Otter et al. (2020). It can be difficult to accurately consider the propellers' torque in the force allocation process, as pointed out by Hmedi et al. (2020). On the other hand, cable actuators are capable of reproducing moments effectively. However, controlling the cables can be more complex compared to propellers. Additionally, the cable's frame requires a larger space on the top of the tower, unlike propellers, which occupy smaller space. It is worth noting that the pretension of the cables can slightly affect the results of free decay tests, as mentioned by Sauder et al. (2016). In contrast, conducting free decay tests with propeller actuators turned off is simpler. These considerations highlight the trade-offs and challenges associated with choosing between propeller systems and cable actuators in hybrid testing, depending on the specific objectives and constraints of the study.

Propellers, due to their high rotational speed, can introduce unwanted vibrations to the model being tested. In contrast, cables tend to induce fewer vibrations, making them a more desirable choice in terms of minimizing vibrations in hybrid testing setups. Another important consideration when using propellers is the temperature of the active emulator. It is crucial to monitor and control the temperature to avoid overheating and potential damage to the propeller's electrical motor or demagnetization. In multi-actuator systems with propellers, it is essential to take into account the interaction between the propellers when tuning them. The wakes generated by adjacent propellers can modify the air inflow of other propellers, leading to changes in their performance. This wake interaction effect can result in performance variations of up to 10%, as highlighted by Urbán et al. (2020). These factors emphasize the need for careful attention to vibration control, temperature management, and wake interactions when using propellers in hybrid testing setups. Alternatively, cable actuators can provide a smoother and less problematic solution in terms of vibrations and temperature management.

The selection of hybrid testing in a wind tunnel or a wave basin depends on the specific phenomena being investigated. If the primary focus is on studying wakes and the interaction between turbines, hybrid testing in wind tunnels is more appropriate. Wind tunnels allow for the replication of wind conditions and the observation of wake behavior and turbine interactions. On the other hand, if the objective is to study hydrodynamics, such as the behavior of floating platforms, hybrid testing with propellers or cables in wave basins is preferred. Wave basins provide a controlled environment for studying the effects of waves and water on the platform's performance. When thrust loading is the dominant load being considered in the tests, a single propeller or a ducted fan is recommended. These setups accurately replicate the thrust forces experienced by the platform. For analyses that require the consideration of aerodynamic and gyroscopic moments, a multi-cable winch system is more suitable. This system allows for the emulation of these moments and provides a comprehensive analysis of the platform's behavior.

In summary, the selection of the appropriate hybrid testing setup depends on the specific phenomena being studied, the dominant load being considered, and the desired analysis objectives.

4.4 Benchmark Test Program for Cyber-Physical Hydrodynamic Testing Involving Wind Loads

The specifications for a benchmark test program for wind loads and their influence on the motions of floating structures are developed as follows. It aims to compare the wind loads developed using SiL to model the wind loads versus using fans to produce an actual model scale wind. Among other data, repeatability, and consistency between the methods and between different facilities should be reported if the test is carried out by voluntary participants within the 31st ITTC at different facilities following the specifications. The benchmark study may also include CFD comparisons.

(1) Background

A major issue related to hydrodynamic testing complex structures exposed to wind is the Froude-Reynolds scaling conflict, which prevents accurate modelling of aerodynamic loads in hydrodynamic laboratories. This issue concerns particularly floating wind turbines (Martin et al., 2015) or sail-assisted propulsion of ships.

Cyber-physical testing is a method that alleviates this issue by combining numerical simulations with experimental testing in real time (Azcona et al., 2014; Sauder et al., 2016). A physical model located in a hydrodynamic laboratory interacts in real-time with a simulator computing the wind loads. An actuator applies these loads on the physical model. Motions are recorded and fed back to the simulator, creating a closed-loop system.

The actuator can take the form of an individual winch, a cable-driven parallel robot (several winches acting in parallel on the floater), a single fan, or a multi-rotor platform.

The wind load simulator can be based on a set of wind coefficients (relevant for e.g. topside), or a more complex numerical model such as lifting line (for sail-assisted propulsion) or blade element momentum theory (for floating wind turbines).

(2) Test objectives

The present benchmark aims at assessing and ensuring the quality of cyber-physical testing of floating structures subjected to wind loads that are generated numerically and applied with actuators. The benchmark targets the hardware and low-level software components of the laboratory setup.

The benchmark will employ a floating wind turbine model, but for simplicity, the wind loads will be considerably simplified compared to realistic rotor loads.

Important remark #1: The present benchmark does not address the *validity of the numerical model* used to generate the wind loads as it is strongly application-dependent.

Important remark #2: Purely *physical* solutions to apply wind loads, that rely on laboratory-fixed fans generating a wind field are not part of the scope of the present benchmark,

(3) Physical model

The open floating wind turbine design INO WINDMOOR 12MW , fully described in (Souza et al., 2021), is used as an object for benchmark. This report is available online and contains a full description of the model properties.

Main particulars for the floater are repeated here for convenience:

- Column diameter (m) 15.0
- Column height (m) 31.0
- Column Center-Center distance (m) 61.0
- Draught (m): 15.5
- Deck height above waterline (m): 15.5
- Pontoon width x height (m) 10.0 x 4.0

- Deck beam width (m) 3.5
- Deck beam height (m) 3.5
- Mass floater (t) 11974.0
- Total mass (t) 14176.0

See (Souza et al., 2021) for a complete definition of the floater and tower dimensions and inertia.

Figure 89: Open INO WINDMOOR 12MW concept. Courtesy Inocean.

A scale of 1:40 should preferably be employed for the model. Only full-scale values are provided in the following.

Water depth should preferably be 150m. If not feasible, at least 75 m which will ensure deep water wave kinematics.

The platform shall be moored as indicated in the report with a horizontal mooring attached to the column top and suspended over the water surface (as to generate a minimum amount of damping). The restoring from the mooring shall be 102.0 kN/m, 98.3 kN/m and 5204 kNm/deg in surge, sway and yaw respectively.

Nautral periods targets are 97.3s 98.0s, 16.3s, for the surge, sway and heave motions, and 29.5s, 31.4s, and 88.0s for the roll pitch and yaw motions.

Unless otherwise mentioned, loads generated by the actuator shall be applied at the location of the tower top, that is 125.7m above water line (i.e. 110.20m over deck).

(4) Coordinate systems

Notations consistent with (Souza et al., 2021) are used. The XYplane of the, Earth-fixed coordinate system coincides with the mean water level, and the Z-axis is positive upwards. A *local* coordinate system is also defined. Its origin is at mean water level and over the platform's horizontal geometric center is also defined. This system is fixed to the body and translates/rotates along with the body.

Loads to be applied by the actuators are provided in the *local* coordinate system.

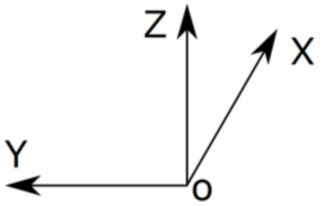

(a) Global (Earth-fixed) coordinate system.

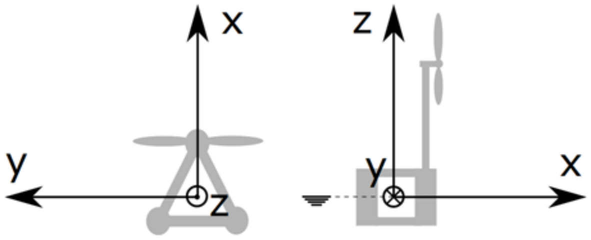

(b) Local (body-fixed) coordinate system.

Figure 90: Global and local coordinate systems

(5) Waves

Waves propagate in the negative X-direction.

For the purpose of the benchmark, a wave that follows a JONSWAP spectrum with Hs=6.19m Tp=12.0s gamma=1.23, shall be calibrated. An example of wave spectrum / time series is provided as an electronic appendix to the present document. The wave shall last at least one hour at full-scale.

The calibration point shall be the equilibrium position of the model in the basin when no external loads are applied.

(6) Wind load model

Three reference wind spectra / velocity time series are provided as an electronic appendix to the present document. They correspond to uniform but time-varying turbulent wind with mean velocities 8 m/s, 11.5 m/s and 25 m/s at a height of 131.7m (slightly above tower top), Kaimal spectrum, with turbulence intensity of 0.166, 0.133 and 0.106, respectively.

The wave and wind realizations shall be synchronized such that they start at the same time and do not drift with respect to each other.

Depending on the case, wind will propagate either in the negative X- direction, or with 45 degrees offset from that direction such that it has a positive mean Y-velocity component.

The relative wind velocity at tower top and in the local coordinate system Ur=(Ur,1,Ur,2,Ur,3) (3 components) shall be computed at all times. It is the vector difference between the (undisturbed) incoming wind and the tower top velocity (estimated by the laboratory).

The modulus of the relative wind velocity, and its direction in the plane orthogonal to the tower are defined by Uw = |Ur| and hangle = atan2(Ur,2,Ur,1)

The relative velocity shall be combined with the thrust curve provided below to compute the thrust generated at tower top.

The surge load shall be F1=Thrust * cos(hangle)

The sway load shall be F2=Thrust * sin(hangle)

The heave load shall be null F3=0

We recall that these loads are given in the local coordinate system.

A positive moment *about the tower top* should be applied based on the torque curve provided in the figure above.

Roll moment M4 = Torque (positive)

Pitch moment shall be null M5 = 0

Yaw moment shall be null M6 = 0

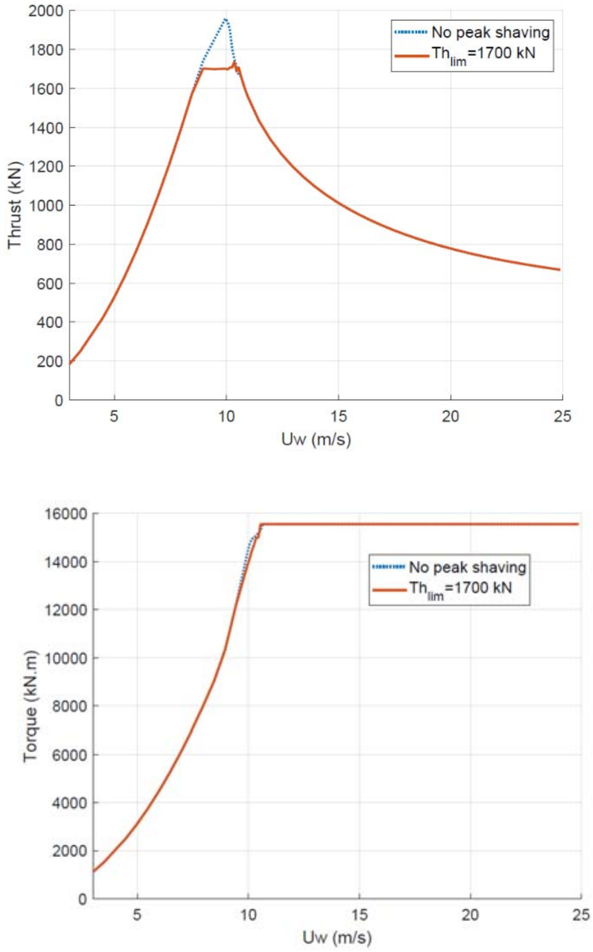

Figure 91: Wind loads vs relative wind velocity

(7) Instrumentation and data acquisition

The following quantities shall be recorded for all the tests, at the minimum sampling frequency given between parentheses (model scale):

- 6 degrees of freedom motions of floater (100 Hz.)
- 3-components accelerations at tower top (200Hz)
- Wind velocity, computed relative velocity, and 6 components of the computed loads to be applied to the model (200Hz).
- 6 component of the loads actually applied from the actuator to the model (200Hz), including those not controlled by the actuator.
- Wave elevation in the basin at calibration point, and at another location kept constant during calibration and testing (100Hz)

No filtering shall be applied except anti-aliasing filter.

(8) Test matrix

The following tests shall be conducted by order of priority.

Wave calibration/documentation (1 test)

Prior to placing the model in the basin, the wave described above shall be calibrated.

Excursion and decay tests (6+6 tests)

Actuator shall be deactivated.

Excursion tests (up to 30m surge/sway and 30deg yaw offset) shall be performed to verify the stiffnesses provided above.

Decay tests shall be performed to ensure that natural periods match the targets above. Initial offsets shall be at least 10m for surge and sway, at least 6 degrees for roll/pitch, and 10 degrees for yaw.

Chirp tests in calm water (2 tests)

Chirp tests consist of applying a constant amplitude load centered on 0 N, at an increasing frequency ranging from range [0, 1 Hz] full scale (that is about [0, 6.5Hz] at scale 1:40). The duration of the chirp shall be at least 100s.

Two load directions should be tested, first surge, then sway. They will induce a pitch and roll moment about tower base, respectively.

The load actually applied by the actuators should be measured and compared to the desired load.

Free decay with actuators activated in "zero-load" mode. (6 tests)

This test is not relevant for e.g. fan- or multi-rotor-based actuators as deactivating the actuator will have the same effect as activating them with zero load.

This benchmark consists in free decay tests, where the actuator shall be activated while applying zero net load on the floater.

The initial conditions for the decays shall be as close as possible to the ones performed without actuator connected. This force shall be suddenly removed, triggering a free decay.

Motions time series, natural periods and damping ratios for the excited degrees of freedom should be compared to the free decays performed without actuator.

Free decay in pitch with constant wind velocity (3 tests)

Free decay tests in pitch shall be performed in three *constant* wind velocities 8m/s, 11.5m/s and 25m/s. At least 5 degrees of additional pitch as an initial condition

Wave only tests (1 test)

Actuators shall be deactivated. The model shall be exposed to the calibrated wave.

Wave tests with actuators activated in "zero-load" mode (1 test)

This test is not relevant for e.g. fan- or multi-rotor-based actuators as deactivating the actuator will have the same effect as activating it with zero load.

In this benchmark test, the actuator is bound to apply zero load, but this time the motions of the floater are triggered by the wave.

Motions time series measured during these tests should be compared to these measured during a test involving the same wave.

Wind only tests – aligned conditions (3 tests)

The model shall be exposed to the turbulent winds with velocities 8m/s, 11.5m/s and 25m/s.

Wave tests with constant thrust force (2 tests)

The model shall be exposed to the wave, and the actuators should generate a constant thrust force of 1600kN, first along the surge direction. Then the test shall be repeated with the thrust force acting along the sway direction.

The load actually applied by the actuators should be measured and compared to the desired load.

Wind and wave tests – aligned conditions (3 tests)

The model shall be exposed to the wave and to the turbulent winds with velocities 8m/s, 11.5m/s and 25m/s. Wind and wave directions are colinear.

Wind/Wave tests – misaligned conditions (3 tests)

The model shall be exposed to the wave and to the turbulent winds with velocities 8m/s, 11.5m/s and 25m/s. Wind direction makes a 45 degrees angle with the wave.

Wind tests with large changes of wind direction (1 tests)

The model shall be exposed to turbulent wind with mean velocity of 11.5m/s. The *wind direction* (*not* force direction) shall be varied as the following function of time: windDir = 90deg * abs(sin(2*pi/120 * t)) such that the wind rotates by a quadrant in a minute at full scale.

Wind tests with additional yaw moment (1 test)

The model shall be exposed to turbulent wind with mean velocity 11.5m/s and direction 0 degrees. However an additional positive yaw moment shall be applied equal to the (time varying) thrust force x 20m.

(9) Data analysis

A short memo including pictures should summarize the test setup. The actuator system should be described. It should be in particular stated how many load components are controlled.

Results shall be reported at full-scale, using Froude scaling. The scaling of loads shall include the ratio between the specific weights of sea water and fresh water in the basin ($\gamma_{\mathrm{w}} \approx 1.025$).

4.5 State-of-the-art for Wave-Current Interactions

SC on Modelling Environmental Conditions of the 28th ITTC presents mostly a review of current generation in experiments with only few studies related to wave-current interactions. For the 29th ITTC, the issues associated with an accurate and reliable measurement of current in the field are pointed out. A set of model scale experiments coupled to the corresponding nonlinear simulations analyze the effect of current on extreme wave occurrence (Toffoli et al. (2019)). The effect of current on breather-type solutions is also studied experimentally (constant current) and numerically with a linear shear.

Ducrozet et al. (2021) discuss the dynamics of unidirectional random wave fields that propagate against an opposing current through laboratory experiments and direct numerical simulations of the Euler equations solved with a high-order spectral method. Both approaches demonstrate that the presence of a negative horizontal velocity gradient increases the probability of the occurrence of extreme and rogue waves in the course of their propagation with the emergence of a rapid transition from weakly to strongly non-Gaussian properties. Numerical simulations capture quantitatively well the statistical properties of laboratory observations and substantiate that underlying physics are associated to quasiresonant nonlinear interactions triggered by the background current.

Zhou et al. (2024) investigate numerically the impact of uniform currents on nonlinear characteristics of double-wave-group focusing. The analysis was carried out by a fully nonlinear numerical wave–current model established based on the high-order spectral method. Different current speeds covering strongly opposing current, weekly opposing current as well as following current were considered. Seastates with sea-swell energy equivalent are selected to study the influence of uniform current on focused double wave group. Among other interesting conclusions, the study reveals that, for bimodal waves, the asymmetries of the wave crest and that of the wave envelop influenced by the currents are not synchronous, unlike the case of unimodal waves.

Nguyen et al. (2020) describe the design of a recirculating wave-current flume as well as the methods used to obtain such design, taking into consideration the different constraints in the project.

Zheng et al. (2023) study numerically the statistics of weakly nonlinear waves on currents with strong vertical shear. A unidirectional irregular sea state following JONSWAP spectrum is studied with different vertical current profiles. It is found that that opposing vertical shear leads to increased wave height and skewness while a following shear has opposite effects. This supports the need to account for shear current in wave modelling.

Regarding the importance of including shearing current in wave-current interaction analysis, Soffer et al. (2023) discuss the effects of shearing current on the estimation of wave direction from data collected by measurement devices such as buoys, pressure gauges and acoustic Doppler current profilers. The authors numerically generated data for a predefined spread and then processed the data based on potential irrotational flow theory (i.e. not accounting for the rotational shearing current). The analysis shows significant errors in estimation of wave directional spread. An approach is proposed for estimating the directional spectrum accounting for wave-shearing current interaction.

Ellingsen et al. (2024) studied the evolution and kinematics of dispersive focusing of a waves' group atop a shearing current, considering linear theory. They derived analytical approximate relations assuming long crested linear waves and different current profiles (e.g., current varying with depth linearly and exponentially etc.) with arbitrary angles between them. The analysis shows that while the shear current has modest effect on the evolution of the wave group's envelop, it affects the individual crests and troughs rising and falling inside the group. They show that shearing currents change wave kinematics significantly and highlight the importance of considering current profiles in maritime operations.

Wang et al. (2021) present a numerical study on the properties of extreme waves in directional seas subjected to current in different directions. For the waves with strong nonlinearity, the nonlinear wave-current interactions have significant impacts on the wave statistics and spectral properties. Main elements are: i) enhancement of the tail of the wave crest probability of exceedance and kurtosis with a maximum effect at 135°, ii) broadening of the spectra for angles larger than 110° iii) large asymmetry in vertical and horizontal direction induced by the current and iv) at fix incident angle, effect is more pronounced for steeper wave conditions.

Zhang et al. (2023) conducted an experimental study of propagating unidirectional irregular waves with following current over a varying seabed resembling coastal areas with ambient currents. The results show that an accelerating following current can increase the freak wave occurrence. In the experiment, the incident irregular waves were generated following the JONSWAP spectrum. The current was uniform in the vertical direction but due to the presence of a submerged trapezoidal bar, the current speed was varied in the horizontal direction. The results indicate that a following current entering a shallow-water area can increase the probability of freak waves. The effect is related to non-equilibrium dynamics induced by inhomogeneity of the seabed and current field, while the modulation instability is considered to be insignificant.

For nearshore areas, a review of the state of research in the interaction of waves and currents is provided in Zhang et al. (2022). In this field, the concern is more associated to turbulent currents with possible applications to sediment transport or dispersion of pollutants. The review proposes an overview of experimental and numerical investigations with a synopsis of advantages and limitations of previous studies.

5. STATE-OF-THE-ART IN OFFSHORE AQUACULTURE SYSTEMS

The state-of-the-art in offshore aquaculture systems was reviewed based on the articles since the 2021 report of the Ocean Engineering committee including large volume closed containment systems, extreme wave environments, and modelling of entire systems.

Aquatic products are one of the main sources of food in the world. According to a survey reported by the Food and Agriculture Organization (FAO, 2018), aquaculture production has increased significantly in the past few decades.

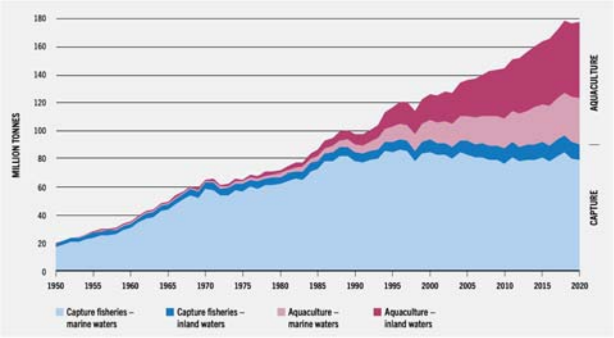

Figure 92: World capture fisheries and aquaculture production (FAO, 2022).

Although most of the aquaculture products are still farmed inland, the portion of marine and coastal cultured seafood has increased rapidly (FAO, 2018). With the expansion of the nearshore fisheries, conflicts have appeared in some aspects such as shipping, tourism, and recreation (Tidwell et al. 2012; Shainee et al., 2013;). Marine fish farming should move towards offshore regions to pursue more space and better water quality.

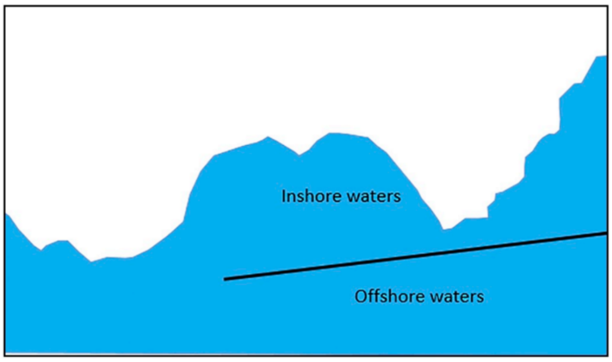

Figure 93: Definition of offshore waters according to Spanish law (Chu et al., 2020).

According to Chu et al. (2020), the definition of offshore fish farming should involve:

(i) unsheltered waters outside a straight line joining two major capes or promontories, at least about 3 km distance from the shoreline but still within the Exclusive Economic Zone (EEZ).

(ii) water depth that is larger than 50 m or larger than 3 times the cage height and no less than 15 m between the cage bottom and the seabed.

(iii) current speed ranging from 0.1 m/s to 1 m/s.

(iv) wave height exceeding 3m.

There is a variety of studies concerning the classifications or design analyses of offshore aquaculture systems. Relevant reviews can be found in Chu et al. (2023), Morro et al. (2021), and Fan et al. (2023). In the following, several dominant types of offshore aquaculture systems will be presented with examples emphasizing their advantages and disadvantages. The challenges and considerations for design and operation are also summarized concisely.

5.1 Classification

Offshore fish farms can be categorized based on their structural materials (rigid or flexible), shapes (spar, column, ship-shaped), or operating floating forms (floating, semi-submersible, and submersed). There have been some attempts at fish cage classifications by researchers or by the maritime communities (DNV, 2017; ABS, 2018; Chu et al., 2020). In this section, several representative types of offshore aquaculture systems are classified and presented with examples. A rigorous review of the classification can be referred to Chu et al. (2023).

5.1.1 Flexible cage system

Flexible cages are assembled mostly with floatable flexible elements. They were first invented in the 1970s and have been widely used in nearshore regions. Their buoyancy is mainly provided by floating pipes made of high-density polyethylene (HDPE). A series of brackets are applied to hold the pipes together to suspend the fish net (Cardia et al., 2016).

Typical examples of floating flexible cages are PolarCirkel (Figure 94 (a)), a plastic cage concept invented in Norway in 1974 using circular cages with circumferences of 60m to 240m, and Triton (Figure 94 (b)), developed by FusionMarine covering open sizes up to a circumference of 180 m.

(a) PolarCirkel fish cage

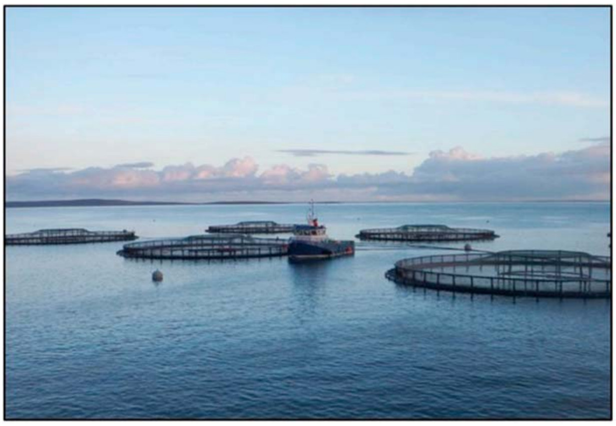

(b) FusionMarine fish cage

Figure 94: Typical examples of floating flexible cages

This kind of cage usually has a high resilience to wave forces (Zhang et al., 2022). The applied HDPE material can dissipate the wave energy and reduce surface wave forces by structural deformation. Besides, the material is easily-formed and has a high resistance to rotting and biofouling at a relatively low cost.

The cages are usually constructed inland and the towing and installation procedure is convenient.

The main problem of the floating flexible cages is that they might have severe deformations under very harsh waves or current actions, as shown in Figure 95. This limits their application in offshore regions with stronger wave energy. Apart from that, the feeding systems are usually difficult to be placed due to the waves, and large service vessels are thus necessary for the flexible cages.

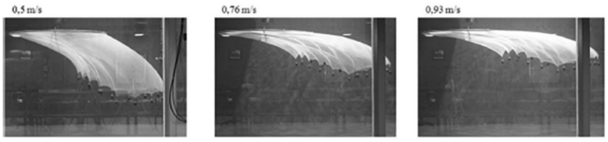

Figure 95: Deformation of flexible net cages subjected to high flow velocity (Moe-Føre et al., 2016)

One way to adapt flexible cages to deep seas is by utilizing a semi-submersible structure. The semi-submersible flexible cages are characterized by the capability to submerge during harsh weather to avoid the high-energy surface waves. Relevant examples can be shown in Figure 96, the Refa tension leg cage (TLC) concept, in which the buoyancy frame is held in place by mooring lines attached to the seabed.

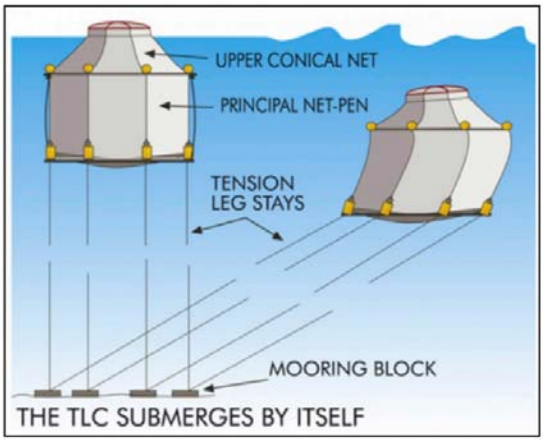

Figure 96: Semi-submersible flexible cage concept: Refa tension leg cage (TLC)

The concept can survive in very hazardous weather conditions. However, there are also concerns that a long period of submergence may affect the fish's welfare. Besides, it needs a sub-surface feeding system and the tension leg mooring systems might be difficult to be installed, especially on the soft seabed.

5.1.2 Ship-shaped cage system

Ship-shaped cage system belongs to the floating rigid cages and has been widely developed in recent years (Ma et al., 2023； Pang et al., 2023). A relevant example is shown in Figure 97. Instead of attempting to dissipate wave energy, this concept withstands waves by rigid structural components usually made of steel.

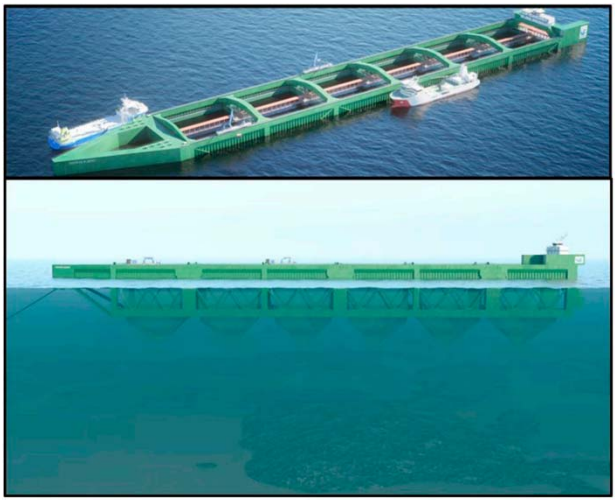

Figure 97: Ship-shaped farm Havfarm

Owing to their vessel-like shape, the cage system can be integrated with various operational and management infrastructures. Their transportation is especially convenient with enough fuel loaded. In addition, the construction and repair operation can be easily conducted in a conventional shipyard (Scott and Muir, 2000).

On the flip side, rigid cages might require large and heavy structures, which can be expensive and difficult to install. In operation status, the vessel-shape cage should be moored to be held in a settled station for the fish's well-being, which may not be easy due to their large mass.

5.1.3 Semi-submersible rigid cage system

Semi-submersible rigid cage has a similar structure to the traditional platforms utilized in the oil and gas industry. As shown in Figure 98, the cage is usually designed with a large-space rigid framework to restrict movement or volume change under external loads (Liu et al., 2021). The rigid framework makes it possible for the ballast adjustment and thus changes the draft under harsh weather.

(a) Shenlan 1

(b)Shenlan 2

Figure 98: Semi-submersible rigid cage (a) Shenlan 1 and (b) Shenlan 2

The semi-submersible rigid cage may provide the longest service life as has been validated by other traditional platforms. The rigid structure allows the installation of infrastructures, such as feeding systems, harvest cranes, and surveillance systems. Moreover, the cages can keep fish in a relatively stable place, where the volume of space is also maintained.

The disadvantage of such cages is that they requires extremely high capital costs. The structure should be rigorously analyzed during the design procedure to ensure safety in offshore operations. The towing and installation might also be difficult and regular maintenance should be planned in advance.

5.1.4 Submerged cage system

For a submerged cage system, the primary mode for normal operation is in a submerged position (Scott and Muir, 2000). Studies were carried out to investigate the health condition of salmon at long-period submerged positions (Dempster et al., 2008). Examples of submerged rigid cage designs are AquaPod (Figure 99a) and NSENGI sinking fish cages (Figure 99b).

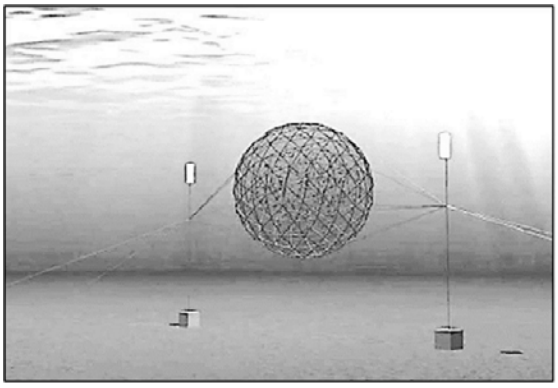

(a) AquaPod cage

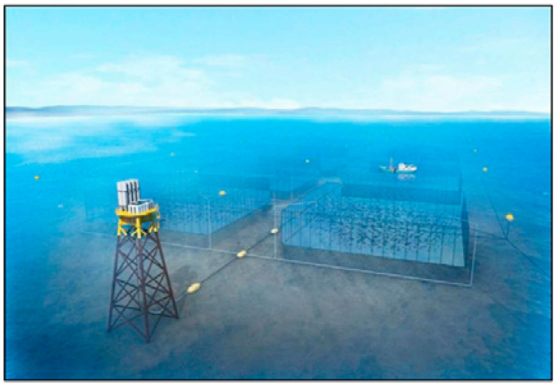

(b) NSENGI Sinking fish cage

Figure 99: Submerged cage system (a) AquaPod cage and (b) NSENGI Sinking fish cage

Submerged cages have the best responses to avoid strong surface waves and the effects of storms. The structural components can thus be less strong, which can save the capital costs significantly. The length of moored lines can also be reduced or even replaced by locating the cages on the seabed.

Their disadvantages are also distinct. Since the cages are normally submerged, regular operation and maintenance might be difficult to be performed due to the lack of visibility. Besides, if they are located near the seabed, the transportation of waste might be hindered, affecting the welfare of the fish.

5.1.5 Closed containment tank system

The closed containment tank system concept was developed to control the water quality (oxygen, temperature, and salinity) and the production process in the 1990s (Beveridge, 2004). An example of a floating closed containment tank is the egg-shaped fish farm developed by Hauge Aqua (Figure 100). The water quality and volume can be controlled, ensuring stable oxygen levels.

Figure 100: Closed egg-shaped fish tank developed by Hauge Aqua

The concept has the potential of achieving the best production rate because it can guarantee optimized physical parameters for fish welfare. By dividing the internal layers with external environments, the organic wastes and problems of predators are solved thoroughly.

The cost of optimized water quality is that the tank system requires an additional power supply system when it is deployed in offshore regions. In addition, the system might incur significant construction and equipment costs for monitoring and intervention. Another problem is that sloshing might occur and injure the fish inside (Cui et al., 2022).

5.2 General Design Considerations

Offshore fish farms are usually deployed at exposed sites with better water quality, larger spaces, and more energetic environments. The structures face several challenges that have not been recognized or considered thoroughly in previous studies. A general summarization would help provide confidence for the decision-making of fish farmers.

In the following some general design considerations for offshore fish farm systems are presented, relevant reviews can be referred to Chu et al. (2020), Zhang et al. (2023), and Fan et al. (2023).

5.2.1 Water depth and sea bed

Water depth has a direct influence on the capital cost of mooring systems. The cost for installation and maintenance increases proportionally with the length of mooring lines and is thus close related to the water depth. On the other hand, a smaller water depth might induce difficulties in the transportation of feed pellets and feces, which is harmful to the health of fish (Cardia et al., 2016). Therefore, the water depth is recommended to be over three times the cage height and to have at least 15 m between the cage bottom and the seabed (Chu et al., 2020).

The properties of the seabed in particular affect the anchor of the mooring system. A detailed seabed analysis should be performed to determine a suitable anchor method for the deployment of other submarine fiber optic cables, lines, or pipelines. A large water depth might induce challenges for the survey of seabed conditions.

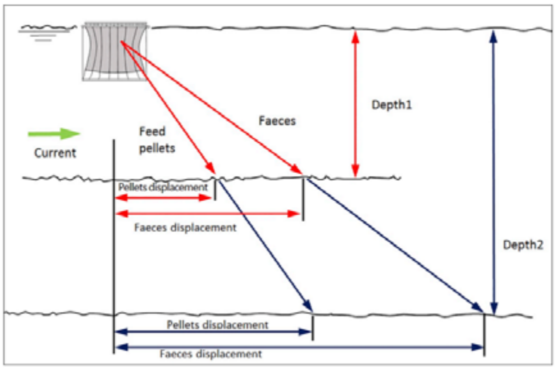

Figure 101: Influence of water depth on transportation of feed pellets and feces for fish cages (Cardia et al., 2016)

5.2.2 Wave action and storm incident

The wave energy in offshore sites can be stronger and more harmful to not only the structures but also the fish. The continuous severe wave actions can also hinder the regular operation of fish farmers.

One possible approach to control the wave actions is to employ breakwater systems (Dai et al., 2018). The systems were regularly used in coastal regions with their bottom fixed on the seabed. In offshore regions, floating breakwaters are more feasible but would require more techniques for their design and installation.

Another short-term strategy is to submerge the fish cages in very bad weather such as storms or typhoons. The submergence can help avoid the impacts of strong surface waves and guarantee oxygen in harsh weather. It also entails more efforts for the design and monitoring of the fish cages and requires consideration for the prediction of the sea state.

5.2.3 Current speed

Current speed is essential for fish farms because it ensures the replenishment of oxygen and the transportation of wastes. With moderate current flows, the fishes can swim in a similar natural status as in wild seas. However, a harsh current flow might cause extremely dangerous conditions for fish and structures.

The horizontal drag forces acting on the cages and mooring lines increase with the current speed, which can induce large deformations of the net and reduce the space and volume. The current speed inner the cages is reduced when using nets with high solidity, but it requires more strengthening for the cage design. (Moe-Føre et al., 2016).

5.2.4 Fish welfare

Fish farms are different from traditional offshore structures because they should ensure fish welfare. The welfare usually includes water temperature, salinity, dissolved oxygen, PH, turbidity and etc. (Pillay et al., 2004). The best water quality is species-dependent and should be considered before the structural design.

Moreover, to guarantee a healthy, abundant, and clean environment, infrastructures are required for routine operation and regular maintenance. Owing to the long distance away from land, water-based infrastructures should be developed and validated in practice to reduce the reliance on land-based supporting facilities (Chu et al., 2020).

5.3 Recent Challenges & Developments

Wang, H. et al. (2023) performed a series of physical experiments to investigate the hydrodynamic interaction between nets and the cylindrical supporting structure for some typical offshore aquacultural structures. The drag and lift forces of only the cylinder, only nets and combined cylinder-net structures under uniform inflow are measured and analyzed systematically. Results in this paper can be used to improve the design of fish farms and other relevant offshore structures by revealing the influence of the interaction between the cylinder and nets on their hydrodynamic characteristics, which is often ignored in present hybrid numerical models (by combining the potential flow theory, Morison and screen models).

Nasyrlayev et al. (2023) investigated the tensions on anchor lines of different arrangements of salmon fish cages under various environmental conditions, including strong currents and waves, by the FEM based AquaSim program. Three orientations (i.e., 2x2, 1x4 and 2x4 multi-cage fish farm), each with two sinker tube weights, were simulated for both current and current and wave loads and varying angles of attack. Through an extensive sensitivity analysis, the study provides insights into the range of possible mooring line loads for different configurations that could be valuable for the design and optimization of aquaculture mooring lines.

Cheng et al. (2021) investigated the effects of mooring line breakage on respectively a single-cage and a 1×4 multi-cage fish farm by conducting time-domain simulations using the program FhSim. Based on the simulations, a method is further developed to predict the maximum tension increment within the remaining mooring lines. The results indicate that structural collapses and fish escapes might occur with the breakages. Recommendations are proposed to improve the mooring design and monitor to prevent fish escapes.

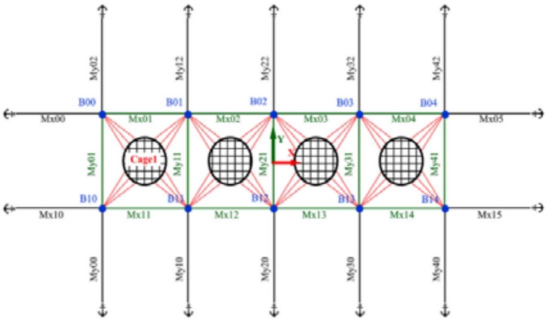

Figure 102: Top view of the 1 × 4 multi-cage fish farm (Cheng et al., 2021)

Cheng et al. (2022a) developed an open-source numerical library for the structural analyses of gravity-type fish cages under the toolbox Code_Aster. The library was then applied for time-domain simulations of gravity fish cages with various commonly-used physical parameters including depths, weights, collar circumferences, and current velocities. The study is valuable for structural optimization. Moreover, the toolbox Code_Aster is coupled with OpenFOAM by Cheng et al. (2022b) for the fluid-structure interaction analysis of submerged nets. The algorithm could handle the wake effects of thin, flexible, and highly permeable structures with complex geometries. The coupled method has been validated with published experiments for both fixed and flexible nets.

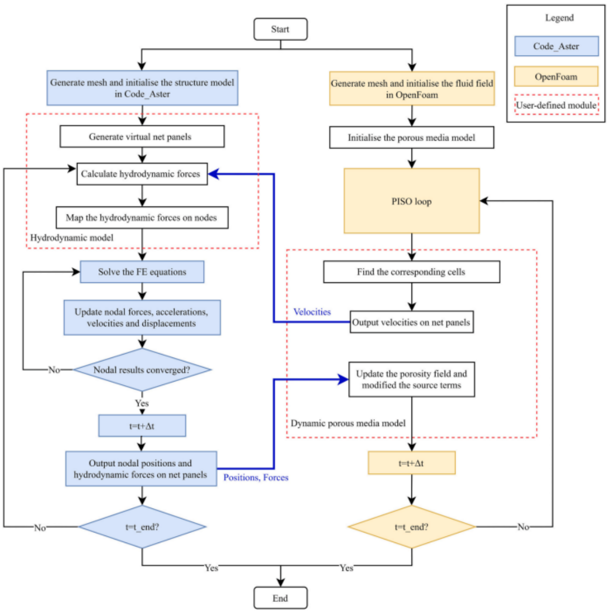

Figure 103: Flow chart of the coupled algorithm (Cheng et al., 2022b)

Sim et al. (2021) investigated the influences of multi-cage interactions on the response of the fish farm. The time-domain simulation program FhSim is employed to model the mooring tensions, drag force, and cultivation volume of each cage in a full-scale 4 × 2 multi-cage fish farm. It is found that the wake effects can overestimate the total drag force of the eight cages and underestimate the total cultivation volume, indicating that wake effects can be significant for a multiple-cage system.

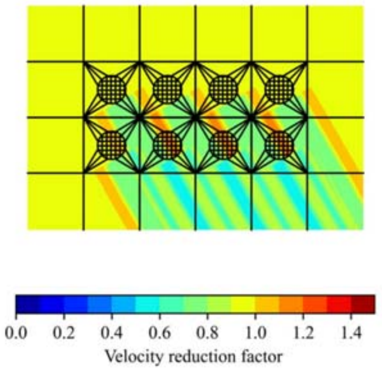

Figure 104: Flow field around the fish farm for illustration of cage-to-cage wake effects (Sim et al., 2021)

Ma et al. (2021) developed a semi-analytical model for the wave field description around a single gravity-type cylindrical open fish net cage. The fish cage net is modeled as a flexible porous membrane while the net chamber is modeled by the transverse vibration equation of strings. The velocity potential is expanded in the form of the Fourier–Bessel series based on the small-amplitude wave theory. The model was employed to investigate the effects of several important design parameters on hydrodynamic actions of the net cage by parametric studies (Ma et al., 2022a). It is concluded that increasing the net porosity and flexibility can alleviate the hydrodynamic actions and wave scattering.

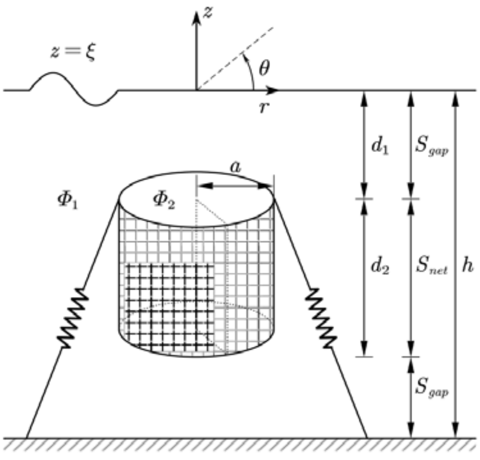

Figure 105: Side view of a cylindrical net cage submerged in a finite water depth (Ma et al., 2021)

The developed semi-analytical method was expanded by Ma et al. (2022b) to investigate the dynamic responses of an array of submersible flexible fish cages. The solution is expanded as a series of eigenfunctions in the local coordinate system of each cage based on the potential flow theory. The mean wave drift effect was also explored. It was found that the first-order wave force could vanish at a certain ratio of cage diameter to wavelength. These studies provide a benchmark for understanding the hydroelastic characteristics of multi-cage systems.

Zhao et al. (2021) analyzed the flow patterns inside and around a semi-submersible aquaculture platform by developing a method combining porous media and rigid walls. The fish nets and other mainframes are modeled by porous media and rigid wall conditions, respectively. The model was verified by experiments and the results indicate that fish nets play a vital role in the attenuation of flow velocity. In addition, the risk of resonance is found to increase when the frequency of the vortex shedding is close to the natural frequency of the structure.

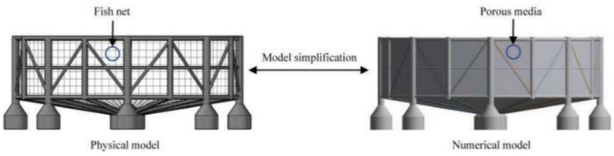

Figure 106: Model simplification of the semi-submersible aquaculture platform (Zhao et al., 2021)

Yu et al. (2023) presents an experimental and numerical study on hydrodynamic forces and mooring performance of an aquaculture platform with a regular hexagonal prism shape. The analysis was performed for both the operation draft as well as for the typhoon survival draft when the platform is fully submerged and sitting on the seabed. A spread mooring system with a hybrid mooring line composition, containing steel chain and fibre rope in each line, was designed and its performance was assessed.

Figure 107: Physical model of the floating aquaculture platform in operational (left) and extreme bottom-sitting (right) conditions (Yu et al. 2023)

Slagstad et al. (2023) proposed a simplified analytical model for the fatigue life prediction of aquaculture nets. The axial force is first estimated in the ropes supporting the fishnet, for which the hydrodynamic loads are calculated using a screen model. The results from the simplified calculations are compared to numerical simulations performed in RIFLEX. It is concluded that the simplified method is extremely efficient with acceptable accuracy. The model is of interest for the preliminary design of fish nets.

In a follow up work, Slagstad et al. (2024) further developed the model described in the previous paragraph and presented a simplified force response calculation for circular aquaculture nets in waves and current conditions. The basis for the method is a quasi-static solution calculated using the principle of virtual displacements. In the analysis they considered a cylindrical net connected to a steel frame inspired by fish farm facilities located in harsh environments such as Ocean farm 1. The method provides fast and simple estimates of the forces with good accuracy which is suitable for the design or optimization process.

Zhao et al. (2022a) performed an experiment study on a multi-body floating aquaculture platform to investigate the influences of coastal topography. In the experiment, the wave slamming of the net cage is captured and the wave breaking inside the cage becomes more evident if the incident wavelength is close to the width of the cage. It is concluded that the low-frequency component of the surge motion of the cage increases significantly under the influence of the sloping seabed while the vertical motions change slightly.

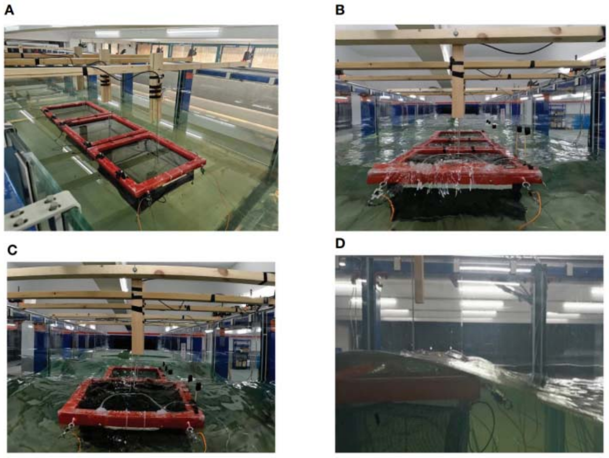

Figure 108: Physical model of the floating aquaculture platform: (A) model in the calm water, (B) wave slamming of the net cage, (C) wave reflection inside the cage, (D) completely submerged net cage (Zhao et al., 2022a)

Another experiment study was carried out by Zhao et al. (2022b) to verify a digital twin model for rapid detection of damage to a fixed panel. The model is developed based on the artificial neural network where the wave parameters and rope tensions are used as input while the intact and damaged states of the fishing net are considered as outputs. The model accuracy was ensured regarding different wave-current directions. Moreover, the model can accurately detect net damage when sea conditions and sensor data are not included in the training.

Miao et al. (2021) proposed a hybrid numerical method for the hydrodynamic performances of a semi-submersible offshore fish farm. The three-dimension dimensional potential theory, Morison's equation, and the screen model are employed respectively for the large pontoon, the frame system, and the net system. The method is validated against the experiment with good agreement. The developed codes were then used to investigate the effects of some key parameters on the motion responses, such as draft, wave height, and net solidity ratio.

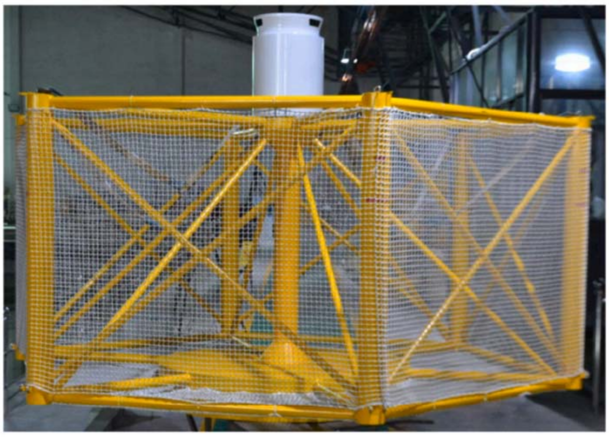

Figure 109: Physical model of the semi-submersible fish farm (Miao et al., 2021)

Wang et al. (2022) investigated the loads on a vessel-shaped fish cage based on the potential theory. The global hydrodynamic responses of the floating body are first calculated by the state-space method. Based on the time-domain simulations, velocity transfer functions are obtained and then their effects on the forces of the nets and steel frames are calculated by Morison equations. The internal loads of the main steel structures are calculated by employing a quasi-static method. The method was expanded to consider irregular load effects by Wang et al. (2023) and it is found that the diffraction and radiation waves make a significant difference in the twine tension and connector load effect.

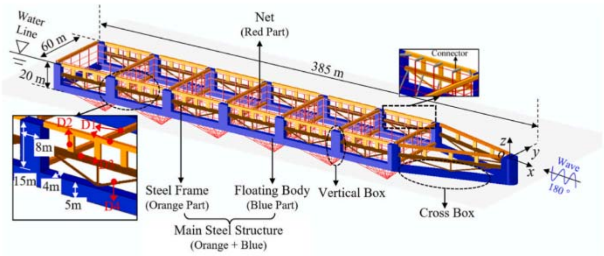

Figure 110: Model of the vessel-shaped fish cage (Wang et al., 2023)

The semi-submersible aquaculture platform "Pu Sheng 1" is the first marine breeding equipment in South China. The platform is equipped with photovoltaic power generation equipment, utilizing clean energy and ensuring its green and environmentally friendly operation. (Ding et al. 2023) conducted a numerical study of the hydrodynamic performance of this semi-submersible aquaculture platform with fully coupled analysis in OrcaFlex.

Figure 111: Semi-submersible aquaculture platform "Penghu" (Ding et al. 2023)

Shen et al. (2022) conducted a comparative analysis between a closed cage (CC) and a semi-closed/open-bottom cage (OC) to examine the similarities and differences of the hydrodynamic behaviors under wave actions. Experimental results show that the two cages have similar performance in surge motion, ovalizing deformations, interior wave elevation, and mean drift loads in shorter waves, which also indicates that the linear potential flow solver WAMIT can provide a reasonable prediction for OC in shorter waves. In addition, survival conditions are also considered for both cages where the platform freeboard is identified as the most critical parameter. The study provides a valuable reference for the experimental analyses of closed cages.

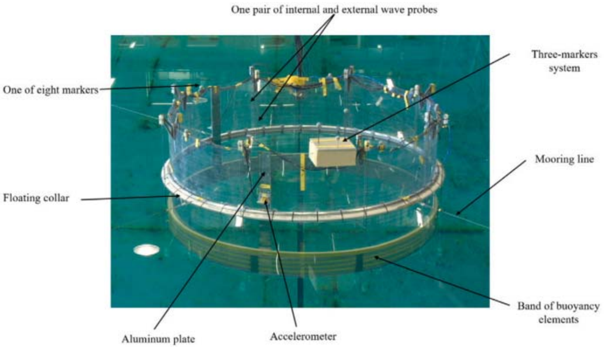

(a) Open-bottom cage

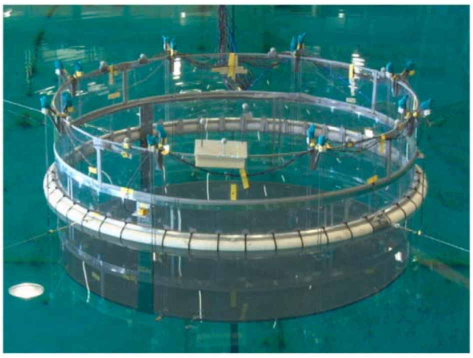

(b) Closed cage

Figure 112: Physical model for the (a) open-bottom cage and (b) closed cage (Shen et al., 2022)

Another experimental study was conducted by Wiegerink et al. (2023) focusing on the inner water surface of the floating closed fish tank. The study developed a slosh suppression block for mitigating sloshing in floating closed containment fish tanks. Different designs of suppression blocks are tested to investigate their effectiveness in mitigating sloshing considering the state of the internal fluid for fish well-being. Results show that slosh suppression blocks can effectively reduce the overall sloshing amplitudes, which makes it possible for deploying closed containment systems in offshore fish farming sites with higher energy.

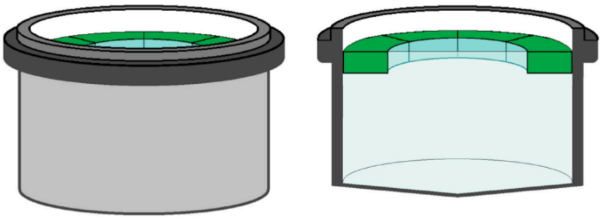

Figure 113: Concept of a slosh suppression block applied to a cylindrical floating closed fish tank system (Wiegerink et al., 2023)

Dong et al. (2021a) experimentally measured the drag force, cage deformation, and flow field inside and around a scaled net cage model with different bottom weights in a flume tank. The cage is originally used to farm the Pacific bluefin tuna in Japan. A complex fluid–structure interaction is observed owing to the significant deformation of the flexible net cage. Later, a full-scale test involving a sea trial at a silver salmon farm site is conducted by Dong et al. (2021b), the drag force values of the full-scale net cage are lower than the converted values by model-scale experiments.

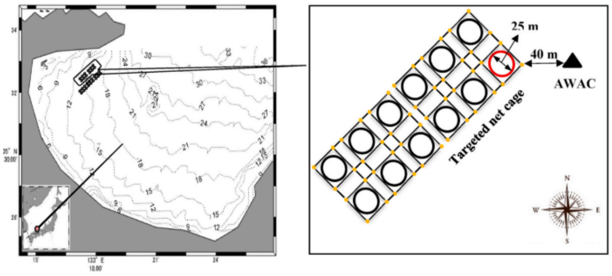

Figure 114: Layouts of the full-scale fish farm site for silver salmon (Dong et al., 2021b)

Chu et al. (2022) established a frequency-domain approach for motion analyses of an integrated offshore fish cage and wind turbine (named COSPAR). The frequency-domain analyses are first performed by ANSYS AQWA to obtain response amplitude operators (RAOs) for motions and mooring tension. Wind thrust was estimated by using a linearization method and incorporated in AQWA for the integrated analysis. The model is validated and it is concluded that COSPAR can provide a stable working platform for offshore fish farms subjected to wind, wave, and current loads. The pitch angles are also acceptable for wind turbine operation.

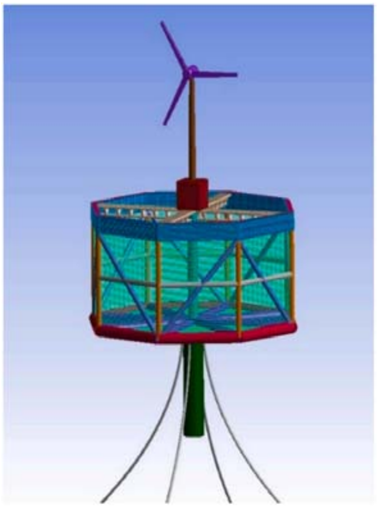

Figure 115: Integrated COSPAR fish cage and wind turbine (Chu et al., 2022)

Figure 116 shows an illustration of the FOWT-SFFC concept which combines a conic steel fish cage and a multi-megawatt wind turbine (Lei et al. 2024). OrcaFlex was used to perform a time domain analysis of the system responses to wind and waves and the results compared with model test data to calibrate the numerical model.

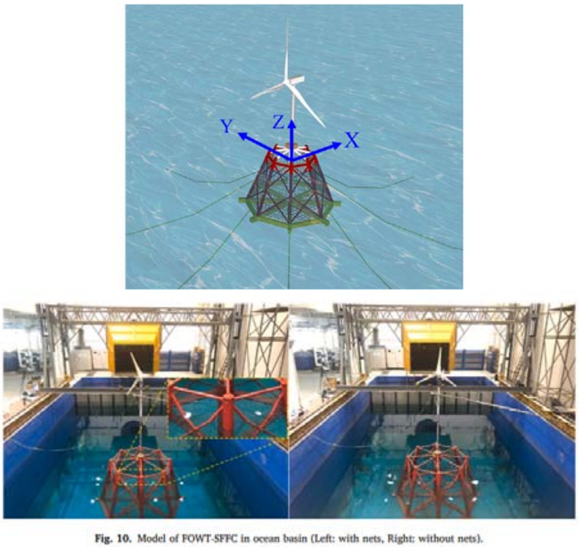

Figure 116: Top: FOWT-SFFC concept, bottom figure: model test setup with (left) and without nets (right) (Lei et al. 2024)

Another integrated concept was proposed by Li et al. (2023) using a jacket-supported wind turbine, named JOWT-SC. The depth of the closed cage can be changed to adapt to various waters and prevent fish from escaping. Time-domain simulations are conducted by the software SACS and the dynamic responses are compared with and without the fish cage. The results demonstrate that the aquaculture steel cage significantly influences the dynamic responses of the integrated JOWT-SC and the pile-foundation shear responses are more sensitive to the wave frequency.

One more integrated concept with fixed foundation was studied by Tu et al. (2023). The authors propose a design scheme for a multi-pile-support offshore wind turbine foundation integrated with an aquaculture net cage. The hydrodynamic analysis of the combined structure was performed to study the effect of the net on hydrodynamic loads on the foundation of the wind turbine. The analysis shows that the hydrodynamic loads on the structure increases while the natural frequency remained largely unaffected.

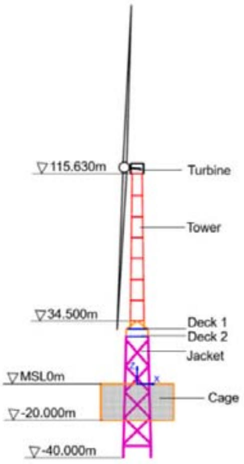

Figure 117: Design concept of the integrated JOWT-SC structure (Li et al., 2023)

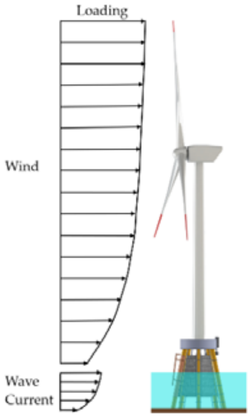

Figure 118: Model of an integrated offshore wind turbine with an aquaculture net cage (Tu et al. 2023)

Liu et al. (2022) investigated the feasibility of the idea to integrate an open ocean aquaculture ship with a NREL 5 MW wind turbine. A fully coupled analysis was performed with the turbine aerodynamic loads and responses calculation in FAST and hydrodynamic calculations in AQWA. Figure 119 shows the schematic sketch of the concept, where the internal turret mooring system installed at the bow aligns the wind turbine with the wind direction.

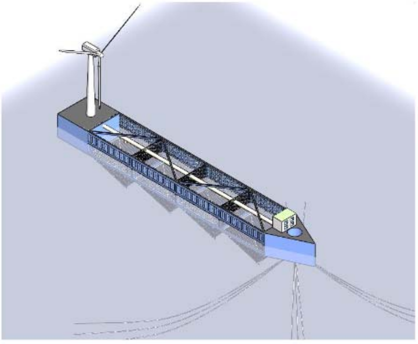

Figure 119: Integrate an open ocean aquaculture ship with a NREL 5 MW wind turbine (Liu et al. 2022)

Zheng et al. (2021) conducted a feasibility study of the wind-solar-aquaculture concept (WSA) that combines multi vertical-axis wind turbines (VAWTs) and solar panels with a steel fishing cage as the supporting substructure. A simulation package is developed to couple with WAMIT, OrcaFlex and validated against ANASYS under combined wind-wave actions. The results show that aerodynamic loads have greater influences on platform surge and pitch motions, tower bending moments and mooring tensions. The responses are further analyzed in the frequency domain to identify contributions from various environmental loads.

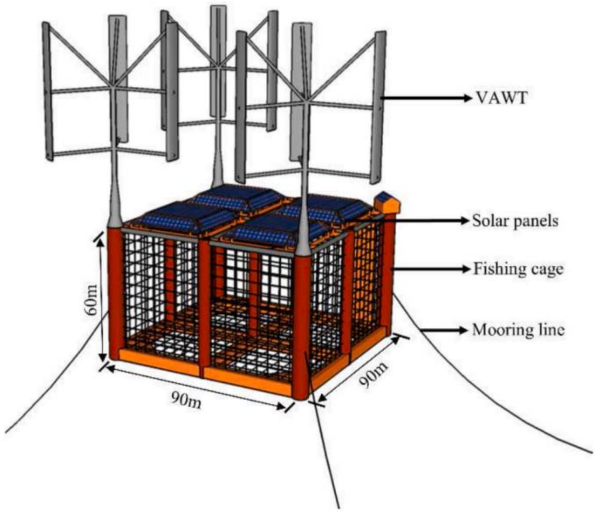

Figure 120: Concept of the wind-solar-aquaculture (WSA) system (Zheng et al., 2021)

6. EXTENDED EXPERIMENTAL WAVE RUN-UP BENCHMARK STUDIES — FOUR SQUARED VERTICAL CYLINDERS

More experimental studies were conducted for four-column cases with more extreme waves such as focused waves, due to the complicated wave-column interactions. In addition, local wave impact loads on the columns are also critical and further in-depth studies were completed.

6.1 Experimental Program for Four-Squared-Cylinder System

The extended experiments for wave run-ups on fixed four-squared-cylinder systems with different configurations and extreme waves such as focused waves were carried out by SKLOE (State Key Laboratory of Ocean Engineering) of Shanghai Jiao Tong University. The benchmark data are summarized in the following sections.

A series of model tests on a fixed four-squared-cylinder array with focused waves were conducted in a wave tank at the State Key Laboratory of Ocean Engineering (SKLOE), Shanghai Jiao Tong University. As shown in Figure 121, the total length, width and depth of the wave tank were 300, 16 and 7.5 m, respectively. Multi-flap wavemakers were installed at one end of the tank to generate different types of waves, which were defined as the for wave-generation origin ($X = 0\,m$). A right-handed coordinate system O-XYZ used in this test is also depicted in Figure 121. The coordinate origin was set to the still-water level. The positive X-axis points towards the incident wave direction, and the direction of the Z-axis is vertically upward. Additionally, wave-absorbing beaches were installed to effectively eliminate reflected waves. One configuration of fixed four-truncated-square-cylinder system is considered, in which the half column breadth $a = 8$ m and the column spacing $b = 34$ m, respectively. The fillet radius of all columns is 3 m, the height of all columns is 60 m, and the constant draft is 20 m. The model scales are 1:50.

The column array was made of fibre reinforced plastic (FRP), which offers the advantages of lower density and adequate strength. The overall appearance of the physical model is displayed in Figure 122. During the test, the column array was installed on the external frame, with the upstream surface of the front column at 15 m ($X = 15\,m$) from the wavemakers.

There is a total of 35 different focused waves, as shown in Table 3, where A denotes the amplitude of focused wave, T is the spectral peak period, γ is the peak enhancement factor, T_f is the focus time point, x is the focus position, Δx is the forward distance of the focus position. The focused wave steepness was defined as H/λ, where λ and H are the length and height of a Stokes wave whose period is equal to the spectral peak period T. For a focused wave of given T and H/λ, the linear amplitude sum A was set equal to the crest elevation of the corresponding Stokes wave of period T and height H. The periods of wave components were uniformly ranged from 0.2s to 2.8s. The focus position of FW1 is at the front face of the front column. Based on original focused wave, other focused waves are obtained by shifting the focus position forward by a distance of Δx. In this way, waves with different degrees of breaking are obtained. Model tests were conducted by SKLOE for fixed four-squared-cylinder systems of two different wave direction as 0° and 45° (F1 series for 0° wave direction, F2 series for 45° wave direction, as shown in Table 4).

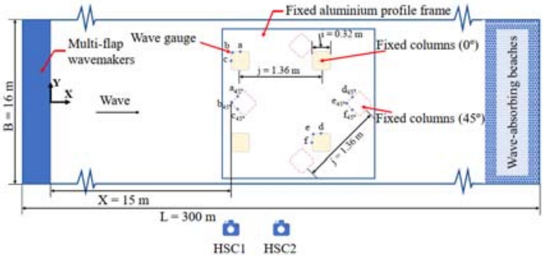

(a) Top view

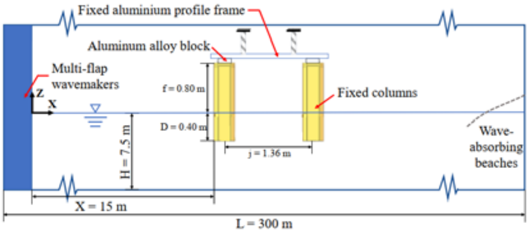

(b) Side view

Figure 121: Schematic of the experimental setup in the wave tank

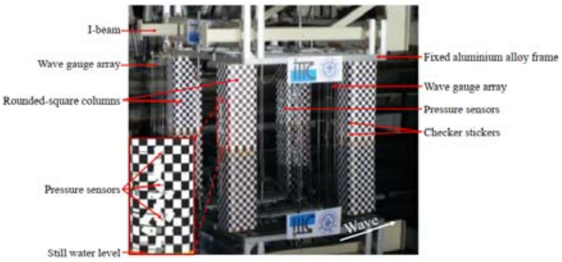

Figure 122: Overall appearance of physical model

Table 3: Environment matrix (focused waves)

	Scale: 1:50						
Wave No.	A	T	γ	T_f	x	Δx	H/λ
	(m)	(s)		(s)	m	m	
FW1	0.3	2.4	2.5	40	15	0.00	0.07
FW2	0.27	2.3	2.5	40	15	0.00	0.07
FW3	0.25	2.2	2.5	40	15	0.00	0.07
FW4	0.235	2.0	2.5	40	15	0.00	0.08
FW5	0.21	2.0	2.5	40	15	0.00	0.07
FW6	0.21	2.0	2.5	40	15	-0.40	0.07
FW7	0.21	2.0	2.5	40	15	-0.20	0.07
FW8	0.21	2.0	2.5	40	15	0.32	0.07
FW9	0.21	2.0	2.5	40	15	1.36	0.07
FW10	0.21	2.0	2.5	40	15	1.68	0.07
FW11	0.19	2.0	3.3	40	15	0.00	0.06
FW12	0.16	2.0	3.3	40	15	0.00	0.05
FW13	0.16	1.5	2.5	40	15	0.00	0.09
FW14	0.14	1.5	2.5	40	15	0.00	0.08
FW15	0.12	1.5	2.5	40	15	0.00	0.07
FW16	0.12	1.5	2.5	40	15	-0.40	0.07
FW17	0.12	1.5	2.5	40	15	-0.20	0.07
FW18	0.12	1.5	2.5	40	15	0.32	0.07
FW19	0.12	1.5	2.5	40	15	1.36	0.07
FW20	0.12	1.5	2.5	40	15	1.68	0.07
FW21	0.11	1.5	3.3	40	15	0.00	0.06
FW22	0.09	1.5	3.3	40	15	0.00	0.05
FW23	0.11	1.2	2.5	40	15	0.00	0.10
FW24	0.1	1.2	2.5	40	15	0.00	0.09
FW25	0.09	1.2	2.5	40	15	0.00	0.08
FW26	0.08	1.2	2.5	40	15	0.00	0.07
FW27	0.08	1.2	2.5	40	15	-0.40	0.07
FW28	0.08	1.2	2.5	40	15	-0.20	0.07
FW29	0.08	1.2	2.5	40	15	0.32	0.07
FW30	0.08	1.2	2.5	40	15	1.36	0.07
FW31	0.08	1.2	2.5	40	15	1.68	0.07
FW32	0.07	1.2	3.3	40	15	0.00	0.06

FW33	0.06	1.2	3.3	40	15	0.00	0.05
FW34	0.055	1.0	2.5	40	15	0.00	0.07
FW35	0.035	0.8	2.5	40	15	0.00	0.07

Table 4: Test matrix

Wave No.	Case No. (Dir. 0°)	Case No. (Dir. 45°)
FW1	101	201
FW2	102	202
FW3	103	203
FW4	104	204
FW5	105	205
FW6	106	
FW7	107	
FW8	108	
FW9	109	
FW10	110	
FW11	111	211
FW12	112	212
FW13	113	213
FW14	114	214
FW15	115	215
FW16	116	
FW17	117	
FW18	118	
FW19	119	
FW20	120	
FW21	121	221
FW22	122	222
FW23	123	223
FW24	124	224
FW25	125	225
FW26	126	226
FW27	127	
FW28	128	
FW29	129	
FW30	130	
FW31	131	
FW32	132	232
FW33	133	233
FW34	134	234
FW35	135	235

The locations of wave probes are shown in Figure 123. The coordinates of wave probes are given in Table 5.

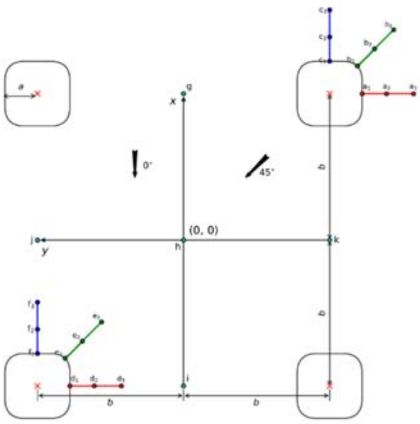

Figure 123: Locations of wave probes

Table 5: Coordinates of wave probes

Scale: 1:50		
	x (m)	y (m)
a_1	0.6800	-0.8400
a_2	0.6800	-0.9300
a_3	0.6800	-1.0300
b_1	0.8224	-0.8224
b_2	0.8861	-0.8861
b_3	0.9568	-0.9568
c_1	0.8400	-0.6800
c_2	0.9300	-0.6800
c_3	1.0300	-0.6800
d_1	-0.6800	0.5200
d_2	-0.6800	0.4300
d_3	-0.6800	0.3300
e_1	-0.5376	0.5376
e_2	-0.4739	0.4739
e_3	-0.4032	0.4032
f_1	-0.5200	0.6800
f_2	-0.4300	0.6800
f_3	-0.3300	0.6800
g	0.6800	0.0000
h	0.0000	0.0000
i	-0.6800	0.0000
j	0.0000	0.6800
k	0.0000	-0.6800

To measure the local wave impact pressure, the four-square-vertical-cylinders are covered by 31 miniature pressure sensors, as shown in Figure 124. The locations of all pressure sensors are summarized in Table 6.

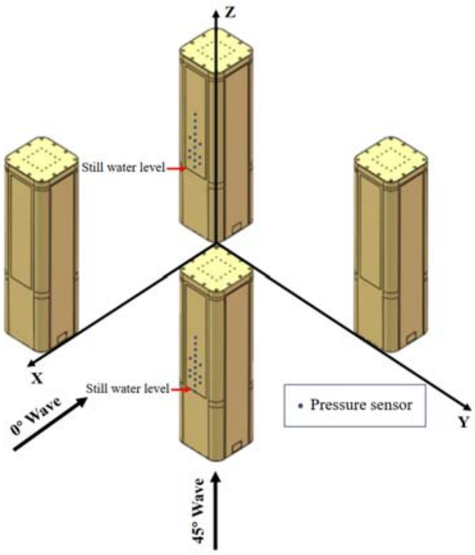

Figure 124: Pressure sensor location

Table 6: Coordinates of thirty-one (31) pressure sensors

Sensor No.	Scale: 1:50			
	Unit	X	Y	Z
Slam001	mm	840.00	680.00	0.00
Slam002	mm	840.00	680.00	50.00
Slam003	mm	840.00	630.00	100.00
Slam004	mm	840.00	680.00	100.00
Slam005	mm	840.00	730.00	100.00
Slam006	mm	840.00	630.00	150.00
Slam007	mm	840.00	680.00	150.00
Slam008	mm	840.00	730.00	150.00
Slam009	mm	840.00	680.00	200.00
Slam010	mm	840.00	630.00	250.00
Slam011	mm	840.00	680.00	250.00
Slam012	mm	840.00	730.00	250.00
Slam013	mm	840.00	680.00	300.00
Slam014	mm	840.00	680.00	350.00
Slam015	mm	840.00	680.00	400.00
Slam016	mm	840.00	680.00	450.00
Slam018	mm	-520.00	-680.00	50.00
Slam019	mm	-520.00	-730.00	100.00
Slam020	mm	-520.00	-680.00	100.00
Slam021	mm	-520.00	-630.00	100.00
Slam022	mm	-520.00	-730.00	150.00
Slam023	mm	-520.00	-680.00	150.00
Slam024	mm	-520.00	-630.00	150.00
Slam025	mm	-520.00	-680.00	200.00
Slam026	mm	-520.00	-730.00	250.00
Slam027	mm	-520.00	-680.00	250.00
Slam028	mm	-520.00	-630.00	250.00
Slam029	mm	-520.00	-680.00	300.00
Slam030	mm	-520.00	-680.00	350.00
Slam031	mm	-520.00	-680.00	400.00
Slam032	mm	-520.00	-680.00	450.00

The sampling rate was 100 Hz for wave probes. For the impact pressure, a high-speed measurement system of a sampling rate of 20 kHz was used. The 100 Hz and 20 kHz measurements were synchronized and the recordings were started simultaneously. The wave calibration should be performed prior to placing the model in the basin. The effective record duration of each focus wave test shall be twice than the focus time T_f.

In the benchmark studies, the max results of following measured items were compared at various wave periods, focus positions and wave steepness in terms of H/λ:

1) Wave elevations at 23 wave probe locations.

2) Wave impact pressure at 31 pressure sensor locations.

6.2 Wave Run-up Characteristics in Focused Waves

6.2.1 Wave run-up height at 0°

For the wave direction of 0°, Figure 125-Figure 128 depict the maximum values of wave run-up ratios at six locations (a_1, b_1, c_1, d_1, e_1, f_1) for the fixed four-square-column array at various wave steepness, spectral peak periods, and focus positions, respectively. In the figures, y denotes the lateral position from the column center, and D represents the column width. The maximum wave run-up height η_{max} is normalized by the incident focused wave amplitude (A). The vertical dotted line represents the wave probes, and the blue area represents the front projection of the column.

For the front column, the peak value is observed at the central location (c_1), while the lowest value is found at the shoulder (a_1). Figure 125 shows that for waves of relatively small steepness (H/λ=0.05), the maximum wave run-up ratio is significantly smaller (~1.2 to 1.6) than that of larger waves with steeper steepness. As illustrated in Figure 128(a), the reason of this phenomenon is that the process of wave run-up is primarily manifested by the gentle uplift of the local water as the focused wave crest approaches and passes through the column. Due to the relatively gentle steepness of the focused wave, only minor diffraction and disturbance occur during the interaction between the wave and the front column, without any significant phenomena taking place. As the steepness of the focused waves increases (H/λ =0.06), a more pronounced wave upwelling can be observed during the wave-column interaction as depicted in Figure 128(b). And the ratio of wave run-up height has reached to 1.6-1.8. When the incident wave steepness continues to increase (H/λ=0.07), more obvious wave upwelling occurs on the surface of front column as shown in Figure 128 (c). As a result, the wave run-up ratio is significantly increased (~1.6 to 2.2). And there is no breaking and water jet in the whole process. For the focused waves with larger wave steepness (H/λ =0.08), the waves near breaking or break precisely at the focal point, a water jet can be generated by the uprush flow, as shown in Figure 128 (d), and hence increases the run-up ratio significantly (~1.8 to 2.8). Especially for T=2.0s, the wave run-up ratio at steepness of 0.08 increases significantly. In general, the effect of wave steepness is more pronounced for long waves compared to short waves.

Figure 126 illustrates that when the wave steepness is relatively low (H/λ=0.05~0.06), there is a declining trend in the wave run-up ratio with increasing wave period, although the differences are minor. This is because, when the wavelength is significantly larger than the column width, the nonlinear wave-column interaction diminishes as the wave period increases. Especially for H/λ=0.06, Figure 127 shows that the wave run-up ratio is almost consistent at all spectral peak periods. However, for higher wave steepness values (H/λ=0.07~0.08), changes in the spectral peak period leads to significant variations in wave run-ups. When the wave steepness is 0.08 and the spectral peak period is 2.0s, the maximum wave run-up ratio reaches 2.79, emphasizing the significant impact of wave steepness on long waves, as mentioned earlier.

For the rear column, the positive peak value of the wave run-up height almost appears at the center (f_1), and appears at the filet point (e_1) in a minority of cases. It is noteworthy that the difference in wave run-up ratios between locations f_1 and e_1 is not significant, which indicating that the interference between the columns has a significant effect on the rear column, and the design of the upper deck structure at the rounded corner is also important. Due to the dissipation of wave energy, the maximum wave run-up ratio for the rear column is lower than that of the front column.

Figure 127 demonstrates that the focus position has a substantial influence on the wave run-up ratio. For the front column, the wave run-up ratio is maximized when the focus position is situated behind the rear surface of the front column. Although the focusing position is on the rear surface, the incident waves have already begun to go up on the front surface. Due to the obstruction of the column, the wave is compelled to persistently run-up, leading to a significantly greater run-up ratio compared to those under other focus positions. Conversely, for the rear column, the wave run-up ratio attains its maximum value when the focus position is located at the front surface of the rear column. This is because even though the focusing position is on the rear column, a portion of the wave energy dissipates as it passes through the front column.

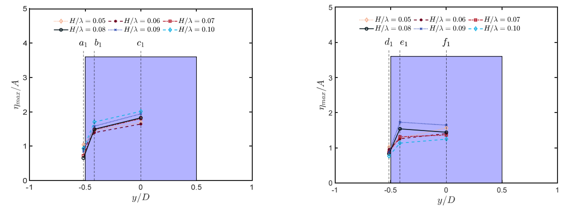

(a) T=1.20s, front column (b) T=1.20s, rear column

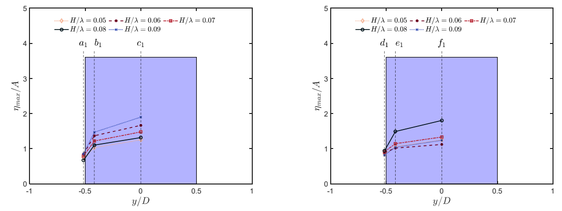

(c) T=1.50s, front column (d) T=1.50s, rear column

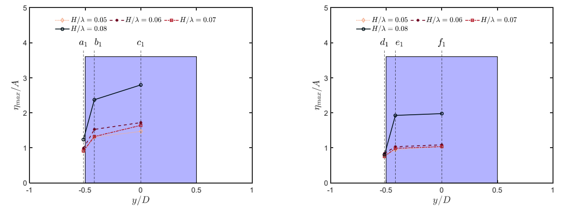

(e) T=2.00s, front column (f) T=2.00s, rear column

Figure 125: Maximum wave run-up ratios at various wave steepness (heading 0°)

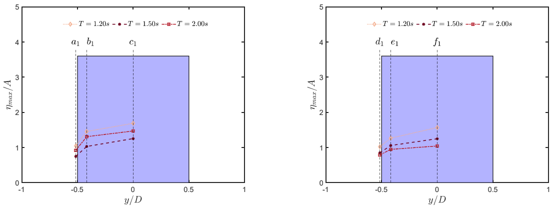

(a) *H/λ*=0.05, front column (b) *H/λ*=0.05, rear column

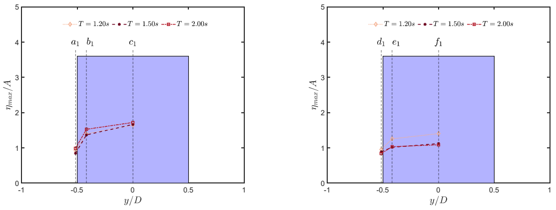

(c) *H/λ*=0.06, front column (d) *H/λ*=0.06, rear column

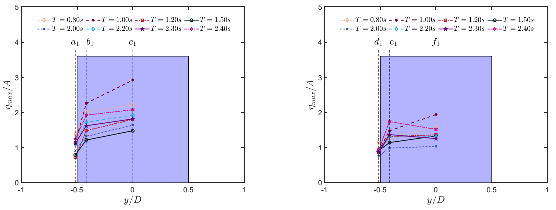

(e) *H/λ*=0.07, front column (f) *H/λ*=0.07, rear column

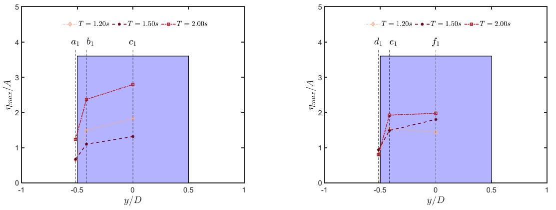

(g) *H/λ*=0.08, front column (h) *H/λ*=0.08, rear column

Figure 126: Maximum wave run-up ratios at various wave periods (heading 0°)

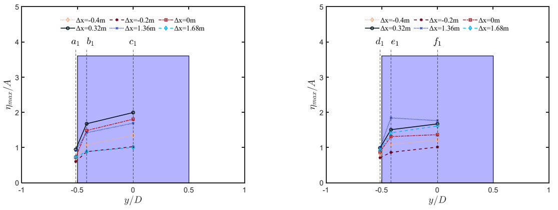

(a) *T*=1.20s, front column (b) *T*=1.20s, rear column

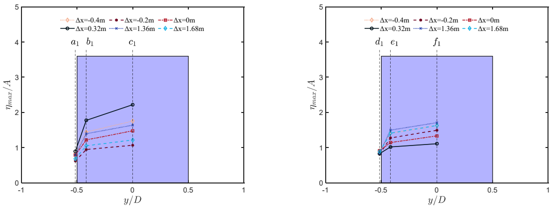

(c) *T*=1.50s, front column (d) *T*=1.50s, rear column

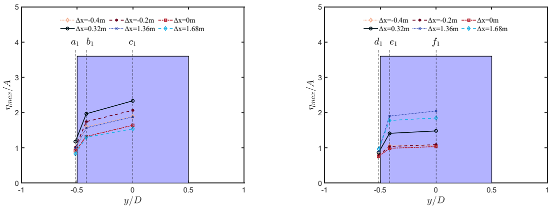

(e) *T*=2.00s, front column (f) *T*=2.00s, rear column

Figure 127: Maximum wave run-up ratios at various focus positions (heading 0°, H/λ=0.07)

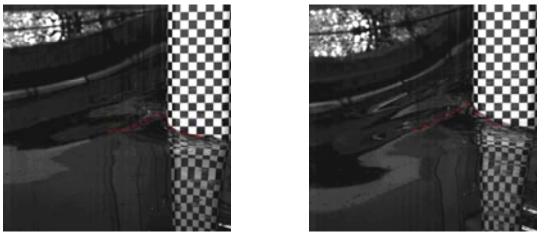

(a) H/λ=0.05, T=2.0s (b) H/λ=0.06, T=2.0s

(c) H/λ=0.07, T=2.0s (d) H/λ=0.08, T=2.0s

Figure 128: The wave run-up along the surface of the front column.

6.2.2 Wave run-up height at 45°

For the wave direction of 45°, Figure 129 and Figure 130 show the maximum wave run-up ratios at 6 locations (a_1, b_1, c_1, d_1, e_1, f_1) represented by y/D_1, where y denotes the distance along the diagonal to the column center, D_1 is column diagonal width.

For both the front and rear columns, the maximum wave run-up ratio occurs at the rounded corner (b_1 and e_1).

For the front column, the conclusion is the same as that of the 0° wave direction. When the focused wave steepness is small (H/λ=0.05), the maximum ratio of the wave run up is significantly smaller than that of other large wave steepness. As the steepness of the wave increases gradually, so does the maximum ratio of wave run-up. It's also attributed to varying degrees of interaction between the wave and the local water in front of the column.

For the rear column, due to the dissipation of wave energy, the wave run up ratio at the surface is significantly lower than that of the front column. By comparing the results at probes c_1 and f_1 in Figure 129, it illustrates that the wave steepness variation has a different effect on the wave run-up ratio at the center of the front and rear columns. This may be attributed to the complex wave interactions among the columns. In addition, the highest wave run up ratio point shifts from the front of the column to the rounded corner, indicating that the wave interference among the columns has a significant effect on the rear column, and the design of the upper deck structure at the rounded corner is also important.

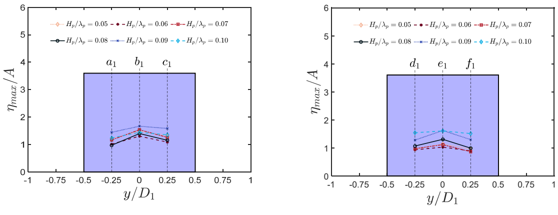

(a) *T*=1.20s, front column (b) *T*=1.20s, rear column

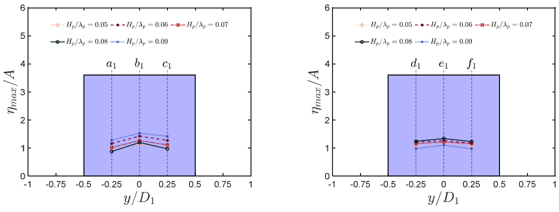

(c) *T*=1.50s, front column (d) *T*=1.50s, rear column

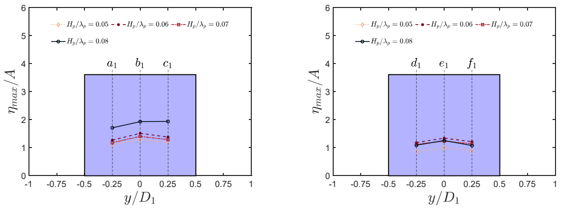

(e) *T*=2.00s, front column (f) *T*=2.00s, rear column

Figure 129: Maximum wave run-up ratios at various wave steepness (heading 45°)

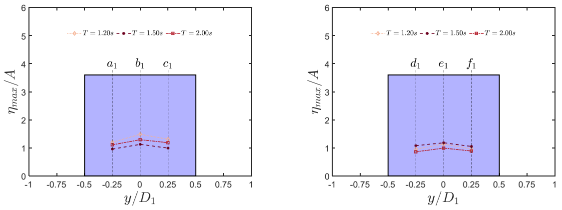

(a) *H/λ*=0.05, front column (b) *H/λ*=0.05, rear column

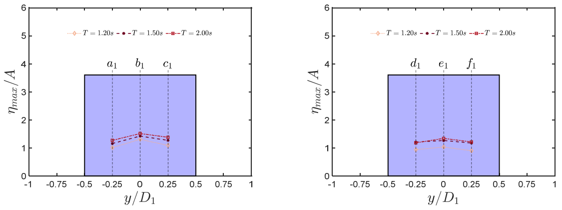

(c) *H/λ*=0.06, front column (d) *H/λ*=0.06, rear column

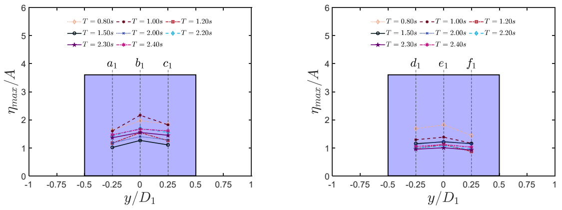

(e) *H/λ*=0.07, front column (f) *H/λ*=0.07, rear column

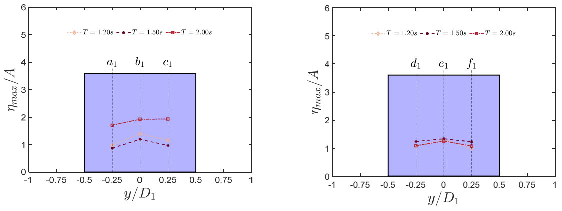

(g) *H/λ*=0.08, front column (h) *H/λ*=0.08, rear column

Figure 130: Maximum wave run-up ratios at various wave periods (heading 45°)

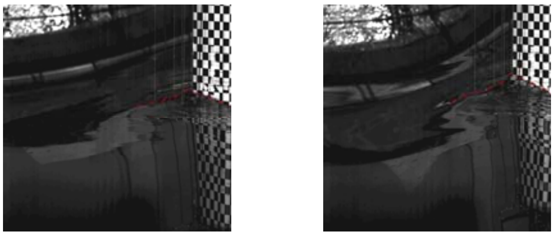

(a) *H/λ*=0.05, *T*=2.00s (b) *H/λ*=0.06, *T*=2.00s

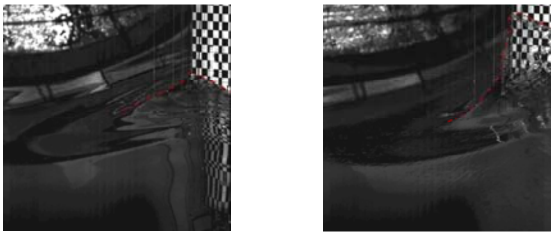

(c) *H/λ*=0.07, *T*=2.00s (d) *H/λ*=0.08, *T*=2.00s

Figure 131: Snapshots of visual observations during the focused wave acting on the front column (heading 45°)

6.2.3 Wave run-ups around fixed four squared cylinders

Figure 132 show the max value of wave elevations at 18 locations ($a_1 \sim a_3$, $b_1 \sim b_3$, $c_1 \sim c_3$, $d_1 \sim d_3$, $e_1 \sim e_3$, $f_1 \sim f_3$) for fixed four-squared-cylinder systems of each case with 0° wave heading direction. In the figure, x means the distance from wave probe to the column surface, D means the column width. Figure 133 shows the max values for each case with 45º wave direction.

From these images, it can be observed that under varying wave steepness, spectral peak periods, and focus positions, the wave run-up evolution follows a consistent pattern: the closer the waves are to the column surface, the more pronounced the wave run-up becomes, with the maximum run-up occurring near the column surface. Furthermore, the steeper the focused wave, the more pronounced the wave run-up evolves with *x/D*, resulting in stronger wave run-up phenomenon. However, for the rear column, the wave run-up evolution with *x/D* is much gentler, and the run-up phenomenon only intensifies under short wave period and large wave steepness.

Figure 132 illustrates that for the front column, when the spectral peak period is smaller (T= 1.20s, T = 1.50s), and the focus position is near the column surface, the wave run-up evolves more steeply with x/D. Conversely, when the focus position is near the surface of the rear column, the evolution is nearly flat. This is because, with constant wave steepness, a shorter wave period results in lower wave energy. Consequently, when the focus position is near the rear column, the wave energy has reduced at the front column, leading to a less noticeable wave run-up phenomenon. Conversely, when the focus position is near the front column, the wave energy is concentrated in its vicinity, amplifying the wave run-up phenomenon. With a larger period, the wave energy increases. Therefore, even with the focus position near the rear column, a notable wave run-up phenomenon is observed at the front column, reflected in a steeper evolution. However, for the rear column, due to the wave energy dissipation, even with a larger period, there won't be a significantly pronounced climbing phenomenon.

Figure 133 illustrates the wave run-up evolutions at 18 locations ($a_1 \sim a_3$, $b_1 \sim b_3$, $c_1 \sim c_3$, $d_1 \sim d_3$, $e_1 \sim e_3$, $f_1 \sim f_3$) for fixed four-squared-cylinder systems of each case with 45°. It can be observed that the wave run-up evolution follows a pattern similar to that observed at 0°.

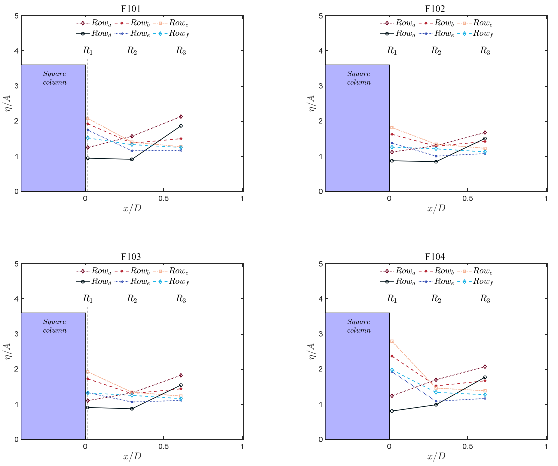

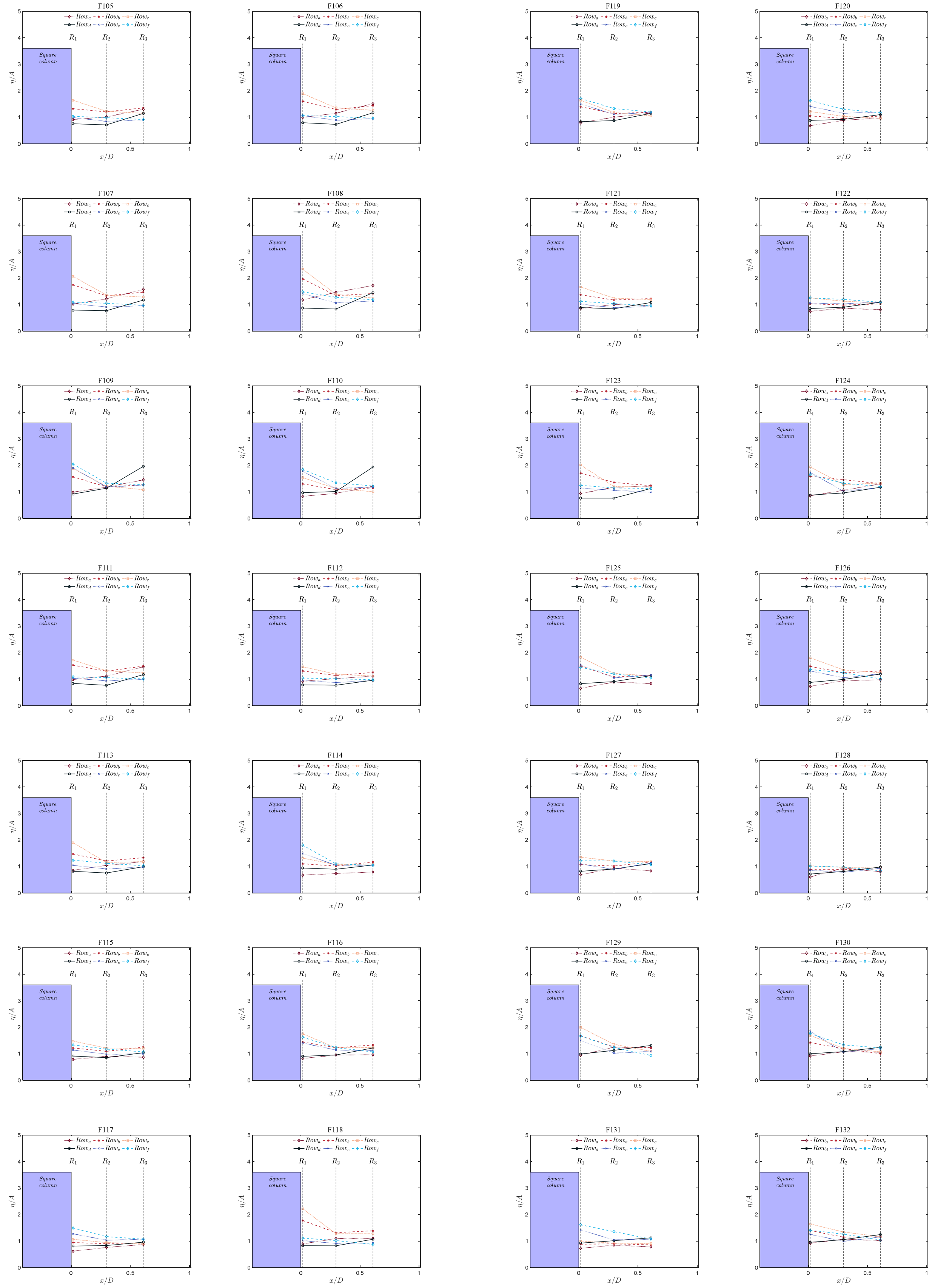
F105
F106
F119
F120
F107
F108
F121
F122
F109
F110
F123
F124
F111
F112
F125
F126
F113
F114
F127
F128
F115
F116
F129
F130
F117
F118
F131
F132
Row_a Row_b Row_c Row_d Row_e Row_f
R_1 R_2 R_3
Square column
η/A
x/D
0 0.5 1
0 1 2 3 4 5

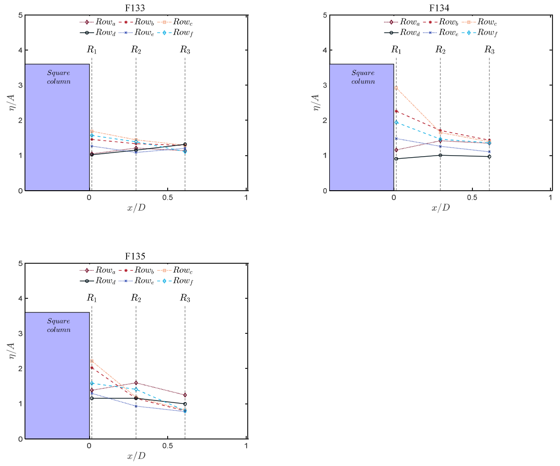

Figure 132: Wave run-up evolution in front of columns (heading 0°)

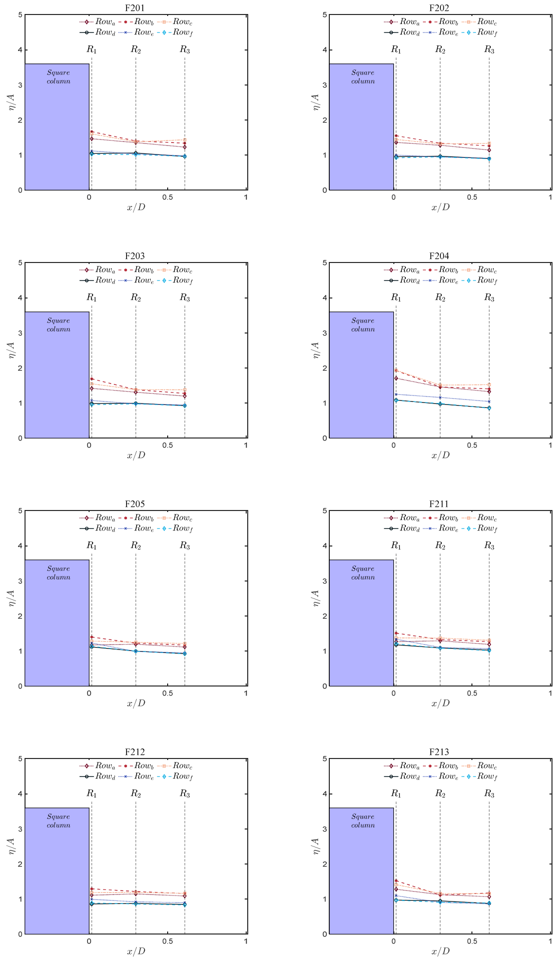

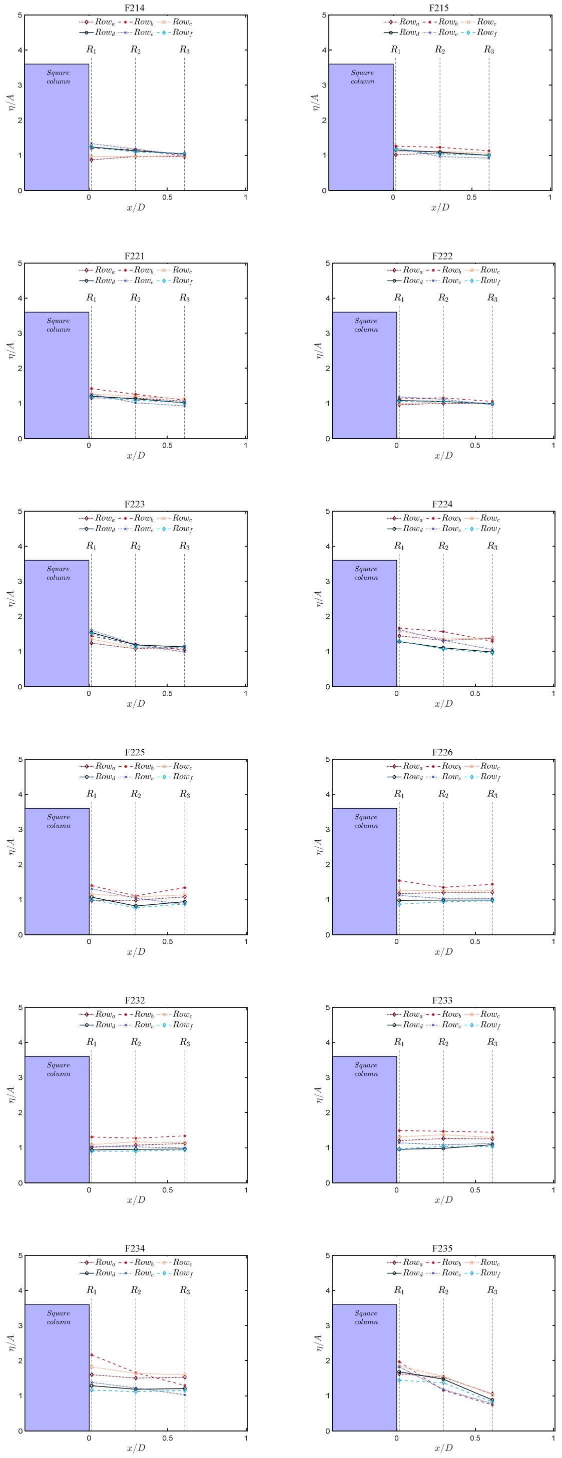

Figure 133: Wave run-up evolution in front of columns (heading 45°)

6.3 Wave Impact Pressures in Focused Waves

6.3.1 Load separation

Before load separation, the wavelet denoising method is employed to eliminate noise interference in the wave impact measurements. Figure 134 and Figure 135 present the denoise wave pressure P_{total} on fixed four-squared-cylinder systems, measured by the pressure sensor in case F101 and F201. P_{total} consists of quasi-static wave pressure P_{qs} and wave impact pressure P_{imp} in a wave impact event. Since this study aims to investigate local wave impact loads on the columns, it is crucial to separate the quasi-static component P_{qs} from the P_{total}.

A robust locally weighted LOESS smoother is applied to estimate the quasi-static wave pressure. The smoothing method is realized by local regression using weighted linear least squares and a second-degree polynomial model. The fitted data outside five mean absolute residuals are assigned zero weight in the procedure.

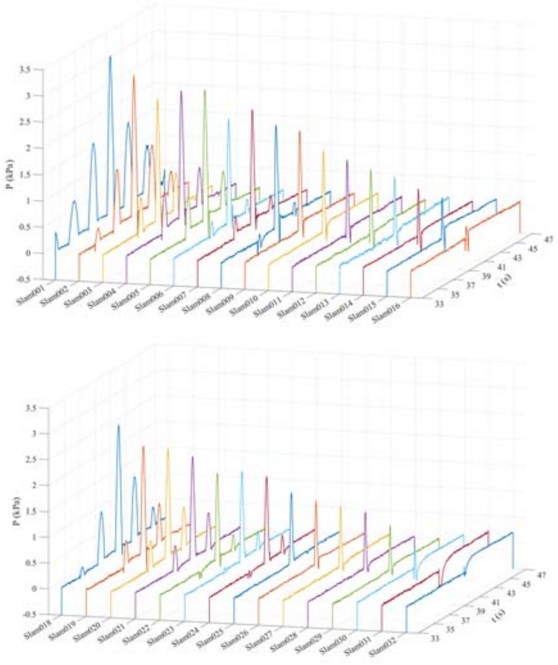

Figure 134: Wave pressure time histories for all pressure sensors for case F101

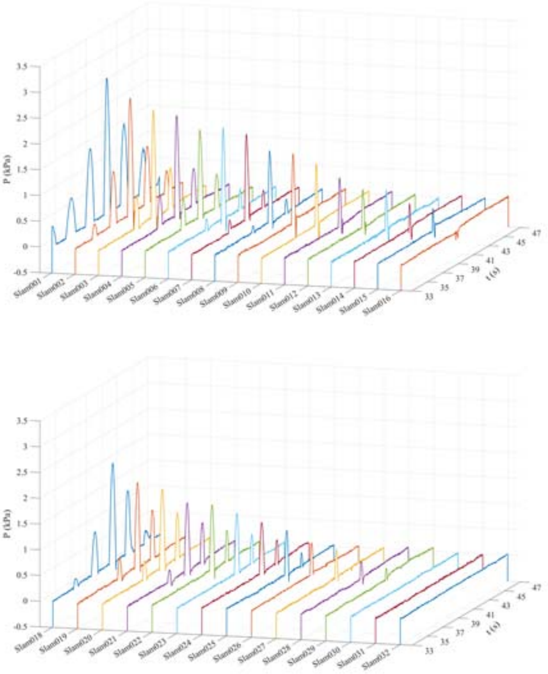

Figure 135: Wave pressure time histories for all pressure sensors for case F201

The wave impact pressure P_{imp} equals the total wave pressure minus the quasi-static part, as shown in Figure 136. The wave impact pressure increases rapidly with a strong nonlinearity. Then, the pressure decreases and a negative valley appears. This is because the entrapped air pocket occurs in wave impact, as illustrated in Figure 137. The air pocket, serving as a cushion between wave and structure during the impact, induces a negative pressure when the liquid separates from the structure's surface. In addition, the wave impact has a relatively long duration due to the air pocket.

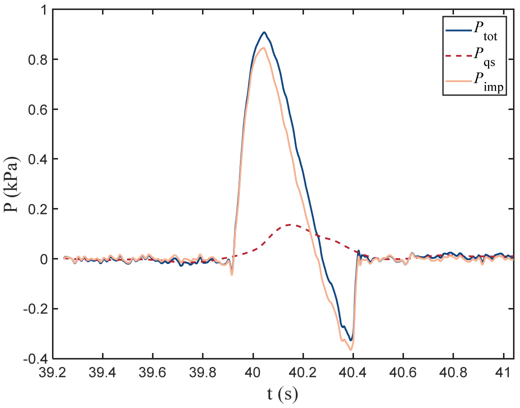

Figure 136: Example of the separation of different load components (Slam012 in case F103)

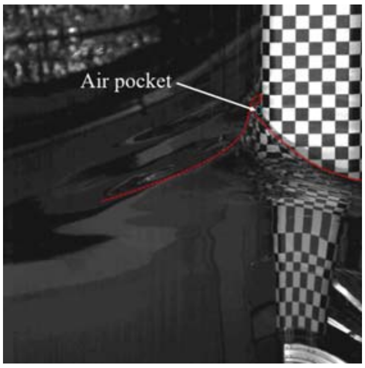

Figure 137: Snapshot of the wave impact instant on the front column for case F103 (the dashed red line denotes the incident wave profile)

6.3.2 Effects of wave periods

Figure 138 and Figure 139 display the spatial distribution of wave impact pressure peaks on the surface measurement points with different height (0~45 cm) at various wave periods with 0° and 45° wave direction, respectively. In the figure, 0 cm represents the still water level.

Figure 138 and Figure 139 illustrates that wave impact pressure increases first and then decreases with the height increasing. According to the nonlinear dispersion relation of waves, the wave height increases with an increase in the period for a given wave steepness. It is not difficult to understand that the wave impact pressure induced by focused waves tends to be distributed over a broader spatial range, as the wave period increases from 0.8 to 2.4 s. For the largest wave period ($T_p = 2.4$ s), the wave impact pressure is generally larger than that of the other focused waves, revealing that a large wave period remarkably increases the wave impact pressure.

In this subsection, the focus position was located at the front surface of the front column. Therefore, wave impact events are mainly dominated by the front column, called fore-column dominating wave impacts, in which the impact pressure of the rear column was notably lower than that of the front column, regardless of the variations in the incident wave period. In this study, the elementary loading processes (ELPs) primarily consisted of ELP2, which is the most common process used in engineering applications. ELP2 is characterised by the run-up (or downward) of the wave along the structure, inducing hydrodynamic loads due to the rapid upwelling jet parallel to the surface of the column, as depicted in Figure 140(a). After the wave passes through the front column, the partial energy of the wave dissipates because of the upwelling jet and wave breaking (Figure 140(b)), causing a lower wave run-up around the rear column. Consequently, the amplitude and spatial range of the impact pressure in the rear column were substantially smaller than those in the front column.

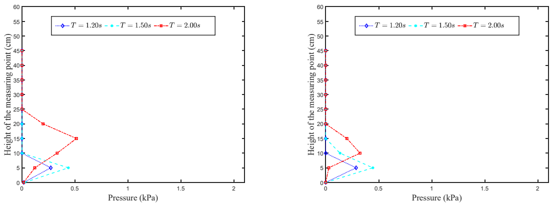

(a) H/λ=0.05, front column (b) H/λ=0.05, rear column

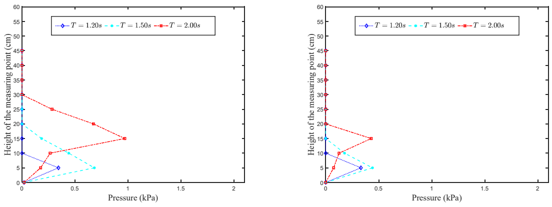

(c) H/λ=0.06, front column (d) H/λ=0.06, rear column

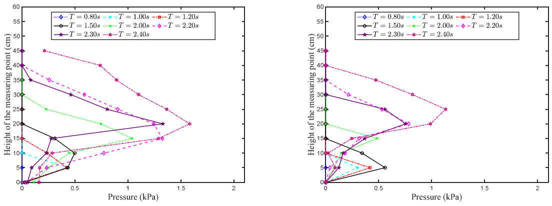

(e) H/λ=0.07, front column (f) H/λ=0.07, rear column

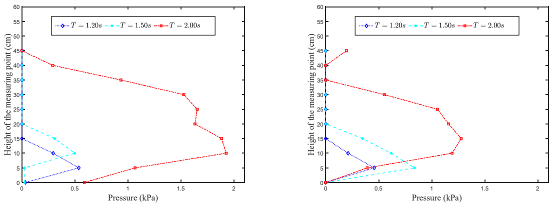

(g) H/λ=0.08, front column (h) H/λ=0.08, rear column

Figure 138: Spatial distributions of wave impact pressure at different wave periods (heading 0°)

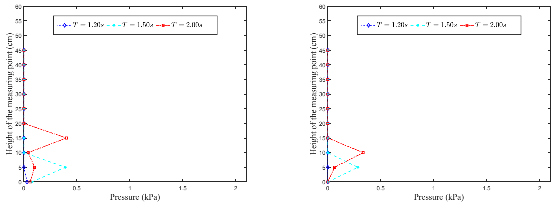

(a) *H/λ*=0.05, front column (b) *H/λ*=0.05, rear column

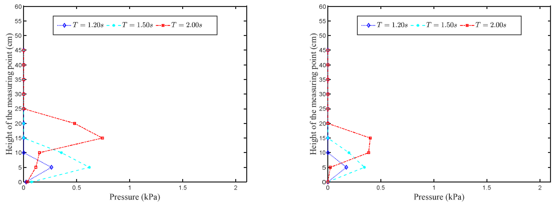

(c) *H/λ*=0.06, front column (d) *H/λ*=0.06, rear column

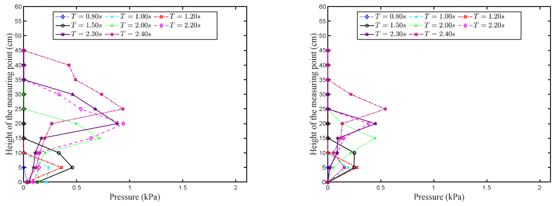

(e) *H/λ*=0.07, front column (f) *H/λ*=0.07, rear column

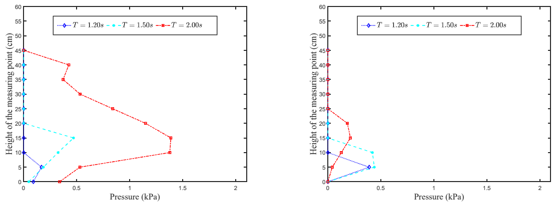

(g) *H/λ*=0.08, front column (h) *H/λ*=0.08, rear column

Figure 139: Spatial distributions of wave impact pressure at different wave periods (heading 45°)

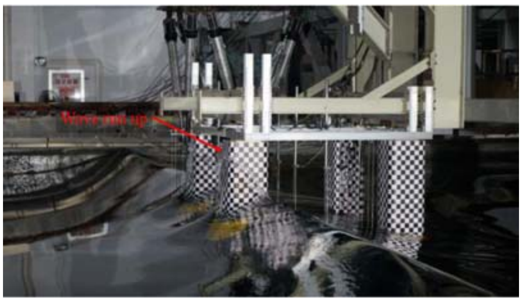

(a) Severe wave run-up in the front column

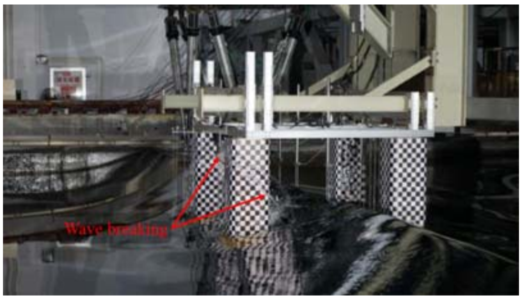

(b) Obvious wave breaking after passing through the front column

Figure 140: Wave propagation snapshots as the main crest acts on the front column

6.3.3 Effects of wave steepness

In addition to the spectral peak period, the wave pressure on the rounded-square column is significantly influenced by the shape of the incoming focused wave. Wave steepness is a key parameter for characterising the shape and stability of waves.

Figure 141 and Figure 142 present the spatial distribution of wave impact pressure peaks on the surface measurement points with different height (0~45 cm) at various wave steepness (0.05, 0.06, 0.07, 0.08, 0.09, 0.10) with 0° and 45° wave direction, respectively. Generally, the wave impact caused by large steepness wave (such as $H/\lambda = 0.10$) is more severe than that caused by small steepness wave. The volume of water impacting the column increased with the wave steepness in the wave-propagation direction, causing a greater transfer of kinetic energy to the column. Comparing Figure 141(a) with (c), it is evident that the steep wave with short wave periods can also induce large impact pressure, such as focused wave FW23 ($T = 1.20s,\ H/\lambda = 0.09$). This partially illustrates that the wave steepness has a considerable effect on the wave impact pressure spatial distribution.

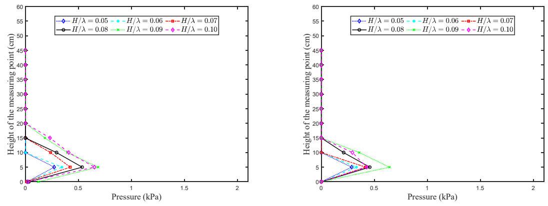

(a) *T*=1.20s, front column

(b) *T*=1.20s, rear column

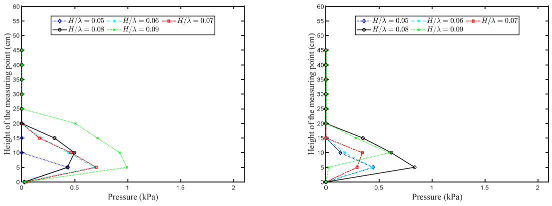

(c) *T*=1.50s, front column

(d) *T*=1.50s, rear column

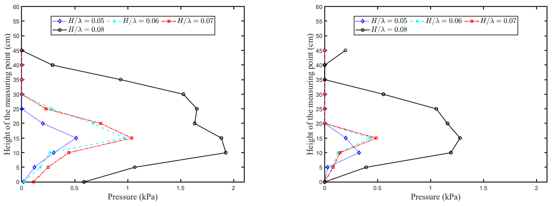

(e) *T*=2.00s, front column

(f) *T*=2.00s, rear column

Figure 141: Spatial distributions of wave impact pressure at different wave steepness (heading 0°)

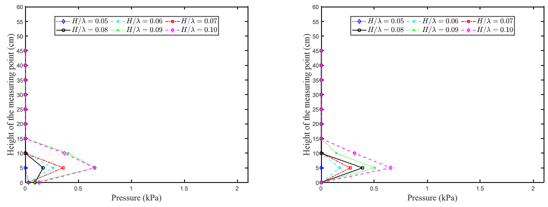

(a) *T*=1.20s, front column

(b) *T*=1.20s, rear column

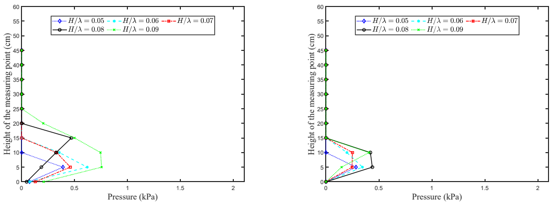

(c) *T*=1.50s, front column

(d) *T*=1.50s, rear column

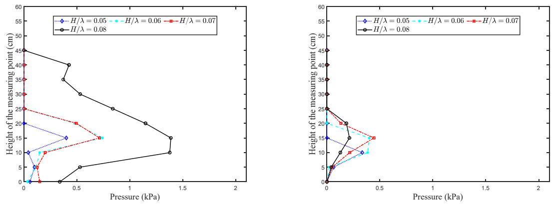

(e) *T*=2.00s, front column

(f) *T*=2.00s, rear column

Figure 142: Spatial distributions of wave impact pressure at different wave steepness (heading 45°)

6.3.4 Effects of focus positions

The focus position is a crucial parameter of the focused wave that directly affects the processes of waves impacting the structure by influencing the wave energy aggregation and wave run-up capacity.

Figure 143 shows the spatial distribution of wave impact pressure peaks on the surface measurement points with different height (0~45 cm) at various focus positions with 0° wave heading direction. The front column suffers the greatest impact when the focus position is located on the rear surface of the front column ($\Delta X = 0.32$ m), while in rear column when the focus position is set on the front surface of the rear column ($\Delta X = 1.36$ m). Combined with Figure 127(e) and (f), this result can be explained by the variations in the wave run-up height for different focus positions. For the front column, the maximum wave run-up ratio is observed in front column at focused waves with $\Delta X = 0.32$ m. Although the focus position is on the rear surface, the wave has already started to move upwards on the front surface and is forced to persistently run-up by the obstruction of the column, resulting in a notably greater run-up height compared with other focus positions. For the rear column, the wave run-up ratio reaches its maximum under the focused waves with $\Delta X = 1.36$ m . Due to the disturbance of front column, the wave run-up decreases markedly when the wave focus position is $\Delta X = 1.68$ m, smaller than the test for $\Delta X = 1.36$ m . This further demonstrates that the wave impact pressure is closely associated with the wave run-up along the structure, as mentioned in the previous section. Therefore, adding appropriate structures to suppress the wave run-up height is an effective method for mitigating the wave impact load on columns.

Previous studies have primarily focused on wave impact events with a focus position around the front column, and little research has been conducted on wave impact pressure with a focus position at the rear column. In this study, when the focus position was $\Delta X = 1.36$ m, the spatial distributions of peak pressure exhibit evident different features, especially at an impact position height of 35 cm. As illustrated in Figure 144, the total wave pressure is primarily composed of the impact pressure with a few quasi-static wave pressure. It is speculated that this instantaneous large impact was caused by accelerated water jets or wave amplification due to interference with the front and rear columns. The duration of this phenomenon was remarkably short, aligning with the typical characteristics of the impact induced by splashing.

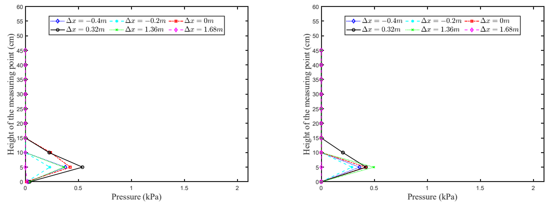

(a) *T*=1.20s, front column (b) *T*=1.20s, rear column

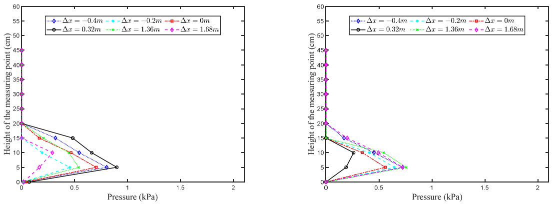

(c) *T*=1.50s, front column (d) *T*=1.50s, rear column

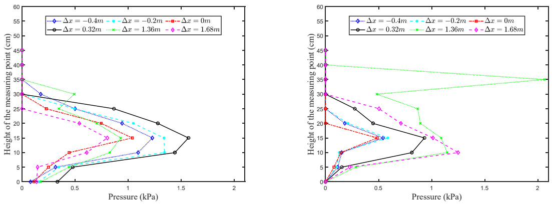

(e) *T*=2.00s, front column (f) *T*=2.00s, rear column

Figure 143: The spatial distribution of wave impact pressure peaks on the surface measurement points with different height at various focus positions (heading 0°, $H/\lambda = 0.07$)

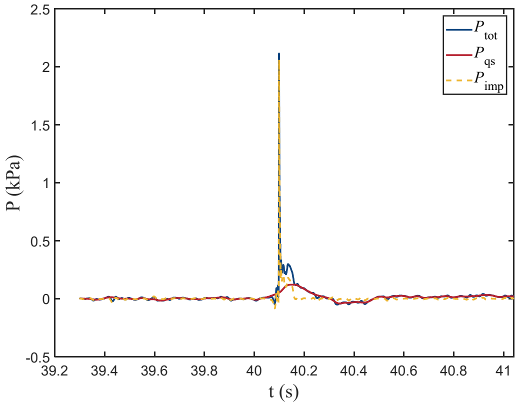

Figure 144: Wave pressure time histories for Slam030 (measuring point height: 35cm) for case F109

7. CFD BENCHMARK STUDY ON TWO-BODY INTERACTIONS IN CLOSE PROXIMITY

7.1 Literature Review on Recent Studies of Two-body Interactions

In decades, numerous studies were conducted to understand the interactions between two ships by experimental and numerical methods for various cases of ship-ship operating conditions. The studies could be classified into 4 sub-groups based on the operating conditions (Zhou et al., 2023), as shown in Figure 146. In this task, the literature on ship-ship interaction with rectangular boxes and the case of lightering, including the studies for simplified models in a static condition, were considered to focus on gap resonance, which means violent water column oscillations in the gap of the structures when incident wave frequency is close to the natural frequency of the oscillating fluid mass.

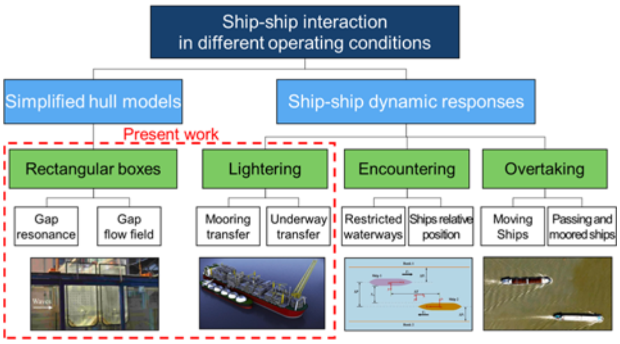

Figure 145. Classification of studies for two-body interactions

7.1.1 Experimental studies on two-body interactions

To be used as benchmark data for numerical methods, the experimental studies in early stages were conducted in 2-D with simplified structures. Tan et al. (2019) investigated the effect of the geometry of structures in gap resonance between the structures under regular wave conditions with suggestions of a modified potential flow model with a damping mechanism to estimate the phenomenon. The experimental results showed that the resonant amplitude and frequency could increase when the shape of the structure changed from sharp to round corners.

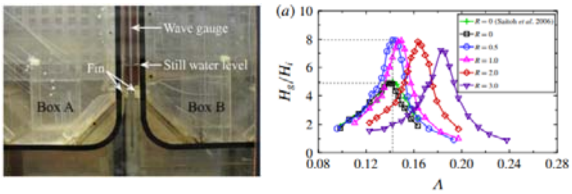

Figure 146: Experimental setup and results of Tan et al. (2019)

Ning et al. (2018) performed a series of experiments to study the gap resonance with various draft of the structures, showing that the wave frequency decreased with a higher draft for both structures, and the water height increased with the higher draft of the lee-side structure.

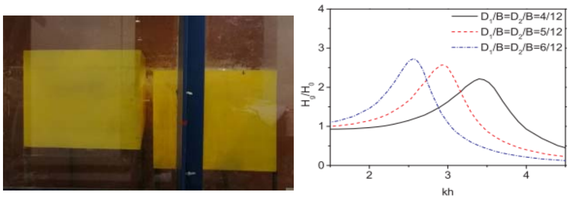

Figure 147: Experimental setup and results of Ning et al. (2018)

There also have been some 3-D experiments with ship-type structures. Xu et al. (2014) investigated the hydrodynamic performances of two identical structures to study the effect of gap distance. In the results, single and multi-peaks were observed at resonance and shorter periods, respectively, and some discrepancies were found in the resonance period between the cases of motion-limited and free structures.

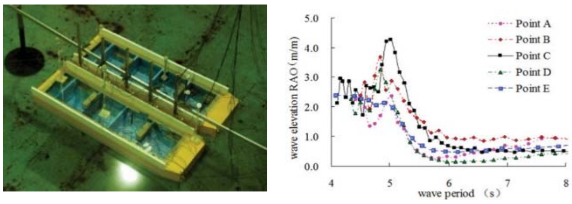

Figure 148: Experimental setup and Results of Xu et al. (2014)

Jin et al. (2018) studied the wave responses in the gap with structural interactions of FLNG and LNG varying those lateral spacings. The paper observed that the resonance happened when incident wave frequency approached to the natural frequency of the fluid between the two ships, and the reduction of the gap distance made greater exaggeration of the responses shifting to a higher frequency levels.

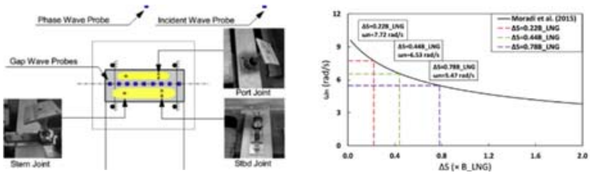

Figure 149: Experimental setup and results of Jin et al. (2018)

Zhao et al. (2018) performed a series of experiments on the two-body interactions in 3-D, measuring the resonance RAO in the gap, and showed that the RAO agreed well with a numerical model suggested by Molin et al. (2021) with a linear viscous damping results from Stokes oscillatory laminar boundary layers.

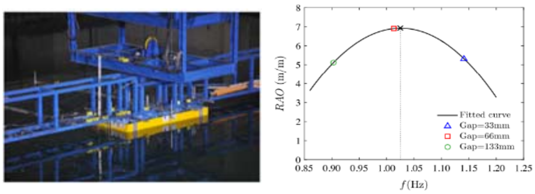

Figure 150: Experimental setup and results of Zhao et al. (2018)

Zhang et al. (2019) also conducted experiments to study the motions and wave field between the barges and showed that the barge motion and the wave elevation in the gap generally increased with the reduction of the gap distance.

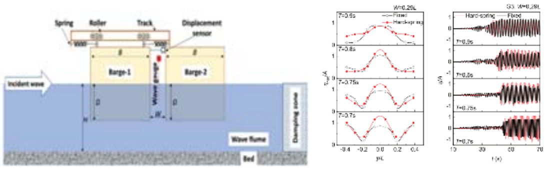

Figure 151: Experimental setup and results of Zhang et al. (2019)

Chua et al. (2018) performed a series of model tests for the two-body interactions to investigate the free surface response in the gap between two barges in irregular waves. The study was extended to study the effect of the structural bilge geometry (Chua et al., 2019) and cases with liquid sloshing effect (Liang et al., 2022).

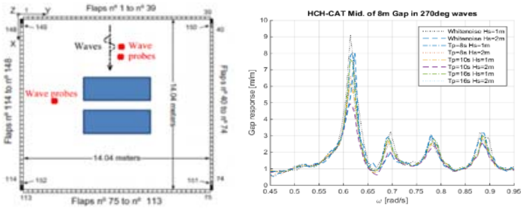

Figure 152: Experimental setup and results of Chua et al. (2018)

To provide experimental benchmark data f for the two-body interactions, a series of experiments have been carried out by ITTC 27th and 28th Ocean Engineering Committee in four phases below (Qiu et al., 2019),

- 1st phase: Model test with simplified identical ships in the towing tank of Memorial University (MUN), measuring wave elevations and motions for three different gaps between the structures (Zhou et al., 2015).

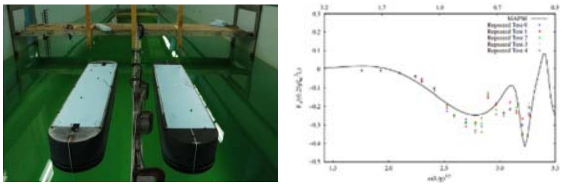

Figure 153: Experimental setup and results in MUN (Zhou et al., 2015)

- 2nd phase: Experiments in 1st phase were extended to measure drift forces, and the same experiments were conducted in the wave basin of Ecole Centrale de Nantes (ECN, 2016).

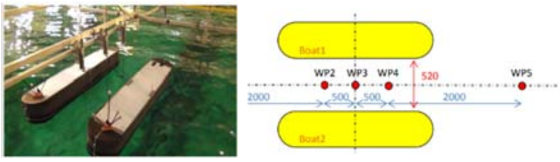

Figure 154: Experimental setup and results in ECN (ECN, 2016)

- 3rd phase: Same experiments were carried out in the wave basin of LabOceano at Rio de Janeiro, Brazil with the same models.

- 4th phase: Large models were tested in the wave basin of Ecole Centrale de Nantes to investigate the scale effect.

7.1.2 Numerical studies on two-body interactions

Due to the limitations and difficulties of experiments to implement and measure complex physical phenomena, many studies used numerical methods to investigate the two-body interactions. In the early days to study the phenomena, most of the numerical studies tried to simulate the two-body interaction using potential methods, which require relatively less computational load than CFD. However, the studies showed that the resonant RAO can be overestimated with the potential method due to its characteristics not to consider the viscous effect (Li and Zhang, 2016), most studies with potential methods focused to suggest an artificial resistance coefficient to simulate the two-body interaction with higher accuracy.

In recent, the CFD method is widely used to consider the viscous effect in the simulation of two-body interaction. For the simulations in 2-D, Moradi et al. (2016) simulated the two-body interaction using OpenFOAM to study the effect of the geometry on the resonant water height. The study investigated the grid dependency in the gap and showed that curved edges could make a significant increase in the resonant water height.

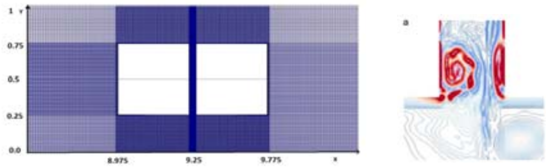

Figure 155: Simulation setup and results of Moradi et al. (2016)

Zhang et al. (2019) also simulated the phenomena using OpenFOAM and showed the best accuracy for the gap resonance water height with Laminar flow.

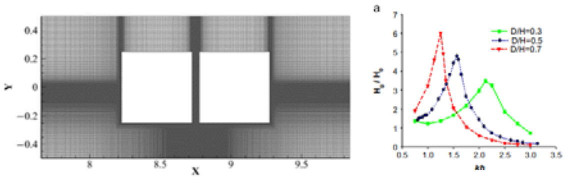

Figure 156: Experimental setup and results of Zhang et al. (2019)

In 3-D simulation study, Zhou et al. (2018) tried to apply artificial damping-lid methods in the simulation and showed that the incident wave directions have a significant influence on the phenomena, especially with the oblique wave because it made more violent motions of the structures.

Wang et al. (2019) also performed the simulation with OpenFOAM with a series of grid dependency tests and showed that the cell height for normal to wall in the gap is the most important parameter in the simulation of two-body interactions.

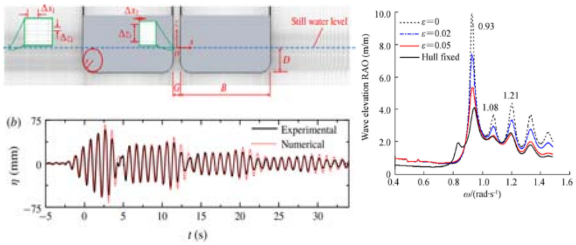

Figure 157: Experimental setup and results of Wang et al. (2019) and Zhou et al. (2018)

The two-body interaction is a phenomenon that is complex and can be affected by various parameters, such as incident wave period, height, and direction, gap distance, and properties of structures like mass, draft, motion characteristics, and so on. Numerous studies have been conducted to study the complex hydrodynamic features of the two-body interactions, but it still requires more studies to understand the physical characteristics of the phenomena. Especially, due to the limitations in experiments, the numerical methods seem more reasonable, using the CFD method to consider the viscous effect, and it is needed to study the parameters in the CFD simulations with those effects in the results for the two-body interactions.

7.2 Experiments to Validate the CFD Benchmark Study

To validate the CFD benchmark study on two-body interactions with focusing on gap surface elevation, the model tests of single barge and two identical rectangular barges were performed in the 2-D wave tank of Pusan National University.

7.2.1 Experiment of single-body motion

a. Experimental setup

The experiment was carried out for the motions of a rectangular barges ($C_M = 1$) in a 2-D wave tank. Table 7 shows the main dimensions of the barges and the wave tank. The soft spring system was designed so that the natural periods of the motions were not affected by the mooring system, especially for sway and roll motions. Free decay tests were performed in the conditions with and without the soft spring and natural period of the roll motion was recorded and checked and both conditions showing almost similar roll natural periods.

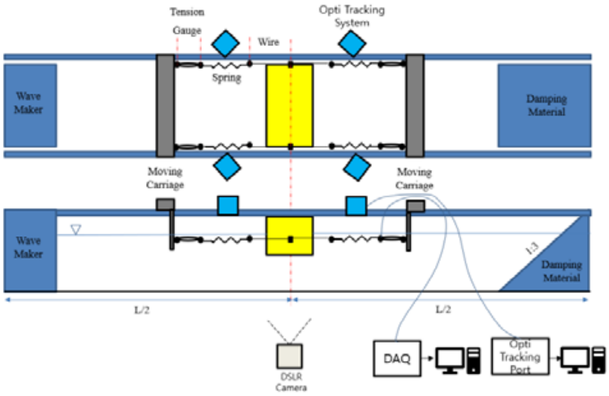

Figure 158: Experiment setup for single body motions

For motion measurements, the Opti-Track motion tracking system was used. The system was able to track the model motions in 6DOF. In this experiment, only sway, heave and roll were measured. The camera system was set up at 100 Hz sampling frequency. All the measurement systems and wave maker were synchronized.

Table 7: Main dimensions of the wave tank and models

Wave tank	Length	30 m
	Breath	0.6 m
	Depth	1.0 m
Barge	Length (L)	0.595 m
	Breath (B)	0.30 m
	Depth (D)	0.25 m
	Draft (T)	0.12 m
	VCG	0.08 m
	K_{xx}	0.35B
	T_{roll}	1.17 s
	T_{heave}	0.95 s

b. Experimental conditions

The incident wave periods are presented in Table 8, the wave height was kept as 1 cm. All the incoming waves are considered as linear wave cases.

Table 8. Incident wave conditions for single-body motions

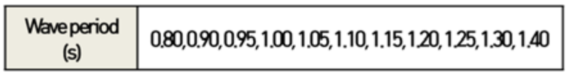

Wave period (s)	0.80,0.90,0.95,1.00,1.05,1.10,1.15,1.20,1.25,1.30,1.40

c. Experimental results

Figure 159 shows the time series of the roll free decay experiment.

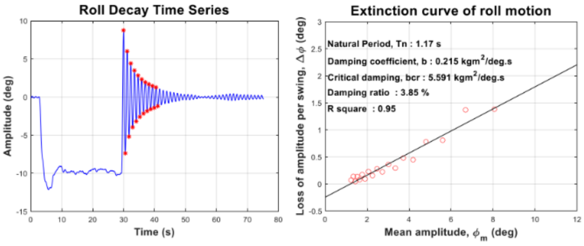

Figure 159: Time series of roll free decay test and the extinction curve

The motion response from experiment were compared with the first order motion response from linear hydrodynamic analysis with additional damping correction calculated by Ansys Aqwa software. The results show a good agreement between the measured motions and the numerical calculations.

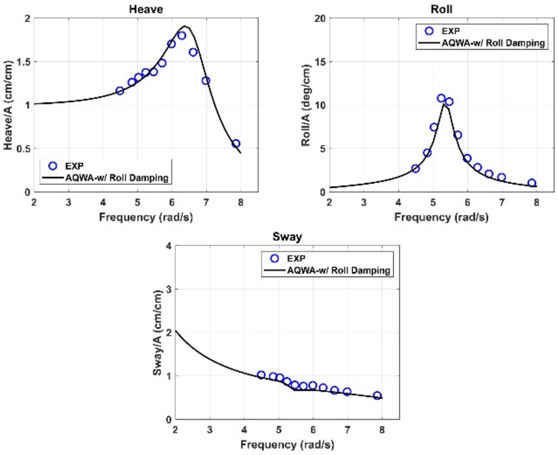

Figure 160: Motion responses of single body motion in regular waves.

7.2.2 Experiment of two-body interactions

a. Experimental setup

The experiment was carried out for the motions of two identical rectangular barges in the same 2-D wave tank in PNU. Each barge was moored by four soft mooring lines, which were connected to the VCG of the model. The stiffness of each spring is 1.0 N/m.

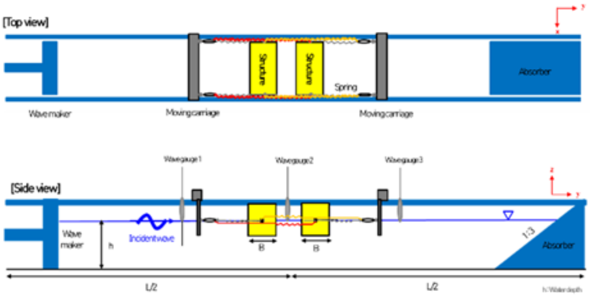

Figure 161: Experimental setup in 2-D wave tank

Three wave gauges were used to measure the wave elevations at upstream, downstream locations and at the gap with sampling frequency of 100 Hz. The Opti-Track motion tracking system was used to measure the motions of the barges.

7.2.3 Experimental conditions

The incident wave periods and frequencies are presented in Table 9, the wave height was kept as 2 cm. The experiment was performed in beam seas. To study the two-body interactions with small gap, the gap width was set at 7.0 cm (0.23B).

Table 9. Incident wave conditions for two-body motions

Condition No.	Wave period (s)	Wavelength (m)	Wave frequency (rad/s)
1	0.8	1.0	7.85
2	0.9	1.26	6.98
3	1.0	1.56	6.28
4	1.1	1.87	5.71
5	1.2	2.2	5.24
6	1.3	2.54	4.83
7	1.4	2.88	4.49

7.2.4 Experimental results

Figure 162 shows the motion RAOs of the two barges. In high frequency range (> 6 rad/s), the heave RAOs of barge 2 are larger than those of barge 1, the opposite observation is shown in low frequency range.

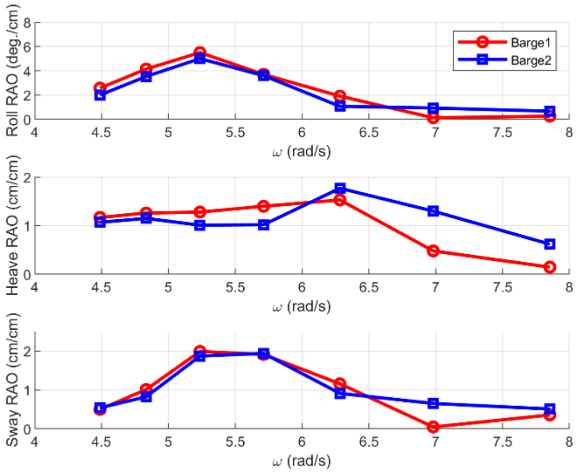

Figure 162: Motion RAOs of the two barges

Figure 163 presents the wave elevations measured at the gap (WG2). The time series of wave elevation reveals a stronger second-order effect for incident wave conditions with a period similar to the natural roll period of the barges (1.17 s).

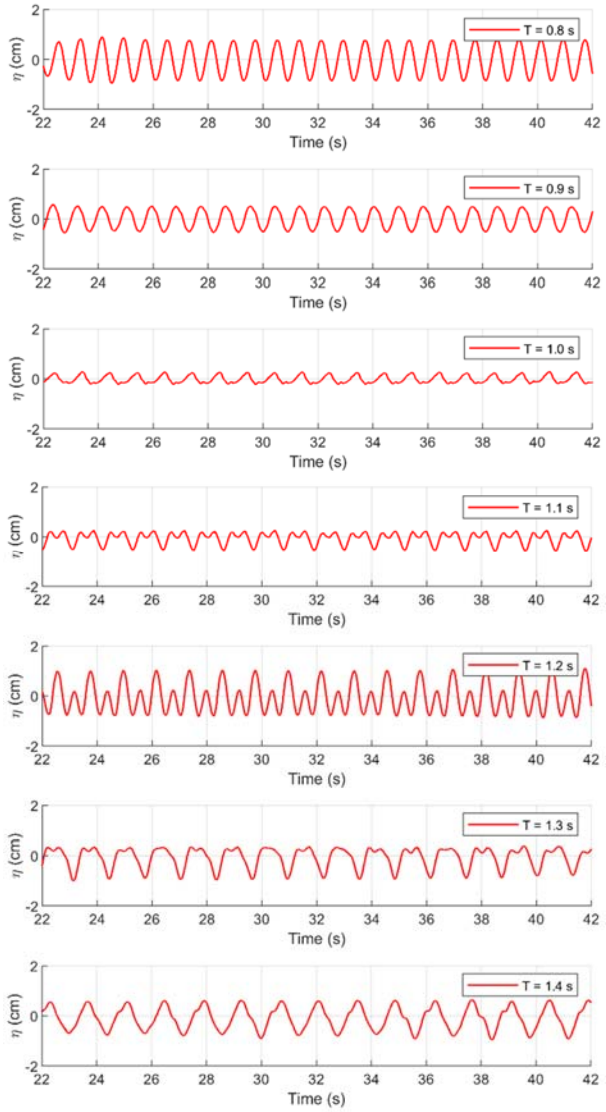

Figure 163: Wave elevation measured at WG2

The FFT results of the measured wave elevations at WG2 are shown in Figure 164. The second-order resonance occurs at the incident wave frequency similar to the roll natural frequency of the barge and the second-order effect reduces for small or high incident wave frequencies.

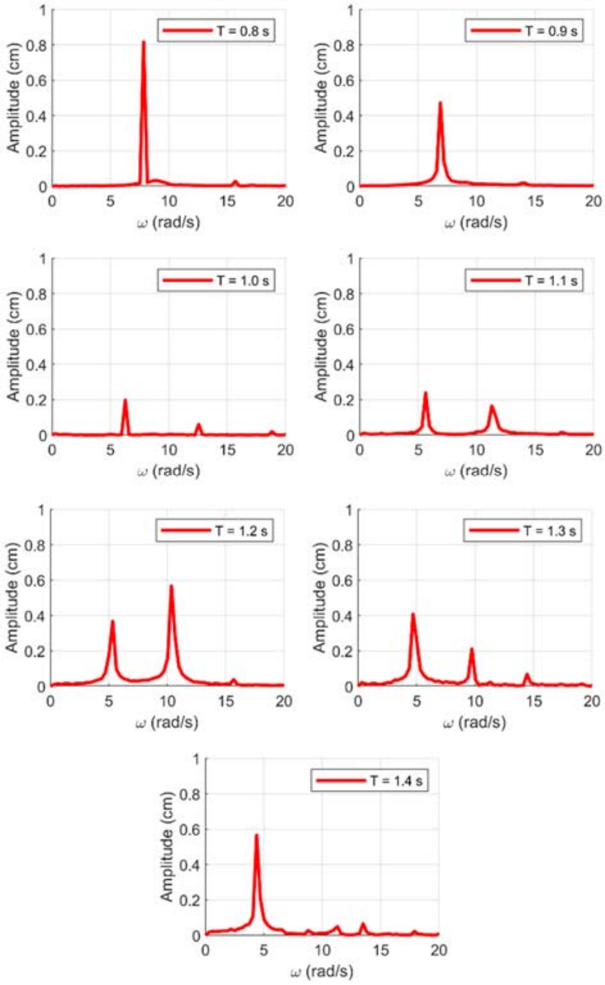

Figure 164: FFT results of the wave elevation measured at WG2

7.3 CFD Benchmark Study on Two-body Interactions

A test procedure was suggested for the CFD benchmark study on two-body interaction, with test parameters to be investigated in each step as shown in Figure 165. The procedure was set to include the whole parameters that may have influenced on the results, and each parameter were studied at each step with that dependency and uncertainty tests.

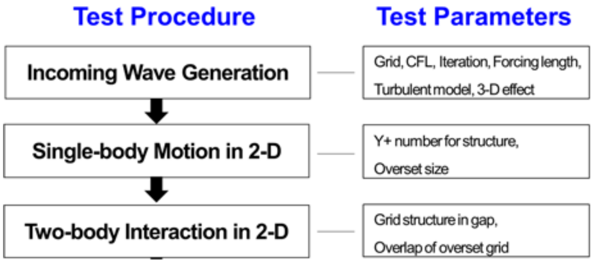

Figure 165: Test procedure and parameters to be studied for the CFD benchmark study on two-body interactions

7.3.1 Incoming wave generation (numerical wave tank setup)

As the first step, incoming wave generation, which is the main factor for the structure's motion, was conducted with the setup of the numerical wave tank. The test parameters to be studied and each number of cases are listed below,

- Grid and CFL condition (5 cases)
- Iteration number (5 cases)
- Wave reflection (5 cases for forcing length, 2 cases for w/ and w/o grid damping)
- Turbulent model (5 cases)
- 3-D effect (5 cases)

For the validation of the wave generation in the CFD simulation, the theoretical wave elevation and water particle velocity profiles were compared to simulate not only the wave shape but also the flow kinematics of the incoming wave.

7.3.2 single-body motion in 2-D

Uncertainty studies for single-body motion simulations were carried out in 2-D to investigate the parameters related to the structure's motion in CFD for the targets below,

- Implementation of viscous effect: Y+ number (5 cases for viscous sub-layer (1, 5), buffer layer (30), and outer layer (100, 200))
- Size of overset grid (5 cases)

The validation was performed with the experiments of single body motion as described in section 6.2, that provided the results of the free decay test, roll, heave and sway RAO under regular waves for a rectangular box in 2-D.

7.3.3 Two-body interaction in 2-D

The CFD will be performed in 2-D conditions, to study the feasibility of the methodologies for two-body motion analysis with less calculation loads than 3-D with investigation on the sensitivity of the wave elevation in the gap that is one of the main purposes of this study. The parameters to be studied in this step are listed below,

- Feasibility study of two-body overset grid system (for overlap of two overset grids).
- Grid system in the gap between two bodies.

In this study, the validation will be conducted with the experimental results of two body interactions mentioned in section 7.2.

7.4 Computational setup for simulation

In this study, commercial software of STAR-CCM+ was used to simulate the two-body interaction in CFD. The general numerical methods are listed below,

- Software: STAR-CCM+ V13.06
- Discretization scheme: Finite Volume Method (FVM)
- Density: Incompressible Flow
- Pressure and velocity field: Segregated SIMPLE method
- Unsteady: Unsteady with dynamic time step (based on CFL number)

Specific numerical schemes are followed below,

- Convection term: 2nd order Upwind
- Temporal term: 2nd order Euler implicit
- Conserved: Mass, momentum, kinetic energy
- Linearization: Newton

- Iterative: Direct matrix inversion
- Pre-conditioning/acceleration: Under relaxation

The simulation was performed using Intel Xeon E5-2690 with 212 processors with MPI paralleling method.

7.5 Simulation Results

7.5.1 Incoming wave generation

As the first step of the CFD benchmark study, a series of uncertainty tests were performed for an accurate simulation of incoming wave generation. Figure 166 shows the computational domain and mesh system for the uncertainty test of the incoming wave generation. The domain has a length of 14m in 2-D, and boundary conditions of velocity inlet for the inlet, top and bottom planes, respectively; the pressure outlet boundary condition was used for the outlet plane, and symmetry boundary conditions were applied for the side planes. The grid system was generated with hexahedral mesh in Cartesian coordinates. The $k-\omega$ STT turbulence model was used to perform the simulation.

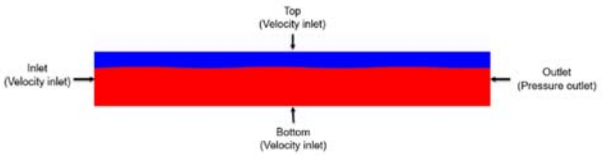

(a) Computational domain

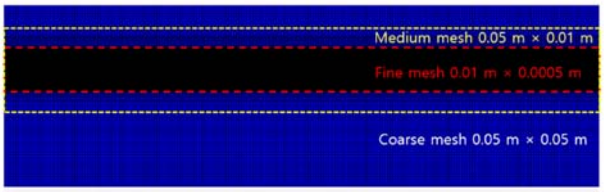

(b) Mesh system

Figure 166: Computational domain and mesh system for incoming wave generation

Figure 167 shows a good agreement between the measured and simulated wave elevations for the wave period of 1.2 s with 2.6% difference in wave height.

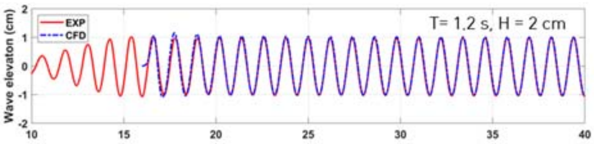

Figure 167: Comparison of the measured and simulated wave elevations

The uncertainty tests for the incoming wave generation were processed following the verification and validation methodology suggested by Stern et al. (2001) and ITTC (2007) for the parameters of the grid, CFL, number of iterations, wave reflection, and turbulent model to determine the proper value with an estimation of the error of the spatial and temporal discretization.

The uncertainty test requires at least three solutions, i.e., between medium-fine $\varepsilon_{i,21} = S_{i,2} - S_{i,1}$ and coarse-medium $\varepsilon_{i,32} = S_{i,3} - S_{i,2}$, to define the convergence ratio R_i as below,

$$R_i = \varepsilon_{i,21}/\varepsilon_{i,32}$$

Five solutions were used for higher accuracy of the uncertainty test. When the ratio was from 0 to 1, the uncertainty was obtained using the method of Richardson Extrapolation using below equations,

$$p_i = \frac{ln\left|\varepsilon_{i,32}/\varepsilon_{i,21}\right|}{ln(r_i)}$$

$$C = \frac{r_i^{p_i} - 1}{r_i^{p_{i,est}} - 1}$$

where p_i is the order of accuracy, C is correction factor, and r is the refinement ratio. Then, the uncertainty U) and corrected uncertainty (U_C) can be calculated using the equations below,

$$U_i = \left|C\frac{\varepsilon_{i,21}}{r_i^{p_i}-1}\right| + \left|(1-C)\frac{\varepsilon_{i,21}}{r_i^{p_i}-1}\right|$$

$$U_{i_C} = \left|(1 - C)\frac{\varepsilon_{i,21}}{r_i^{p_i} - 1}\right|$$

Table 10 and Table 11 show the simulation cases and uncertainty test results for the grid setup for the wave generation. The tests were performed with the refinement ratio of $\sqrt{2}$, and five cases were simulated from very coarse to very fine. The results of incoming wave height showed monotonic convergence for the coarse-medium-fine cases with an uncertainty of 0.005% as shown in Figure 168(a).

Table 10: Simulation cases for grid uncertainty test

	Very coarse	Coarse	Medium	Fine	Very fine
Cell length (m)	0.06	0.042426	0.03	0.021213	0.015
Cell height (m)	0.008	0.005657	0.004	0.002828	0.002
No. of cells in length	68	96	135	191	271
No. of cells in height	17	24	34	48	68
Result (Wave height, m)	0.13397	0.13429	0.13437	0.13449	0.13440

Table 11: Uncertainty test results for grid setup

Case	1-2-3	2-3-4	3-4-5	1-3-5
R (Convergence Ratio)	4.19	0.614	-1.31	13.3
P (Order of Accuracy)		1.41		
C (Correction Factor)		0.630		
U_G(Uncertainty)		0.012%	0.006	
$U_{G,C}$ (Corrected Uncertainty)		0.005%		

Table 12 and Table 13 show the simulation cases and uncertainty test results for the CFL number for the wave generation. The tests were performed with the refinement ratio of $\sqrt{2}$,, and five cases were simulated from 1.0 to 0.25. The results of incoming wave height showed monotonic convergence for the coarse-medium-fine cases with an uncertainty of 0.009% as shown in Figure 168(b).

Table 12: Simulation cases for CFL uncertainty test

	Very coarse	Coarse	Medium	Fine	Very fine
CFL Number	1.0	0.71	0.50	0.35	0.25
T/Δt	459	647	918	1312	1837
Result (Wave height, m)	0.13453	0.13441	0.13438	0.13433	0.13435

Table 13: Uncertainty test results for CFL number

Case	1-2-3	2-3-4	3-4-5	1-3-5
R (Convergence Ratio)	3.43	0.778	-2.25	6.20
P (Order of Accuracy)		0.725		
C (Correction Factor)		0.286		
U_G(Uncertainty)		0.001%	0.002	
$U_{G,C}$ (Corrected Uncertainty)		0.009%		

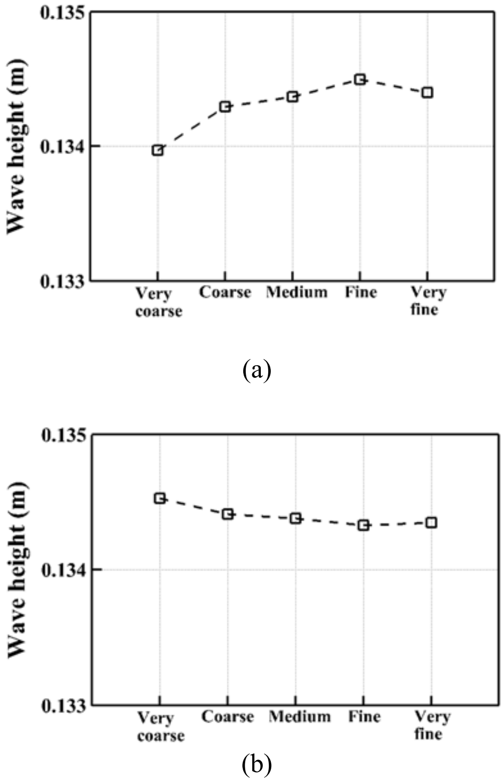

(a)

(b)

Figure 168: Uncertainty test results for various grid size (a) and CFL number (b)

In this study, the forcing method (Siemens, 2023) was applied to avoid wave reflection in the numerical wave tank. The forcing method is to damp the source term in the transport equation as below.

$$q_{\emptyset} = -\gamma\rho(\emptyset - \emptyset^{*})$$

where γ is the forcing coefficient,ρ is the fluid density, $\emptyset$ is the current solution of the transport, and $\emptyset^{*}$ is the value towards which the solution is forced. To determine the forcing lengths in the simulation domain, the reflection coefficients were calculated for various forcing length from 1 wavelength to 4 times of the wavelength with a refinement ratio of $\sqrt{2}$ as shown in Table 14. The reflection coefficient was obtained using the method suggested by Goda and Suzuki (1976) to estimate the incoming and reflected wave heights using two-point methods.

Table 14: Uncertainty test results for wave reflection

	Very short	Short	Medium	Long	Very long
Forcing Length	2.03	2.87	4.06	5.74	8.12
Result (Reflection Coff.)	7.26%	3.68%	1.47%	5.90%	Diverged

The results showed the lowest reflection coefficient of 1.47% when the forcing length was 4.06m, which corresponds to double of incoming wavelength.

The turbulent model for the wave generation was also tested with 5 different models as listed below,

- Laminar
- 1-equation model: Spalart-Allamas (SA)
- 2-equation model: $k-\varepsilon$, $k-\omega$
- 7-equation model: Reynolds Stress Model (RSM)

Figure 169 shows the comparison of incoming wave elevations for each turbulent model. The wave shapes were almost similar for all of the turbulent models, and the wave heights were also similar as shown in Figure 170. In this study, the turbulent model of $k-\omega$ was applied for the simulation considering the simulation of the structure's motion (Kim et al., 2020).

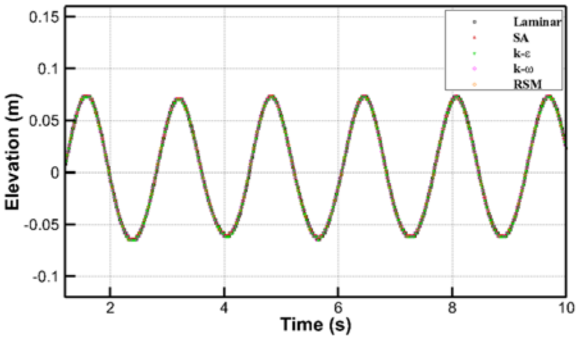

Figure 169: Comparison of wave elevation for various turbulent model

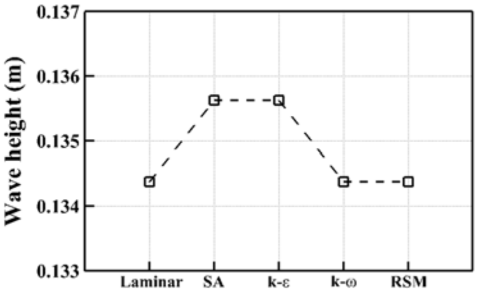

Figure 170: Comparison of wave height for various turbulent model

Figure 171 and Figure 172 show the final wave elevation and water particle velocity profiles in comparison with the theoretical value of Stokes' 3rd order wave theory. The wave elevation and water particle velocity profile agreed well with the theoretical values using the parameters determined by the uncertainty tests for the grid, CFL, iteration, wave reflection, and turbulent model.

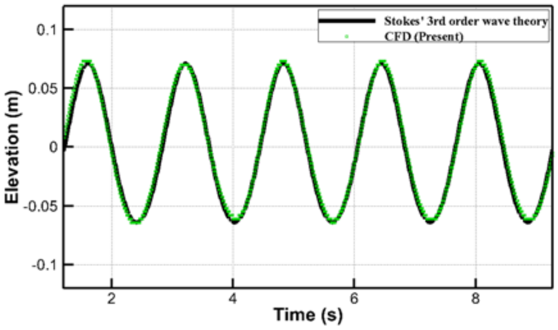

Figure 171: Wave elevation in comparison with theoretical results of Stokes' 3rd order wave theory

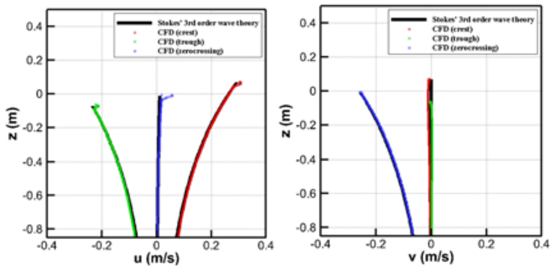

Figure 172: Water particle velocity profile in comparison with theoretical results of Stokes' 3rd order wave theory

7.5.2 Single-body motion in 2-D

In this section, single-body motions were performed for a simplified structure in 2-D to study the parameters related to the motions such as Y+ number, and size of the overset grid. A series of simulations was performed to simulate the experimental results described in section 7.2.

Figure 173 shows the mesh system to perform the single-body motion in waves. Here, the overset buffer, fine mesh and overset mesh had the same mesh size of 0.01 m × 0.0005 m, which was similar to the simulation setup for the incoming wave generation.

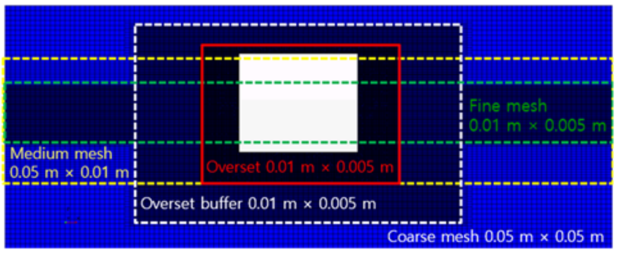

Figure 173: Mesh system for single-body motion simulations

The free roll decay simulations with initial angle of 5° and 10° were conducted to determine the proper size for the overset grid. Figure 174 compares the time histories of the free roll decay test. The numerical results agreed well with the experimental data.

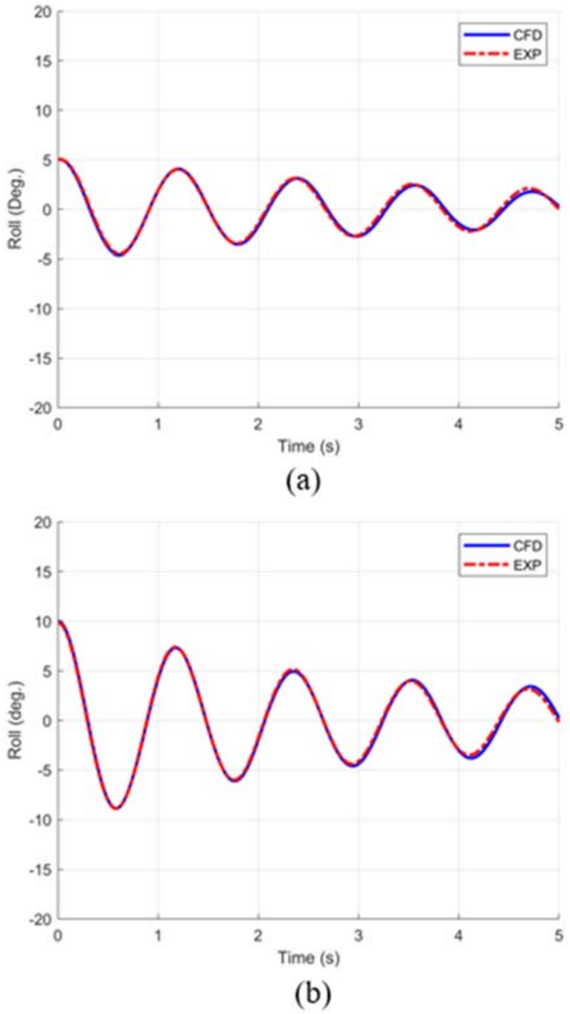

(a)

(b)

Figure 174: Time history of free decay test. (a) initial angle of 5°, (b) initial angle of 10°

The parametric study of the roll free decay will be performed to determine influence of the size for the overset grid. The size will vary from very small to very large with the refinement ratio of $\sqrt{2}$ and the results for the time history and extinction curve for the free decay tests will be included in the forthcoming report.

The single-body motions in waves, in which the same numerical setup to the free roll decay test was used, were simulated and compared to the experimental results and the numerical results obtained from AQWA.

Figure 175 shows the comparison of motion RAOs obtained by the experiments, AQWA and CFD calculations. The simulation results need refinement, particularly concerning the roll and heave natural periods. To improve the CFD results of single-body motions, the Y+ number, the initial condition values of turbulent model's parameters should be tested such as k and ω.

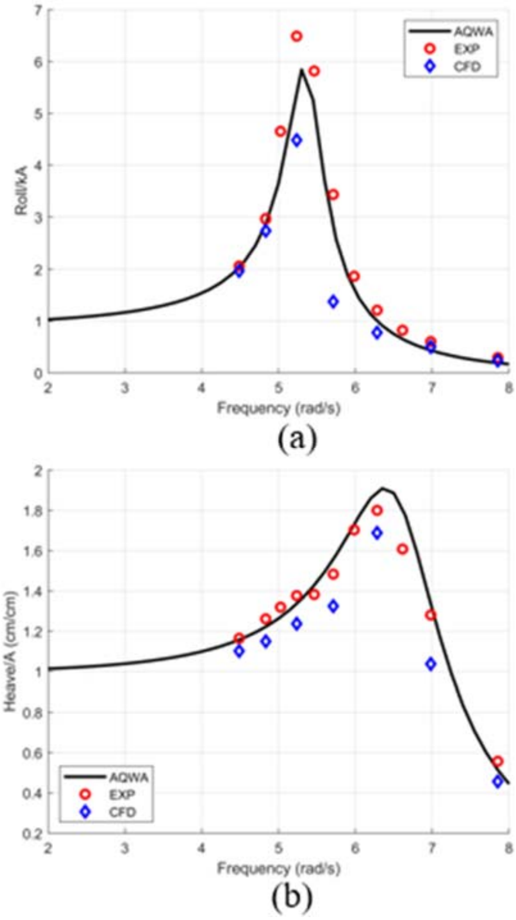

(a)

(b)

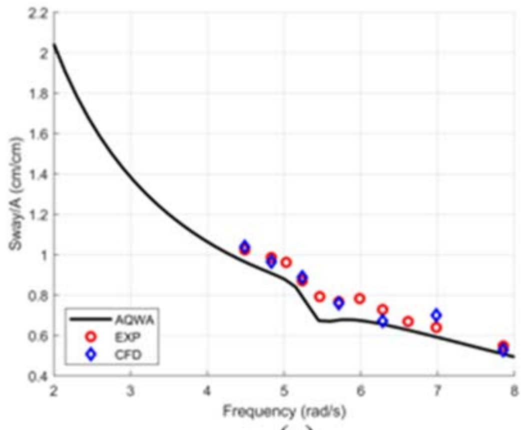

(c)

Figure 175: Comparison of motion RAOs between the experiments, AQWA and CFD calculations. (a) Roll RAO, (b) Heave RAO, (c) Sway RAO

7.5.3 Two-body motions in 2-D

In this section, the CFD simulations of two-body motions were performed for a simplified structure in 2-D to study the parameters related to the motions such as Y+ number, and size of the overset grid. A series of simulations was performed to simulate the experimental results described in section 7.2.

Figure 176 shows the mesh system used in the two-body motion simulations, in which the mesh sizes were similar to the simulations of single-body motions. The two-body motion subjected to the incident wave condition 5, whose period was equal to the roll natural period of the structures, was simulated and compared the experimental data.

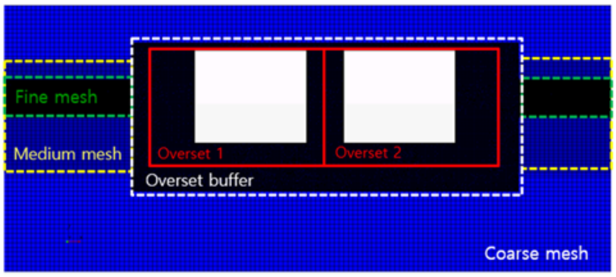

Figure 176: Mesh system for two-body motion simulations

Figure 177 compares the experimental and numerical results of the wave elevations observed at wave gauges (WG) 1 to 3. The wave elevations at WG1 and WG3 matches well with the experimental data, meanwhile the wave elevation at WG2 shows differences with the measured elevation.

Figure 178 compares the FFT results of the wave elevations observed at WG2. It is obvious that the second order component effect obtained by CFD is much smaller than that of the experiment.

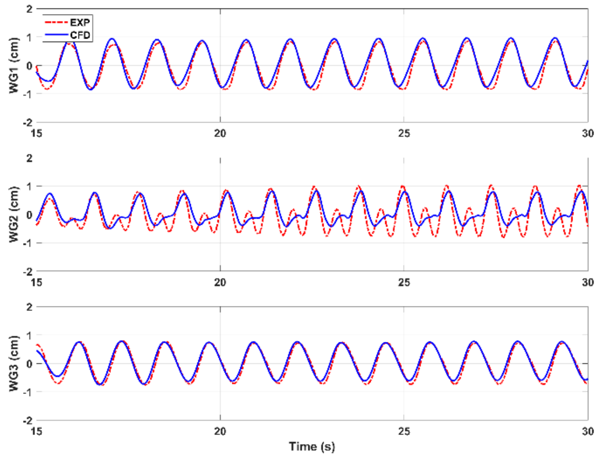

Figure 177: Wave elevations observed at WG1 - 3

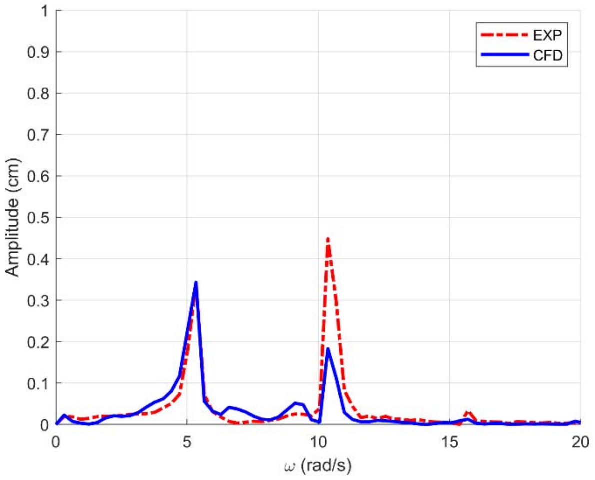

Figure 178: FFT results of the wave elevations observed at WG2

Figure 179 and Figure 180 show the time series of roll, heave motions of the barges obtained by experiment and CFD. The CFD result of the roll motion of barge 1 shows a good match with the experimental data, whereas the roll motion of barge 2 show a phase lag between the CFD and experimental results. The similar observations are seen at the results of heave motions.

The benchmark study on the simulations for the two-body interactions will be performed following the test procedures, and the results will be included in the report for the next term.

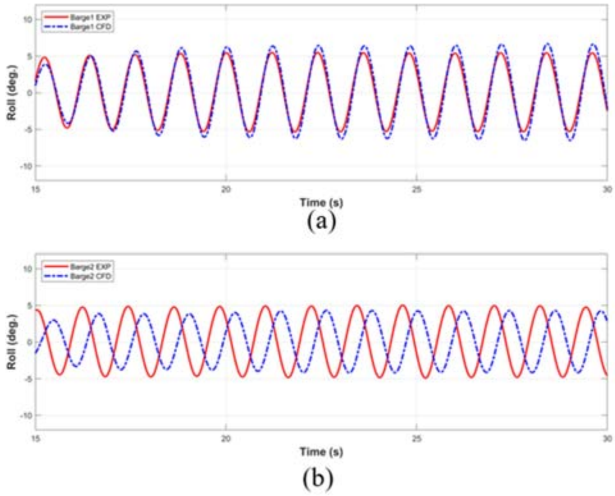

Figure 179: Time series of roll motions. (a) barge 1, (b) barge 2

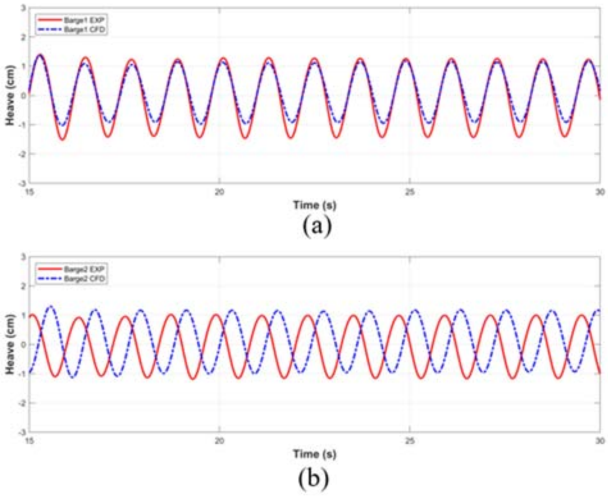

Figure 180: Time series of heave motions. (a) barge 1, (b) barge 2

8. EXTRACTION METHODS OF NODULES FROM THE SEABED

Deep-sea mining technology has been gradually developed since the 1960s to alleviate the contradiction between the supply and demand for land-based mineral resources (Simon-Lledó et al. (2019)). The most commonly used deep-sea mining system consists of the mother ship, hydraulic lifting pipe and seabed mining vehicle, which is proposed by OMI, as shown in Figure 181 (Hong et al. (2010)). Among the three parts, the seabed mining vehicle fulfills the function of extracting nodules from the seabed. At present, methods of nodule extraction mainly include mechanical, hydraulic and hybrid hydraulic-mechanical types.

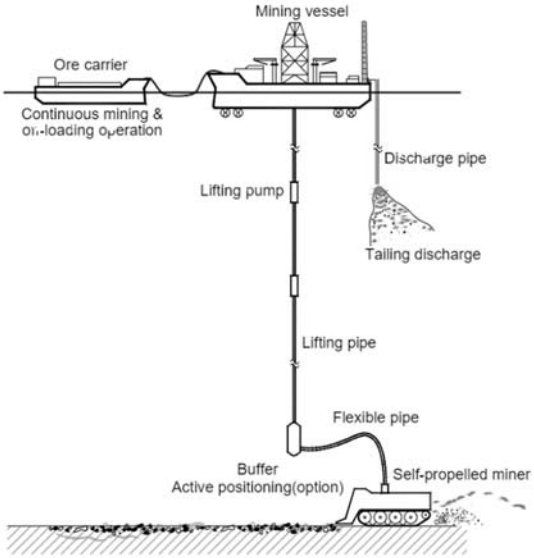

Figure 181: Typical deep-sea mining system (Hong et al. (2010))

The studies on nodule extraction methods are mainly focused on two aspects (Boetius et al. (2018)): (1) high collection efficiency, to collect as many nodules as possible with the same energy consumption, and (2) low environmental disturbance, to disturb and damage the seabed sediment and the native ecological environment as little as possible. Relevant scholars and institutions have conducted research on different nodule extraction methods using numerical calculations, model experiments and in situ experiments.

8.1 Mechanical Nodule Extraction Methods

Mechanical nodule extraction methods undercut the seabed with a rake-like front to dislocate the nodules, and then lift the nodules through a steep incline belt conveyor (Cho et al. (2019)). OMCO's nodule extraction facility used a rotary chain tooth structure to collect and transport nodules to the seafloor mining vehicle (Welling et al. (1981)). Combined comb shovels have been used in India to collect nodules from the seafloor and deliver them to a rotating chain plate during sea trials (Deepak et al. (2007)).

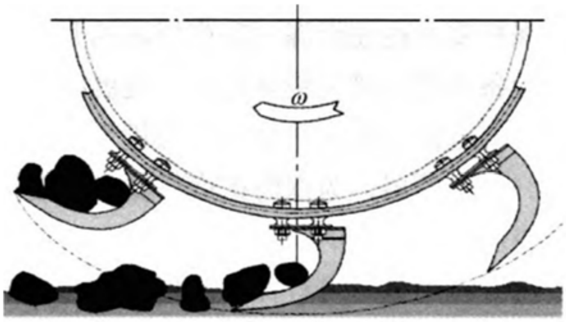

Figure 182: OMCO's nodule extraction facility (Welling et al. (1981))

The mechanical nodule collector developed by IKS is mounted on a cable to keep it at a certain distance from the ground (Handschuh et al. (2001)). The other end is connected to the lower conveyor drum shaft. The frame consists mainly of profiled metal plates assembled with a comb grid structure. The tooth-like front of the structure undercuts the seabed to allow for smooth displacement of the manganese nodules. In addition, a mechanically driven mobile comb structure moves through the gaps of the frame structure. In this way, the nodules are lifted and moved onto the belt conveyor. In order to clean the nodules before discharging them onto the conveyor belt, a vibrator is mounted on the basic frame. The two comb-like structures clean each other of sediment residue by relative motion. The nodules are then lifted from the picker or loader unit by the steeply inclined belt conveyor and conveyed to the crusher before entering the piston pump inlet.

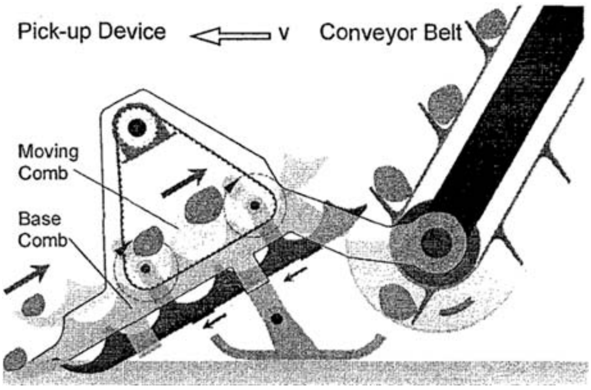

Figure 183: Concept of IKS's mechanical nodule collector (Handschuh et al. (2001))

However, the results of many experiments show that, although the collection efficiency of the mechanical nodule extraction methods is relatively high, the moving parts in the structure are easy to be damaged. The nodules are easy to be trapped in the moving parts, so the requirements of long-time and continuous work cannot be satisfied. Moreover, the mechanical method will dig up a large amount of sediment while extracting the nodules, which is more destructive to the environment. As a result, mechanical nodule extraction methods are less frequently used in existing sea trial equipment.

8.2 Hydraulic Nodule Extraction Methods

The hydraulic methods use water currents to separate and move nodules that are deposited on the surface of the seabed, and capture manganese nodules with hydrodynamic low-pressure action (Jia et al. (2022)). The mechanism is relatively simple and durable. However, due to the eddy current effect, the hydraulic methods have a lower collection efficiency and higher energy consumption compared to the mechanical methods. According to the characteristics of the flow field structure, the typical hydraulic nodule extraction methods can be divided into three types: suck-up-based method, Coandă-effect-based method, and double-jet hydraulic method.

8.2.1 Suck-up-based method

The principle of the suck-up-based method is similar to a vacuum cleaner, generally using axial vane pumps to absorb the nodules. The flow field formed by the suction current drives the nodules to move. In the OMA DEEPSEA MINER II sea trials in 1977-1978, the suck-up-based method collected about 500 tons of nodules continuously in a single day, basically achieving the expected collection results. The performance was generally acceptable in terms of reliability, but it was also found to have high energy consumption and low hydraulic efficiency (Kaufman et al. (1985)).

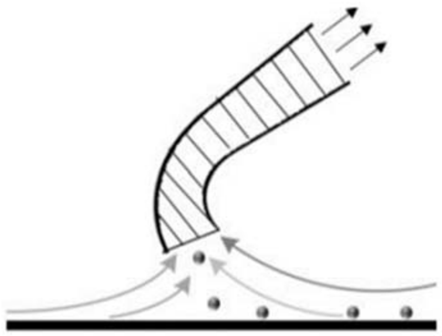

Figure 184: Principle of the suck-up-based method (Kaufman et al. (1985))

Xiong et al. (2018) abstracted the physical model of the flow of spheres inside a vertical pipe from the suck-up-based method. A numerical model of solid-liquid two-phase flow with a large particle was established based on the coupled Resolved CFD-DEM method, and the effect of particle size on its motion characteristics and flow field structure inside the pipe was investigated. The force analysis of single spherical particles in the fluid provided the equations of motion of the particles and revealed the relationship of each parameter in the equations. The results showed that the flow field velocity is large in the middle of the vertical pipe and small near the pipe wall, and both the settling velocity and floating velocity of the particles increased with the increase of particle size.

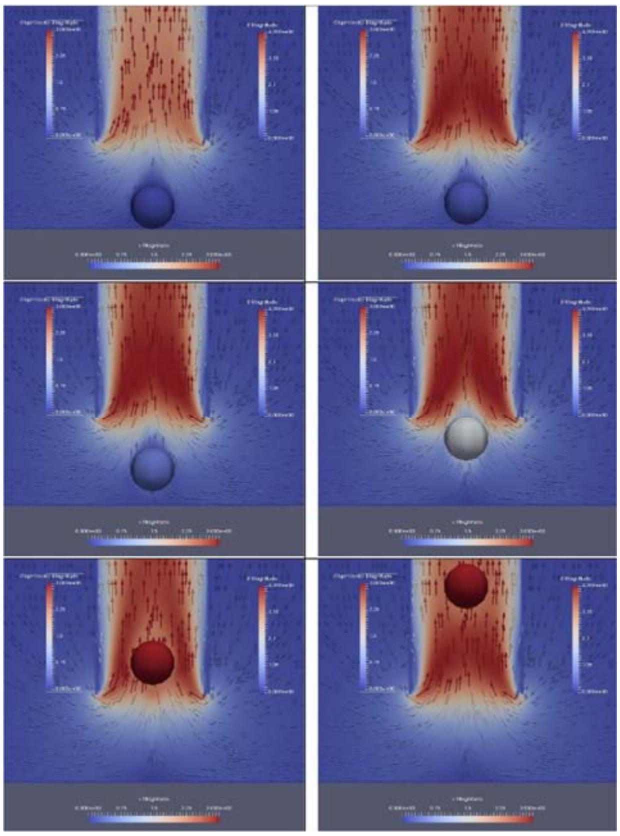

Figure 185: Numerical simulation diagram by Xiong et al. (2018)

Zhao et al. (2018) set up a model test system and tested 253 cases, and established an empirical model for the prediction of collection performance by studying the vertical force characteristics and vertical initial motion characteristics of the particles in the suction flow field. The study revealed the effects of the parameters of the particle size, round tube size, and height of the collector head off the bottom on the vertical force characteristics and vertical initial motion characteristics of the particles. The results showed that the vertical suction force coefficient decreases exponentially with the ratio of bottom clearance to the diameter of the particle, increases linearly with the ratio of the diameter of the suction pipe to the diameter of the particle, and is almost unaffected by the Reynolds number (Re). In addition, a new experimental phenomenon in which the vortex could help strengthen the suction force was observed.

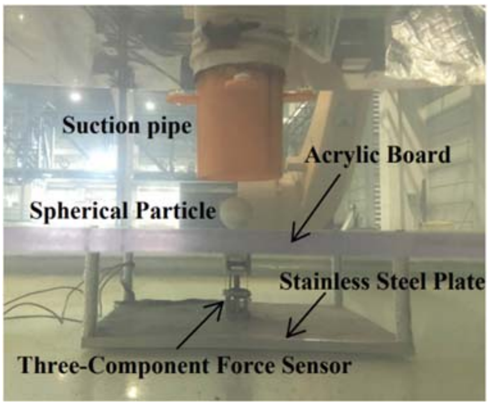

Figure 186: The experimental system by Zhao et al. (2018)

Based on the principle that the vertical axis vortex can induce particle initiation, Zhao et al. (2021) proposed a new concept of using spiral flow to collect nodules. Five types of tests (fixed suction, moving suction, suction flow field, sediment-water mixture, and vertical incipient motion tests) were conducted to investigate the similarities and differences in the collection performance of pick-up devices with and without spiral deflectors. In addition, the study measured velocity vectors and velocity distributions using the particle image velocimetry (PIV) system to reveal suction flow field characteristics. The results proved that the pick-up device using the spiral flow principle can realize enhanced suction forces on the nodules, an increased *h*' for a certain *v*, as well as a significantly increased occurrence probability of the circular motion of nodules.

Furthermore, Liu et al. (2023) designed a new type of sucker-shaped hydraulic nodule pick-up device equipped with four tangential jet nozzles. The study investigated the characteristics of flow field velocity distribution, the nodule initiation trajectory and collection rate under three different collecting flow models of low, medium, and high swirling strength. The results showed that the nodules are affected by the vertical axis vortex, which produces an obvious circular motion when moving vertically in the high swirling strength, and are lifted near the center region of the collecting head. When the nodule collection rate exceeds 90%, the necessity of collecting flow reduces as the swirling strength rises.

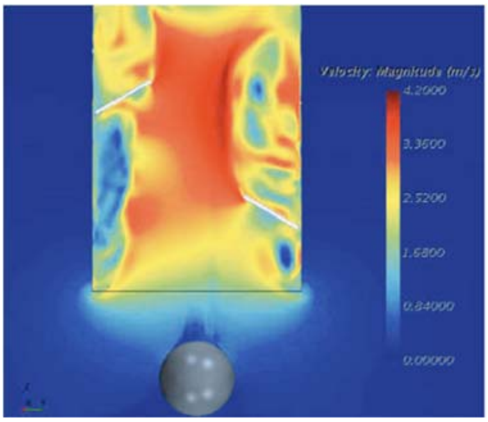

Figure 187: Velocity distribution in spiral flow (Zhao et al. (2021))

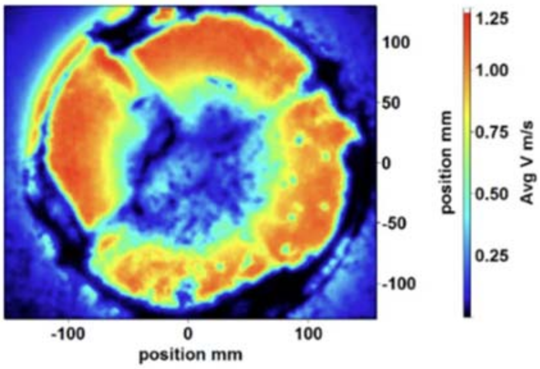

Figure 188: Numerical simulation diagram by Liu et al. (2023)

8.2.2 Coandă-effect-based method

The Coandă-effect-based method creates a flow structure with low pressure near the wall and high pressure at the far wall. The nodules are lifted by the vertical pressure difference. In 1997, the manganese nodule collection test in Japan verified that the collection efficiency of the attached-wall jet technology could reach a maximum of 87% (Yamada et al. (1998)).

Rodman et al. (1989) simulated two-dimensional straight and curved wall jet flows by axial jetting on a cylinder, and showed that integral momentum analysis was able to accurately predict the effect of curvature on the mean flow in both two-dimensional and annular attached-wall jets, and that the transverse curvature of the upstream portion of the jet had a smaller effect on the mean flow and the turbulent shear stress.

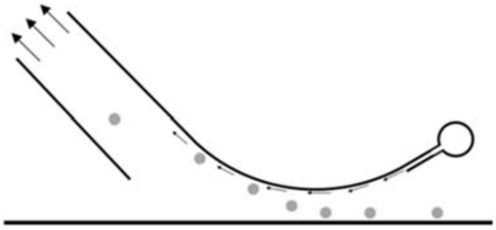

Figure 189: Principle of the Coandă-effect-based method (Kim et al. (2019))

Lim et al. (2015) investigated the distribution of flow velocity and streamlines and the change of turbulent kinetic energy in the flow field during the operation of the collector by numerical calculation.

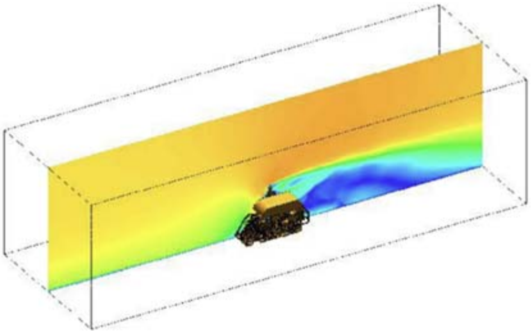

Figure 190: Velocity distribution in numerical simulation by Lim et al. (2015)

The results showed that the operation flow rate and the behavior of polymetallic nodules would largely affect the characteristics of the flow field of the attached-wall jet. The outflow discharge effect reaches to about 2~3 times of the collecting device in the back while the front flow field of the device was slightly affected by the outflow discharge, and the degree of influence is also dependent on the travel speed of the collector. Additionally, averaged turbulent kinetic energy is up to 7.5 times higher than that of other areas where flow is not influenced by the device while its variation in vertical and side directions is rather limited near the collecting device.

Lee et al. (2012) synthesized numerical simulations and physical experiments to study the collection effect of the Coandă-effect-based method, and proposed an optimized design for the mining machine using the multidisciplinary design optimization (MDO) method. Cho et al. (2019) simulated the collection process of nodules through model experiments, and designed optimization of the deep-seabed pilot miner system with coupled relations between constraints. The study considered the influence of variables such as nozzle structure, collector plate radius, and flow rate on the collection effect, and investigated the coupling relationship among the sub-systems. The total power consumption of the collector after the final optimized design was reduced by about 14.1% compared with that of a general collector.

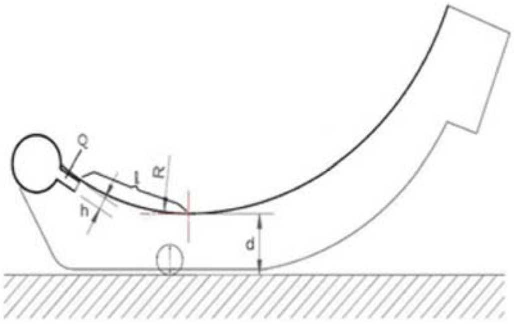

Figure 191: Design variables of collector part of pilot mining robot system by Cho et al. (2019)

Jia et al. (2023) carried out a simplified model of jets on the surface of a logarithmic spiral, and studied the lift ability of the reduced form of a Coandă-effect-based collector model. It is found that the Coandă effect on the logarithmic spiral becomes stronger with higher jet exit velocity, larger local curvature, and non-dimensional jet slot height. The growth rate, which represents the width of the main jet flow, went up in proportion to the downstream distance. The lift capability of jet flow in a logarithmical spiral of $x/R = 1$ is significantly better than that of $x/R = 2/3$.

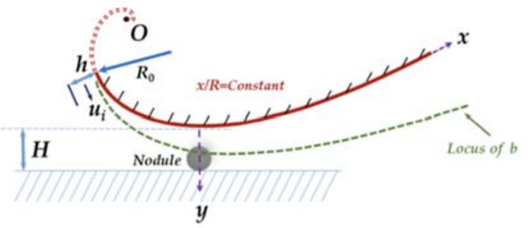

Figure 192: Schematic diagram of a turbulent jet flow over logarithmic spiral wall surface by Jia et al. (2023)

8.2.3 Double-jet hydraulic method

The double-jet hydraulic method uses two rows of opposite nozzles to spray water jets diagonally to the seabed. Water jets intersecting in the intermediate area lift the surrounding nodules into the conveying tube. The OMI sea trials in 1978 used high-pressure water jets to blow nodules up from the seafloor and collect them on the mining vehicle (McFarlane et al. (2008)). The results demonstrated that the hydraulic extraction method had a higher collection efficiency compared to the mechanical method.

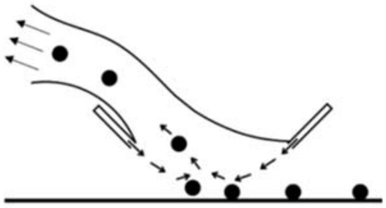

Figure 193: Principle of the double-jet hydraulic method (Handschuh et al. (2001))

Hong et al. (1999) built a double-jet hydraulic nodule extractor consisting of jet pipes and baffles and carried out experiments in a two-dimensional flume. The effects of parameters such as the jet flow rate, the moving speed of the collecting head, the bottom clearance, and the position and shape of the baffles on the collection rate of the collecting head and the fluctuation of the bottom pressure were investigated, and the relationship between the characteristics of the bottom pressure distribution and the pick-up efficiency was revealed. The results showed that the most dominant factor governing the pick-up performance is the water-jet power. To increase the water-jet's power required enormous energy supply, whereas a good design of baffle plates saved costs with the operation. In addition, the function of the rear water jets was predominant, so enforcement of the rear water-jet by using larger nozzles can improve the pick-up performance at high tow speeds.

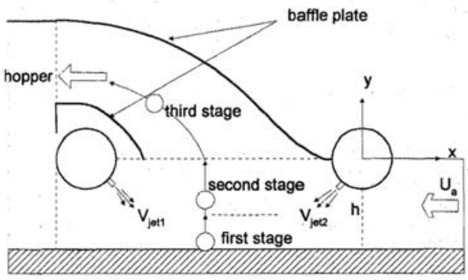

Figure 194: Schematic illustration of nodule lifting process (Hong et al. (1999))

Yang et al. (2003) studied the influence of the shape, size, and mutual position of the baffleplates, jet angle and size of the conveying pipe on the collection effect and power consumption of the double-jet hydraulic method. The results showed that the distance between two rows of the jets should be between 500 and 550 mm, and it will be the best nodules' catching for the heights of two rows of the jets to vary between 90 and 190mm. Additionally, when the distance between the upper and lower walls of the conveying pipe is about 1.3-1.5 times the maximum diameter of the nodule particles, the collection rate of polymetallic nodules is most effective.

Liu et al. (2023) studied the three-dimensional flow structure near the double-jet hydraulic collector based on numerical simulation, and analyzed the effects of jet flow speed and nodule size on the local flow field, bed shear stress and nodule collecting energy efficiency. The results showed that the bed shear stress increased rapidly from the hysteresis point to the inner side and reached the maximum value near the middle of the two hysteresis points. The maximum bed shear stress increased linearly with the increase of the jet flow speed.

The maximum bed shear stress increased by 197.93% when the jet flow speed increased from 6 m/s to 11 m/s. The effective area of incipient motion of nodules and collecting energy efficiency decreased with the increase of nodule diameter, and the nodules of smaller size were easier to be stripped and initiated. In addition, the effective area increased exponentially with the increase in jet flow speed. considering the combined influence on both the collecting productivity and the energy efficiency, it is recommended that the flow rate of the collector head jet should be 8-9 m/s.

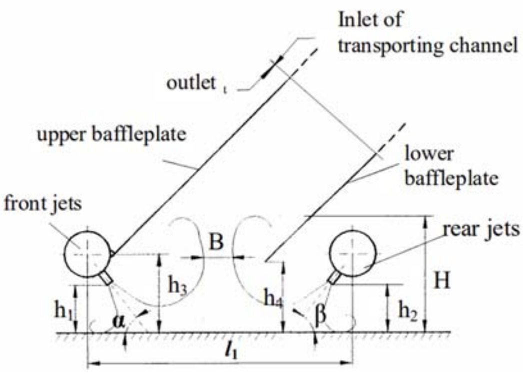

Figure 195: Mechanism of capturing of pick-up device by Yang et al. (2003)

Some scholars have also conducted a comprehensive comparative study of the above three hydraulic nodule extraction methods. Yue et al. (2021) used numerical simulation to compare these three hydraulic methods in terms of both nodule collection performance and the degree of environmental disturbance, and investigated the effects of flow rate and tow speed on collection rate. The suck-up-based method was found to have the smallest flow field disturbance and require the largest flow rate under the same operating conditions. The double-jet hydraulic method has a significant advantage in terms of collection rate, but has large seafloor disturbances. The Coandă-effect-based method is able to maintain a high collection rate while reducing the disturbance to the sediment, and has greater research value and development prospects.

8.3 Hybrid Hydraulic-Mechanical Methods

The hybrid hydraulic-mechanical pick-up device generally uses a pair of water jets to lift the nodules. These nodules are moved through a baffle plate to a mechanical conveyor, which transports them inside the collector by using a fin scraper. Hybrid pick-up devices have been intensively studied and applied to pilot mining robots because of their environmental friendliness and reliability.

The Korean research team designed a hybrid hydraulic-mechanical pick-up collector as shown in Figure 196 (Kim et al. (2019)), where the nodules are blown up by high-pressure water from nozzles, channeled through a baffle, and then carried up the collector on a rotating chain plate with a scraper. For this device, Kim et al. (2019) used reliability-based design optimization (RBDO) to improve the reliability of the collection efficiency under environmental uncertainties. A computational model based on the Coandă effect was first developed for predicting the collection efficiency of pick-up devices. Next, RBDO based on the Akaike information criterion method was employed to design the pick-up device by using this model. The results showed that the proposed design method significantly improved the design of the pilot mining robot pick-up device.

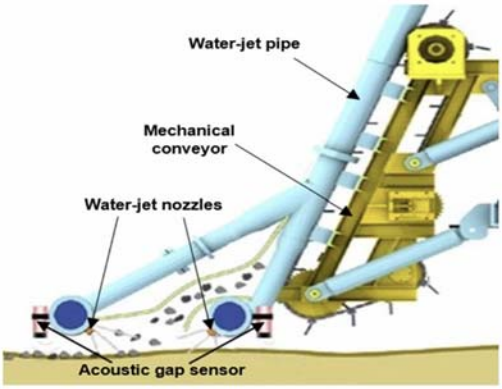

Figure 196: Hybrid hydraulic-mechanical pick-up collector designed by Korea (Kim et al., 2019)

9. TESTING METHODS TO CHARACTERISE THE INFLUENCE OF CHANGING BOTTOM BATHYMETRY AND COASTLINE FOR TANKERS AT OFFLOADING TERMINALS

9.1 Introduction

Ships play a crucial role in global trade as a key component of maritime transportation. They can be categorized into various types based on their specific functions, including commercial vessels, service vessels, and warships. Among these, commercial vessels encompass tankers, which are specifically designed for transporting cargo, as shown in Figure 197 (Ghosh *et al.*, 2015). When conducting a generic, high-level risk assessment for tankers, the research ultimately concluded that the major risk factors associated with tanker transportation originate from five general accident categories: collision, grounding, contact, fire and explosion, and incidents occurring during tanker loading and unloading at terminals (Yeo *et al.*, 2016).

In maritime transportation, tanker offloading operations at terminals are of paramount importance (Vanem *et al.*, 2008). Bottom bathymetry and coastline constitute vital environmental factors that influence the operational conditions and safety of tanker offloading terminals. The adequacy of bottom bathymetry is a critical factor in ensuring safe berthing and unloading of tankers, while changes in the coastline may impact port sedimentation and navigation channels, thereby affecting the safety and efficiency of tanker berthing and operations. By conducting a thorough assessment and continuous monitoring of these factors, a better understanding and proactive response to potential changes and challenges can be achieved, thereby ensuring the smooth and safe conduct of tanker offloading processes.

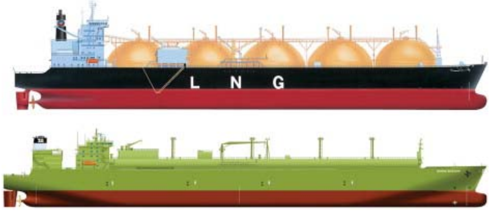

Figure 197: Main types of LNG carriers: moss spherical tankers (top) and membrane tankers (bottom)(Vanem *et al.*, 2008)

9.2 Physical Model Testing Methods

There have been numerous studies focused on investigating operational challenges during tanker offloading processes resulting from a series of environmental changes using physical model testing methods.

9.2.1 Testing methods focusing on coastline

The proximity of tankers anchored near a breakwater, such as those utilizing berth "A" terminal, highlights the notable impact of the coastline. Creating a scaled model that models both the tanker and the breakwater is a feasible approach. The Hydraulics Laboratory at the Faculty of Engineering - University of Porto (FEUP) conducted physical model tests to study the behavior of moored ships at berth "A" terminal (Santos *et al.*, 2008). A properly calibrated physical model has the potential to provide valuable insights into the effectiveness of potential interventions at the berth "A" oil terminal. As part of a newly approved research project in Portugal, the findings from these physical model tests will be supplemented by motion measurements taken on the prototype (at the berth "A" oil terminal) as well as numerical simulations.

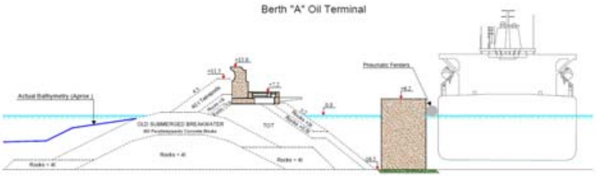

(a)

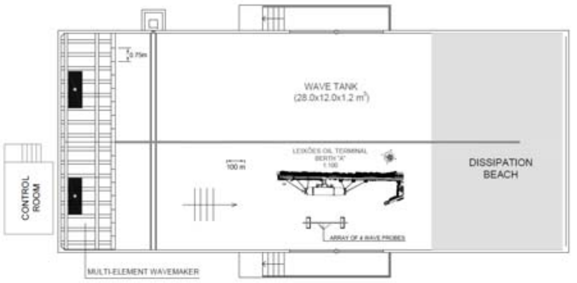

(b)

Figure 198: Model testing of tankers at berth "A" oil terminal: (a) Front view and (b) Top view (Santos *et al.*, 2008)

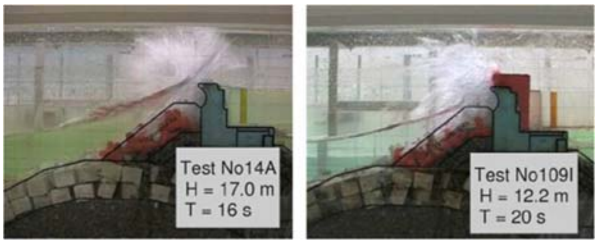

Figure 199: Samples of images taken from the video record of the tests (Santos *et al.*, 2008)

To investigate the influence of breakwater on the wave field near tanker, 2D physical model is feasible. Following the model tests above, the 2D physical model tests were conducted using both regular and irregular waves. The primary objective of these tests was to juxtapose the current operational conditions with ten diverse proposed alternatives, focusing on variables such as the amount of water overtopping the studied breakwater cross section and the stability of the armor layer blocks.

In addition, if the nature coastline should be modelled, movable bed physical model as shown in Figure 200 is feasible. The model was constructed in the wave tank of the hydraulics laboratory of FEUP, in order to reproduce a small stretch of the Portuguese northwest coast, undergoing an erosion situation, having been defined based on typical conditions (hydrodynamic and sedimentary).

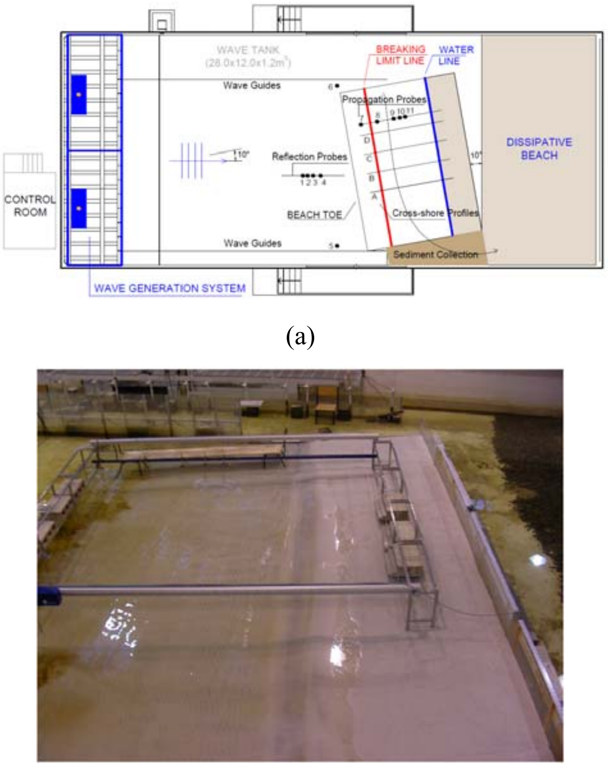

(a)

(b)

Figure 200: 3D movable bed physical model: (a) Top view and (b) Physical model (Taveira-Pinto *et al.*, 2010)

9.2.2 Testing methods focusing on changing bottom bathymetry

The inadequacy of state-of-the-art methods to accurately predict the slow-drift motion of moored structures in changing bottom bathymetry and coastline has been demonstrated (Liu *et al.*, 2023). This deficiency arises from the fact that not only do the second-order long waves fail to achieve the amplitudes predicted by the flat bottom model, but their phases are also altered in relation to the short wave envelopes. While these phenomena have long been recognized in coastal engineering (Battjes *et al.*, 2004), the full implications of the phase modification on the Quadratic Transfer Functions may not have been fully grasped.

An experimental campaign was conducted to study the slow-drift motion of a rectangular barge moored at different positions along an inclined beach, across water depths ranging from 54 cm to 21 cm. Utilizing the shoaling model for the barge tests led to notably improved concordance between numerical and experimental results for its slow-drift sway motion (Liu *et al.*, 2011).

Figure 201: Barge model undergoing irregular wave tests at the shallowest position (Liu *et al.*, 2011)

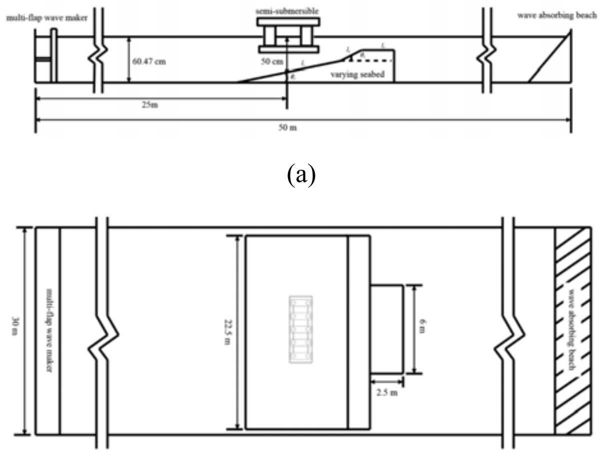

(a)

(b)

Figure 202: (a) Side view and (b) Top view of basin bottom modeling varying sea floor (Wang *et al.*, 2022)

Similar testing method was also used to investigate the linear and quadratic damping coefficients over variable bathymetry (Wang *et al.*, 2022). An artificial steel-made bottom is installed on the basin bottom modeling the varying seafloor. The seafloor consists of two sloping angles. A 4.5 m-long and 22.5 m-wide plate is installed first to form a 2 deg sloping seafloor. A 1 m-long plate is utilized as the second 7 deg sloping seabed. The module is deployed at 3 m away from the origin of the long plate. The water depth changes from 60.47 cm to 33.11 cm. This multi-slope seafloor is modeled based on the underwater environment of the practical operating location.

9.3 Field Measurements and Data Collection

From the perspective of investigating the influence of changing bottom bathymetry and coastline on tankers at offloading terminals, there are also studies that have utilized field trials as a method of data collection for model tests.

In the context of investigating the impact of changing bottom bathymetry and coastline on tankers at offloading terminals, six distinct methodologies were examined for characterizing the initial surf zone and nearshore bottom boundary conditions at both Narrabeen and Duck (Turner *et al.*, 2016). These methodologies encompass three "representative" bathymetries, which were developed using abundant historical survey data from both locations, as well as two "synthetic" bathymetries derived from equilibrium beach profile theory (Matheen *et al.*, 2021).

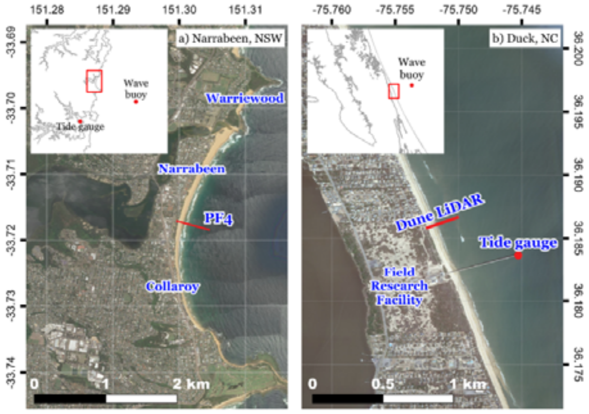

(a) (b)

Figure 203: (a) Narrabeen and (b) Duck study sites used in the study (Turner *et al.*, 2016)

As an example, considering the case of a pre-storm surveyed bathymetry, which is designed to represent the most optimal scenario. In this approach, an in-situ survey is conducted shortly before each individual storm, serving as the initial bottom boundary condition for XBeach modeling. At Narrabeen, these pre-storm surveys of the surf zone and nearshore areas were performed using a single-beam echo sounder mounted on a jet-ski (Turner *et al.*, 2016). Meanwhile, at Duck, the pre-storm bathymetry was derived by combining approximate monthly surveys of the surf zone and nearshore areas with an available regional dataset (Young *et al.*, 2018). This process also yielded a seamless bathymetry extending up to the offshore model boundary.

During the months of July and August in 1976, the research vessel R/V KARLUK conducted a series of soundings across the entrance channel of Prudhoe Bay and in the vicinity of the newly constructed causeway to the west of the channel. Additionally, a smaller boat was utilized to collect data by running lines between Stump Island and the causeway. This collected data was then juxtaposed with the detailed coastal outlines and nearshore bathymetry provided by the U.S. Coast and Geodetic Survey's smooth sheet (7857) and 1970 U.S. Geological Survey orthophotos. This comparison allowed for the identification of qualitative changes in bathymetry and coastal configurations. Ultimately, this assessment established a foundational point from which to evaluate both natural alterations and human-induced changes that have occurred since 1950 (Barnes *et al.*, 1977).

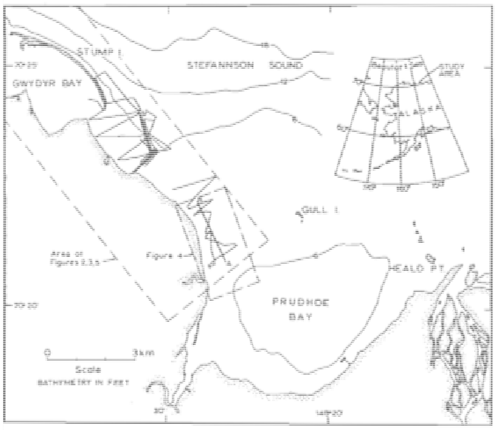

Figure 204: a series of sounding lines (Barnes *et al.*, 1977)

10. CONCLUSIONS & RECOMMENDATIONS

10.1 State-of-the-art Reviews on Bottom Founded and Floating Offshore Structures

In the present ITTC period (2021-2024), the review has allowed the identification of some issues of concern associated with bottom-founded structures and stationary floating structures, including FPSOs, Semi-submersibles, TLPs, Spars, VLFS, FLNGs, FSRUs, and their riser/mooring and dynamic positioning systems. Artificial intelligence methods are being introduced in the global performance evaluation of the floating platforms. The hydrodynamic behavior has been investigated numerically and experimentally, focusing on responses under extreme and damage conditions. The experimental work related to vortex-induced motions also continues. The focus of the spar studies is on heave plate, strake performance, viscous drag and parametric resonance in relation to the floater motions.

10.2 Review of the Existing Procedures

The Committee has reviewed and updated fourteen (14) procedures and guidelines. In general, minor revisions have been made. The detailed comments from the Advisory Committee have also been incorporated.

Concerning the existing procedures and guidelines, the Ocean Engineering Committee would like to make the following recommendations to the 30th ITTC:

- Adopt the updated guideline: 7.5-02-07-01.1 Laboratory Modelling of Multidirectional Irregular Wave Spectra;
- Adopt the updated guideline: 7.5-02-07-01.2 Laboratory Modelling of Waves;

- Adopt the updated procedure: 7.5-02-07-01.4 Confidence Intervals for Significant Wave;
- Adopt the updated guideline: 7.5-02-07-01.5 Laboratory Modelling of Wind;
- Adopt the updated guideline: 7.5-02-07-01.6 Laboratory Modelling of Currents;
- Adopt the updated procedure: 7.5-02-07-03.1 Floating Offshore Platform Experiments;
- Adopt the updated procedure: 7.5-02-07-03.2 Analysis Procedure for Model Tests in Regular Waves;
- Adopt the updated procedure: 7.5-02-07-03.5 Passive Hybrid Model Tests of Floating Offshore Structures with Mooring Lines;
- Adopt the updated procedure: 7.5-02-07-03.6 Dynamic Positioning System Model Test Experiments;
- Adopt the updated guideline: 7.5-02-07-03.10 Guideline for VIV Testing;
- Adopt the updated guideline: 7.5-02-07-03.11 Guideline for model tests of stationary multi-bodies operating in close proximity;
- Adopt the updated guideline: 7.5-02-07-03.13 Guideline for VIM Testing;
- Adopt the updated procedure: 7.5-02-07-03.14 Analysis Procedure of Model Tests in Irregular Waves.
- Adopt the updated guideline: 7.5-02-07-03.16 Model Construction of Offshore Systems.

10.3 Review and Identify Areas of Concern in Modelling and Simulation of Waves, Wind and Currents

The recent literature findings regarding the modelling of extreme waves are reported. Most of the recent works involving the generation of extreme wave events are based on the approaches described previously. Some new methodologies are focused on within the report, such as using the envelope soliton solutions for generating tailored extreme design waves, a High-Order Spectral NWT with an optimization algorithm based on First-Order Reliability Method (FORM). The effects of wave breaking and statistics of occurrence on the wave spectrum, and the role of wind-wave interaction on wave breaking occurrence are examined by review of recent numerical and experimental works.

The state-of-the-art reviews for wave-current interactions are reported. The studies focused on the impact of uniform currents, opposing and following vertical shear currents on the extreme and rogue waves, unidirectional and directional irregular waves.

The exact shape of the wind profile depends on surface roughness and atmospheric stability. The influence of the vertical wind profile is significant on the aerodynamic loads experienced by platforms. Some standard vertical wind profiles for model testing purposes are reported, such as Power-Law Wind Profile, Logarithmic Wind Profile, IEC Wind Profile, Low-Level Jet Wind Profile and API Wind Profile.

Both propeller systems and cable actuators have been used successfully to replicate the thrust force in hybrid model testing. However, there are some challenges associated with using propellers to reproduce the aerodynamic moment and controlling the cables with more complexity. The selection of hybrid testing in a wind tunnel or a wave basin depends on the specific phenomena being investigated. Wind tunnels allow for the replication of wind conditions and the observation of wake behavior and turbine interactions. Wave basins provide a controlled environment for studying the effects of waves and water on the platform's performance. A single propeller or a ducted fan can accurately replicate the thrust forces. For analyses that require the consideration of aerodynamic and gyroscopic moments, a multi-cable winch system is more suitable for the emulation of these moments and provides a comprehensive analysis of the platform's behavior.

The software in the loop (SIL) system used in the hybrid testing is still under development and there are some issues with regard to repeatability and experimental methodology which require further refinement.

10.4 State-of-the-art in Offshore Aquaculture Systems

Offshore aquaculture systems continue to attract attention, with particular focus on larger floating structures. A variety of studies concern the classifications or design analyses of offshore aquaculture systems. Close containment tank systems have been proposed to avoid the effects of sea lice on fish. Hydrodynamic interactions among the main floating structure, mooring system, and the fishing nets continue to be a major concern, especially under harsh environmental conditions. Several dominant types of offshore aquaculture systems, including flexible cage system, ship-shaped cage system, semi-submersible rigid cage system, submerged cage system and closed containment tank system, are presented with examples emphasizing their advantages and disadvantages. The general considerations, recent challenges and developments for design and operation are also summarized concisely.

10.5 Extend Experimental Wave Run-up Benchmark Tests (Four Squared Vertical Cylinders)

As an extension of the benchmark tests of wave run-ups on four squared vertical cylinders conducted during the 29th ITTC, the present benchmark tests were conducted to measure the wave run-ups and local wave impact loads on fixed four squared cylinders under focused waves. Through systematic analyses, including variations in wave period, steepness and incidence angle, the spatial distribution and vertical variations of wave run-ups and wave impact loads are revealed and the dependence on the wave parameters is examined. A set of benchmark data and results were provided for validating related numerical simulations. Owing to the complicated wave-column interactions, CFD studies are recommended in consideration of four-square-column cases with different configurations and extreme waves.

10.6 CFD Benchmark Study on Two-body Interactions, Focusing on Gap Surface Elevation

The CFD benchmark study for two-body interactions in close proximity is on-going and the conclusion can be summarized as below.

- To study the two-body interactions with small gap (0.23B), the experiments of two-body motion in beam sea were carried out in 2-D wave tank.

- Experimental results indicate that second-order resonance occurs at the incident wave frequency similar to the roll natural frequency of the barge. Additionally, the second-order effect diminishes at low or high incident wave frequencies.

- A CFD study of incoming wave generation, a key factor influencing the structure's motion, was performed. The target wave generation results closely matched the measured wave elevation.

- CFD simulations of single-body motions were also carried out. The roll free decay tests for initial angles of 5 and 10 degrees showed good agreement with experimental data. However, the simulations for single-body motion in waves require further refinement, particularly regarding the roll and heave natural periods.
- CFD study of the two-body motion in 2-D was conducted but not completed. There is a need to enhance the wave profiles in the gap between the two structures and refine the motions of the structures. Further testing of CFD parameters is required, including the overset grid system, CFL number, wave generation forcing length, Y+ number, and turbulence models.

It is recommended that further CFD benchmark studies on two bodies in close proximity continue within the 31st ITTC. These studies should focus on matching CFD results with experimental data for two-body interactions with small gaps (0.23B) in beam seas. Final conclusions will be drawn upon the completion of CFD benchmark studies with small gap.

10.7 Extraction Methods of Nodules from the Seabed

In general, breakthroughs have been made in some separate technical areas of deep-sea mining, and more and more nodule extraction methods are being proposed. However, the sea trials that have been conducted so far are only individual partial subsystem tests, with limited sea trial time and performance verification. The high productivity, reliability and environmental requirements of commercial deep-sea mining have brought new challenges and opportunities to the development of deep-sea polymetallic nodule mining technologies.

It is also urgent to improve the ability to intelligently sense and recognize the abundance of nodules on the seafloor during the collection process, and to realize the intelligent evaluation and decision-making adjustments of the relevant parameters in order to improve the collection efficiency.

10.8 Testing Methods to Characterise the Influence of Changing Bottom Bathymetry

The impact of changing bottom bathymetry and coastline on tankers at offloading terminals was investigated through a comprehensive analysis of various testing methods. It allowed for an improved understanding of factors such as the water volume overtopping the breakwater cross section and the impacts of water depths. Furthermore, the results of the field measurements and data collection efforts complemented the findings from the physical model tests. This integrated approach enabled a comprehensive assessment of the operational conditions at the tanker offloading terminal. The obtained insights have implications for both safety and efficiency considerations in tanker offloading operations.

In light of these findings, it is recommended that ongoing research in this area continues to employ a combination of physical model testing and field measurements. This multi-faceted approach will contribute to a more accurate understanding of the complex interactions between changing bottom bathymetry, coastline alterations, and their impact on the operational performance of oil terminals.

10.9 New Guideline for Testing Nodule Mining Machines in a Towing Tank

The Ocean Engineering Committee would like to make the following recommendation to the 30th ITTC:

- Adopt the new guideline: 7.5-02-07-03.17 Testing Nodule Mining Machines in a towing tank.

11. REFERENCES

ABS, 2020. Guide for Building and Classing, Aquaculture Installations; American Bureau of Shipping: Houston, TX, USA.

Antonutti, R., Poirier, J. C., Gueydon, S., 2020. Coupled testing of floating wind turbines in waves and wind using winches and software-in-the-loop. In Offshore Technology Conference (p. D021S019R001). OTC. https://doi.org/10.4043/30555-MS

Aydın, Ç., Ünal, U. O., Sarıöz, K., 2022. Computation of environmental loads towards an accurate dynamic positioning capability analysis. Ocean Engineering, 243, 110201. https://doi.org/10.1016/ j.oceaneng.2021.110201

Azcona, J., Bouchotrouch, F., González, M., Garciandía, J., Munduate, X., Kelberlau, F., Nygaard, T. A., 2014. Aerodynamic thrust modelling in wave tank tests of offshore floating wind turbines using a ducted fan. In Journal of Physics: Conference Series (Vol. 524, No. 1, p. 012089). IOP Publishing. doi:10.1088/1742-6596/524/1/012089

Aziminia, M. M., Abazari, A., Behzad, M., Hayatdavoodi, M., 2022. Stability analysis of parametric resonance in spar-buoy based on Floquet theory. Ocean Engineering, 266, 113090. https://doi.org/10.1016/j.oceaneng.2022.113090

Bachynski, E. E., Thys, M., Dadmarzi, F. H., 2020. Observations from hydrodynamic testing of a flexible, large-diameter monopile in irregular waves. In Journal of Physics: Conference Series (Vol. 1669, No. 1, p. 012028). IOP Publishing. doi:10.1088/1742-6596/1669/1/012028

Bachynski, E. E., Thys, M., Sauder, T., Chabaud, V., Sæther, L. O., 2016. Real-time hybrid model testing of a braceless semi-submersible wind turbine: Part II—Experimental results. In International Conference on Offshore Mechanics and Arctic Engineering (Vol. 49972, p. V006T09A040). American Society of Mechanical Engineers. https://doi.org/10.1115/OMAE2016-54437

Battjes, J. A., Bakkenes, H. J., Janssen, T. T., van Dongeren, A. R., 2004. Shoaling of subharmonic gravity waves. Journal of Geophysical Research: Oceans, 109(C2). https://doi.org/10.1029/2003JC001863

Boetius, A., Haeckel, M., 2018. Mind the seafloor. Science, 359(6371), 34-36. doi: 10.1126/science.aap7301

Bouscasse, B., Califano, A., Choi, Y. M., Haihua, X., Kim, J. W., Kim, Y. J., Lee, S. H., Lim, H., Park, D. M., Peric, M., Shen, Z., Yeon, S. M., 2021. Qualification criteria and the verification of numerical waves: Part 2: CFD-based numerical wave tank. In International Conference on Offshore Mechanics and Arctic Engineering (Vol. 85116, p. V001T01A007). American Society of Mechanical Engineers. https://doi.org/10.1115/OMAE2021-63710

Canard, M., Ducrozet, G., Bouscasse, B., 2022. Experimental reproduction of an extreme sea state in two wave tanks at various generation scales. In OCEANS 2022-Chennai (pp. 1-6). IEEE. doi:10.1109/OCEANSChennai45887.2022.9775216

Cardia, F., Lovatelli, A. (2015). Aquaculture operations in floating.

Carmo, L. H., Simos, A. N., de Mello, P. C., 2023. A second-order slender-body approach for computing wave induced forces with application to a simplified semi-submersible FOWT model. Ocean Engineering, 285, 115410. https://doi.org/10.1016/j.oceaneng.2023.115410

Chacon-Torres, A., Ross, L. G., Beveridge, M. C., 1988. The effects of fish behaviour on dye dispersion and water exchange in small net cages. Aquaculture, 73(1-4), 283-293. https://doi.org/10.1016/0044-8486(88)90062-2

Chen, L. F., Taylor, P. H., Ning, D. Z., Cong, P. W., Wolgamot, H., Draper, S., Cheng, L., 2021. Extreme runup events around a ship-shaped floating production, storage and offloading vessel in transient wave groups. Journal of Fluid Mechanics, 911, A40. https://doi.org/10.1017/jfm.2020.1072

Chen, M., Ouyang, M., Li, T., Zou, M., Ye, J., Tian, X., 2023. Numerical modelling of a catamaran float-over deck installation for a spar platform with complex hydrodynamic interactions and mechanical couplings. Ocean Engineering, 287, 115905. https://doi.org/10.1016/j.oceaneng.2023.115905

Chen, Y., Zhang, X., Shen, K., Ren, X., 2023. Extension of the discrete-module-finite-element method into the interconnected large floating flexible structures. Ocean Engineering, 269, 113549. https://doi.org/10.1016/j.oceaneng.2022.113549

Chen, Y., Zhang, Y., Tian, X., Guo, X., Li, X., Zhang, X., 2022. A numerical framework for hydroelastic analysis of a flexible floating structure under unsteady external excitations: Motion and internal force/moment. Ocean Engineering, 253, 111288. https://doi.org/10.1016/j.oceaneng.2022.111288

Cheng, H., Li, L., Ong, M. C., Aarsæther, K. G., Sim, J., 2021. Effects of mooring line breakage on dynamic responses of grid moored fish farms under pure current conditions. Ocean Engineering, 237, 109638. https://doi.org/10.1016/j.oceaneng.2021.109638

Cheng, H., Li, L., Ong, M. C., 2022. Comparative study of five commonly used gravity type fish cages under pure current conditions. Ocean Engineering, 250, 110977. https://doi.org/10.1016/j.oceaneng.2022.110977

Cheng, H., Ong, M. C., Li, L., Chen, H., 2022. Development of a coupling algorithm for fluid-structure interaction analysis of submerged aquaculture nets. Ocean Engineering, 243, 110208. https://doi.org/10.1016/j.oceaneng.2021.110208

Cheng, S., Yu, Y., Yu, J., Wu, J., Li, Z., Huang, Z., 2021. Mechanistic research on the complex motion response of a TLP under tendon breakage. Ocean Engineering, 240, 109984. https://doi.org/10.1016/j.oceaneng.2021.109984

Cho, S. G., Park, S., Oh, J., Min, C., Kim, H., Hong, S., Jang, J., Lee, T. H., 2019. Design optimization of deep-seabed pilot miner system with coupled relations between constraints. Journal of Terramechanics, 83, 25-34. https://doi.org/10.1016/j.jterra.2019.01.003

Chu, Y. I., Wang, C. M., Park, J. C., Lader, P. F., 2020. Review of cage and containment tank designs for offshore fish farming. Aquaculture, 519, 734928. https://doi.org/10.1016/j.aquaculture.2020.734928

Chu, Y. I., Wang, C. M., Zhang, H., 2022. A frequency domain approach for analyzing motion responses of integrated offshore fish cage and wind turbine under wind and wave actions. Aquacultural Engineering, 97, 102241. https://doi.org/10.1016/j.aquaeng.2022.102241

Chu, Y. I., Wang, C. M., Zhang, H., Abdussamie, N., Karampour, H., Jeng, D. S., Baumeister, J., Aland, P. A., 2023. Offshore fish farms: a review of standards and guidelines for design and analysis. Journal of Marine Science and Engineering, 11(4), 762. https://doi.org/10.3390/jmse11040762

Chua, K. H., de Mello, P. C., Nishimoto, K., Choo, Y. S., 2019. Model experiments of floating side-by-side barges. In International Conference on Offshore Mechanics and Arctic Engineering (Vol. 58882, p. V009T12A008). American Society of Mechanical Engineers. https://doi.org/10.1115/OMAE2019-95238

Cinello, A., Pétrié, F., Rousse, B., Le Cunff, C., 2022. On the Real Time Hybrid Modelling of Floating Offshore Wind

Turbine Using Ducted Fan (s). In International Conference on Offshore Mechanics and Arctic Engineering (Vol. 85932, p. V008T09A024). American Society of Mechanical Engineers. https://doi.org/10.1115/OMAE2022-78985

Craciunescu, C. C., Christou, M., 2020. Wave breaking energy dissipation in long-crested focused wave groups based on JONSWAP spectra. Applied Ocean Research, 99, 102144. https://doi.org/10.1016/j.apor.2020.102144

Cui, M., Li, Z., Zhang, C., Guo, X., 2022. Statistical investigation into the flow field of closed aquaculture tanks aboard a platform under periodic oscillation. Ocean Engineering, 248, 110677. https://doi.org/10.1016/j.oceaneng.2022.110677

Dai, J., Wang, C. M., Utsunomiya, T., Duan, W., 2018. Review of recent research and developments on floating breakwaters. Ocean Engineering, 158, 132-151. https://doi.org/10.1016/j.oceaneng.2018.03.083

Deepak, C. R., Ramji, S., Ramesh, N. R., Babu, S. M., Abraham, R., Shajahan, M. A., Atmanand, M. A., 2007. Development and testing of underwater mining systems for long term operations using flexible riser concept. In ISOPE Ocean Mining and Gas Hydrates Symposium (pp. ISOPE-M). ISOPE.

Dempster, T., Juell, J. E., Fosseidengen, J. E., Fredheim, A., Lader, P., 2008. Behaviour and growth of Atlantic salmon (Salmo salar L.) subjected to short-term submergence in commercial scale sea-cages. Aquaculture, 276(1-4), 103-111. https://doi.org/10.1016/j.aquaculture.2008.01.018

Ding, W. W., Jiang, J. Q., Yue, W. Z., Li, Y. Z., Wang, W. S., Sheng, S. W., Chen, M., 2023. Numerical Study on Hydrodynamic Performance of a New Semi-Submersible Aquaculture Platform. Applied Sciences, 13(23), 12652. https://doi.org/10.3390/app132312652

DNV, 2017. DNV-RU-OU-0503: Offshore Fish Farming Units and Installations.

DNVGL, 2021. DNV-ST-0111: A station-keeping capability standard for better benchmarking of dynamic positioning vessels. Technical Report. DNVGL.

Do, Q. T., Ghanbari-Ghazijahani, T., Prabowo, A. R., 2023. Developing empirical formulations to predict residual strength and damages in tension-leg platform hulls after a collision. Ocean Engineering, 286, 115668. https://doi.org/10.1016/j.oceaneng.2023.115668

Dong, S., You, X., Hu, F., 2021. Experimental investigation on the fluid–structure interaction of a flexible net cage used to farm Pacific bluefin tuna (Thunnus orientalis). Ocean Engineering, 226, 108872. https://doi.org/10.1016/j.oceaneng.2021.108872

Dong, S., Park, S. G., Kitazawa, D., Zhou, J., Yoshida, T., Li, Q., 2021. Model tests and full-scale sea trials for drag force and deformation of a marine aquaculture net cage. Ocean Engineering, 240, 109941. https://doi.org/10.1016/j.oceaneng.2021.109941

Du, Z., Yang, J., Xu, W., Yang, Y., Li, X., Feng, J., 2023. An experimental investigation on flow-induced motion and fluid force of a tension leg platform in complex flows. Ocean Engineering, 281, 114790. https://doi.org/10.1016/j.oceaneng.2023.114790

Ducrozet, G., Abdolahpour, M., Nelli, F., Toffoli, A., 2021. Predicting the occurrence of rogue waves in the presence of opposing currents with a high-order spectral method. Physical Review Fluids, 6(6), 064803. https://doi.org/10.1103/PhysRevFluids.6.064803

Ducrozet, G., Bonnefoy, F., Mori, N., Fink, M., Chabchoub, A., 2020. Experimental reconstruction of extreme sea waves by time reversal principle. Journal of Fluid Mechanics, 884, A20. https://doi.org/10.1017/jfm.2019.939

Ecole Centrale de Nantes, 2016. Experimental investigations of the interactions between two FPSO in waves, Experimental report for ITTC 27th benchmark study.

Eeltink, D., Branger, H., Luneau, C., He, Y., Chabchoub, A., Kasparian, J., van den Bremer, T. S., Sapsis, T. P., 2022. Nonlinear wave evolution with data-driven breaking. Nature communications, 13(1), 2343. https://doi.org/10.1038/s41467-022-30025-z

Ellingsen, S. Å., Zheng, Z., Abid, M., Kharif, C., Li, Y., 2024. Dispersive wave focusing on a shear current: Part 1—Linear approximations. Water Waves, 1-45. https://doi.org/10.1007/s42286-024-00085-3

Esandi, J. M., Buldakov, E., Simons, R., Stagonas, D., 2020. An experimental study on wave forces on a vertical cylinder due to spilling breaking and near-breaking wave groups. Coastal Engineering, 162, 103778. https://doi.org/10.1016/j.coastaleng.2020.103778

Fan, Z. Q., Liang, Y. H., Yun-Peng, Z., 2023. Review of the research on the hydrodynamics of fishing cage nets. Ocean Engineering, 276, 114192. https://doi.org/10.1016/j.oceaneng.2023.114192

FAO (Food and Agriculture Organization), 2022. The State of World Fisheries and Aquaculture 2022, Towards blue transformation.

Fontes, J. V., Hernández, I. D., Mendoza, E., Silva, R., Brandão da Silva, E., Rocha de Sousa, M., Gonzaga, J., Kamezaki, R. S., Torres, L., Esperança, P. T., 2021. On the evolution of different types of green water events. Water, 13(9), 1148. https://doi.org/10.3390/w13091148

Fontes, J. V., Mendoza, E., Silva, R., Hernández, I. D., González-Olvera, M. A., Torres, L., 2022. On the Evolution of Different Types of Green Water Events—Part II: Applicability of a Convolution Approach. Water, 14(4), 510. https://doi.org/10.3390/w14040510

Fornshell, G., Hinshaw, J., Tidwell, J. H., 2012. Flow-through raceways. Aquaculture production systems, 173-190. doi:10.1002/9781118250105

Fouques, S., Croonenborghs, E., Koop, A., Lim, H. J., Kim, J., Zhao, B., Canard, M., Ducrozet, G., Bouscasse, B., Wang, W., Bihs, H., 2021. Qualification Criteria for the Verification of Numerical Waves–Part 1: Potential-Based Numerical Wave Tank (PNWT). In International Conference on Offshore Mechanics and Arctic Engineering (Vol. 85116, p. V001T01A011). American Society of Mechanical Engineers. https://doi.org/10.1115/OMAE2021-63884

Geological Survey (US), Barnes, P. W., 1977. Bathymetric and shoreline changes, northwestern Prudhoe Bay, Alaska. US Geological Survey.

Ghosh, M. K., Kumar, L., Roy, C., 2015. Monitoring the coastline change of Hatiya Island in Bangladesh using remote sensing techniques. ISPRS Journal of Photogrammetry and Remote Sensing, 101, 137-144. https://doi.org/10.1016/j.isprsjprs.2014.12.009

Gopmandal, F., Ghosh, A., Kumar, A., 2022. LQ optimal robust multivariable PID control for dynamic positioning of ships with norm-bounded parametric uncertainties. Ocean Engineering, 266, 113054. https://doi.org/10.1016/j.oceaneng.2022.113054

Gusev, O. I., Khakimzyanov, G. S., Skiba, V. S., Chubarov, L. B., 2023. Shallow water modeling of wave–structure interaction over irregular bottom. Ocean Engineering, 267, 113284. https://doi.org/10.1016/j.oceaneng.2022.113284

Ha, Y. J., Ahn, H., Park, S., Park, J. Y., Kim, K. H., 2023. Development of hybrid model test technique for performance evaluation of a 10 MW class floating offshore wind turbine considering asymmetrical thrust. Ocean Engineering, 272, 113783. https://doi.org/10.1016/j.oceaneng.2023.113783

Halvorsen, H. S., Øveraas, H., Landstad, O., Smines, V., Fossen, T. I., Johansen, T. A., 2021. Wave motion compensation in dynamic positioning of small autonomous vessels. Journal of Marine Science and Technology, 26, 693-712. https://doi.org/10.1007/s00773-020-00765-y

Handschuh, R., Grebe, H., Panthel, J., Schulte, E., Wenzlawski, B., Schwarz, W., Atmanand, M.A., Keyamani, R., Shajahan, M.A., Deepak, C.R., Ravindran, M., 2001. Innovative deep ocean mining concept based on flexible riser and self-propelled mining machines. In ISOPE Ocean Mining and Gas Hydrates Symposium (pp. ISOPE-M). ISOPE.

Hegde, P., Nallayarasu, S., 2023. Hydrodynamic response of buoy form spar with heave plate near the free surface validated with experiments. Ocean Engineering, 269, 113580. https://doi.org/10.1016/j.oceaneng.2022.113580

Hmedi, M., 2020. Development of a wind turbine emulator for the experimental testing of a floating offshore wind turbine in a wave tank. Ecole Central Nantes.

Hmedi, M., Uzunoglu, E., Soares, C. G., Medina-Manuel, A., Mas-Soler, J., Abad-Gibert, V., Souto-Iglesias, A., Vittori, F., Pires, O., Azcona, J., 2022. Experimental analysis of a free-float capable tension leg platform with a 10 MW turbine. Trends in Renewable Energies Offshore, 549-557.

Hogenboom, S., Vinnem, J. E., Utne, I. B., Kongsvik, T., 2021. Risk-based decision-making support model for offshore dynamic positioning operations. Safety science, 140, 105280. https://doi.org/10.1016/j.ssci.2021.105280

Hong, S., Choi, J. S., Kim, J. H., Yang, C. K., 1999. Experimental study on hydraulic performance of hybrid pick-up device of manganese nodule collector. In ISOPE Ocean Mining and Gas Hydrates Symposium (pp. ISOPE-M). ISOPE.

Hong, S., Kimg, H. W., Choi, J. S., Yeu, T. K., Park, S. J., Lee, C. H., Yoon, S. M., 2010. A self-propelled deep-seabed miner and lessons from shallow water tests. In International Conference on Offshore Mechanics and Arctic Engineering (Vol. 49118, pp. 75-86).

Hosseinnajad, A., Loueipour, M., 2020. Dynamic positioning system design for a marine vessel with unknown dynamics subject to external disturbances including wave effect. China Ocean Engineering, 34(5), 651-663. https://doi.org/10.1007/s13344-020-0058-9,

Houtani, H., Sawada, H., Waseda, T., 2022. Phase convergence and crest enhancement of modulated wave trains. Fluids, 7(8), 275. https://doi.org/10.3390/fluids7080275

Hu, C., Wu, D., Liao, Y., Hu, X., 2021. Sliding mode control unified with the uncertainty and disturbance estimator for dynamically positioned vessels subjected to uncertainties and unknown disturbances. Applied Ocean Research, 109, 102564. https://doi.org/10.1016/j.apor.2021.102564

Huang, H., Chen, X. J., Liu, J. Y., Ji, S., 2022. A method to predict hydroelastic responses of VLFS under waves and moving loads. Ocean engineering, 247, 110399. https://doi.org/10.1016/j.oceaneng.2021.110399

Huang, S., Hu, Z., Chen, C., 2023. Application of CFD–FEA coupling to predict hydroelastic responses of a single module VLFS in extreme wave conditions. Ocean Engineering, 280, 114754. https://doi.org/10.1016/j.oceaneng.2023.114754

Iijima, K., Ma, C., Pambela, A. R., Maeda, T., 2022. DIC measurement of deflection waves travelling along a thin flexural plate floating at water surface. Ocean Engineering, 266, 113079. https://doi.org/10.1016/j.oceaneng.2022.113079

Islam, M., Lau, M., Brown, J., Gash, R., Pearson, W., Mills, J., 2022. Investigation of the effects of managed ice field characteristics on a dynamic positioning AHTS vessel using physical modelling techniques. Ocean Engineering, 246, 110485. https://doi.org/10.1016/ j.oceaneng.2021.110485

Islam, M., Mills, J., Gash, R., Pearson, W., 2022. Modelling of Dynamically Positioned vessels and managed ice-field interactions using multiple regression techniques. Ocean Engineering, 243, 110248. https://doi.org/10.1016/ j.oceaneng.2021.110248

Islam, M., Mills, J., Gash, R., Pearson, W., 2022. Modelling of Dynamically Positioned vessels and managed ice-field interactions using multiple regression techniques. Ocean Engineering, 243, 110248. https://doi.org/10.1016/ j.oceaneng.2021.110248

Islam, M., Wang, J., Gash, R., Pearson, W., Mills, J., 2021. Physical model testing I for investigating the effects of managed ice-field characteristics on a dynamic positioning vessel. Cold Regions Science and Technology, 192, 103376. https://doi.org/10.1016/j.coldregions.2021. 103376

Islam, M., Wang, J., Mills, J., Sayeed, T., Gash, B., Lau, M., Millan, D., Millan, J., 2016. Dp in ice environment-improving safety and efficiency of arctic operations. In OTC Arctic Technology Conference (pp. OTC-27349). OTC. https://doi.org/10.4043/27349-MS

Islam, S., Wang, J., Brown, J., Lau, M., Gash, R., Millan, D., Ocean, J. M., 2018. Physical model testing for supporting ice force model development of DP vessels in managed ice. In OTC Arctic Technology Conference (p. D023S009R005). OTC. https://doi.org/10.4043/29157-MS

ITTC, 2017. Uncertainty Analysis in CFD Verification and Validation Methodology and Procedures.

Jahani, K., Langlois, R. G., Afagh, F. F., 2022. Structural dynamics of offshore Wind Turbines: A review. Ocean Engineering, 251, 111136. https://doi.org/10.1016/ j.oceaneng.2022.111136

Jeon, W., Park, S., Cho, S., 2023, Moored motion prediction of a semi-submersible offshore platform in waves using an OpenFOAM and MoorDyn coupled solver, International Journal of Naval Architecture and Ocean Engineering, Volume 15, 2023, 100544, ISSN 2092-6782, https://doi.org/10.1016/j.ijnaoe.2023.100544.

Jia, H., Yang, J., Su, X., Wang, Y., Wu, K., 2023. Flow characteristics and hydraulic lift of coandă effect-based pick-up method for polymetallic nodule. Coatings, 13(2), 271. https://doi.org/10.3390/coatings13020271

Jia, H., Yang, J., Su, X., Xia, Q., Wu, K.. 2022. Theoretical prediction on hydraulic lift of a coandă effect-based mining collector for manganese nodule. Energies, 15(17), 6345. https://doi.org/10.3390/en15176345

Jiang, C., Xu, P., Bai, X., Zhao, Z., el Moctar, O., Zhang, G., 2023. A review of advances in modeling hydrodynamics and hydroelasticity for very large floating structures. Ocean Engineering, 285, 115319. https://doi.org/10.1016/ j.oceaneng.2023.115319

Jiang, D., Tan, K. H., Dai, J., Ang, K. K., Nguyen, H. P., 2021. Behavior of concrete modular multi-purpose floating structures. Ocean Engineering, 229, 108971. https://doi.org/10.1016/j.oceaneng.2021.108971

Jiang, X., 2020. Software-in-the-loop applications for improved physical model tests of ocean renewable energy devices using artificial intelligence. doi: 10.48730/vkf6-vh23

Jin, R., Jiang, Y., Shen, W., Zhang, H., Geng, B., 2021. Coupled dynamic response of a tension leg platform system under waves and flow at different heading angles: An experimental study. Applied Ocean Research, 115, 102848. https://doi.org/10.1016/j.apor.2021.102848

Jin, Y., Chai, S., Duffy, J., Chin, C., Bose, N., 2018. URANS predictions on the hydrodynamic interaction of a conceptual FLNG-LNG offloading system in regular waves. Ocean Engineering, 153, 363-386. https://doi.org/10.1016/j.oceaneng.2018.01.102

Jung, K.H, Park, S.B., Park, H., Mohamed, A.H., Kim, H.S. 2022, Hydrodynamic Characteristics of Rectangular Structure in Various Water Depth, 15th International Symposium on Practical Design of Ships and Other Floating Structures PRADS 2022.

Kang, D., Kim, T., Lim, J., Yoo, D., 2022. One Side Spread Mooring System Applied for Floating LNG in West Africa. In Offshore Technology Conference (p. D011S011R007). OTC. https://doi.org/10.4043/32067-MS

Kang, Z., Chang, R., Meng, W., 2023. Mechanistic research on the complex motion response of a TLP in a tender-assisted drilling state. Ocean Engineering, 288, 115935. https://doi.org/10.1016/j.oceaneng.2023.115935

Kanner S, Yeung R W, Koukina E., 2016. Hybrid testing of model-scale floating wind turbines using autonomous actuation and control//OCEANS MTS/IEEE Monterey. IEEE, 1-6.

Kaufman, R., Latimer, J. P., Tolefson, D. C., Senni, S., 1985. The Design and Operation of a Pacific Ocean Deep-Ocean Mining Test Ship: R/V Deepsea Minner 2. In Offshore Technology Conference (pp. OTC-4901). OTC. https://doi.org/10.4043/4901-MS

Khait, A., Ma, Z., Qian, L., Bai, W., Lin, Z., 2022. Energy Dissipation and Nonpotential Effects in Wave Breaking. International Journal of Offshore and Polar Engineering, 32(01), 87-96. https://doi.org/10.17736/ijope.2022.ak43

Kharazmi, R., Ketabdari, M. J., 2022. Numerical modeling to develop strake design of Spar platform for Vortex-Induced motions suppression. Ocean Engineering, 250, 111060. https://doi.org/10.1016/j.oceaneng.2022.111060

Kim J., Lim, H.J., 2019. JIP on Reproducible CFD Modeling Practices for Offshore Applications. NWT Preparation Workgroup Year 1 Report, Rev. H., TechnipFMC.

Kim, M., Jung, K. H., Park, S. B., Lee, G. N., Duong, T. T., Suh, S. B., Park, I. R., 2020. Experimental and numerical estimation on roll damping and pressure on a 2-D rectangular structure in free roll decay test. Ocean Engineering, 196, 106801. https://doi.org/10.1016/j.oceaneng.2019.106801

Kim, S., Bouscasse, B., Ducrozet, G., Canard, M., De Hauteclocque, G., Housseine, C. O., Ferrant, P., 2022. Numerical and experimental study of a FORM-based design wave applying the HOS-NWT nonlinear wave solver. Ocean Engineering, 263, 112287. https://doi.org/10.1016/j.oceaneng.2022.11228

Kim, S., Cho, S. G., Lee, M., Kim, J., Lee, T. H., Park, S., Hong, S., Kim, H., Min, C., Choi, J., Ko, Y., Chi, S. B., 2019. Reliability-based design optimization of a pick-up device of a manganese nodule pilot mining robot using the Coandă effect. Journal of Mechanical Science and Technology, 33, 3665-3672. doi: 10.1007/s12206-019-0707-1

Klein, M., Clauss, G. F., Hoffmann, N., 2021. Introducing envelope soliton solutions for wave–structure investigations. Ocean engineering, 234, 109271. https://doi.org/10.1016/j.oceaneng.2021.109271

Klein, M., Wang, S., Clauss, G., Guedes Soares, C., 2023. Experimental study on the effect of extreme waves on a LNG carrier. Journal of marine science and application, 22(1), 52-74. https://doi.org/10.1007/s11804-023-00321-1

Kung, A., Svobodova, K., Lèbre, E., Valenta, R., Kemp, D., Owen, J. R., 2021. Governing deep sea mining in the face of uncertainty. Journal of Environmental Management, 279, 111593. https://doi.org/10.1016/j.jenvman.2020.111593

Lee, J. H., Monty, J. P., 2020. On the interaction between wind stress and waves: Wave growth and statistical properties of large waves. Journal of Physical Oceanography, 50(2), 383-397. https://doi.org/10.1175/JPO-D-19-0112.1

Lee, M., Cho, S. G., Choi, J. S., Kim, H. W., Hong, S., Lee, T. H., 2012. Metamodel-Based Multidisciplinary Design Optimization of a Deep-Sea Manganese Nodules Test Miner. Journal of Applied Mathematics, 2012(1), 326954. https://doi.org/10.1155/2012/326954

Lei, Y., Li, W., Zheng, X. Y., Zheng, H., Gao, S., Zhao, S., 2024. A floating system integrating a wind turbine with a steel fish farming cage: experimental validation of the hydrodynamic model. Marine Structures, 93, 103525. https://doi.org/10.1016/j.marstruc.2023.103525

Leroy, V., Bachynski-Polić, E. E., Babarit, A., Ferrant, P., Gilloteaux, J. C., 2021. A weak-scatterer potential flow theory-based model for the hydroelastic analysis of offshore wind turbine substructures. Ocean Engineering, 238, 109702. https://doi.org/10.1016/j.oceaneng.2021.109702

Li, J., Xiang, X., Yang, S., 2022. Robust adaptive neural network control for dynamic positioning of marine vessels with prescribed performance under model uncertainties and input saturation. Neurocomputing, 484, 1-12. https://doi.org/10.1016/j.neucom.2021.03.136

Li, M. Y., Xie, W. B., Wang, Y. L., Hu, X., 2022. Prescribed performance trajectory tracking fault-tolerant control for dynamic positioning vessels under velocity constraints. Applied Mathematics and Computation, 431, 127348. https://doi.org/10.1016/j.amc.2022.127348

Li, M. Y., Xu, J., Xie, W. B., Wang, H. B., 2022. Finite-time composite learning control for trajectory tracking of dynamic positioning vessels. Ocean Engineering, 262, 112288. https://doi.org/10.1016/j.oceaneng.2022.112288

Li, N., Shi, W., Han, X., Li, X., Verma, A. S., Liu, C., 2023. Dynamic analysis of an integrated offshore structure comprising a jacket-supported offshore wind turbine and aquaculture steel cage. Ocean Engineering, 274, 114059. https://doi.org/10.1016/j.oceaneng.2023.114059

Li, W., Ke, S., Chen, J., Zhu, T., Ren, H., 2022. Hydrodynamic response and energy analysis in a very large floating structure supporting a marine airport under typhoon-driven waves. Ocean Engineering, 266, 112987. https://doi.org/10.1016/j.oceaneng.2022.112987

Li, Y., Zhang, C., 2016. Analysis of wave resonance in gap between two heaving barges. Ocean Engineering, 117, 210-220. https://doi.org/10.1016/j.oceaneng.2016.03.042

Liang, H., Chua, K. H., Wang, H. C., & Choo, Y. S., Chua, K. H., de Mello, P., Malta, E., Vieira, D., Watai, R., Ruggeri, F., Taylor, R. E., Nishimoto, K., Choo, Y. S., 2018. Irregular seas model experiments on side-by-side barges. In ISOPE International Ocean and Polar Engineering Conference (pp. ISOPE-I). ISOPE.

Liang, H., Liu, X., Chua, K. H., de Mello, P. C., Choo, Y. S., 2022. Wave actions on side-by-side barges with sloshing effects: fixed–free arrangement. Flow, 2, E20. https://doi.org/10.1017/flo.2022.14

Liang, K., Lin, X., Chen, Y., Liu, Y., Liu, Z., Ma, Z., Zhang, W., 2021. Robust adaptive neural networks control for dynamic positioning of ships with unknown saturation and time-delay. Applied Ocean Research, 110, 102609. https://doi.org/10.1016/j.apor.2021.102609

Lim, S. J., Kim, J. W., Jung, S. T., Cho, H. Y., Lee, S. H., 2015. Deep seawater flow characteristics around the manganese nodule collecting device. Procedia Engineering, 116, 544-551. https://doi.org/10.1016/j.proeng.2015.08.324

Liu, H., Chen, M., Han, Z., Zhou, H., Li, L., 2022. Feasibility study of a novel open ocean aquaculture ship integrating with a wind turbine and an internal turret mooring system. Journal of Marine Science and Engineering, 10(11), 1729. https://doi.org/10.3390/jmse10111729

Liu, H. F., Bi, C. W., Xu, Z., Zhao, Y. P., 2021. Hydrodynamic assessment of a semi-submersible aquaculture platform in uniform fluid environment. Ocean Engineering, 237, 109656. https://doi.org/10.1016/j.oceaneng.2021.109656

Liu, J., Liu, M., Xiao, L., Wei, H., Li, X., 2023. Experimental study on the effect of flare barriers on wave run-up and motion response of a semi-submersible platform. Ocean Engineering, 281, 114998. https://doi.org/10.1016/j.oceaneng.2023.114998

Liu, J., Xu, D., Ji, C., Xia, J., Ran, Q., 2023. Numerical investigations on the flow structures around the hydraulic mining header of deep-sea polymetallic nodule collectors. The Ocean Engineering, 41: 123-136.

Liu, Y., Ren, N., Ou, J., 2022. Hydrodynamic analysis of a hybrid modular floating structure system under different wave directions. Applied Ocean Research, 126, 103264. https://doi.org/10.1016/j.apor.2022.103264

Liu, Y. N., Molin, B., Kimmoun, O., Remy, F., Rouault, M. C., 2011. Experimental and numerical study of the effect of variable bathymetry on the slow-drift wave response of floating bodies. Applied Ocean Research, 33(3), 199-207. https://doi.org/10.1016/j.apor.2011.02.004

Liu, Y., Yao, Y., Liao, Z., Li, S., Zhang, C., Zou, Q., 2023. Fully nonlinear investigation on energy transfer between long waves and short-wave groups over a reef. Coastal Engineering, 179, 104240. https://doi.org/10.1016/j.coastaleng.2022.104240

Liu, Z., Zhao, G., Xiao, L., 2023. Experimental study of submarine nodules collection method based on the hydrodynamic characteristics of vertical axis vortex. The Ocean Engineering: 1-10.

Ma, C., Zhao, Y. P., Bi, C. W., 2022. Numerical study on hydrodynamic responses of a single-point moored vessel-shaped floating aquaculture platform in waves. Aquacultural Engineering, 96, 102216. https://doi.org/10.1016/j.aquaeng.2021.102216

Ma, M., Zhang, H., Jeng, D. S., Wang, C. M., 2021. A semi-analytical model for studying hydroelastic behaviour of a cylindrical net cage under wave action. Journal of Marine Science and Engineering, 9(12), 1445. https://doi.org/10.3390/jmse9121445

Ma, M., Zhang, H., Jeng, D. S., Wang, C. M., 2022. Hydroelastic interactions between waves and an array of submersible flexible fish cages. Ocean Engineering, 266, 113035. https://doi.org/10.1016/j.oceaneng.2022.113035

Ma, M., Zhang, H., Jeng, D. S., Wang, C. M., 2022. Analytical solutions of hydroelastic interactions between waves and submerged open-net fish cage modeled as a porous cylindrical thin shell. Physics of Fluids, 34(1). https://doi.org/10.1063/5.0076659

Ma, Y., Tai, B., Dong, G., Fu, R., Perlin, M., 2022. An experiment on reconstruction and analyses of in-situ measured freak waves. Ocean Engineering, 244, 110312. https://doi.org/10.1016/j.oceaneng.2021.110312

Mackay, E., Shi, W., Qiao, D., Gabl, R., Davey, T., Ning, D., Johanning, L., 2021. Numerical and experimental modelling of wave interaction with fixed and floating porous cylinders. Ocean Engineering, 242, 110118. https://doi.org/10.1016/j.oceaneng.2021.110118

Mao, Y., Wang, T., Duan, M., 2022. A DNN-based approach to predict dynamic mooring tensions for semi-submersible platform under a mooring line failure condition. Ocean Engineering, 266, 112767. https://doi.org/10.1016/j.oceaneng.2022.112767

Martelli, M., Faggioni, N., Donnarumma, S., 2020. A novel model based-design approach for a dynamic positioning system. In Conference Proceedings of iSCSS. https://doi.org/10.24868/issn.2631-8741.2020.002

Martelli, M., Faggioni, N., Donnarumma, S., 2022. A time-domain methodology to assess the dynamic positioning performances. Ocean Engineering, 247, 110668. https://doi.org/10.1016/j.oceaneng.2022.110668

Martin, S., Day, S., Gilmour, C. B., 2015. Rotor scaling methodologies for small scale testing of floating wind turbine systems. In International Conference on Offshore Mechanics and Arctic Engineering (Vol. 56574, p. V009T09A045). American Society of Mechanical Engineers. https://doi.org/10.1115/OMAE2015-41599

Matheen, N., Harley, M. D., Turner, I. L., Splinter, K. D., Simmons, J. A., Thran, M. C., 2021. Bathymetric data requirements for operational coastal erosion forecasting using XBeach. Journal of Marine Science and Engineering, 9(10), 1053. https://doi.org/10.3390/jmse9101053

Mauro, F., Nabergoj, R., 2022. A probabilistic approach for Dynamic Positioning capability and operability predictions. Ocean Engineering, 262, 112250. https://doi.org/10.1016/j.oceaneng.2022.112250

Mauro, F., Prpić-Oršić, J., 2020. Determination of a DP operability index for an offshore vessel in early design stage. Ocean engineering, 195, 106764. https://doi.org/10.1016/j.oceaneng.2019.106764

McFarlane, J., Brockett, T., Huizingh, J. P., 2008. Analysis of Mining Technologies Developed in the 1970s and 1980s. Kingston: International Seabed Authority.

Miao, Y. J., Ding, J., Tian, C., Chen, X. J., Fan, Y. L., 2021. Experimental and numerical study of a semi-submersible offshore fish farm under waves. Ocean Engineering, 225, 108794. https://doi.org/10.1016/j.oceaneng.2021.108794

Moe-Føre, H., Lader, P. F., Lien, E., Hopperstad, O. S., 2016. Structural response of high solidity net cage models in uniform flow. Journal of Fluids and Structures, 65, 180-195. https://doi.org/10.1016/j.jfluidstructs.2016.05.013

Moradi, N., Zhou, T., Cheng, L., 2016. Two-dimensional numerical study on the effect of water depth on resonance behaviour of the fluid trapped between two side-by-side bodies. Applied Ocean Research, 58, 218-231. https://doi.org/10.1016/j.apor.2016.03.018

Morro, B., Davidson, K., Adams, T. P., Falconer, L., Holloway, M., Dale, A., Aleynik, D., Thies, P. R., Khalid, F., Hardwick, J., Smith, H., Giollibrand, P. A., Rey-Planellas, S., 2022. Offshore aquaculture of finfish: Big expectations at sea. Reviews in Aquaculture, 14(2), 791-815. https://doi.org/10.1111/raq.12625

Nakashima, M., Kato, H., Takaoka, E., 1992. Development of real-time pseudo dynamic testing. Earthquake engineering & structural dynamics, 21(1), 79-92. https://doi.org/10.1002/eqe.4290210106

Nasyrlayev, N., Dyson, A. P., Kefayati, G., Tolooiyan, A., 2023. Modelling the response of offshore aquaculture fish pens to environmental loads in high-energy regions. Applied Ocean Research, 135, 103541. https://doi.org/10.1016/j.apor.2023.103541

Nguyen, N., Davis, J., Alshuwaykh, A., Sharman, K. T., 2020. Design, Analysis, and Development of a Wave-Current Laboratory. In International Conference on

Offshore Mechanics and Arctic Engineering (Vol. 84379, p. V06AT06A019). American Society of Mechanical Engineers. https://doi.org/10.1115/OMAE2020-19253

Ning, D., Zhu, Y., Zhang, C., Zhao, M., 2018. Experimental and numerical study on wave response at the gap between two barges of different draughts. Applied Ocean Research, 77, 14-25. https://doi.org/10.1016/j.apor.2018.05.010

Niu, X., Ma, X., Ma, Y., Dong, G., 2020. Controlled extreme wave generation using an improved focusing method. Applied Ocean Research, 95, 102017. https://doi.org/10.1016/j.apor.2019.102017

Nwafor, J. C., 2022. Numerical Investigation on Coupling Dynamic Performance of FLNG and LNG Carriers. In ISOPE International Ocean and Polar Engineering Conference (pp. ISOPE-I). ISOPE.

Oguz, E., Clelland, D., Day, A. H., Incecik, A., López, J. A., Sánchez, G., Almeria, G. G., 2018. Experimental and numerical analysis of a TLP floating offshore wind turbine. Ocean Engineering, 147, 591-605. https://doi.org/10.1016/j.oceaneng.2017.10.052

Otter, A., Murphy, J., Pakrashi, V., Robertson, A., Desmond, C., 2022. A review of modelling techniques for floating offshore wind turbines. Wind Energy, 25(5), 831-857. https://doi.org/10.1002/we.2701

Otter, A., Murphy, J., Desmond, C. J., 2020. Emulating aerodynamic forces and moments for hybrid testing of floating wind turbine models. In Journal of Physics: Conference Series (Vol. 1618, No. 3, p. 032022). IOP Publishing. doi: 10.1088/1742-6596/1618/3/032022

Pang, G., Zhang, S., Liu, H., Zhu, S., Yuan, T., Li, G., Han, X., Huang, X., 2023. Hydrodynamic response analysis for a new semi-submersible vessel-shaped fish farm platform based on numerical simulation. Frontiers in Marine Science, 10, 1135757. https://doi.org/10.3389/fmars.2023.1135757

Park, D. M., Kwon, Y. J., Nam, H. S., Nam, B. W., Lee, K., 2022. An experimental study of wave impact pressure on an FPSO bow under head sea conditions. Ocean Engineering, 249, 110993. https://doi.org/10.1016/j.oceaneng.2022.110993

Pillay, T. V. R., 2008. Aquaculture and the Environment. John Wiley & Sons.

Qi, K., Zhao, Y., LIU, L., Gan, S., Luo, X., Tian, X., 2021. Experimental Investigation on the Hydrodynamic Performance of Quay-moored FSRU and LNG Carrier, Journal of Ship Mechanics, 25(6).

Qiu, W., Meng, W., Peng, H., Li, J., Rousset, J. M., Rodríguez, C. A., 2019. Benchmark data and comprehensive uncertainty analysis of two-body interaction model tests in a towing tank. Ocean Engineering, 171, 663-676. https://doi.org/10.1016/j.oceaneng.2018.11.057

Ransley, E. J., Brown, S. A., Edwards, E. C., Tosdevin, T., Monk, K., Reynolds, A. M., Greaves, D., Hann, M. R., 2023. Real-time hybrid testing of a floating offshore wind turbine using a surrogate-based aerodynamic emulator. ASME Open Journal of Engineering, 2. https://doi.org/10.1115/1.4056963

Rao, M. J., Nallayarasu, S., Bhattacharyya, S., 2021. CFD approach to heave damping of spar with heave plates with experimental validation. Applied Ocean Research, 108, 102517. https://doi.org/10.1016/j.apor.2020.102517

Rao, M. J., Nallayarasu, S., Bhattacharyya, S., 2021. Numerical and experimental studies of heave damping and added mass of spar with heave plates using forced oscillation. Applied Ocean Research, 111, 102667. https://doi.org/10.1016/j.apor.2021.102667

Rockel, S., Camp, E., Schmidt, J., Peinke, J., Cal, R. B., Hölling, M., 2014. Experimental study on influence of pitch motion on the wake of a floating wind turbine model. Energies, 7(4), 1954-1985. https://doi.org/10.3390/en7041954

Rockel, S., Peinke, J., Hölling, M., Cal, R. B., 2016. Wake to wake interaction of floating wind turbine models in free pitch motion: An eddy viscosity and mixing length approach. Renewable Energy, 85, 666-676. https://doi.org/10.1016/j.renene.2015.07.012

Rodman, L. C., Wood, N. J., Roberts, L., 1989. Experimental investigation of straight and curved annular wall jets. AIAA journal, 27(8), 1059-1067. https://doi.org/10.2514/3.10221

Rodrigues, J. M., Viuff, T., Økland, O. D., 2022. Model tests of a hydroelastic truncated floating bridge. Applied Ocean Research, 125, 103247. https://doi.org/10.1016/j.apor.2022.103247

Rosa-Santos, P., Veloso-Gomes, F., Taveira-Pinto, F., Brógueira-Dias, E., Guedes-Lopes, H., 2008. Improving operational conditions at Leixões oil terminal–Portugal. In Proc. of the 7th International Conference on Coastal and Port Engineering in Developing Countries (COPEDEC VII), Dubai, United Arab Emirates, February (pp. 24-28).

Rudan, S., Karačić, J., Ćatipović, I., 2021. Non-linear response of a moored LNG ship subjected to regular waves. Ships and Offshore Structures, 16(sup1), 44-57. https://doi.org/10.1080/17445302.2021.1907064

Sadraddin, H. L., 2022. Developing Distributed Real-Time Hybrid Simulation for Dynamic Response Evaluation of Floating Wind Turbine. Western Michigan University.

Sakthivel, S., Kumar, N., Poguluri, S. K., 2023. Dynamic responses of serially connected truss pontoon-MOB–A numerical investigation. Ocean Engineering, 277, 114209. https://doi.org/10.1016/j.oceaneng.2023.114209

Sakthivel, S., Rajamanickam, P. S., 2022. Hydroelastic responses of a Truss Pontoon Mobile Offshore Base–An experimental investigation. Ocean Engineering, 259, 111889. https://doi.org/10.1016/j.oceaneng.2022.111889

Sauder, T., Chabaud, V., Thys, M., Bachynski, E. E., Sæther, L. O., 2016. Real-time hybrid model testing of a braceless semi-submersible wind turbine: Part I—The hybrid approach. In International conference on offshore mechanics and arctic engineering (Vol. 49972, p. V006T09A039). American Society of Mechanical Engineers. https://doi.org/10.1115/OMAE2016-54435

Sayed, M., Islam, S., Watson, D., Kubat, I., Gash, R., Wright, B., 2017. DP Drillship Stationkeeping in Ice-Comparison between Numerical Simulations and Ice Basin Tests. In ISOPE International Ocean and Polar Engineering Conference (pp. ISOPE-I). ISOPE.

Schliffke, B., Aubrun, S., Conan, B., 2020. Wind tunnel study of a “floating” wind turbine’s wake in an atmospheric boundary layer with imposed characteristic surge motion. In Journal of Physics: Conference Series (Vol. 1618, No. 6, p. 062015). IOP Publishing. doi:10.1088/1742-6596/1618/6/062015

Scott, D. C. B., Muir, J. F., 2000. Offshore cage systems: A practical overview. Option Mediterraneennes-International Centre for Advanced Mediterranean Agronomic Studies, 79-89.

Shainee, M., Leira, B. J., Ellingsen, H., Fredheim, A., 2012. An optimum design concept for offshore cage culture. In International Conference on Offshore Mechanics and Arctic Engineering (Vol. 44946, pp. 85-93). American Society of Mechanical Engineers. https://doi.org/10.1115/OMAE2012-83601

Shen, W., Chen, H., Jiang, Y., Gao, F., 2020. Analysis of resonance characteristics of FSRU and LNG ship under side by side operation. In ISOPE Pacific/Asia Offshore Mechanics Symposium (pp. ISOPE-P). ISOPE.

Shen, Y., Firoozkoohi, R., Greco, M., Faltinsen, O. M., 2022. Comparative investigation: Closed versus semi-closed vertical cylinder-shaped fish cage in waves. Ocean Engineering, 245, 110397. https://doi.org/10.1016/j.oceaneng.2021.110397

Silva de Souza, C. E., Berthelsen, P. A., Eliassen, L., Bachynski, E. E., Engebretsen, E., Haslum, H., 2021. Definition of the INO WINDMOOR 12 MW base case floating wind turbine.

Sim, J., Cheng, H., Aarsæther, K. G., Li, L., Ong, M. C., 2021. Numerical investigation on the cage-to-cage wake effect: a case study of a 4× 2 cage array. Journal of Offshore Mechanics and Arctic Engineering, 143(5), 051301. https://doi.org/10.1115/1.4049831

Simon-Lledó, E., Bett, B. J., Huvenne, V. A., Schoening, T., Benoist, N. M., Jeffreys, R. M., Durden, J. M., Jones, D. O., 2019. Megafaunal variation in the abyssal landscape of the Clarion Clipperton Zone. Progress in oceanography, 170, 119-133. https://doi.org/10.1016/j.pocean.2018.11.003

Slagstad, M., Amdahl, J., Yu, Z., 2024. A simplified force response calculation of circular pre-tensioned aquaculture nets in waves and current. Ocean Engineering, 294, 116825. https://doi.org/10.1016/j.oceaneng.2024.116825

Slagstad, M., Yu, Z., Amdahl, J., 2023. A simplified approach for fatigue life prediction of aquaculture nets under waves and currents. Ocean Engineering, 272, 113859. https://doi.org/10.1016/j.oceaneng.2023.113859

Soffer, R., Kit, E., Toledo, Y., 2023. Method of directional spectrum estimation accounting for the ambient shearing currents. Physical Review Fluids, 8(6), L062801. https://doi.org/10.1103/PhysRevFluids.8.L062801

Somoano, M., Battistella, T., Fernández-Ruano, S., Guanche, R., 2021. Uncertainties assessment in real-time hybrid model for ocean basin testing of a floating offshore wind turbine. In Journal of Physics: Conference Series (Vol. 2018, No. 1, p. 012036). IOP Publishing. doi:10.1088/1742-6596/2018/1/012036

Stansberg C.T., 2020. Wave Front Steepness and Influence on Horizontal Deck Impact Loads. Journal of Marine Science and Engineering, 8(5):314. https://doi.org/10.3390/jmse8050314

Stern, F., Wilson, R. V., Coleman, H. W., Paterson, E. G., 2001. Comprehensive approach to verification and validation of CFD simulations—part 1: methodology and procedures. J. Fluids Eng., 123(4), 793-802. https://doi.org/10.1115/1.1412235

Suja, L., Bachynski, E. E., Pierella, F., Borg, M., Krokstad, J. R., Bredmose, H., 2020. Critical assessment of hydrodynamic load models for a monopile structure in finite water depth. https://doi.org/10.1016/j.marstruc.2020.102743

Sun, C., Song, W., Jahangiri, V., 2022. A real-time hybrid simulation framework for floating offshore wind turbines. Ocean Engineering, 265, 112529. https://doi.org/10.1016/j.oceaneng.2022.112529

Tan, L., Lu, L., Tang, G. Q., Cheng, L., Chen, X. B., 2019. A viscous damping model for piston mode resonance. Journal of Fluid Mechanics, 871, 510-533. https://doi.org/10.1017/jfm.2019.302

Tang, L., Wang, L., Wang, Y., Zhang, Y., 2022. An enhanced trajectory tracking control of the dynamic positioning ship based on nonlinear model predictive control and disturbance observer. Ocean Engineering, 265, 112482. https://doi.org/10.1016/j.oceaneng.2022.112482

Taveira-Pinto, F., Neves, A., Santos, P., Silva, R., Veloso-Gomes, F., 2010, The importance of physical modelling to solve coastal engineering complex problems – Experience from some PhD research projects, Coastal Engineering, PhD Research Projects.

Tay, Z. Y., 2023. Artificial neural network framework for prediction of hydroelastic response of very large floating structure. Applied Ocean Research, 139, 103701. https://doi.org/10.1016/j.apor.2023.103701

Teng, Y., Tan, J. H., 2022. CFD-Based Simulations of Hydrodynamic Behaviors of a Floating Barge Near Shore. In Offshore Technology Conference Asia (p. D021S003R005). OTC. https://doi.org/10.4043/31480-MS

Thys, M., Fontanella, A., Taruffi, F., Belloli, M., Berthelsen, P. A., 2019. Hybrid model tests for floating offshore wind turbines. In International Conference on Offshore Mechanics and Arctic Engineering (Vol. 59353, p. V001T01A023). American Society of Mechanical Engineers. https://doi.org/10.1115/IOWTC2019-7575

Thys, M., Souza, C., Sauder, T., Fonseca, N., Berthelsen, P. A., Engebretsen, E., Haslum, H., 2021. Experimental investigation of the coupling between aero-and hydrodynamical loads on a 12 mw semi-submersible floating wind turbine. In International Conference on Offshore Mechanics and Arctic Engineering (Vol. 85192, p. V009T09A030). American Society of Mechanical Engineers. https://doi.org/10.1115/OMAE2021-62980

Toffoli, A., Ducrozet, G., Waseda, T., Onorato, M., Abdolahpour, M., Nelli, F., 2019. Ocean currents trigger rogue waves. In ISOPE International Ocean and Polar Engineering Conference (pp. ISOPE-I). ISOPE.

Tu, Z., Zhang, C., Liu, H., Zhu, R., 2023. Hydrodynamic analysis of a multi-pile-supported offshore wind turbine integrated with an aquaculture cage. Journal of Marine Science and Engineering, 11(9), 1830. https://doi.org/10.3390/jmse11091830

Turner, I. L., Harley, M. D., Short, A. D., Simmons, J. A., Bracs, M. A., Phillips, M. S., Splinter, K. D., 2016. A multi-decade dataset of monthly beach profile surveys and inshore wave forcing at Narrabeen, Australia. Scientific data, 3(1), 1-13. doi: 10.1038/sdata.2016.24

Urbán, A. M., Guanche, R., 2019. Wind turbine aerodynamics scale-modeling for floating offshore wind platform testing. Journal of Wind Engineering and Industrial Aerodynamics, 186, 49-57. https://doi.org/10.1016/j.jweia.2018.12.021

Vanem, E., Antao, P., Østvik, I., de Comas, F. D. C., 2008. Analysing the risk of LNG carrier operations. Reliability Engineering & System Safety, 93(9), 1328-1344. https://doi.org/10.1016/j.ress.2007.07.007

Veloso-Gomes, F., Taveira-Pinto, F., Rosa-Santos, P., Brógueira-Dias, E., Guedes-Lopes, H., 2005. Berthing characteristics and the behaviour of the oil terminal of Leixões Harbour, Portugal. WIT transactions on the built environment, 79. doi: 10.2495/MH050451

Vittori, F., Azcona, J., Eguinoa, I., Pires, O., Rodríguez, A., Morató, Á., Garrido, C., Desmond, C., 2022. Model tests of a 10 MW semi-submersible floating wind turbine under waves and wind using hybrid method to integrate the rotor thrust and moments. Wind Energy Science, 7(5), 2149-2161. https://doi.org/10.5194/wes-7-2149-2022, 2022.

Vittori, F., Pires, O., Azcona, J., Uzunoglu, E., Soares, C. G., Rodríguez, R. Z., Souto-Iglesias, A., 2020. Hybrid scaled testing of a 10MW TLP floating wind turbine using the SiL method to integrate the rotor thrust and moments. In Developments in Renewable Energies Offshore (pp. 417-423). CRC Press.

Wang, B., Liang, X., Jiang, X., 2022. Experimental and Numerical Investigation on the Dynamic Response of Platform for a Spar-Type Floating Wind Turbine Under Aerodynamic and Hydrodynamic Forces. In International Conference on Offshore Mechanics and Arctic Engineering (Vol. 85932, p. V008T09A062). American Society of Mechanical Engineers. https://doi.org/10.1115/OMAE2022-81290

Wang, H., Wolgamot, H. A., Draper, S., Zhao, W., Taylor, P. H., Cheng, L., 2019. Resolving wave and laminar boundary layer scales for gap resonance problems. Journal of Fluid Mechanics, 866, 759-775. https://doi.org/10.1017/jfm.2019.115

Wang, H., Zhang, X., Zhang, X., Li, X., Tian, X., Shen, Y., Song, W., 2023. Experimental investigations on hydrodynamic interactions between the cylinder and nets of a typical offshore aquacultural structure in steady current. Marine Structures, 88, 103367. https://doi.org/10.1016/j.marstruc.2022.103367

Wang, J., Ma, Q., Yan, S., 2021. On extreme waves in directional seas with presence of oblique current. Applied Ocean Research, 112, 102586. https://doi.org/10.1016/j.apor.2021.102586

Wang, J., Sayeed, T., Millan, D., Gash, R., Islam, M., Millan, J., 2016. Ice model tests for dynamic positioning vessel in managed ice. In OTC Arctic Technology Conference (pp. OTC-27430). OTC. https://doi.org/10.4043/27430-MS

Wang, L., Li, J. X., Liu, S. X., Fan, Y. P., 2020. Experimental and numerical studies on the focused waves generated by double wave groups. Frontiers in Energy Research, 8, 133. https://doi.org/10.3389/fenrg.2020.00133

Wang, S., 2022. Analytical solutions for the dynamic analysis of a modular floating structure for urban expansion. Ocean Engineering, 266, 112878. https://doi.org/10.1016/j.oceaneng.2022.112878

Wang, Y., Fu, S., Xu, Y., Li, S., Moan, T., 2022. Loads on a vessel-shaped fish cage steel structures, nets and connectors considering the effects of diffraction and radiation waves. Marine Structures, 86, 103301. https://doi.org/10.1016/j.marstruc.2022.103301

Wang, Y., Fu, S., Xu, Y., Cheng, T., Li, S., Moan, T., Fu, Q., Liu, F., 2023. Load effects on vessel-shaped fish cage steel structures, nets and connectors considering the effects of diffraction and radiation waves under irregular waves. Marine Structures, 91, 103468. https://doi.org/10.1016/j.marstruc.2023.103468

Wang, Y., Tang, Z., Wang, L., Wang, X., 2022. Linear and quadratic damping coefficients of a single module of a very large floating structure over variable bathymetry: physical and numerical free-decay experiments. Journal of Ocean Engineering and Science, 7(6), 607-618. https://doi.org/10.1016/j.joes.2021.10.011

Wang, Y., Wang, H., Li, M., Wang, D., Fu, M., 2021. Adaptive fuzzy controller design for dynamic positioning ship integrating prescribed performance. Ocean Engineering, 219, 107956. https://doi.org/10.1016/j.oceaneng.2020.107956

Welling, C. G., 1981. An advanced design deep sea mining system. In Offshore Technology Conference (pp. OTC-4094). OTC. https://doi.org/10.4043/4094-MS

Wen, B., Liang, Z., Zhang, H., Fan, K., Wang, Y., Li, D., Tian, X., Peng, Z., 2023. A multi-drive aerodynamic load simulator for floating wind turbine model tests: Development, test and application. Ocean Engineering, 286, 115579. https://doi.org/10.1016/j.oceaneng.2023.115579

Wiegerink, J. J., Baldock, T. E., Callaghan, D. P., Wang, C. M., 2023. Experimental study on hydrodynamic response of a floating rigid fish tank model with slosh suppression blocks. Ocean Engineering, 273, 113772. https://doi.org/10.1016/j.oceaneng.2023.113772

Wright, C. S., Yoshimoto, H., Wada, R., Takagi, K., 2022. Surge slow drift viscous drag damping of an advanced spar: A numerical–experimental method for variable damping rates. Ocean Engineering, 266, 112696. https://doi.org/10.1016/j.oceaneng.2022.112696

Xiong, H., Chen, Y., Yang, N., Xiao, J., Li, L., 2018. Numerical study on settling and floating movements of a sphere particle flowing in a vertical pipe. In ISOPE International Ocean and Polar Engineering Conference (pp. ISOPE-I). ISOPE.

Xu, G., Zhou, Y., Yan, S., Zhang, N., 2022. Numerical investigation of wave amplitude spectra effects on focusing wave generation. Ocean Engineering, 265, 112550. https://doi.org/10.1016/j.oceaneng.2022.112550

Xu, P., Wellens, P. R., 2022. Theoretical analysis of nonlinear fluid–structure interaction between large-scale polymer offshore floating photovoltaics and waves. Ocean Engineering, 249, 110829. https://doi.org/10.1016/j.oceaneng.2022.110829

Xu, S., Wang, X., Yang, J., Wang, L., 2020. A fuzzy rule-based PID controller for dynamic positioning of vessels in variable environmental disturbances. Journal of Marine Science and Technology, 25, 914-924. https://doi.org/10.1007/s00773-019-00689-2

Xu, X., Yang, J. M., Li, X., Xu, L., 2014. Hydrodynamic performance study of two side-by-side barges. Ships and Offshore Structures, 9(5), 475-488. https://doi.org/10.1080/17445302.2014.889368

Yamada, H., Yamazaki, T., 1998. Japan's ocean test of the nodule mining system. In ISOPE International Ocean and Polar Engineering Conference (pp. ISOPE-I). ISOPE.

Yang, J. S., Yang, J. L., Wang, B., 2023. Boundary control for floating beam system in irregular waves under one end pinned to reduce hydroelastic response. Ocean Engineering, 270, 113586. https://doi.org/10.1016/j.oceaneng.2022.113586

Yang, N., Tang, H., 2003. Several considerations of the design of the hydraulic pick-up device. In ISOPE Ocean Mining and Gas Hydrates Symposium (pp. ISOPE-M). ISOPE.

Yeo, C., Bhandari, J., Abbassi, R., Garaniya, V., Chai, S., Shomali, B., 2016. Dynamic risk analysis of offloading process in floating liquefied natural gas (FLNG) platform using Bayesian Network. Journal of Loss Prevention in the Process Industries, 41, 259-269. https://doi.org/10.1016/j.jlp.2016.04.002

Young, D. L., Bak, A. S., Forte, M. F., 2018. Initialization and setup of the Coastal Model Test Bed: integrated bathymetry. http://dx.doi.org/10.21079/11681/30023

Yu, J., Cheng, X., Fan, Y., Ni, X., Chen, Y., Ye, Y., 2023. Mooring design of offshore aquaculture platform and its dynamic performance. Ocean Engineering, 275, 114146. https://doi.org/10.1016/j.oceaneng.2023.114146

Yu, L., Li, C., Wang, S., 2022. Model tests and numerical simulations on the parametric resonance of the deep draft semi-submersible under regular waves. Ocean Engineering, 243, 110273. https://doi.org/10.1016/j.oceaneng.2021.110273

Yu, W., Lemmer, F., Bredmose, H., Borg, M., Pegalajar-Jurado, A., Mikkelsen, R. F., Stoklund Larsen, T., Fjelstrup, T., Lomholt, A. K., Boehm, L., Schlipf, D., Azcona, Armendariz, J., Cheng, P. W., 2017. The triple spar campaign: Implementation and test of a blade pitch controller on a scaled floating wind turbine model. Energy Procedia, 137, 323-338. https://doi.org/10.1016/j.egypro.2017.10.357

Yu, W., Lemmer, F., Lehmann, K., Cheng, P. W., de Guzmán, S., Moreu, J., Battistella, T., 2022. Model test and validation of the CROWN floating offshore wind turbine. In International Conference on Offshore Mechanics and Arctic Engineering (Vol. 85932, p. V008T09A059). American Society of Mechanical Engineers. https://doi.org/10.1115/OMAE2022-81065

Yuan, L., Chen, Y., Zan, Y., Zhong, S., Jiang, M., Sun, Y., 2023. A novel hybrid approach to mooring tension prediction for semi-submersible offshore platforms. Ocean Engineering, 287, 115776. https://doi.org/10.1016/j.oceaneng.2023.115776

Yue, Z., Zhao, G., Xiao, L., Liu, M., 2021. Comparative study on collection performance of three nodule collection methods in seawater and sediment-seawater mixture. Applied Ocean Research, 110, 102606. https://doi.org/10.1016/j.apor.2021.102606

Zeng, X., Shi, W., Michailides, C., Zhang, S., Li, X., 2021. Numerical and experimental investigation of breaking wave forces on a monopile-type offshore wind turbine. Renewable energy, 175, 501-519. https://doi.org/10.1016/j.renene.2021.05.009

Zhang, D., Yuan, Z. M., Du, J., Li, H., 2022. Hydrodynamic modelling of large arrays of modularized floating structures with independent oscillations. Applied Ocean Research, 129, 103371. https://doi.org/10.1016/j.apor.2022.103371

Zhang, G., Yao, M., Xu, J., Zhang, W., 2020. Robust neural event-triggered control for dynamic positioning ships with actuator faults. Ocean Engineering, 207, 107292. https://doi.org/10.1016/j.oceaneng.2020.107292

Zhang, G., Yao, M., Zhang, W., Zhang, W., 2021. Event-triggered distributed adaptive cooperative control for multiple dynamic positioning ships with actuator faults. Ocean Engineering, 242, 110124. https://doi.org/10.1016/j.oceaneng.2021.110124

Zhang, H., Gui, F., 2023. The application and research of new digital technology in marine aquaculture. Journal of Marine Science and Engineering, 11(2), 401. https://doi.org/10.3390/jmse11020401

Zhang, H., Liu, S., Ong, M. C., Zhu, R., 2019. CFD Simulations of the propagation of free-surface waves past two side-by-side fixed squares with a narrow gap. Energies, 12(14), 2669. https://doi.org/10.3390/en12142669

Zhang, H., Tang, W., Yuan, Y., Xue, H., Qin, H., 2022. The three-dimensional green-water event study on a fixed simplified wall-sided ship under freak waves. Ocean Engineering, 251, 111096. https://doi.org/10.1016/j.oceaneng.2022.111096

Zhang, J., Ma, Y., Tan, T., Dong, G., Benoit, M., 2023. Enhanced extreme wave statistics of irregular waves due to accelerating following current over a submerged bar. Journal of Fluid Mechanics, 954, A50. https://doi.org/10.1017/jfm.2022.1022

Zhang, M., Schreier, S., 2022. Review of wave interaction with continuous flexible floating structures. Ocean Engineering, 264, 112404. https://doi.org/10.1016/j.oceaneng.2022.112404

Zhang, X., Simons, R., Zheng, J., Zhang, C., 2022. A review of the state of research on wave-current interaction in nearshore areas. Ocean Engineering, 243, 110202. https://doi.org/10.1016/j.oceaneng.2021.110202

Zhang, Y., Feng, L., Zhang, L., Wang, L., Dong, S., Gao, Q., Hu, X., Li, J., 2024. A study of tension and deformation of flexible net under the action of current. Ships and Offshore Structures, 19(1), 27-44. https://doi.org/10.1080/17445302.2022.2140532

Zhang, Y., Teng, B., 2021. A nonlinear potential flow model for higher-harmonic wave loads and ringing response of a monopile. Ocean Engineering, 222, 108574. https://doi.org/10.1016/j.oceaneng.2021.108574

Zhao, G., Xiao, L., Peng, T., Zhang, M., 2018. Experimental research on hydraulic collecting spherical particles in deep sea mining. Energies, 11(8), 1938. https://doi.org/10.3390/en11081938

Zhao, G., Xiao, L., Yue, Z., Liu, M., Peng, T., Zhao, W., 2021. Performance characteristics of nodule pick-up device based on spiral flow principle for deep-sea hydraulic collection. Ocean Engineering, 226, 108818. https://doi.org/10.1016/j.oceaneng.2021.108818

Zhao, M., Yu, Y., Li, Z., Liu, C., Pang, H., 2023. Effect of bottom unlatch and top breakage mooring lines on the dynamic behavior of a semisubmersible platform system. Ocean Engineering, 276, 114182. https://doi.org/10.1016/j.oceaneng.2023.114182

Zhao, W., Taylor, P. H., Wolgamot, H. A., Taylor, R. E., 2018. Linear viscous damping in random wave excited gap resonance at laboratory scale—NewWave analysis and reciprocity. Journal of Fluids and Structures, 80, 59-76. https://doi.org/10.1016/j.jfluidstructs.2018.03.002

Zhao, Y., Xie, S., Ma, C., 2022. Experimental investigations on the hydrodynamics of a multi-body floating aquaculture platform exposed to sloping seabed environment. Frontiers in Marine Science, 9, 1049769. https://doi.org/10.3389/fmars.2022.1049769

Zhao, Y. P., Lian, L., Bi, C. W., Xu, Z., 2022. Digital twin for rapid damage detection of a fixed net panel in the sea. Computers and Electronics in Agriculture, 200, 107247. https://doi.org/10.1016/j.compag.2022.107247

Zhao, Y. P., Liu, H. F., Bi, C. W., Cui, Y., Guan, C. T., 2021. Numerical study on the flow field inside and around a semi-submersible aquaculture platform. Applied Ocean Research, 115, 102824. https://doi.org/10.1016/j.apor.2021.102824

Zheng, X. Y., Zheng, H. D., Lei, Y., Chen, H., 2021. Nonlinear stochastic responses of a newly developed floating wind-solar-aquaculture system. Ocean Engineering, 241, 110055. https://doi.org/10.1016/j.oceaneng.2021.110055

Zheng, Z., Li, Y., Ellingsen, S. Å., 2023. Statistics of weakly nonlinear waves on currents with strong vertical shear. Physical Review Fluids, 8(1), 014801. https://doi.org/10.1103/PhysRevFluids.8.014801

Zhi, P., Pei, H., Zhang, X., Xu, N., Yang, J., You, Y., 2022. Experimental studies on the effects of draft condition, current heading and mooring stiffness on vortex-induced motions of a Tension-Leg Platform. Ocean Engineering, 266, 112882. https://doi.org/10.1016/j.oceaneng.2022.112882

Zhou, B., Ding, K., Huang, J., Wang, L., Guo, J., Tang, T., 2024. Influence of uniform currents on nonlinear characteristics of double-wave-group focusing. Physics of Fluids, 36(3). https://doi.org/10.1063/5.0190701

Zhou, J., Ren, J., Bai, W., 2023. Survey on hydrodynamic analysis of ship–ship interaction during the past decade. Ocean Engineering, 278, 114361. https://doi.org/10.1016/j.oceaneng.2023.114361

Zhou, K., Hu, Z., Zhao, D., 2018. Time-domain analysis of the relative motions between side-by-side FLNG and LNGC under oblique waves. Journal of Marine Science and Application, 17, 519-530. https://doi.org/10.1007/s11804-018-0038-0

Zhou, Q., Liu, M., Peng, H., Qiu, W., 2015. Experimental studies of hydrodynamic interaction of two bodies in waves. In International Conference on Offshore Mechanics and Arctic Engineering (Vol. 56598, p. V011T12A011). American Society of Mechanical Engineers. https://doi.org/10.1115/OMAE2015-41304